



SENSORDEVICES 2012

The Third International Conference on Sensor Device Technologies and
Applications

WISH 2012

The Second International Workshop on Intelligent Sensor Hub

ISBN: 978-1-61208-208-0

August 19-24, 2012

Rome, Italy

SENSORDEVICES 2012 Editors

Sergey Yurish, IFSA - Barcelona, Spain

Irinela Chilibon, National Institute of Research and Development for
Optoelectronics - Bucharest, Romania

Vítor Carvalho, Minho University, Portugal

Stephane Gervais-Ducouret, Freescale, France

SENSORDEVICES 2012

Foreword

The Third International Conference on Sensor Device Technologies and Applications [SENSORDEVICES 2012], held between August 19-24, 2012 in Rome, Italy, continued a series of events focusing on sensor devices themselves, the technology-capturing style of sensors, special technologies, signal control and interfaces, and particularly sensors-oriented applications. The evolution of the nano-and microtechnologies, nanomaterials, and the new business services make the sensor device industry and research on sensor-themselves very challenging.

SENSORDEVICES 2012 also featured the following workshop:
- WISH 2012, The Second International Workshop on Intelligent Sensor Hub

We take here the opportunity to warmly thank all the members of the SENSORDEVICES 2012 Technical Program Committee, as well as the numerous reviewers. The creation of such a high quality conference program would not have been possible without their involvement. We also kindly thank all the authors who dedicated much of their time and efforts to contribute to SENSORDEVICES 2012. We truly believe that, thanks to all these efforts, the final conference program consisted of top quality contributions.

Also, this event could not have been a reality without the support of many individuals, organizations, and sponsors. We are grateful to the members of the SENSORDEVICES 2012 organizing committee for their help in handling the logistics and for their work to make this professional meeting a success. We hope that SENSORDEVICES 2012 was a successful international forum for the exchange of ideas and results between academia and industry and for the promotion of progress in the area of sensor device technologies and applications.

We are convinced that the participants found the event useful and communications very open. We also hope the attendees enjoyed the historic charm Rome, Italy.

SENSORDEVICES 2012 Chairs:

Vítor Carvalho, Minho University, Portugal

Irinela Chilibon, National Institute of Research and Development for Optoelectronics - Bucharest, Romania

Petre Dini, Concordia University, Canada / China Space Agency Center, China

Vittorio Ferrari, Università di Brescia, Italy

Elena Gaura, Coventry University, UK

Stephane Gervais-Ducouret, Freescale Semiconductor, Inc., France

Thomas Herzog, Fraunhofer Institute for Non-Destructive Testing IZFP - Dresden, Germany

Henning Heuer, Fraunhofer Institute for Non-Destructive Testing IZFP - Dresden, Germany

Subodh Kumar Singhal, National Physical Laboratory, New Delhi, India

Ksenia V. Sapozhnikova D.I. Mendeleev Institute for Metrology - St. Petersburg, Russia

Raluca - Ioana Stefan-van Staden, National Institute of Research for Electrochemistry and Condensed Matter, Bucharest, Romania

Marco Tartagni, University of Bologna - Cesena, Italy

Dongfang Yang, National Research Council Canada - London, Canada

Alberto Yúfera, Centro Nacional de Microelectronica (CNM-CSIC) - Sevilla, Spain

Sergey Yurish, IFSA - Barcelona, Spain

SENSORDEVICES 2012

Committee

SENSORDEVICES Advisory Chairs

Sergey Yurish, IFSA - Barcelona, Spain
Petre Dini, Concordia University, Canada / China Space Agency Center, China
Elena Gaura, Coventry University, UK
Vittorio Ferrari, Università di Brescia, Italy

SENSORDEVICES 2012 Research/Industry Chairs

Raluca - Ioana Stefan-van Staden, National Institute of Research for Electrochemistry and Condensed Matter, Bucharest, Romania
Alberto Yúfera, Centro Nacional de Microelectronica (CNM-CSIC) - Sevilla, Spain

SENSORDEVICES Special Area Chairs

Ultrasonic and piezoelectric sensors
Thomas Herzog, Fraunhofer Institute for Non-Destructive Testing IZFP - Dresden, Germany
Henning Heuer, Fraunhofer Institute for Non-Destructive Testing IZFP - Dresden, Germany

Optical sensors

Vítor Carvalho, Minho University, Portugal
Irinela Chilibon, National Institute of Research and Development for Optoelectronics - Bucharest, Romania

Gas sensors

Dongfang Yang, National Research Council Canada - London, Canada

Nanosensors

Marco Tartagni, University of Bologna - Cesena, Italy

Testing and validation

Ksenia V. Sapozhnikova D.I. Mendeleev Institute for Metrology - St. Petersburg, Russia

Vibration sensors

Subodh Kumar Singhal, National Physical Laboratory, New Delhi, India

SENSORDEVICES 2012 Technical Program Committee

Selcuk Atalay, Inonu University - Malatya, Turkey
Francisco Javier Arcega Solsona, University of Zaragoza, Spain
Faruk Bagci, German University Cairo, Egypt

Sukumar Basu, Jadavpur University - Kolkata, India
Juarez Bento da Silva, Universidade Federal de Santa Catarina, Brazil
Partha Bhattacharyya, Bengal Engineering and Science University, West Bengal, India
Virginie Blondeau-Patissier, Université de Franche-Comté, France
Michal Borecki, Warsaw University of Technology, Poland
Jaime Calvo-Gallego, University of Salamanca - Zamora, Spain
Vítor Carvalho, Minho University, Portugal
Gustavo Cerda-Villafaña, University of Guanajuato, Mexico
Sudhir Chandra, Indian Institute of Technology Delhi - New Delhi, India
Irinela Chilibon, National Institute of R&D for Optoelectronics - Bucharest-Magurele, Romania
Jeong-Woo Choi, Sogang University - Seoul, Korea
Caterina Ciminelli, Politecnico of Bari, Italy
Alberto Corigliano, Politecnico di Milano, Italy
Rodrigo P.B. Costa-Felix, INMETRO, Brazil
Anna Cysewska-Sobusiak, Poznan University of Technology, Poland
Boris Zaitsev Davydovich, Russian Academy of Sciences - Saratov Branch, Russia
Francesco De Leonardis, Politecnico di Bari, Italy
Matthieu Denoual, ENSICAEN, France
Dermot Diamond, Dublin City University, Ireland
Alexandar Djordjevich, City University of Hong Kong, Hong Kong
Miguel Fernandes, UNINOVA - Caparica, Portugal
Vittorio Ferrari, Università di Brescia, Italy
Masato Futagawa, Toyohashi University of Technology, Japan
Jong-in Hahm, Georgetown University - Washington DC, USA
Thomas Herzog, Fraunhofer Institute for Non-Destructive Testing IZFP - Dresden, Germany
Henning Heuer, Fraunhofer Institute for Non-Destructive Testing IZFP - Dresden, Germany
Vladan Koncar, ENSAIT Research, France
Vladimir Laukhin, Institució Catalana de Recerca i Estudis Avançats (ICREA / Institut de Ciència de Materials de Barcelona (ICMAB-CSIC) - Barcelona, Spain
Elena Laukhina, Networking Research Center on Bioengineering, Biomaterials and Nanomedicine (CIBER-BBN) - Bellaterra, Spain
Yann-Aël Le Borgne, Université Libre de Bruxelles, Belgium
Kevin Lee, Murdoch University, Australia
Aihua Liu, Qingdao Institute of Bioenergy & Bioprocess Technology, Chinese Academy of Sciences, China
Salvatore A. Lombardo, CNR-IMM - Catania, Italy
Jerzy P. Lukaszewicz, Nicholas Copernicus University - Torun, Poland
Stefano Mariani, Politecnico di Milano, Italy Iren Kuznetsova, Russian Academy of Sciences - Saratov Branch, Russia
Hamed Sadeghian Marnani, Delft University of Technology, The Netherlands
Marek Miskowicz, AGH University of Science and Technology - Cracow, Poland
Tarek Mohammad, University of Western Ontario - London, Canada
Gaidi Mounir, Centre de Recherches et des Technologies de l'Energie (CRTE), Tunisie
Eros Pasero, Politecnico di Torino, Italy
Vittorio M.N. Passaro, Politecnico di Bari, Italy
Konandur Rajanna, Indian Institute of Science - Bangalore, India
Càndid Reig, University of Valencia, Spain
Teresa Restivo, University of Porto, Portugal
Aldo Romani, University of Bologna, Italy

Mounir Bousbia Salah, University of Annaba, Algeria
Ksenia V. Sapozhnikova D.I. Mendeleev Institute for Metrology - St. Petersburg, Russia
Yuriy Shmaliy, Guanajuato University, Mexico
Subodh Kumar Singhal, National Physical Laboratory - New Delhi, India
Junho Song, Sunnybrook Research Institutes/University of Toronto, Canada
Arvind K. Srivastava, NanoSonix Inc., USA
Nickolaj Starodub, National University of Life and Environmental Sciences of Ukraine, / T. Shevchenko
Kiev State University of Ukraine, Ukraine
Arndt Steinke, CiS Forschungsinstitut für Mikrosensorik und Photovoltaik GmbH - Erfurt, Germany
Raluca - Ioana Stefan-van Staden, National Institute of Research for Electrochemistry and Condensed
Matter, Bucharest, Romania
Chelakara S. Subramanian, Florida Institute of Technology - Melbourne, USA
Roman Szewczyk, Warsaw University of Technology, Poland
Marco Tartagni, University of Bologna - Cesena, Italy
Roald Taymanov, D.I.Mendeleev Institute for Metrology, Russia
Antonio Valente, University of Trás-os-Montes and Alto Douro (UTAD) - Vila Real, Portugal
Manuela Vieira, UNINOVA/ISEL, Portugal
Dongfang Yang, National Research Council Canada - London, Canada
Dan Yaping, Harvard University, USA
Alberto Yúfera, Seville Microelectronics Institute (IMSE-CNM), Spain
Sergey Y. Yurish, IFSA, Spain
Cyrus Zamani, University of Barcelona, Spain
Weiping Zhang, Shanghai Jiao Tong University, P. R. China
Ya-Pu Zhao, Chinese Academy of Sciences - Beijing, China

WISH 2012 PROGRAMM COMMITTEE

Workshop Chair

Stephane Gervais-Ducouret, Freescale Semiconductor, Inc., France

WISH 2012 Technical Program Committee

Stephane Gervais-Ducouret, Freescale Semiconductor, Inc., France

Francois Pacull, CEA-Leti Minatec, France

Laurent Perroton, ESIEE - Cite Descartes, France

Copyright Information

For your reference, this is the text governing the copyright release for material published by IARIA.

The copyright release is a transfer of publication rights, which allows IARIA and its partners to drive the dissemination of the published material. This allows IARIA to give articles increased visibility via distribution, inclusion in libraries, and arrangements for submission to indexes.

I, the undersigned, declare that the article is original, and that I represent the authors of this article in the copyright release matters. If this work has been done as work-for-hire, I have obtained all necessary clearances to execute a copyright release. I hereby irrevocably transfer exclusive copyright for this material to IARIA. I give IARIA permission to reproduce the work in any media format such as, but not limited to, print, digital, or electronic. I give IARIA permission to distribute the materials without restriction to any institutions or individuals. I give IARIA permission to submit the work for inclusion in article repositories as IARIA sees fit.

I, the undersigned, declare that to the best of my knowledge, the article does not contain libelous or otherwise unlawful contents or invading the right of privacy or infringing on a proprietary right.

Following the copyright release, any circulated version of the article must bear the copyright notice and any header and footer information that IARIA applies to the published article.

IARIA grants royalty-free permission to the authors to disseminate the work, under the above provisions, for any academic, commercial, or industrial use. IARIA grants royalty-free permission to any individuals or institutions to make the article available electronically, online, or in print.

IARIA acknowledges that rights to any algorithm, process, procedure, apparatus, or articles of manufacture remain with the authors and their employers.

I, the undersigned, understand that IARIA will not be liable, in contract, tort (including, without limitation, negligence), pre-contract or other representations (other than fraudulent misrepresentations) or otherwise in connection with the publication of my work.

Exception to the above is made for work-for-hire performed while employed by the government. In that case, copyright to the material remains with the said government. The rightful owners (authors and government entity) grant unlimited and unrestricted permission to IARIA, IARIA's contractors, and IARIA's partners to further distribute the work.

Table of Contents

Ability of Acoustic Sensor Devices for Medical Analysis <i>Thomas Rosel, Achim Voigt, and Friederike J. Gruhl</i>	1
Neural Cell Chip to Assess Toxicity Based on Spectroelectrochemical Technique <i>Jeong-Woo Choi and Tae-Hyung Kim</i>	5
Medical Wireless Vibration Measurement System for Hip Prosthesis Loosening Detection <i>Sebastian Sauer, Uwe Marschner, Hagen Graetz, and Wolf-Joachim Fischer</i>	9
Sensing of the Functional State of Fertility of Cows <i>Michal Borecki, Michael L. Korwin-Pawlowski, Marcin Kozicki, Jan Szmidt, Andrzej Jakubowski, Szmidt Maciej, and Kaja Urbanska</i>	14
Bend Sensors Modeling for Fast Signal Recovering in Human Motion Analysis <i>Giancarlo Orengo, Antonino Lagati, and Giovanni Saggio</i>	21
SiC Multilayer Photonic Structures <i>Manuela Vieira, Manuel Vieira, Paula Louro, Alessandro Fantoni, and Vitor Silva</i>	25
A Novel Flexure Parallel Micromanipulator Based on Multi-Level Displacement Amplifier <i>Dan Zhang, Zhen Gao, Matteo Malosio, and Gianmarc Coppola</i>	31
Improvement of the Diffusive Component of Dark Current in Silicon Photomultiplier Pixels <i>Roberto Pagano, Sebania Libertino, Domenico Corso, Salvatore Lombardo, Giuseppina Valvo, Delfo Sanfilippo, Giovanni Condorelli, Massimo Mazzillo, Angelo Piana, Beatrice Carbone, and Giorgio Fallica</i>	38
Impedance Measurements of Ethanol Sensing with Vanadium oxide / Porous Si / Si Structure <i>Katia Chebout, Aicha Iratni Aicha Iratni, Ahmed Bouremana, Kawthar M'hammedi, Hamid Menari, Aissa Keffous, and Nouredine Gabouze</i>	42
Wireless and Passive Sensors for High Temperature Measurements <i>Bruno Francois, Denny Richter, Holger Fritze, Zacharis J. Davis, Christophe Droit, Blandine Guichardaz, Valerie Petrini, Gilles Martin, Jean-Michel Friedt, and Sylvain Ballandras</i>	46
Modeling and Comparing the Linear Performance of non Uniform Geometry Bend Sensors <i>Giancarlo Orengo, Antonino Lagati, and Giovanni Saggio</i>	52
Heat Balanced Bolometer with Sigma-Delta Interface <i>Matthieu Denoual, Mathieu Pouliquen, Gilles Allegre, Damien Brouard, Arthur Veith, Olivier de Sagazan, and Patrick Attia</i>	56

Optical Characterisation of La _{0.7} Sr _{0.3} MnO ₃ Thin Film Based Uncooled Bolometers <i>Ammar Aryan, Jean-Marc Routoure, Bruno Guillet, Pierre Langlois, Cedric Fur, Julien Gasnier, Carolina Adamo, Darrell G. Schlom, and Laurence Mechin</i>	61
Identification of Yarn Periodical Errors Using Signal Processing Techniques Based on Capacitive and Optical Sensors Measurements <i>Vitor Carvalho, Filomena Soares, Michael Belsley, and Rosa Vasconcelos</i>	66
TCR, Responsivity, and Noise Properties of Carbon Nanotube-polymer Bolometric IR Detectors <i>William Riedel, Gustavo Fernandes, Jin Ho Kim, and Jimmy Xu</i>	73
Application of a Conductive Polymer Electronic-nose Device to Identify Aged Woody Samples <i>Alphus D. Wilson</i>	77
A Methanol Sensor Incorporating Nanostructured ZnO and Integrated Micro-heater on Thermally Isolated Planar MEMS Platform <i>Sudhir Chandra, Hardik Pandya, and Anoop Vyas</i>	83
Development of Au Nano-particles Cladding-doped Optical Fiber for Surface Plasmon Resonance Sensor Applications <i>Seongmin Ju, Pramod R. Watekar, Seongmook Jeong, Youngwoong Kim, Poram Jeon, Seongjae Boo, and Won-Taek Han</i>	89
A Smartphone System: Providing a Shoe-Embedded Interface <i>Kaname Takaochi, Kazuhiro Watanabe, and Kazumasa Takami</i>	95
A Low-cost and Portable System for Real-time Impedimetric Measurements and Impedance Spectroscopy of Sensors <i>Michele Rossi, Marco Bennati, Federico Thei, and Marco Tartagni</i>	101
Flexible Lightweight Films-based Physical Sensors with Wireless Data <i>Vladimir Laukhin, Elena Laukhina, Bahareh Moradi, Victor Lebedev, Raphael Pfattnr, Concepcio Rovira, and Jaume Veciana</i>	107
Performance Testing of a Low Power Consumption Wireless Sensor Communication System Integrated with an Energy Harvesting Power Source <i>Vlad Marsic, Alessandro Giuliano, Michele Pozzi, Meiling Zhu, and Stewart Williams</i>	112
On the Need for Low Phase Noise Oscillators for Wireless Passive Sensor Probing <i>Jean-Michel Friedt, Nicolas Chretien, Bruno Francois, Gilles Martin, Sylvain Ballandras, and Pratyush Varshney</i>	119
Efficient Suboptimal Detectors for Maritime Surface Surveillance High-Resolution Radar <i>Blas Pablo Dorta-Naranjo, Jaime Calvo-Gallego, Cristina Carmona-Duarte, and Felix Perez-Martinez</i>	126

Acoustic Emission Sensor Module <i>Irinela Chilibon, Marian Mogildea, and George Mogildea</i>	132
Investigation on Electrode Size of High Frequency Ultrasonic Transducers <i>Yangjie Wei, Thomas Herzog, and Henning Heuer</i>	137
Surface Acoustic Wave Devices Exploiting Palladium Layer Properties for Selective Detection of Hydrogen <i>Meddy Vanotti, Virginie Blondeau-Patissier, David Rabus, Loic Richard, and Sylvain Ballandras</i>	143
Protocol Awareness: A Step Towards Smarter Sensors <i>Hoel Iris and Francois Pacull</i>	148

Ability of Acoustic Sensor Devices for Medical Analysis

Thomas Rösel, Achim Voigt, Friederike J. Gruhl

Institute for Microstructure Technology (IMT)

Karlsruhe Institute of Technology (KIT)

Eggenstein-Leopoldshafen, Germany

thomas.roesel@kit.edu, achim.voigt@kit.edu, friederike.gruhl@kit.edu

Abstract—There is an increasing demand to monitor course of disease or therapy success of certain diseases via determining concentrations of specific protein markers in blood. For such biomedical applications implying the detection of multiple proteins a cost-effective and rapid analysis system with small sample consumption is required. Biosensor packaging is a useful means to interface the biosensor with the surroundings while ensuring its integrity and performance. We recently developed surface acoustic wave (SAW) biosensor chips, which allow the label-free, sensitive and cost-effective detection of proteins. For that, single SAW devices first are embedded in polymer housings, however, the sensitive sensor area still remains accessible for surface modification. The sensor surface is modified with capture molecules binding specifically to the analyte. Unspecific binding reactions are prevented via intermediate hydrogel layers, such as dextran. Advantages of those SAW biosensor chips are simple handling, low consumption of chemicals used in the coating process and enabling parallel analysis of multiple analytes in one sample. Hence, when applying biosensor surface modifications to a packaging, it is essential that both the effect on the housing and the impact on the biosensor signal response in a subsequent assay are investigated. Our housed SAW chips enable a user-friendly, easy and rapid way to detect different clinical analytes.

Keywords—SAW biosensors; array; point-of-care; cancer diagnosis

I. INTRODUCTION

In many cases, it is possible to diagnose diseases, such as cancer, via determining concentrations of several specific protein markers in blood to create a marker profile of the patient. Such a marker profile can also be used for monitoring the success of the therapy applied to cure those diseases. For example, therapy of breast cancer patients often has to be modified to achieve best possible chances for healing. In many cases, the critical time already lies within the first six weeks after therapy start [1]. For such Point of Care (POC) applications based on the detection of multiple proteins analytes in one sample a cost-effective and rapid analysis system with small sample consumption is required.

It has been shown by numerous publications [2] and patents [3] that biosensors allow rapid and accurate detection and determination of analyte concentrations in a comparatively easy way. Still, compared to the scientific output, the number of complete biosensor systems which are actually commercialized is rather small. One of the reasons could be that research projects often deal with optimization

of individual biosensor system components only, but real system integration into a reliable instrumentation is neglected [4]. System integration includes, among others, the protection of the biosensor element in the system against external negative influences, while its mechanical, electrical, and biological integrity is ensured, for instance, accessibility to sample solutions. These requirements can be met with an appropriate biosensor packaging which provides both mechanical protection and suitable connections to the system's surroundings required for operation, such as a fluidic delivery system [5].

SAW biosensors allow the label-free, sensitive and cost-effective detection of biomolecules. They have been applied successfully to detect proteins, deoxyribonucleic acid (DNA) and bacteria [6]. For the detection of proteins the sensor surface is modified with capture molecules, specific analyte binding partner. Unspecific binding reactions were prevented by coupling the binding molecules via an intermediate hydrogel layer, such as dextran, on the sensor surface. This is a crucial issue for all biosensors based on label-free detection of analytes in serum samples due to the high protein background [7]. Capture molecules can be immobilized by amine coupling via reactive esters using a carbodiimide, e.g., 1-ethyl-3-(3-dimethylaminopropyl)carbodiimide (EDC), and N-hydroxysuccinimide (NHS). Due to its flexibility, relative ease of use, high coupling yields and robustness, the EDC/NHS coupling procedure is the most frequently employed immobilization method [8]. Therefore, if hydrogel layers supply amino groups instead of carboxyl groups, it might be useful to convert the amino groups to carboxyl groups prior to protein coupling, e.g., by means of dicarboxylic acid anhydrides [9], to obtain a higher coupling yield.

Our previous set-up was used successfully in several affinity binding experiments [10], however, it is not suited for medical applications: Aside from the SAW device itself it consists of non-disposable components making it inappropriate for a POC device.

We recently developed a SAW biosensor system consists of a SAW device embedded in a polymer housing, which is connected to an external flow injection analysis (FIA) system. Using acoustic biosensors, such as SAW biosensors, it additionally has to be considered that aside from mass change the change of viscoelasticity of the sensing layer (including layer thickness and penetration depth of the SAW) also contributes to the SAW biosensor signal response. The effect of the latter strongly depends on the morphology of the sensing layer and hence could be

influenced by the surface modification procedure [11] [12]. To guarantee the suitability of a newly developed biosensor chip, after ensuring intactness of the materials involved, it is essential to test the effect of this procedure in a subsequent binding experiment. This will be shown in the following, by using the example of streptavidin/biotin assay.

II. MATERIALS AND METHODS

A. SAW device and fluidic set-up

The shear horizontal SAW resonator is based on a small ($4 \times 4 \text{ mm}^2$) $36^\circ\text{YX-LiTaO}_3$ device with gold transducers and has a frequency of operation of 428.5 MHz. SAW measurements were performed in an oscillator circuit developed in-house with the SAW resonator as frequency-determining element. Difference frequencies relative to a permanently oscillating reference oscillator, featuring a constant frequency in the range of 434 MHz, were used as signal output. The frequency resolution was 1 Hz. Experiments were performed using a flow injection analysis (FIA) system equipped with two peristaltic pumps (Ismatec, Wertheim, Germany) and an injection valve (Besta-Technik, Wilhelmsfeld, Germany). PTFE tubes served as connections between single units and as sample loop. The SAW resonator was included by means of a flow cell which was designed as part of an electronic circuit board integrated in the oscillator unit. The SAW device was mounted upside down onto isolated contact pads on the electronic board and coupled capacitively. The milled flow channel in between the contact pads allowed the fluid to pass along the SAW path. Details of the previous measurement setup (Fig. 1) have been described earlier [10].

Our new developed SAW chips were mounted in a flow cell adapter, which connects the sensor device with FIA system (Fig. 2). The principle of measurement setup is the same as aforementioned.

B. Parylene coating

All SAW devices used in the following experiments were first coated with $0.1 \mu\text{m}$ parylene C to obtain a chemically homogeneous surface. This improves success and reproducibility of further preparation steps. Details of the process have been published earlier [10].

C. Covalent binding of hydrogel

Aminodextrane (AMD) with M_r 3.000 was used as intermediate hydrogel layer. The parylene C layer was activated by oxidation via plasma treatment and subsequent silanization with (3-glycidyloxypropyl)trimethoxysilane. After rinsing with acetone the sensors were treated overnight with an aqueous solution of hydrogel, $c = 2 \text{ mg/ml}$. Then sensors were rinsed thoroughly with bidistilled water and dried.

D. Immobilization of biotinylated BSA (b-BSA)

The affinity system of streptavidin with biotin was used for exemplary measurements. The capture molecule b-BSA

was immobilized on the AMD coated sensors. The amino groups were converted to carboxyl groups via glutaric anhydride dissolved in aqueous solution, $c = 2 \text{ mg}/\mu\text{l}$. Details of the process have been published earlier [11]. Protein immobilization was performed on-line by means of the external FIA system. Phosphate-buffered saline (PBS) was used as carrier stream. First, the carboxylized surface was activated with a solution of 0.05 M N-hydroxy succinimide and 0.2 M N-(3-dimethylamino-propyl)-N'-ethylcarbodiimide hydrochloride in bidistilled water and rinsed with PBS. Second, the surface was incubated with a solution of $1.8 \mu\text{M}$ b-BSA in acetate buffer, pH 5, and rinsed with PBS. Third, the remaining reactive groups on the surface were deactivated by flushing with a solution of 1 M ethanolamine, pH 8.5. After rinsing with PBS, the sensor was immediately used for the assay.

E. Streptavidin assay

Experiments were performed with PBS, pH 7.4, as carrier stream. The flow rate was set to 0.05 ml/min. Samples were loaded in the sample loop, injected into the carrier stream via the injection valve, and transported to the sensor. The injection interval was set to 60-300 s. After each injection the sensor was rinsed with PBS. Sensors with covalently immobilized b-BSA or BSA were used. Samples containing, $c = 0$ (1; 5; 10) $\mu\text{g/ml}$ streptavidin were injected in the carrier stream.

III. RESULTS AND DISCUSSION

SAW biosensors enable label-free and direct detection of DNA, proteins, and bacteria in real-time. Aiming at multi-parameter analysis, we developed a disposable SAW biosensor chip based on an array-compatible biosensor housing which encapsulated a SAW sensor (Fig. 1 A) except for an opening in the area of the active sensing structure (Fig. 2 A) to permit common surface modification steps for immobilizing the sensing layer as described in section II.

The effects of the packaging of the newly developed SAW biosensor chips on the signal responses were compared to those of the previous SAW biosensor devices to investigate the suitability of the new housing regarding the biosensor's performance. Therefore, SAW measurements based on the affinity system streptavidin/biotin were performed with SAW biosensors integrated in the flow cell (Fig.1) and with newly developed SAW biosensor chips in the flow cell adapter (Fig.2) with the external FIA system. Biotinylated BSA was immobilized on the SAW sensor surface via an intermediate AMD layer, samples contained streptavidin. Each sensor was tested by injection of several concentrations of streptavidin, $c = 0$ (1; 5; 10) $\mu\text{g/ml}$. Exemplary signal responses are shown in Figure 3, the signals were reproducible (data not shown). Using a sensor with immobilized binding partner, i.e., b-BSA, the SAW signal response increases with higher concentrations of streptavidin until saturation is reached (Fig. 3A).

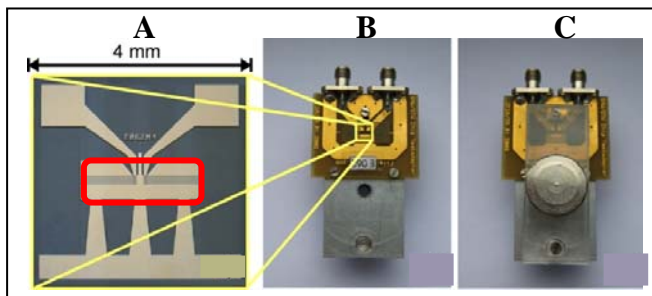


Figure 1. Previous set-up with inserting of the SAW device. SAW device (a), flow cell, open (b) and flow cell, closed.

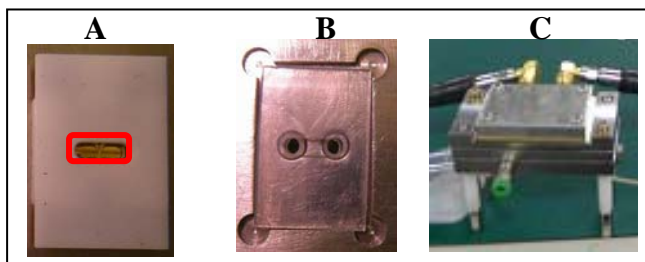


Figure 2. Current set-up with inserting of the SAW chip. SAW chip (SAW device embedded in a polymer housing) (A), cavity of flow cell adapter, open (B) and flow cell adapter, closed (C).

In this work, the ability of the use of SAW biosensor for specific protein detection was shown with measurements in our previous flow cell in general. Significant streptavidin signals were obtained when the corresponding binding partner, b-BSA, was immobilized on the SAW biosensor surface. Aside from being specific, direct and label-free, the protein binding is monitored time-resolved enabling the determination of kinetic parameters of the binding reaction. However, the SAW set-up with flow cell is not suitable for medical applications. It contains mainly non-disposable components which could lead to carry-over effects between different measurements. An additional disadvantage is the comparatively large dimensions of flow cell (and tubing) leading to a significant delay of signal response times and increase of sample volumes. In consequence, the flow cells are not array compatible.

Therefore, we investigated if inserting SAW devices in disposable polymer housings are not only enable simple handling and reduction of coating chemicals but also the signal response of streptavidin assay is comparable to those obtained with unpacked SAW devices. The signal response of SAW biosensor chips resulting from binding of different concentrations of streptavidin to b-BSA on the surface is significantly higher (Fig. 3 B) than obtained with the previous set-up (Fig. 3 A). We think that the increased signals obtained with SAW biosensor chips result from the different channel geometry of the two described setups. In consequence, this would apply the use of SAW biosensor chip system to develop a suitable platform for biomedical applications.

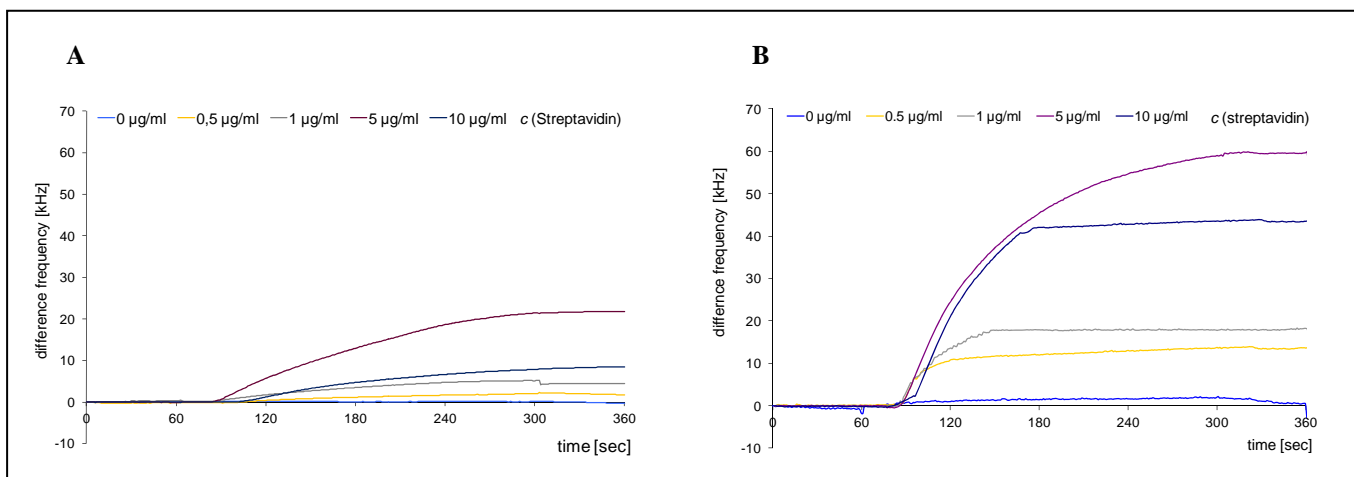


Figure 3. Streptavidin assay. Typical measurement curves of the SAW biosensor. Biotinylated BSA immobilized on sensor surface coated with AMD 3.000. Different concentrations of streptavidin (0 – 10 µg/ml) were used as analyte. (A) Previous set-up with SAW devices. (B) Actual set-up with housed SAW devices (B).

IV. CONCLUSIONS AND FUTURE WORK

We presented a set-up for analysis of future POC applications. In particular, this set-up offers a simple and cost-effective method for the detection of multiple protein

analytes out of one sample, i.e., a protein marker profile. Such a profile could give a quick answer about the state of health of a patient (Figure 4) allowing an immediate adaptation of therapy. In the next step, the SAW biosensor chip array is optimized for biological applications with regard to real samples and required detection limits.

In this work, we investigated that surface modification procedure established for unpacked SAW biosensors was successfully adapted to SAW biosensor chips in which the SAW devices were integrated in polymer housings. SAW biosensor signal responses obtained with streptavidin/biotin affinity system were not only similar to signals obtained with the previous setup, but even higher. Therefore, SAW biosensor chips permit a better biosensor efficiency. Our housed SAW chips will now used for medical applications, e.g., detection of different disease markers.

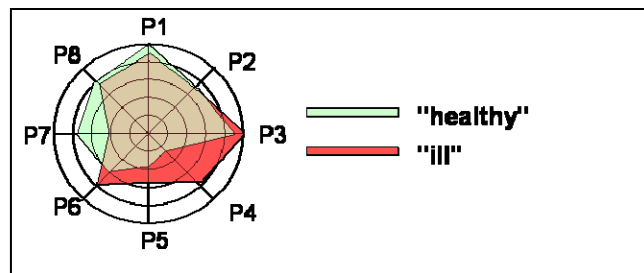


Figure 4. Model of a potential marker profile. Concentration of distinct proteins (here: 8) in serum can give quick information about state of health of patient.

REFERENCES

- [1] D. Lüftner et al., "Serum HER-2/*neu* in the management of breast cancer patients", Clin. Biochem. vol. 36, pp. 233-240, 2003.
- [2] P. D’Orazio P, "Biosensors in clinical chemistry—2011 update.", Clin Chim Acta vol. 412, pp.1 749–1761, 2011.
- [3] J.H.T. Luong, K.B. Male and J.D. Glennon, "Biosensor technology: technology push versus market pull.", Biotechnol. Adv., vol. 26, pp. 492–500, 2008.
- [4] P. D’Orazio, "Biosensors in clinical chemistry – 2011 update", Clin. Chim. Acta, vol. 412, pp. 1749-1761, 2011.
- [5] T. Tekin, "Review of Packaging of Optoelectronic, Photonic, and MEMS Components", IEEE J. Sel. Top. Quantum Electr., vol. 17, pp. 704-719, 2011.
- [6] F.J. Gruhl, B.E. Rapp and K. Länge, „Biosensors for Diagnostic Applications”, Adv. Biochem. Eng. Biotechnol., 2012, doi: 10.10007/10_2011_130.
- [7] G. Gauglitz and G. Proll, "Strategies for label-free optical detection ", Adv. Biochem. Engin./Biotechnol. vol. 109, pp. 395-435, 2008.
- [8] R.B.M. Schasfoort and A.J. Tudos, Handbook of surface plasmon resonance, RCS Publishing, Cambridge, 2008, pp. 173-220
- [9] G.T. Hermanson, Bioconjugate Techniques, 2nd ed., Academic Press, London, 2008, pp 101-109
- [10] F.J. Gruhl and K. Länge, „Surface modification of an acoustic biosensor allowing the detection of low concentrations of cancer markers”, Anal. Biochem. vol. 420, pp. 188-190, 2012.
- [11] G. McHale, M.I. Newton, M.K. Banerjee and J.A. Cowen, "Acoustic wave–liquid interactions", Mat. Sci. Eng. C vol. 12, pp. 17-22, 2000.
- [12] K. Länge, F.J. Gruhl and M. Rapp, „Influence of preparative carboxylation steps on the analyte response of an acoustic biosensor”, IEEE Sensors Journal, vol. 9, pp. 2033-34, 2009.

Neural Cell Chip to Assess Toxicity Based on Spectroelectrochemical Technique

Jeong-Woo Choi^{1,2*} and Tae-Hyung Kim¹

¹ Department of Chemical & Biomolecular Engineering and ² Graduate School of Management of Technology, Sogang University,

Seoul, Republic of Korea

E-mail: jwchoi@sogang.ac.kr, thkim0512@gmail.com

Abstract—A cell chip is an useful tool for the toxicity assessment of various kinds of chemicals, drugs or nanomaterials. Nanoscale film was fabricated on a conducting electrode surface to establish a cell-friendly environment which is effective for increasing cell adhesion, spreading and proliferations. Biofilm was further developed to three dimensional peptide nanopillar arrays which were more efficient than two dimensional peptide film in regard to various kinds of cellular functions. The electrochemical signals obtained from cells were found to be proportional to the cell viability which can be used as indicator for the toxicity evaluation of various kinds of toxic chemicals and nanomaterials quickly and sensitively. Surface-enhanced Raman spectroscopy (SERS) was further developed as powerful supplementary tool to identify cell cycles at different stage, to distinguish different cell lines, to discriminate alive- or dead- cells and to investigate toxicity of anticancer drugs on target cells. The combination of electrical detection and SERS technique was found to be excellent to investigate the changes of intracellular composition of cells, as well as to study the internal redox properties of single neural cell. Proposed cell chip based on spectroelectrochemical technique that combined electrochemical and SERS methods can be applied as an *in vitro* analysis tool in various kinds of biotechnology fields.

Keywords—Toxicity assessment; Spectroelectrochemical method; Surface-enhanced Raman spectroscopy; Cell chip

I. INTRODUCTION

In vitro techniques are efficient tools for the assessment of toxic effects of newly developed chemicals and environmental toxins on human beings, as well as for the cytological diagnosis which are not possible in DNA-, proteins- or even animal-based researches [1-2]. However, most of the *in vitro* methods utilize optical and/or biological tools that are laborious and hard to integrate. Moreover, materials containing fluorescence dyes or fluorophores itself used for cellular study can cause light/fluorescence interference and also cause the variations of optical signals that directly affect the determination of cell viability [3]. A variety of electrochemical methods have been carried out to detect the cell viability without utilizing optical sources, such as electrochemical impedance spectroscopy (EIS), amperometry and cyclic voltammetry (CV) [4-6]. Most of these techniques showed proper performance for the detection of cell viability; however, the sensitivity of electrochemical methods was found to be not enough to overcome the problems of conventional optical techniques.

We have previously reported a cell-based chip composed of nano-scale peptide layer to attach cells directly on electrode surface and to enhance the sensitivity of

electrochemical signals [7-9]. Since the intensities of redox signal generated or transferred from cells are the indicator of cell viability, establishment of cell-friendly environment on the artificial electrode surface using biomaterials is most important factor for the enhancement of sensitivity of cell chip. RGD-MAP-C peptide, a peptide containing arginine-glycine-aspartic acid (RGD) and cysteine terminal, was proved as very effective material for enhancing cell proliferation and electrochemical signals of cells [10-11]. The RGD-MAP-C peptide modified cell chip further used as efficient drug screening tool that successfully monitoring the effects of various kinds of anticancer drugs on cancer cells with high sensitivity and reproducibility.

In this paper, we report a cell chip composed RGD-MAP-C peptide layer or nanopillar array to detect electrochemical characteristics of neural cells and to evaluate the toxicity of environmental toxins, chemicals and nanoparticles. Surface-enhanced Raman spectroscopy (SERS) technique was further utilized to detect intracellular composition of target cells, as well as to assess the toxicity of anticancer drugs on several cell lines. Finally, both electrochemical and SERS methods were combined as spectroelectrochemical tool to monitor the changes of cell viability and bio-composition of target cells simultaneously (Fig. 1).

II. TOXICITY ASSESSMENT BASED ON ELECTROCHEMICAL METHODS

Although the exact origin of redox signals generated from cells were not fully discovered yet, electrochemical tools are still very effective label-free tool for the determination cell viability. The redox signals obtained from target cells can be translated to cell viability which are excellent indicator for assessing various kinds of materials of interest. Almost all of the materials including drugs, chemicals, biological materials and even nanoparticles are the candidates whose toxicity can be assessed by cell chip based on electrochemical tools.

A. Modification of cell chip using RGD-MAP-C peptide

Cell-friendly environment was established by using RGD-MAP-C synthetic peptide. Since RGD-MAP-C peptide contains cysteine residue at the end of its sequence, nanoscale RGD peptide film was fabricated by simple self-assembly technique via strong Au-S bond. RGD peptide film was very effective for enhancing cell adhesion on the artificial electrode surface; however, peptide that physically absorbed on the electrode surface increased the thickness of biofilm and contributed to increase of the resistance between

cell and electrode interface which was a big barrier for enhancing the sensitivity of cell chip based on electrochemical methods.

Anodic aluminum oxide (AAO) mask consist of homogeneous cylindrical nanopores was used to fabricate peptide nanopatterned array on the artificial electrode surface [12]. The structures of peptide could be easily controlled by adjusting the concentrations of RGD-MAP-C peptide that resulted in the different shapes of peptide structures such as nanodots, nanorods and nanopillars. The peptide nanopillar array among several RGD peptide nanopatterned array was found to provide the best condition for enhancing various kinds of cell functions including cell adhesion, spreading and proliferation rates. The enhanced cell functions contributed to the increase of sensitivity of cell chip which was 50% higher than RGD-MAP-C peptide monolayered surface [13].

B. Toxicity assessment of environmental toxins

Cells on RGD-MAP-C functionalized surface were exposed to two kinds of toxic chemicals to assess its cytotoxicity on neural cells. 2,2',4,4',5,5'-Hexachlorobiphenyl (PCB) was exposed to rat neural cancer (PC12) cells for 24 hours and its toxicity was analyzed by differential pulse voltammetry. Current intensities representing cell viability were linearly decreased with increasing the concentrations of PCB from 40nM to 80nM [13]. In case of bisphenol A (BPA), a common plastic monomer widely used in the manufacture products, dual-mode correlation was found between the concentrations of BPA and the current intensities from neural cells (SH-SY5Y). The intensities of peak current increased with the concentration of BPA up to 300nM and then start to decrease at the concentration of BPA above 300 nM due to the stimulation and cytotoxic effects of BPA on cancer cells, respectively [14].

C. Toxicity assessment of nanoparticles

Next, we tested potential cytotoxicity of two kinds of nanomaterials which have been widely applied in various kinds of cell-based research fields. 100nm-sized silica nanoparticles (SNP) with positive charge on its surface were added to SH-SY5Y cells on chip and its toxicity was evaluated by cyclic voltammetry (CV). 50 $\mu\text{g/ml}$ SNP was found to be slightly toxic for neural cells; however, acute toxicity was found at 200 $\mu\text{g/ml}$ SNP that decreased the current intensity as almost 70% versus control group [15]. We also evaluated the cytotoxicity of mercaptoacetic acid (MAA) functionalized green- and red-emitting CdSe/ZnS quantum dots (QDs) via CV (Fig 2a, c). Cathodic (E_{pc}) and anodic potential (E_{pa}) of neuroblastoma cells were 210mV and 290mV, respectively, and the E_{pc} values were used as indicators for determining cell viability. As a result, red-emitting QDs (6.3nm in diameter) were found to decrease cell viability slightly at 5 $\mu\text{g/ml}$ while green-emitting QDs (2.1nm in diameter) hugely decreased cell viability at 1 $\mu\text{g/ml}$ (Fig. 2b). Huge decrease of cell viability was observed when cells were exposed to 30 $\mu\text{g/ml}$ of red-emitting QDs, indicating that green-emitting QDs were more toxic for the human neural cells than red-emitting QDs (Fig. 2d).

D. Toxicity assessment of graphene oxide

Graphene, planar sheets of carbon atoms densely packed in a honeycomb structure, is an excellent conducting material with high optical transparency and rigidity. Unlike graphene, graphene oxide (GO) is an insulating material that contains many hydroxyl groups on its surface suitable for drug carriers and/or photothermal therapeutic agents. Hence, we evaluated the toxicity of GO nanopellets using neural stem cell chip. Unfortunately, GO itself was found to be toxic for human neural stem cells even at the low concentration of GO (25 $\mu\text{g/ml}$). Similar toxicity was found from MTT viability assay, indicating that GO have acute toxicity for human neural cells and should be functionalized with cell-friendly materials to reduce its toxicity.

III. TOXICITY ASSESSMENT BASED ON SERS METHOD

SERS phenomenon offers an exciting opportunity to overcome the weak intensity of normal Raman method. Using the SERS technique, the intensity of Raman signal can be increased by the structured metal surface and measured effectively by low laser power with short signal acquisition time suitable for biological applications. Although metal nanostructures or nanogaps are essential for the enhancement of Raman signals, SERS method is still powerful for detecting the toxicity of target materials on cells with high sensitivity.

A. Fabrication of SERS-active surface

Since the enhancement of Raman signal is generated in 'hot spots' which normally exist in the gap between the metal nanostructures, a great deal of attention has been focused on synthesis of shape-controlled SERS structures with different morphologies. However, a fabrication of SERS-active surface was found to have numerous problems such as low signal enhancement, uniformity and further removal process of the template and/or byproducts. Therefore, an improved technique for fabrication of the substrate that enhance Raman signal effectively is still crucial for more effective enhancement of Raman signals. We fabricated uniformly deposited Au nanopatterned surface on an ITO electrode using AAO mask as a template, which provides low signal variances with high intensity and reproducibility of SERS signals [16].

The superiority of AAO-assisted Au nanopatterned ITO substrate as SERS-active surface was confirmed by comparing the signals intensities and variations of peak intensities of aminothiophenol (ATP) with that from randomly distributed Au nanoparticle on ITO surface. The Raman signals of PATP/Au nanopatterned surface from nine different positions showed significantly enhanced signal intensities with very low variations. These results indicate that the newly fabricated SERS-active surface is proper for analyzing the characteristics of cells and also useful for assessing the toxicity of various kinds of chemicals.

B. Characterization of target cells

The intracellular composition of target cells was detectable by analyzing each peak from various kinds of cell

lines [17]. Based on the Raman spectra of each cell, identification of different cancer cell lines was also possible using SERS method due to the difference of intracellular composition of each cell. We also successfully characterized the difference between normal and cancer cells which was derived from same organ and species. From the results, we concluded that cancer cell might express more proteins containing β -pleated sheet structures than normal cell, which induce the mitotic activity. The discrimination of alive- or dead- cells were also available by comparing the Raman spectra obtained from each cell.

C. Toxicity assessment of anticancer drugs

Cells were treated with anticancer drug to confirm the application potentialities of cell chip based on SERS method as effective *in vitro* analysis tool. Living HepG2 cells were exposed to hydroxyurea (200 μ M) and the Raman spectra from HepG2 cells was recorded 5 times in 24 hours to assess the time-dependent toxicity of hydroxyurea. Intensities of several peaks in Raman spectra were found to decrease in time-dependent manner, indicating that the changes of cell viability can be sensitively measured by SERS method [18].

IV. TOXICITY ASSESSMENT BASED ON SPECTROELECTROCHEMICAL METHOD

Integration of electrochemical and SERS method is not simple process; however, this combined technology can give an opportunity to investigate the biochemical changes of various kinds of cellular components (signaling molecules, DNA/RNA, proteins, enzymes, etc.) simply and sensitively. Hence, we combined linear sweep voltammetry and SERS as spectroelectrochemical tool to evaluate the toxicity of anticancer drug on neural cancer cells precisely. The DNA components in Raman spectra and the electrochemical responses of PC12 cells were significantly decreased when cells were exposed to 50 μ M cisplatin for 24 hours (data not shown). Hence, we concluded that the proposed spectroelectrochemical tool provide many invaluable information including the damages caused by anticancer drugs for whole cells, single cell and even for the specific region in single cell, which is not possible in conventional *in vitro* tool, electrochemical and SERS method itself.

V. CONCLUSION

A cell chip was fabricated to determine toxicity of various kinds of environmental toxins, drugs and functional nanoparticles based on electrochemical and/or SERS method. Both electrochemical and SERS method were proved as suitable *in vitro* tool for evaluating the cytotoxicity of materials that showed high sensitivity and reproducibility. Remarkably, electrochemical method was found to be more proper than SERS for the toxicity assessment on large numbers of cells, while SERS method showed superior characteristics to voltammetric tool for the toxicity evaluation of specific materials on single cell and/or the specific region in single cell. Hence, the proposed cell chip based on spectroelectrochemical technique that enables both electrochemical and Raman analysis is very promising for toxicity assessment, drug screening and diagnostics.

ACKNOWLEDGMENT

This work was supported by the National Research Foundation of Korea (NRF) grant funded by the Korea government (MEST) (2012-0000163) and by the Nano/Bio Science & Technology Program (M10536090001-05N3609-00110) of the Ministry of Education, Science and Technology (MEST), and by Korea Institute for Advancement in Technology (KIAT) through the Workforce Development Program in Strategic Technology.

REFERENCES

- [1] C. -H. Yea, J. Min, and J. -W. Choi, "The fabrication of cell chip for use as bio-sensors", *Biochip J.*, vol. 1, 2007, pp. 219-227.
- [2] J. -H. Lee, B. -K. Oh, S. Jeong and J. -W. Choi, "Electrical detection-based analytic biodevice technology", *Biochip J.*, vol. 4, 2010, pp. 1-8.
- [3] T. -H. Kim, W. A. El-Said, J. -W. Choi, "Highly sensitive electrochemical detection of potential cytotoxicity of CdSe/ZnS quantum dots using neural cell chip", *Biosens. Bioelectron.*, vol. 32, 2012, pp. 266-272.
- [4] C. -Y. Lin, N. -C. Teng, S. -C. Hsieh, Y. -S. Lin, W. -J. Chang, S. -Y. Hsiao, H. -S. Huang and H. -M. Huang, "Real-time detection of β 1 integrin expression on MG-63 cells using electrochemical impedance spectroscopy", *Biosens. Bioelectron.*, vol. 28, 2011, pp. 221-226.
- [5] N. Borghol, L. Mora, T. Jouenne, N. Jaffézie-Renault, N. Sakly, A. C. Duncan, Y. Chevalier, P. Lejeune and A. Othmane, "Monitoring of E. coli immobilization on modified gold electrode: A new bacteria-based glucose sensor", *Biotechnol. Bioprocess Eng.*, vol. 15, 2010, pp. 220-228.
- [6] J. -W. Choi, R. Bhusal, T. -H. Kim, J. H. An, H. Kim, "Electrochemical Detection of Bisphenol A - Induced Neuronal Toxicity Using RGD Peptide Modified ITO Electrode Cell Chip", *Mol. Cryst. Liq. Cryst.*, vol.519, 2010, pp. 36-42.
- [7] W. A. El-Said, C. -H. Yea, H. Kim, B. -K. Oh, J. -W. Choi, "Cell-based Chip for the Detection of Anticancer Effect on HeLa Cells using Cyclic Voltammetry", *Biosens. Bioelectron.*, vol. 24, 2009, pp. 1259-1265.
- [8] W. A. El-Said, C. -H. Yea, I. -K. Kwon, J. -W. Choi, "Fabrication of Electrical Cell Chip for the Detection of Anticancer Drugs and Environmental Toxicants Effect", *Biochip J.*, vol. 3, 2009, pp. 105-112.
- [9] M. A. Kafí, T. -H. Kim, J. H. An, J. -W. Choi, "Fabrication of Cell Chip for Detection of Cell Cycle Progression Based on Electrochemical Method", *Anal. Chem.*, vol. 83, 2011, pp. 2104-2111.
- [10] C. -H. Yea, H. Kim, J. Kim, S. -U. Kim, J. -W. Choi, "Fabrication of Mouse Embryonic Stem Cell Chip using Self-assembled Layer of Cysteine-modified RGD Oligopeptide", *Mol. Cryst. Liq. Cryst.*, vol.492, 2008, pp. 548-555.
- [11] C. -H. Yea, B. Lee, H. Kim, S. -U. Kim, W. A. El-Said, J. Min, B. -K. Oh, J. -W. Choi, "The Immobilization of Animal Cells using the Cysteine-modified RGD Oligopeptide", *Ultramicroscopy*, vol.108, 2008, pp. 1144-1147.
- [12] M. A. Kafí, W. A. El-Said, T. -H. Kim, J. -W. Choi, "Cell adhesion, spreading, and proliferation on surface functionalized with RGD nanopillar arrays", *Biomaterials*, vol. 33, 2012, pp. 731-739.
- [13] M. A. Kafí, T. -H. Kim, C. -H. Yea, H. Kim, J. -W. Choi, "Effects of nanopatterned RGD peptide layer on electrochemical detection of neural cell chip", *Biosens. Bioelectron.*, vol. 26, 2010, pp. 1359-1365.

- [14] M. A. Kafi, T. -H. Kim, J. -H. An, J. -W. Choi, "Electrochemical cell-based chip for the detection of toxic effects of bisphenol-A on neuroblastoma cells", *Biosens. Bioelectron.*, vol. 26, 2011, pp. 3371-3375.
- [15] T. -H. Kim, S. -R. Kang, B. -K. Oh, J. -W. Choi, "Cell Chip for Detection of Silica Nanoparticle-induced Cytotoxicity", *Sens. Lett.*, vol. 9, 2011, pp. 861-865.
- [16] S. -M. Kang, T. -H. Kim, J. -W. Choi, "Cell chip to detect effects of graphene oxide nanopellet on human neural stem cell", *J. Nanosci. Nanotechnol.*, vol. 12, 2012, pp. 5185-5190.
- [17] W. A. El-Said, T. -H. Kim, H. Kim, J. -W. Choi, "Analysis of Intracellular State Based on Controlled 3D Nanostructures Mediated Surface enhanced Raman Scattering", *PLoS One*, vol. 6, 2011, p. e15836.
- [18] W. A. El-Said, T. -H. Kim, H. Kim, J. -W. Choi, "Detection of effect of chemotherapeutic agents to cancer cells on gold nanoflower patterned substrate using surface enhanced raman scattering and cyclic voltammetry", *Biosens. Bioelectron.*, vol. 26, 2010, pp. 1486-1492.

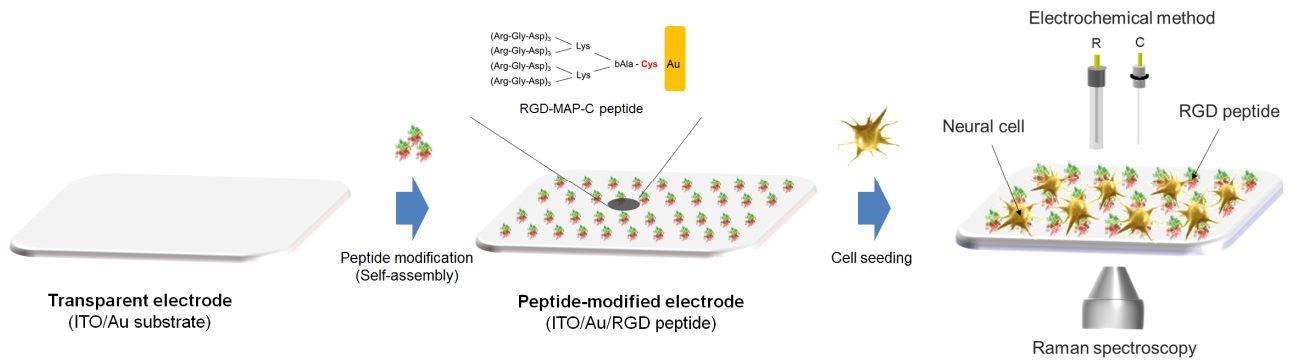


Figure 1. Schematic diagram of cell chip based on spectroelectrochemical method. A Gold attached transparent ITO electrode was first modified with RGD-MAP-C peptide for successful cell adhesion on the artificial electrode surface. RGD-MAP-C peptide can be directly self-assembled on the gold surface due to the cysteine residue via Au-S bond. After the cell adhesion, both electrochemical and Raman spectroscopy can be applied for intensive cell analysis.

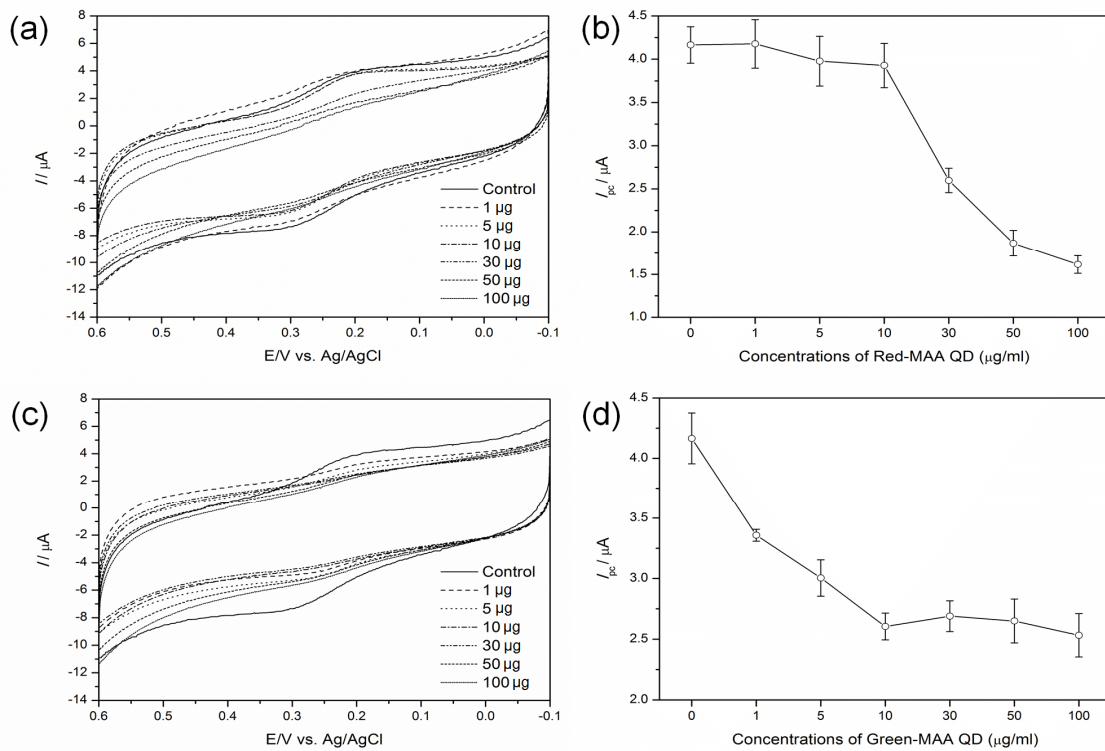


Figure 2. Voltammetric response of SH-SY5Y cells treated with different concentrations of (a) Red-MAA QDs and (c) Green-MAA QDs. (b) and (d) represent the intensities of cathodic currents (I_{pc}) obtained from (a) and (c), respectively. Data represent mean \pm SE of three different experiments under similar condition. Cyclic voltammetry was measured using phosphate buffered saline (10mM, pH 7.4) as electrolyte at a scan rate of 50mV s^{-1} .

Medical Wireless Vibration Measurement System for Hip Prosthesis Loosening Detection

Sebastian Sauer, Uwe Marschner
Institute of Semiconductor and Microsystems
Dresden University of Technology (TUD)
Dresden, Germany
e-mail: sebastian.sauer@tu-dresden.de
e-mail: uwe.marschner@tu-dresden.de

Hagen Grätz, and Wolf-Joachim Fischer
Wireless Microsystems
Fraunhofer IPMS
Dresden, Germany
e-mail: hagen.graetz@ipms.fraunhofer.de
e-mail: fischer@ipms.fraunhofer.de

Abstract—Vibration analysis is a promising approach in order to detect early hip prosthesis loosening, with the potential to extend the range of diagnostic tools currently available in clinical routine. Ongoing research efforts and developments in the area of smart implants, which integrate sensors, wireless power supply, communication and signal processing, provide means to obtain valuable in vivo information otherwise not available. In the current work a medical wireless measurement system is presented, which is integrated in the femoral head of a hip prosthesis. The passive miniaturized system includes a 3-axis acceleration sensor and signal pre-processing through a lock-in amplifier circuit. Bidirectional data communication and power supply is reached through inductive coupling with an operating frequency of 125 kHz in accordance with the ISO 18000-2 protocol standard. The system allows the acquisition of the acceleration frequency response of the femur-prosthesis system between 500 to 2500 Hz. Applied laboratory measurements with system prototypes on artificial bones and integrated prostheses demonstrate the feasibility of the measurement system approach, clearly showing differences in the vibration behavior due to an implant loosening.

Keywords-hip prosthesis loosening detection; vibration analysis; wireless medical system.

I. INTRODUCTION

Established and widely used diagnostic techniques in clinical routine, such as plain radiography, bone scintigraphy or arthrography (subtraction or nuclear), are yet to unreliable in order to determine the fixation state of a hip prosthesis in the bone as for example discussed in [1],[2],[3]. Under these circumstances, a reliable predication of the loosening state is still challenging and leaves room for misinterpretation. This leads to either revision of sufficiently osseointegrated endoprostheses (false-positive result) or a late diagnosis with bone stock destruction and difficulties in implant revision (false-negative result).

Therefore, there are continuing efforts to establish new or enhance established diagnosis techniques to increase sensitivity and specificity. In [4], a shaft integrated loosening sensor based on the conservation of momentum theory is described and evaluated with an oversized demonstrator; in [5], an ultrasound based extracorporeal testing method is

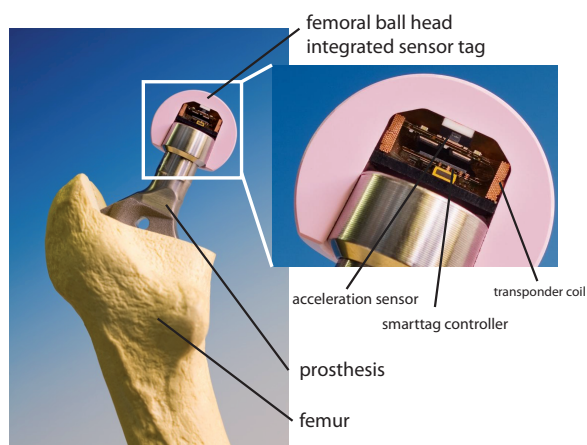


Figure 1. Medical wireless system (cross sectional cut) integrated in the femoral head of the hip implant.

presented. A promising alternative approach to determine the loosening state is vibration analysis, e.g., frequently used in mechanical structural analysis. A measurement system, capable of delivering amplitude and phase information of a femurs' frequency acceleration response due to a mechanical excitation, is the required base to extract system resonance frequencies. By monitoring the shift of these resonances, predictions about the loosening state are possible. Several early attempts used both extracorporeal vibration excitation and extracorporeal acceleration measurement in order to determine the system response in frequency or time domain. Especially for an extracorporeal acceleration measurement the obtained signal amplitude is heavily damped due to the influence of tissue. Is a miniaturized system directly incorporated into the prosthesis, as, e.g., realized by Puers [6], the negative influences of tissue in the measurement path are minimized. In difference to a previous realization with a prosthesis shaft integrated system [7], a solution with a femoral ball head integrated measurement system is

presented (Fig. 1). Within this work the proposed overall medical system is described, a detailed view of the integrated lock-in amplifier is given and experimental results of applied measurements on an artificial bone-prosthesis system, demonstrating the influence of loosening, are presented.

II. DIAGNOSTIC MEASUREMENT SYSTEM

The diagnostic measurement system (Fig. 2) consists of two main components: the prosthesis integrated wireless sensor system (intracorporeal unit) and a reader station combined with a mechanical vibration excitation and measurement system, both connected to a PC (extracorporeal unit).

The wireless sensor tag is placed in the femoral ball head of the hip implant, in difference to the previous placement in the stem [7]. This approach follows the request of the medical industry project partners due to the following reasons: 1) it simplifies the manufacturing process (modifying stems involves higher costs) 2) it permits an unproblematic sterilization process (stems exhibit a special micro porous surface coating supporting osseointegration, which requires a gamma sterilization process with devastating effect on integrated hard- and firmware) and 3) it reduces the required number of system variations (there are less femoral ball head types and embodiments). The intracorporeal system is built around a freely programmable transponder unit called Smart Tag 1 (Fraunhofer IPMS ST1). A solution on chip designed specifically for transponder applications requiring a sensor interface in order to monitor physical quantities besides providing identification information. It includes a 16 bit MSP430 microcontroller core, 16 kByte Flash, 8 kByte RAM and 512 Byte EEPROM memory, 16 digital I/O signals, 2 counter/interval timers, a Real-time clock, RF front end, 10 bit A/D converter with four channels, I²C bus module and an integrated voltage regulator. Wireless energy transmission and bidirectional data communication between tag and reader is in accordance to ISO 18000-2 standard at a carrier frequency of 125 kHz. Transponder coil and a tuning resonance capacity are connected directly to the chip.

In order to perform vibration analysis, the application specific circuitry incorporates a low power acceleration sensor (ADXL327, Analog Devices) for x, y and z axis measurements with a mechanical resonance frequency of 5.5 kHz. It provides a typical measurement frequency range (3dB cutoff frequency) of 0.5 to 1600 Hz in x, y direction and 0.5 to 550 Hz in z direction and a typical mechanic sensitivity of 420 mV/g with a measurement range of ±2.5g. Since the acceleration sensor output is strongly affected by noise, additional signal preprocessing is required. For this purpose a lock-in amplifier, based on the chopper principle, has been integrated in the sensor tag in order to improve the signal-to-noise ratio.

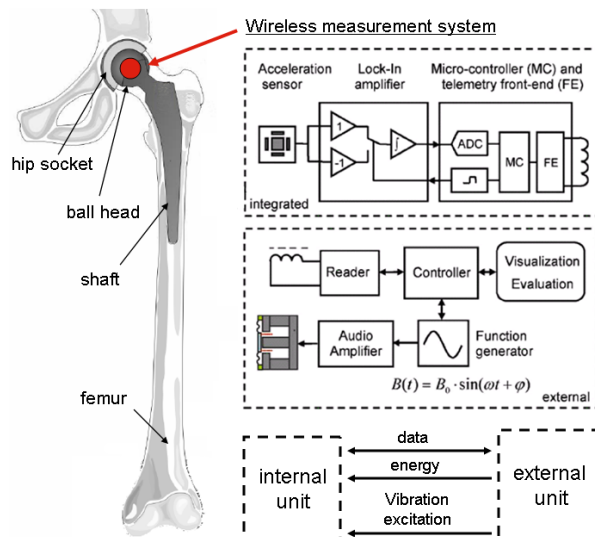


Figure 2. Overview of the diagnostic measurement system.

The mechanic excitation system consists of an electro dynamic vibration excitation (S50018, TIRA vib) with a maximum force of 18 N (unloaded) and a working frequency range from 2 Hz to 18 kHz. It is connected to a power amplifier and measurement unit. Besides amplification of the excitation signal provided by the reader, it is responsible for measurements of excitation current and voltage as well as acceleration and static pressure at the point of force application. For a medical diagnosis system, these additional measurements are necessary in order to detect faults and to ensure reproducibility between different measurements.

The external reader unit is responsible for magnetic field generation, data extraction and provides the low frequency input signal for the sinusoidal mechanical vibration excitation. Further measurement flow control, processing and visualization of measurement data as well as data storage and maintenance is carried out on a PC connected to the reader.

III. INTEGRATED LOCK-IN MEASUREMENT

The lock-in measurement technique, as an application of cross-correlation in signal processing, has been identified as a very useful approach to reduce the noise influence in the measured acceleration sensor signal [8]. It is integrated in the wireless sensor tag as a discrete circuit. The approach is feasible due to the facts that the mechanical system (prosthesis, femur and surrounding tissue) is excited through the shaker with a signal of known frequency and phase, the acceleration response is time-periodic and shows a fix phase relation for each frequency, and the mechanical excitation signals frequency and phase information is available in the wireless sensor tag in order to generate the lock-in reference

signal. The integrated lock-in can be described through Eq. 1, in which U_L is the voltage after applying the lock-in technique, U_M is the measured signal amplitude, ω_M the measured signal frequency, ω_{ref} the reference signal frequency and ϕ_{ref} the reference signal phase, which are averaged over the time period T .

$$U_L = \frac{1}{T} \int_{t_0}^{t_0+T} \underbrace{U_M \sin(\omega_M t)}_{\text{measured}} \cdot \underbrace{\sin(\omega_{ref} t + \phi_{ref})}_{\text{reference}} dt \quad (1)$$

When the excitation signal has the same frequency as the reference signal ($\omega_M = \omega_{ref}$) and an integration time from $0 \leq t \leq T$ is used, the integral solves to Eq. 2.

$$U_L = \underbrace{\frac{U_M \cos(\phi_{ref})}{2}}_{\text{wanted}} + \underbrace{\frac{U_M}{4T\omega} \cdot [\sin(\phi_{ref}) - \sin(\phi_{ref} + 2T\omega)]}_{\text{unwanted}} \quad (2)$$

The unwanted parts in Eq. 2 are of increasing influence in the case of small integration times and signal frequencies. If for a given frequency a phase match is reached (phase difference $\phi_{ref} = 0$) the lock-in amplified signal reaches its maximum signal output (Eq. 3).

$$U_L = \frac{U_M}{2} \quad (3)$$

Due to technical constraints, such as available energy and space in the sensor tag, the generation of a sinusoidal reference can be too costly. In this case a periodic rectangular signal can be used, as reference for the lock-in amplifier (chopper principle), an approach also chosen for the sensor tag. The associated special circumstances (i.e., higher order harmonics) have been discussed in [7].

The acceleration sensor signal is AC coupled and split into two signal paths, which are separately amplified (inverted and non-inverted) and passed through a switch to an integrator (low pass). Switching is controlled with the rectangular reference signal (with ω_{ref}, ϕ_{ref}) by the transponder unit ST1. The base frequency, for both excitation and lock-in reference signal, is the 125 kHz telemetry frequency of an internal oscillator (synchronized with reader station), which is divided by the factor n . This leads to a large step width with increasing frequencies. The controller can adjust the phase shift to obtain measurements with an arbitrary phase angle. A disadvantage of the chopper principle is the occurrence of harmonics, due to the fact that the reference signal is rectangular. These are damped by the low pass before digitized through the 10 bit A/D converter in the sensor tag.

The magnitude information, in general, is easier to interpret in order to identify the initially unknown system resonances. If the extrema of a single phase measurement are evaluated a changing phase relation (i.e., change of

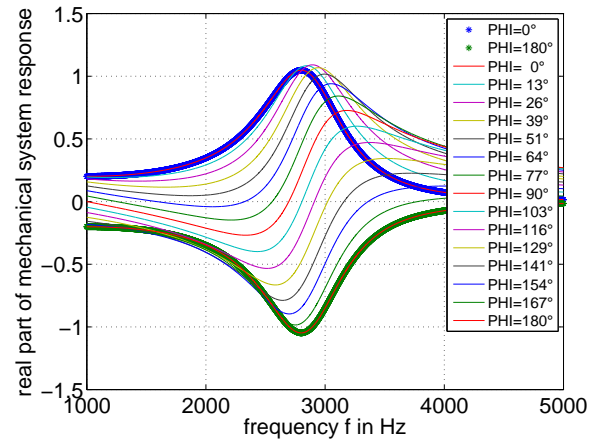


Figure 3. Influence of a varying reference phase onto real part of simulated mechanical system response, leading to falsely interpreted resonance frequency values (extremal value frequency in plot).

excitation or measurement equipment) can influence a determined extrema frequency value (Fig. 3). By performing two measurements for each examined frequency ($U_{L,A}, U_{L,B}$), with a 90° phase difference, the magnitude can be calculated. The result is independent from an unknown reference phase angle (Eq. 4) and the behavior of a dual phase lock-in amplifier can be reproduced (regarding the magnitude).

$$|U_L| = \sqrt{U_{L,A}^2 + U_{L,B}^2} = \frac{U_M}{2} \sqrt{\cos(\phi_{ref})^2 + \sin(\phi_{ref})^2} \quad (4)$$

Fig. 4 and Fig. 5 demonstrate the feasibility of the approach with both numerically simulated and experimentally obtained data from the measurement system. For the applied measurements with the measurement system, the reference phase value has been varied in steps of 10° between 0° and 90° . For each frequency point the two consecutive measurements ($\phi_{ref} = x^\circ, \phi_{ref} = x^\circ + 90^\circ$) were made instantly after each other.

IV. EXPERIMENTAL RESULTS

The overall system prototype has been tested in a measurement setup, which allows a varying anchorage of a prosthesis (Bicontact S, Aesculap) in an artificial femur (Sawbone). The housed sensor tag prototype is placed at the proximal end of the prosthesis stem and pressed onto the stem (Fig. 6). A reproducible anchorage variation is realized through threaded sleeves, placed in the artificial femur, which are distributed evenly around the prosthesis. In order to verify the feasibility of the measurement approach, the influence of loosening (decreasing prosthesis anchorage) on the resonance frequencies in the frequency spectrum is of interest. Therefore, the mechanical setup focuses on this behavior. Other influencing mechanical factors (i.e., surrounding tissue, hip and knee boundary conditions, etc.)

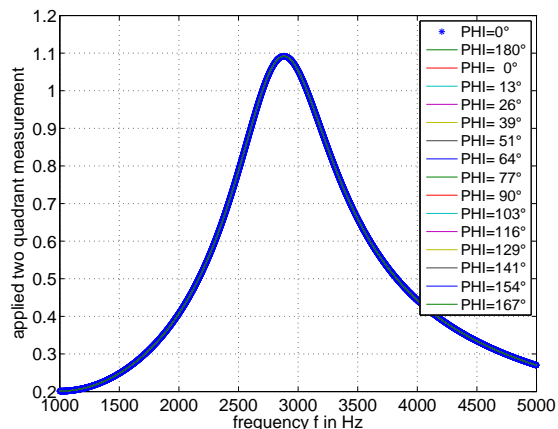


Figure 4. Advantage of combining two measurements with 90° phase difference - the calculated magnitude is independent from an unknown phase angle of excitation and measurement path.

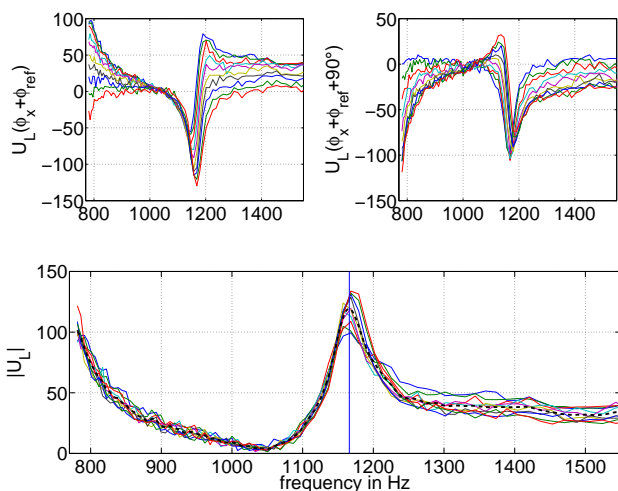


Figure 5. Applied measurement with the INHUEPRO system on a mechanical resonator around a resonance frequency with varied reference phase ($\phi_{ref} = 0^\circ..90^\circ$) of the lock-in amplifier. The top-left plot shows the measurement in the first quadrant ($\phi_{ref} = x^\circ$), the top-right plot shows the measurement in the second quadrant ($\phi_{ref} = x^\circ + 90^\circ$), the bottom plot shows the calculated magnitude (dashed line is averaged and additionally interpolated to increase the frequency resolution since frequency step width increases with increasing frequency). The magnitude response maxima frequency is almost independent from the reference phase angle (ϕ_{ref}).

are not in the scope of this work. The femur-prosthesis system is attached to an electro-dynamic vibration exciter (TIRAvib S522). The mechanic connection is realized via a clamp, placed at the central part of the femur, and a thread bar attached to the shaker. The reader station (with attached coil establishing communication and energy supply) is connected to a PC running the user application. It also provides the mechanic excitation signal for the shaker, which is amplified by a power amplifier (TIRA BAA 60). During

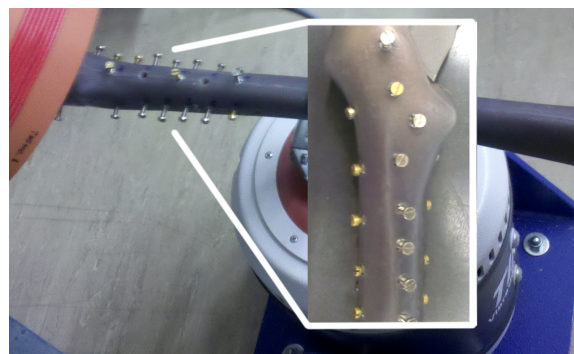


Figure 6. Measurement example with a prosthesis integrated in an artificial bone allowing an adjustable state of anchorage.

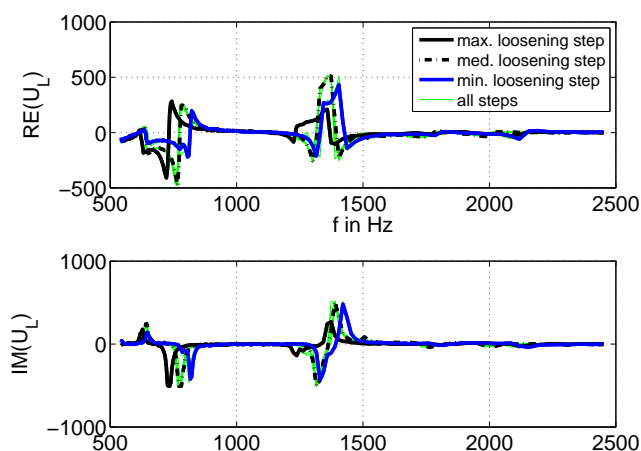


Figure 7. Measurement example with an artificial bone and an artificial prosthesis showing I. quadrant (0°, referenced as real part, top) and II. quadrant measurement (90°, referenced as imaginary part, bottom).

the experiment the state of anchorage has been gradually increased. For each measurement run, screws were fixed step-by-step starting from the distal end, until the well fixed case was reached. The obtained measurement results for a measurement with an initially unknown phase (1. quadrant measurement - claimed real part) and a measurement with a 90° degree offset (2. quadrant measurement - claimed imaginary part) are presented in Fig. 7. For each frequency value the magnitude is calculated, which leads to the results in Fig. 8. The first four magnitude resonance frequencies were evaluated. The absolute values for each loosening case as well as the frequency difference to the initial loose case are presented in Fig. 9.

V. CONCLUSION AND FUTURE WORK

Vibration analysis can be a valuable extension in the range of diagnostic measurement techniques and has the potential to detect hip prosthesis loosening. Through integration of a miniaturized vibration measurement system directly into the

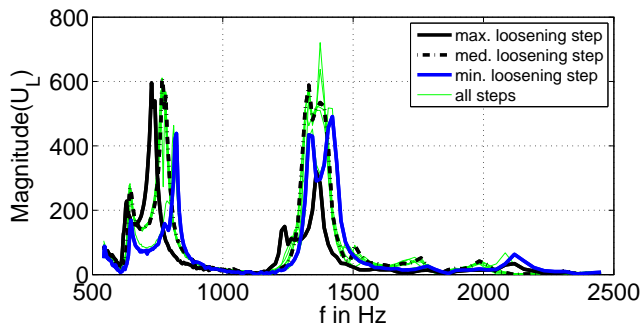


Figure 8. Calculated magnitude of several measurements on the same mechanic system with varied prosthesis anchorage state.

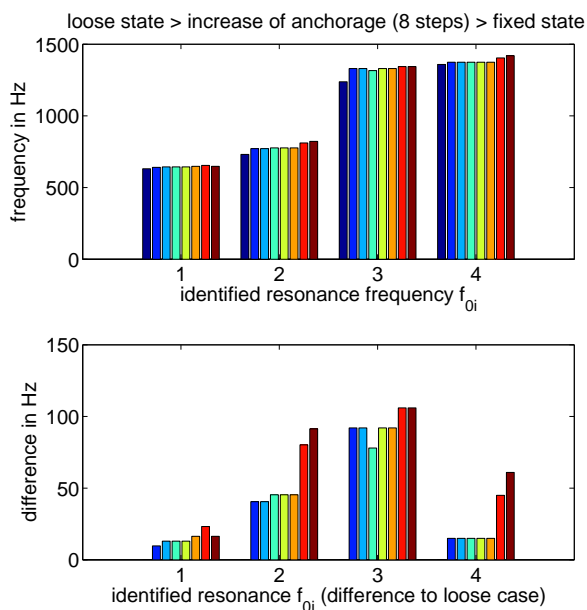


Figure 9. First four extracted resonances as identified with the diagnosis system under the influence of a step-by-step increase of prosthesis fixation (individual bars). The top plot shows the absolute frequency value for each fixation step. The bottom plot shows the absolute difference to the initial loose state.

implant, the damping effects of tissue in the measurement path can be overcome. Different loosening states of the implant can be distinguished in the mechanic frequency response of the bone-prosthesis system as demonstrated in the experimental section. In general, resonance frequencies are shifted to lower values if the loosening increases. When later on performing measurements with real patients, the obtained frequency spectra will be very different between patients (bone and tissue mass/stiffness, muscle tension, etc.). Therefore, a reference data set, obtained from a measurement after the hip replacement and finished prosthesis osseointegration, is needed for each patient. It can serve as a reference for long term patient monitoring and can be part of a medical case database. Additional experiments, not

in the scope of this paper, indicate that mechanic cross-sensitivities, such as static load or mass of surrounding tissue, also influence the detected resonances and need further analysis. Current work focuses on the identification of additional affecting factors and their impact (e.g., influence of lubrication) onto resonance shifts, the improvement of the wireless data transmission within the challenging metal environment (stem and backing), an improved bio-compatible housing and the preparation of the medical approval as well as the development of meaningful data visualization strategies supporting the diagnostic system.

ACKNOWLEDGEMENTS

This Work was supported by the 'German Bundesministerium für Bildung und Forschung (BMBF)', project 'IN-HUEPRO', program grant No. 16SV3916.

REFERENCES

- [1] D. O'Neill and W. Harris, "Failed total hip replacement: assessment by plain radiographs, arthrograms, and aspiration of the hip joint," *The Journal of Bone and Joint Surgery*, vol. 66, pp. 540–546, 1984.
- [2] G. Qi, W. P. Mouchon, and T. E. Tan, "How much can a vibrational diagnostic tool reveal in total hip arthroplasty loosening?" *Clinical Biomechanics*, vol. 18, pp. 444–458, 2003.
- [3] O. Temmerman, P. Raijmakers, J. Berkhof, E. David, R. Pijpers, Marinus, Molenaar, O. Hoekstra, G. Teule, and I. Heyligers, "Diagnostic accuracy and interobserver variability of plain radiography, subtraction arthrography, nuclear arthrography, and bone scintigraphy in the assessment of aseptic femoral component loosening," *Archives of the Orthopaedic and Trauma Surgery*, vol. 126, pp. 316–323, 2006.
- [4] C. Ruther, H. Ewald, W. Mittelmeier, A. Fritsche, R. Bader, and D. Kluess, "A novel sensor concept for optimization of loosening diagnostics in total hip replacement," *Journal of Biomechanical Engineering*, vol. 133, 2011.
- [5] A. Rowlands, F. Duck, and J. Cunningham, "Bone vibration measurement using ultrasound: Application to detection of hip prosthesis loosening," *Medical Engineering and Physics*, vol. 30, p. 278284, 2008.
- [6] R. Puers, M. Catryse, G. Vandevoorde, R. Collier, E. Louridas, F. Burny, M. Donkerwolcke, and F. Moulart, "A telemetry system for the detection of hip prosthesis loosening by vibration analysis," *Sensors and Actuators*, vol. 85, pp. 42–47, 2000.
- [7] U. Marschner, H. Grätz, B. Jettkant, D. Ruwisch, G. Woldt, W.-J. Fischer, and B. Clasbrummel, "Integration of a wireless lock-in measurement of hip prosthesis vibrations for loosening detection," *Sensors and Actuators A: Physical*, vol. 156, pp. 145–154, 2009.
- [8] J. H. Scofield, "A frequency-domain description of a lock-in amplifier," *American Journal of Physics*, vol. 62, pp. 129–133, 1994.

Sensing of the Functional State of Fertility of Cows

Michał Borecki, Marcin Kozicki, Jan Szmidt,
Andrzej Jakubowski
Institute of Microelectronics and Optoelectronics
Warsaw University of Technology
Warsaw, Poland
borecki@imio.pw.edu.pl

Michael L. Korwin-Pawlowski
Département d'informatique et d'ingénierie
Université du Québec en Outaouais
Gatineau, Québec, Canada
michael.korwin-pawlowski@uqo.ca

Maciej Szmidt, Kaja Urbanska
Warsaw University of Life Sciences
Warsaw, Poland.
mszmidt@yahoo.com

Abstract: Sensing of cow functional state of fertility is important for the cattle and dairy industries. Usual medical techniques, like the hormone test in urine or milk and the liquid based cytology, are not ideal when farm environment is considered and there is a need to develop improved methods. The method presented in this paper is based on fiber optic capillaries techniques using neural network analysis. We have investigated the vaginal fluids of healthy cows and of those suffering from vaginitis and have proved that the method allows establishing the estrous state and distinguishing between healthy and sick animals. We present the experimental setup and analyze various aspects of the sensor design and operation principle with special consideration to the ANN part. The results of the measured signals analysis of ANN training showed a correlation of 0.987 for estrus and 0.986 for the classification of functional state of fertile phase. The proposed sensor introduced automatically precise information of possible vaginitis obtained by establishing the presence of antibodies in the vaginal fluid.

Keywords: cow estrous detection; cow vaginitis detection; leukocytes detection; fiber optic sensors, fiber optic capillary sensors.

I. INTRODUCTION

The estrous cycle of cows has been investigated with increasing intensity in the recent years [1-8]. Nowadays, the estrous cycles of cows are often resynchronized [9]. Methods of fertile phase of estrus detection are under continuous investigation and improvement [10-18]. Mathematical, methods and methods using fuzzy logic have also been in development [19-20]. Of interest are methods using radiotelemetry [21] and the future may well see mobile radio networks being used for monitoring [22], in which case the energy consumption is an issue [23].

The state of the art of estrus cycle determination was presented in a comparison of four methods for detection of estrus in dairy cows with resynchronized by artificial insemination estrus cycles by Cavalieri et al. [24]. In that

study the sensitivity and predictive values of pedometers, radiotelemetric transmitters (HeatWatch) tail-paint and heat-mount detectors were compared. The semi-laboratory method based on measuring the milk progesterone concentration was used as the reference standard for cows being in estrus. Sensitivity was defined as the percentage of estrus cows detected to the number of cows in estrus and the positive predictive value as the number of correct detections divided by the sum of correct and false positive detections. The conclusion was that all four methods gave over 80% of the sensitivity, with the pedometer method scoring lowest at 81.4% and the tail-paint method scoring highest at 91.3%. In terms of positive predictive value, the results were closer and ranged from 87.5% for the pedometer method to 100% for the radiotelemetry method, with the other two methods showing about 92% predictive value [24].

An important problem of cow reproduction is keeping the health of the vaginal duct. These are known methods of veterinary medicine used for that purpose, but they are not automated and when the vaginal changes are visible the illness is usually seriously advanced. Moreover, the bacterial vaginitis can be in its initial and hidden state invisible [25].

Therefore, we set ourselves the following objectives:

- To investigate and develop a sensor which would provide the information of functional state of fertility useable to make decisions on insemination of the cows with a significantly higher sensitivity than the existing field methods,
- To develop a sensor which also could be operated in the farm environment, not only in laboratory environment,
- A developing a method that would yield itself easily to automation, miniaturization and be of low cost,
- To evaluate and further optimize the technology of fiber optic capillary sensors with artificial neural network analysis of data from the point of view of the above main objectives.

II. SENSOR SET-UP

A. Principle of sensor work

In this work we present new developments and advances on intelligent photonic sensors and their applications working on the principle of monitoring optical intensity changes that take place in dynamically forced measurement cycles that were first postulated in [26]. The sensors use fiber optic capillaries in which the phase of the filling liquid changes locally to gas when forced by local heating, while the propagation of light across the capillary is monitored, Fig. 1. Therefore, the sensors examine simultaneously many liquid parameters which are then processed in artificial neural networks [27]. When analyzing biological fluids, in order to achieve good reproducibility and to avoid cross-contamination from sample to sample, it is advantageous to use disposable optrodes. The low cost of capillaries make their disposability practically possible [28].

Before the test the capillary optrode is partially filled with liquid, after which both its ends are closed. Care must be taken that there are no bubbles of gas present after filling the optrode; otherwise the optrode has to be eliminated from the tests [29]. When the capillaries are filled uniformly by the liquid, the initial levels of reflected and scattered signals are measured. As the cow's vaginal fluid in functional state is semitransparent, we expect initially high reflection signal levels and low scatter signal levels. When the bubble appears, the reflected and scatter signal decrease.

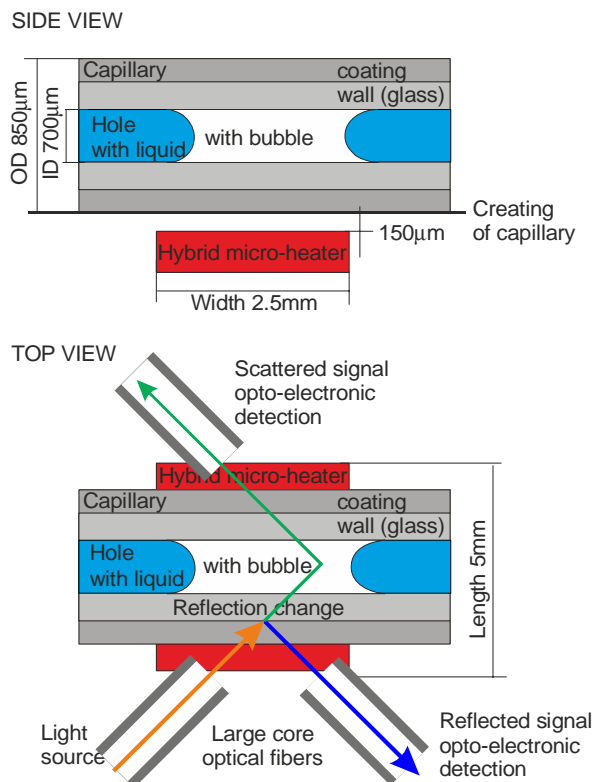


Figure 1. Schematic construction of the capillary head.

When the reflected signal decreases rapidly it gives the impulse to switch off the microheater. Depending on the thermo-dynamical conditions, the gas phase is absorbed in the liquid or remains in the form of a series of small bubbles. Due to structural changes in vaginal fluid induced by heating, the scattered signal can increase.

B. Sensor construction

The capillaries used in our experiments were cut into 10 cm long sections from Polymicro Inc. TSP 700 850 fiber. They had both ends closed. In the measuring head we also installed large core optical fibers BFH 37-600 from Thorlabs, the outer diameter of cladding of which is almost the same as the outer diameter of the capillary. In the previous sensor construction for fertility phase examination we used separate bases and replaceable capillary optrodes [30]. In the present work we implemented improvements of the fiber positioning method in the head base, which were key factors for improvement of the repeatability of signal measured from head to head. We also introduced the detection of the scattered signal, Fig 1. As the light source we used the fiber coupled laser source S1FC675 from Thorlabs at a level from 0.01 to 0.2mW. The light source was modulated with a function generator DG2021 from Rigol. The signal was transmitted to the BFH 37-600 fiber by graded-index multimode patch cables with a FC/SMA adapter. The optoelectronic detection unit of our own construction had an SMA fiber input and consisted of an integrated photo-amplifier and a band-pass filter with amplification and RMS detection. The optoelectronic unit was connected to a personal computer by analog input of IOtech personal Daq 3000 16bit/1MHz USB data acquisition system. We fed the heater from the laboratory power supply through an electric switch. The hybrid micro heater was powered with 5W in periods shorter than 30s during which time it showed resistance changes of 0.5% that can be considered as being stable. We also used two LM35DT [31] circuits connected, with the Daq 3000 system, by low pass filters to monitor the temperatures of the measuring head base and of the surrounding ambient. To operate the system we designed a script in DasyLab 10 with 0.1s sampling rate.

The sensor was calibrated by filling the capillary with deionized water and performing a measurement procedure as on Fig. 2. The deionized water started boiling in a time range from 17.1 to 18.5 seconds of the measurement cycle for different disposable optrodes, but the characteristic shape of the signal was considered repeatable. The formation of the gas bubble caused a decrease of the reflected and the scattered signals. The scattered signal in this experiment came from two layers of capillary coating. However, when the bubble was present the scattered signal came mainly from one only layer of capillary coating and that was the reason of the decrease of the signal. After the heater was switched off, the bubble in the water changed from the gas to the liquid phase. There were no changes in the scattered signal after gas phase resorption. We performed experiments when the ambient temperature was in range from 22°C to 24°C and when the head base temperature was not greater than 0.5°C over the surrounding ambient.

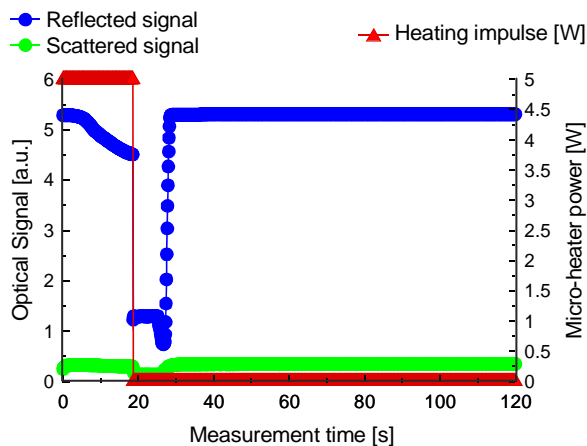


Figure 2. Measurement procedure signals of deionized water.

During the calibration cycle we also registered the temperature distribution in the capillary optrode with a R300 NEC thermo-vision camera and InfReC Analyzer software. The map of temperature just before local boiling of water is presented in Fig. 3. The temperature map at the moment just after the start of boiling is presented in Fig. 4. The positions of the capillary on Fig. 3 and Fig. 4 are rotated by 90 degrees compared with Fig. 1.

The points a, b, c in Figs. 3 and 4 are on the axis of the capillary. The temperature of the capillary was measured in points over the outer edges of the micro-heater. The temperature in point b was determined by the power dissipated in the micro-heater, and exceeded the boiling point of water, putting the steam in the bubble in a superheated condition. Due to good heat conductivity of water the temperature inside the capillary could be considered as almost uniform on the line a-c.

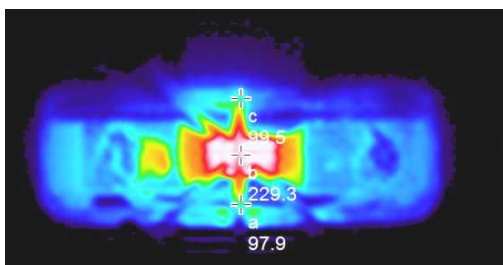


Figure 3. Temperature map just before boiling at 17s of the measurement procedure.

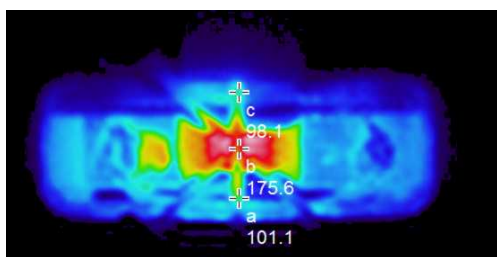


Figure 4. Temperature map just after boiling at 18s of the measurement procedure. The movement of the boiling vapor phase is visible in point a.

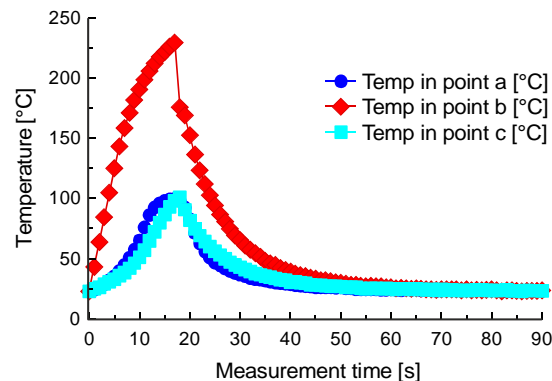


Figure 5. The temperature versus time curve of deionized water filling the capillary measured in the points showed in Fig. 4 and Fig. 5.

The temperature increase in the liquid was considered almost stable in time (see Fig. 5).

III. EXPERIMENT RESULTS

Our experiments were divided in two parts. In the first part we analyzed the optical signals from different components of the vaginal fluids. In the second part we examined the vaginal fluid of cows in the most fertile phase for healthy cows and for cows suffering from vaginitis.

A. Examination of components of vaginal fluid

We used Permeabilization and Blocking Solutions (PBS) from Sigma Aldrich Inc to fabricate the mixture containing antibodies. The purified PBS measurement procedure gave signals very close to those for deionized water. The measurement procedure with PBS antibodies solution is presented in Fig. 6. The gas phase was created in 5.1 second of the measuring procedure, which was three times earlier than for case of deionized water. This phenomenon was repeatable but we found it not easy to interpret. The scattered signal increased significantly from 0.18 a.u. at the initial point of procedure to 0.3 a.u. just before turning the heating off and to average level 1.2 a.u. at the end of procedure. The liquid just above the heater after heating off resorbs the gas phase, the color of this liquid becomes foggy white. This can be explained as antibody protein denaturation. Glycerol is sometimes used as lubricant of cow's vaginal duct. Therefore, we examined next the mixture of e-coli bacteria with glycerol (see Fig. 7). Glycerol and water showed different characteristics of signal reflection, but when the bubble was resorbed, a small increase of the scattered signal from initial 0.76 a.u. to 1.1 a.u. was observed.

The mixtures of antibody and bacteria that we analyzed had similar concentrations of biological components, which combined with the similarity of the amount of energy transferred to the capillary, led us to the conclusion that the analyzed antibody was easier denaturated by temperature than e-coli, and that the scattered signal changes that could be connected with their presence may enable the detection of vaginitis.

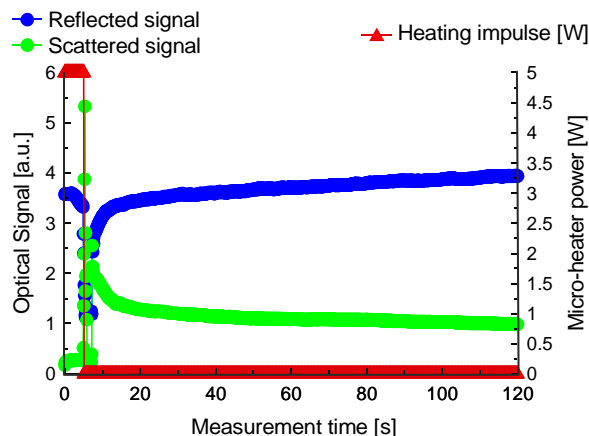


Figure 6. Measurement procedure signals of pbs antibody mixture

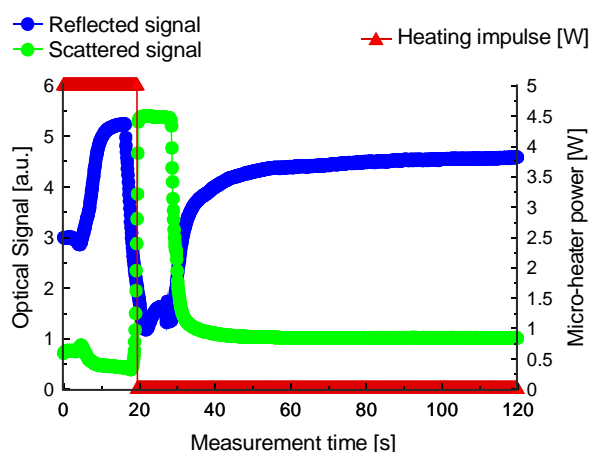


Figure 7. Measurement procedure signals of glycerol e-coli mixture.

B. Examination of cow's vaginal fluid

We analyzed vaginal fluids of Holstein-Friesian and Jersey cow breeds that are typical cattle in Poland. The cows were selected randomly from herds counting from 10 to 100 animals. We examined samples of 15 cows classified as healthy. The vaginal fluid was collected in estrus and the post-estrus state. The vaginal fluid was also collected from 2 cows which were in estrus and had vaginitis diagnosed by a veterinary doctor on the farm and confirmed by microbiological analysis, Fig. 8. The difference between healthy and ill state was not great by the count of the bacteria colony forming units. The vaginal fluid arborization test of cow in functional state of fertility is presented on Fig. 9. The observations of filling of the capillaries with various kinds of vaginal fluids are presented in Table 1.

The vaginal fluid of not fertile phase did not enter the capillary without pumping. This was the simplest test for most fertile period of estrus. When the cow had serious problems of its vaginal duct, the vaginal fluid changes were visible and further diagnostic methods were not required, but there were no visual differences between vaginal fluids of cow with vaginitis or functional state, which called for additional diagnostic tests.

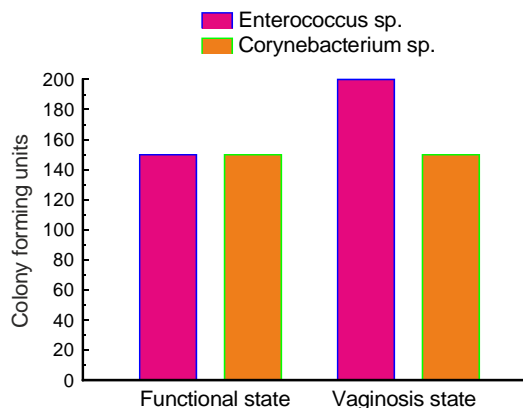


Figure 8. Microbiology classification of vaginal fluids.



Figure 9. Vaginal fluid arborization test of cow in functional state of fertility, photo made with AFM S3400

TABLE I. OBSERVATION OF FILLING OF THE CAPPILARIES

Liquid type	Capillary action [mm]	Capillary filling
Water	28	capillary action
Vaginal fluid at most fertile phase with ovulation	20	capillary action
Vaginal fluid at most fertile phase without ovulation	0	syringe pumping working well
Vaginal fluid of cow with vaginosis	20	capillary action
Vaginal fluid of cow with ovarian cysts	0	syringe pumping working badly

Measurements of healthy cow's vaginal fluid using our method showed conformity with the results of examinations just discussed, Fig. 10. We observed that the vapor phase creation time was short and was about 5 seconds. The vapor phase existed for 2 seconds. The scatter signal did not exceed after heating the level of 1.5 a.u. but would increase correspondingly with the count of present bacteria. The limits of the increase of the signal are marked as red lines on the part B in Fig. 10 and Fig. 11. The result of the examination of the vaginal fluid of cows with vaginitis is presented in Fig. 11.

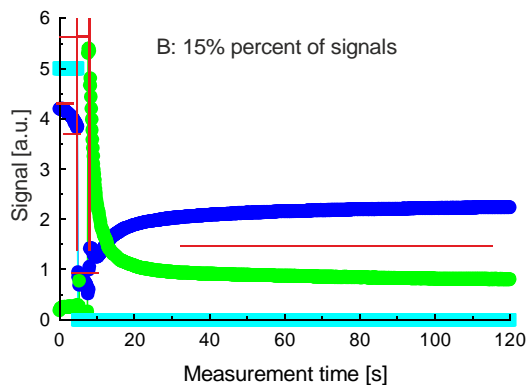
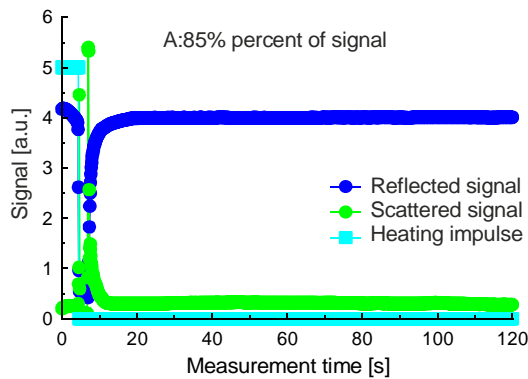


Figure 10. Measurement procedure signals for cows classified as healthy and in estrus state.

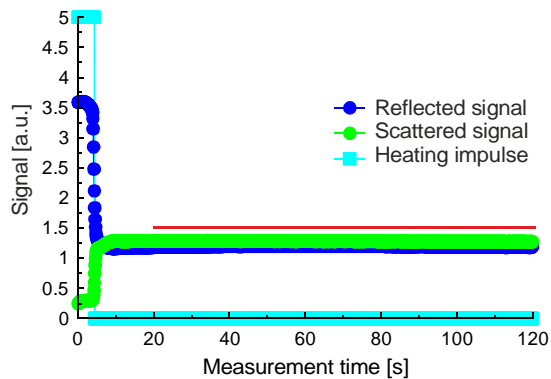


Figure 11. Measurement procedure signal of vaginal fluid of cows with vaginosis.

We observed that the gas phase was either not present or was masked by the denaturation of proteins that would give a significant increase of the scattered signal from the stable level after turning the heating off.

The cow in late estrus state approaches the limits of its readiness for insemination. In our observations on Fig. 12, the signals of vaginal fluid changed compared to Fig. 10. The time of gas phase creation increased significantly to over 10 seconds of the measurement procedure. The generated gas phase accumulated the energy that did not allow the bubble to be resorbed.

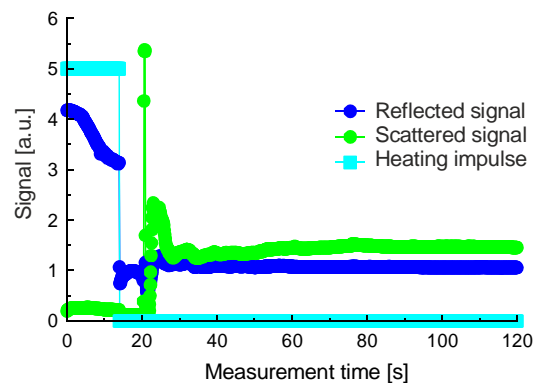


Figure 12. Measurement procedure signals of vaginal fluid of cows after estrus.

IV. ARTIFICIAL NEURAL NETWORK FOR FUNCTIONAL STATE OF FERTILITY CLASSIFICATION

The Qnet artificial neural network ANN used for classification of the vaginal fluid samples showed its advantages in sensor data processing. We examined the multilayer perceptron for classification of measured signals. We assumed two output information levels: a) healthy/unhealthy, b) ready for reproduction/ not ready for reproduction. While the cow is in the unhealthy state we assumed that it was not ready for reproduction, but is ready for veterinary treatment. The input information was the levels of signals and timing of the gas phase creation and the duration of the gas phase. The gas phase creation was evidenced by a rapid drop of the reflected signal. The gas phase duration was defined by the difference of time of the maximum level of the scatter signal and the mentioned drop of the reflected signal when the drop of the reflected signal undershot the level of 0.8 a.u. As the levels of the reflected signal we included into the ANN input: the initial level, the minimal level and the level at the measurement end. For the scattered signal we analyzed the: initial level, the maximum level and the last measured level. Therefore our ANN had 8 inputs, 2 outputs and 4 hidden layers in which the perception used the sigmoid activation function and one hidden input with constant -1 value.

Such ANN training gave a 0.986 correlation coefficient in the training set and a 5% RMS error of outputs when cases from monitored cows but not contained in the training set were analyzed. The output responsible for healthy state with a correlation coefficient of 0.999 was more precise than the estrus output where it was 0.987.

We made test of network output for cow that is not included in training set and has first estrus after miscarry. The RMS error of most fertile state was 21%. It is a large figure, but the third estrus state after miscarry is standard consider as fertile and a question arise of mentioned cow healthy state. Therefore, the 5% of output tolerance of fertile state classification seems reasonable.

The QNet software enabled us to analyze the input node contribution of output signals, Tab. 2. The data analysis showed that in our method the functional state of the cow

examined on base of vaginal fluid was directly and firmly connected with gas phase creation. Taking into account the time of gas phase creation and the time of its lasting, we have a level of 84% of contribution for cow functional state classification. We also could see that the gas creation was also the main information for cow readiness for reproduction at a level of 65% of contribution.

TABLE II. ANN ANALYSIS OF INPUT TO OUTPUT CONTRIBUTION

Input	Input contribution [%]	
	Output for cows ready for reproduction	Output for cows in functional state
Initial level of reflected signal	14	1
Time of gas phase creation	35	83
Time of gas phase lasting	30	1
Minimal level of reflected signal	8	3
End level of reflected signal	2	0.5
Initial level of scattered signal	5	0.5
Maximum level of scattered signal	4	0.5
End level of scattered signal	2	0.5

V. CONCLUSION AND FUTURE WORK

We have proved that the fiber optic capillary sensors with artificial network analysis can provide information on cow estrus state with a sensitivity superior to other existing methods and in addition provide information as to the presence of cow vaginitis.

The results of the measured signals analysis of ANN training showed a correlation of 0.987 for estrus and 0.986 for the classification of functional state of fertile phase. The proposed sensor introduced automatically precise information of possible vaginitis which can be of practical usefulness. We showed that the information on vaginitis was obtained mainly by establishing the presence of antibodies in the vaginal fluid. These antibodies are normally transparent in visible light in standard situations. Moreover, the capillary filling capability can act as an indicator of the most fertile state of cow estrus.

Therefore, we conclude that the proposed construction may be in future the base of commercially marketable instruments. For this purpose the sensor construction has to be integrated into a complete instrument and therefore more resistant to use in harsh environment. The examination of greater number of cases could lead to artificial multilayer perceptron network optimization, mainly by precise the range of output tolerances for cows contained and not contained in training set.

ACKNOWLEDGMENT

This work was supported by the European Union structural funds grant MNS-DIAG task 2.



REFERENCES

- [1] A. Bane and E. Rajakoski “The bovine estrous cycle,” *The Cornell Veterinarian*, vol. 51, pp. 77-95, 1961
- [2] M. D. Royal, A. O. Darwash, A. P. F. Flint, R. Webb, J. A. Woolliams and G. E. Lamming, “Declining fertility in dairy cattle: Changes in traditional and endocrine parameters of fertility,” *Animal Science*, vol. 70, pp. 487-501, 2000
- [3] I. M. Sheldon and H. Dobson, “Reproductive challenges facing the cattle industry at the beginning of the 21st century,” *Reprod Suppl.* vol. 61, pp. 1-13, 2003
- [4] H. Lopez, L. D. Satter, and M. C. Wiltbank, “Relationship between level of milk production and estrous behavior of lactating dairy cows,” *Animal Reproduction Science* vol. 81, pp. 209-223, 2004.
- [5] R. Kasimanickam, J. M. Cornwell and R. L. Nebel, “Fertility following fixed-time AI or insemination at observed estrus in Ovsynch and Heatsynch programs in lactating dairy cows,” *Theriogenology*, vol. 63, pp. 2550-2559, 2005.
- [6] G. C. Lamb, C. R. Dahlen , J. E. Larson, G. Marquezini, and J. S. Stevenson, “Control of the estrous cycle to improve fertility for fixed-time artificial insemination in beef cattle. A review,” *J. Animal Science*, vol. 88, pp. E181-E192, 2010.
- [7] S. W. Walsh, E.J. Williams and A. C. O. Evans, “A review of the causes of poor fertility in high milk producing dairy cows,” *Animal Reproduction Science*, vol. 123, pp. 127-138, 2011
- [8] A. Bonneville-Hébert, E. Bouchard, D. D. Tremblay and R. Lefebvre, “Effect of reproductive disorders and parity on repeat breeder status and culling of dairy cows in Quebec,” *Canadian J. Veterinary Research*, vol. 75, pp. 147-151, 2011.
- [9] M. Sakaguchi, “Practical aspects of the fertility of dairy cattle,” *J Reprod Dev.* vol. 57, pp.17-33, 2011.
- [10] R. Rajamahendran, J. Robinson, S. Desbottes, and J. S. Walton, “Temporal relationships among estrus, body temperature, milk yield, progesterone and luteinizing hormone levels, and ovulation in dairy cows,” *Theriogenology*, vol. 31, pp. 1173-1182, 1989.
- [11] S.E. Kitwood, C.J.C. Phillips and M. Weise, “Use of vaginal mucus impedance meter to detect estrus in the cow,” *Theriogenology*, vol. 40, pp. 559-569, 1993
- [12] A. Y. Ribadu, W. R. Ward, and H. Dobson, “Comparative evaluation of ovarian structures in cattle by palpation per rectum, ultrasonography and plasma progesterone concentration,” *Veterinary Record*, vol. 135, pp. 452-457, 1994.
- [13] J. Rutllant, M. López-Béjar, P. Santolaria, J. Yáñez, and F. López-Gatius, “Rheological and ultrastructural properties of bovine vaginal fluid obtained at estrus,” *Anat.* vol. 201, pp. 53-60, 2002
- [14] O. A. Peralta, R. E. Pearson and R. L. Nebel, “Comparison of three estrus detection systems during summer in a large commercial dairy herd,” *Animal Reproduction Science*, vol. 87, pp. 59-72, 2005.
- [15] J. Rutllant, M. López-Béjar, and F. López-Gatius, “Ultrastructural and rheological properties of bovine vaginal fluid and its relation to sperm motility and fertilization: a review,” *Reprod Domest Anim.* vol.40, pp. 79-86, 2005.
- [16] K. R. Kumar and G Archunan, “Analysis of urinary fatty acids in bovine (*Bos taurus*): An effective method for estrus detection,” *Indian J. Animal Sciences*, vol. 76, 2006. <http://epubs.icar.org.in/ejournal/index.php/IJAnS/article/view/4333/1676>
- [17] K. Herzog et al. “Luteal blood flow is a more appropriate indicator for luteal function during the bovine estrous cycle than luteal size,” *Theriogenology*, vol. 73, pp. 691-697, 2009.

- [18] A. H. Souza et al. "Ultrasonographic evaluation of endometrial thickness near timed AI as a predictor of fertility in high-producing dairy cow," *Theriogenology*, vol. 75, pp. 722-733, 2011
- [19] H. M. T. Boer, C. Stötzel, S. Röblitz, P. Deuflhard, R.F. Veerkamp, and H. Woelders, "A simple mathematical model of the bovine estrous cycle: Follicle development and endocrine interactions," *J. Theoretical Biology*, vol. 278, pp. 20-31, 2011.
- [20] S Leandro dos Anjos Brunassil et al. "Improving detection of dairy cow estrus using fuzzy logic," *Scientia Agricola*, vol.67, 2010, doi: 10.1590/S0103-90162010000500002
- [21] M. B. G. Dransfield, R. L. Nebel, R. E. Pearson, and L. D. Warnick, "Timing of Insemination for Dairy Cows Identified in Estrus by a Radiotelemetric Estrus Detection System," *J. Dairy Science*, vol. 81, pp. 1874-1882, 1998
- [22] D. Bri, M. Garcia, J. Lloret, and P. Dini, "Real deployments of wireless sensor networks" *Sensor Technologies and Applications, 2009, SENSORCOMM '09*. pp. 15-423, DOI. 10.1109/SENSORCOMM.2009.69
- [23] J. Zheng, P. Dini, A. Jamalipour, P. Lorenz, and Do Van Thanh, "Energy-efficient network protocols and algorithms for wireless sensor networks," *Int. J. Communication Systems*, vol 20(7), pp. 743-746, 2007.
- [24] J. Cavalieri, V. Eagles, M. Ryan, and K. L. Macmillan, "Comparison of four methods for detection of oestrus in dairy cows with resynchronised oestrous cycles," *Australian Veterinary Journal*, vol. 81(7), pp. 422-425, 2003.
- [25] H. Wolrath, U. Forsum, P. G. Larsson, and H. Boren, "Analysis of bacterial vaginosis-related amines in vaginal fluid by gas chromatography and mass spectrometry," *Journal of Clinical Microbiology*, vol. 39(11), pp. 4026-4031, 2001.
- [26] M. Borecki, M. L. Korwin-Pawłowski, M. Bełłowska, "A method of examination of liquids by neural network analysis of reflectometric and transmission time domain data from optical capillaries and fibers," *IEEE Sensors*, vol. 8, pp. 1208-1213, 2008.
- [27] M. Borecki, M. L. Korwin-Pawłowski, P. Wrzosek, J. Szmidt, "Capillaries as the components of photonic sensor microsystems," *Meas. Sci. Technol.* vol. 19, pp. 065202, 2008.
- [28] M. Borecki, M. L. Korwin-Pawłowski, "Optical capillary sensors for intelligent microfluidic sample classification," in: *Nanosensors: Theory and Applications in Industry, Healthcare and Defence* Lim T.-C. (Ed.), CRC Press, Boca Raton, FL, USA, 2011, pp. 215- 245.
- [29] M. Borecki, M. L. Korwin-Pawłowski, M. Bełłowska, J. Szmidt, M. Szmidt, M. Duk, K. Urbańska, and A. Jakubowski, "Intelligent photonic sensors for application, in decentralized wastewater systems," in *Waste Water – Evaluation and Management*, F.S.G. Einschlag (Ed.), InTech, Rijeka, 2011, pp. 181-202.
- [30] M. Borecki, M. L. Korwin-Pawłowski, M. Bełłowska, M. Szmidt, K. Urbanska, J. Kalenik, Ł. Chudzian, Z. Szczepanski, K. Kopczynski, A. Jakubowski, and J. Szmidt, "Capillary microfluidic sensor for determining the most fertile period in cows," *Acta Physica Polonica*, vol. 118, pp. 1093-1099, 2010.
- [31] Texas Instruments, "LM35 Precision Centigrade Temperature Sensors", National Semiconductor Corporation, Literature Number: SNIS159B, November 2000, <http://www.ti.com/lit/ds/symlink/lm35.pdf>.

Bend Sensors Modeling for Fast Signal Recovering in Human Motion Analysis

Giancarlo Orengo, Antonino Lagati, Giovanni Saggio

Department of Electronics Engineering

Tor Vergata University

Rome – Italy

orengo@ing.uniroma2.it, antonino.lagati@istruzione.it, saggio@ing.uniroma2.it

Abstract—Investigation on the more suitable technologies to register human body movements in 3D space with great spatial accuracy is a very challenging task, because a wide range of applications are concerned, from registration of post-stroke rehabilitation or sports performance, to monitoring of movement of disabled or elderly people, only to give some examples. In this paper, the possibilities offered by resistive bend sensors to register joint bend angles, for human posture recognition and motion analysis, have been explored. This paper suggests to extract an electrical model either to simulate their electrical behavior during bending and extension movements, and to recover the true bending angles from model simulation. To give an example, the proposed model was applied to track human joint movements, and it was demonstrated that it can lead to recover the original signal waveform, which represents the true joint rotation, also for the fastest human speed.

Keywords– bend sensor; sensor modeling; motion analysis; posture recognition.

I. INTRODUCTION

Technology progress in the last decades have provided the opportunity to observe human behavior in 3D space with great spatial accuracy, thanks to image-based methods or virtual reality tools. This is a very challenging task, because a wide range of applications are concerned, from registration of post-stroke rehabilitation and sports performance, to monitoring of movement of disabled and elderly people, only to give some examples [1].

In order to measure human body kinematics, it is convenient to adopt sensors, which can measure bending angles with good precision despite a low cost. Resistive bend sensors can be made of a polyester base material printed on with a special carbon ink. The polyester acts as a support while the ink's resistance decreases the more it is bent. The ink is screen printed so it can be applied on virtually any custom shape and size film to fit to each body joint. The substrate film material is usually formed by Kapton and/or Mylar for their properties, stands the fact that substrate must be able to bend repeatedly without failure for the sensor to work [2]. The sensor can be over-molded (for instance with silicon or urethane) and it can work in dirty environments (oil, dust). This kind of sensors are available on the market (e.g., Images SI Inc. [3], Flexpoint Sensor Systems Inc. [4]). Figure 1 provides a photo of a sensor strip sample.

Resistive bend sensors can be applied to body joint as electronic goniometers, to realize goniometric sock for rotation assessment of body segments in human posture recognition, or to goniometric gloves, which enable

multiple finger joint positions to be acquired simultaneously, and allow hand patterns to be recognized [5,6,7,8]. However, in order to useful exploit sensor's properties, a complete electromechanical characterization is mandatory [9]. Moreover, a new modeling technique will be developed. Available resistive bend sensor models, in fact, continue to incorrectly employ a merely variable resistance to model the sensor electrical properties under a bending strength. Little experimental study and theoretical analysis has been undertaken on the effect of a range of bend angles and rates on sensor response, as well as investigation on repeatability testing under static and dynamic bending strength [7]. One perceived problem is to calibrate sensor performance in terms of prediction error in high precision and/or high speed applications. As a result, an electrical model is required that not only models the static resistive response, but also characterizes the electrical behavior during bending transitions [10]. A logical choice seems to investigate on sensor behavioral models, as a consequence of the most important manufacturers of commercial bend sensors do not provide any description of their own technological process.

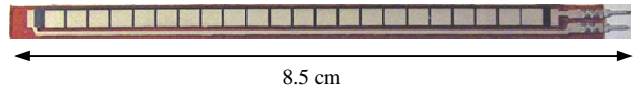


Fig. 1. Photograph of a unidirectional bend sensor, length 4.5", width .25", thickness .020" (Images SI Inc. Staten Island NY USA, <http://www.imagesco.com/sensors/bend-sensor.html>).

In Section II, the experimental apparatus for static and dynamic measurements is described, and the static performance of bend sensors to different bend angles, is provided. In Section III, a new approach to extract electrical behavioral models is described. In Section IV, the behavioral model was applied either to predict sensor performance in tracking slow and fast rotations, and to recover the true sensor rotation angles. Finally, some conclusions are drawn in Section V.

II. EXPERIMENTAL APPARATUS

The apparatus employed for this analysis was designed to emulate, in a controlled environment, the behavior of commercial carbon-ink bend sensors, printed on pet strip substrates, when applied to body joints to track segment rotations. Figure 2 shows a schematic of the experimental set-up. The sensor sample was laid as a cantilever beam on a metal hinge. In order to bend the sensor from 0 to 150 degrees (for set-up mechanical constraints) with different bending rates, the sample side connected to the

electrodes was locked in a stationary clamp, fixed to a rotating platform operated by a step motor. The other side of the sensor strip was put in a sliding clamp to avoid the sample stretching. Bending angle step amplitude was changed reliably with one degree resolution from a Labview interface serial connected to a PC. The step motor is a PD-109-57 sample from Trinamic, connected to the PC through a RS-232 cable. Motor speed rate can be set changing the TMLC (Trinamic Motion Control Language) units (1000 TMCL units correspond to 9.537 RPS or rounds-per-second). In this way, the sensor resistance can be characterized in terms of the expected bending angles at different speed rates [11].

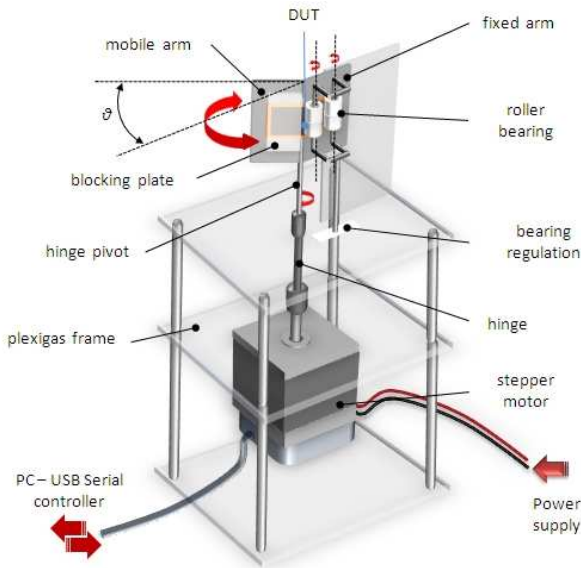


Fig. 2. Schematic of the experimental set-up.

Connecting a digital multimeter, a quasi-static resistance characterization against the bending angle of a bend sensor from Images SI Inc. has been accomplished. Since body segment rotations approximately range from 0 to 150 degrees, they will be tracked exploiting only outward rotations. In this case, the sensor resistive strip must be external with respect to the body joint. Sensor resistance behavior is almost linear with bending rotation degrees, as shown in Fig. 3.

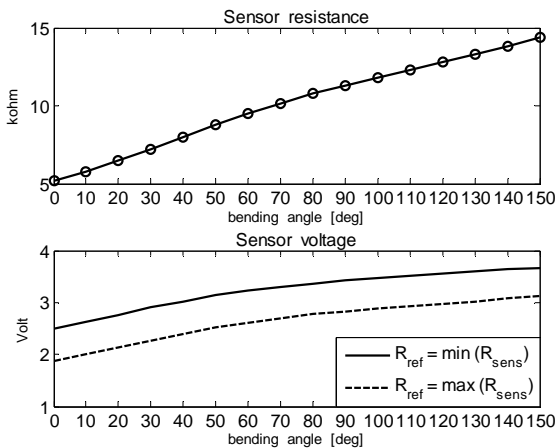


Fig. 3. Static electrical sensor characterization, in terms of resistance and output voltage from a voltage divider.

In most applications, however, the response of the sensor device under test (DUT) is acquired throughout its voltage response in a resistive divider, as shown in Fig. 4. In this case, a linear resistance response does not imply a linear voltage as also reported Fig. 3. As brought out in Fig. 5, the choice of a low or high series reference resistance R_{ref} changes the sensor sensitivity at low or high bending degrees, respectively. To enhance sensor sensitivity at low bending angles, a series resistance equal to the starting value (at 0°) of the sensor is often chosen.

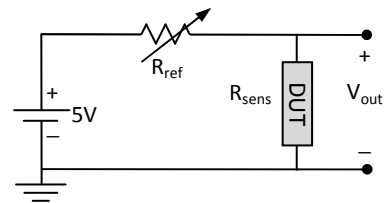


Fig. 4. Resistive divider to read the sensor voltage.

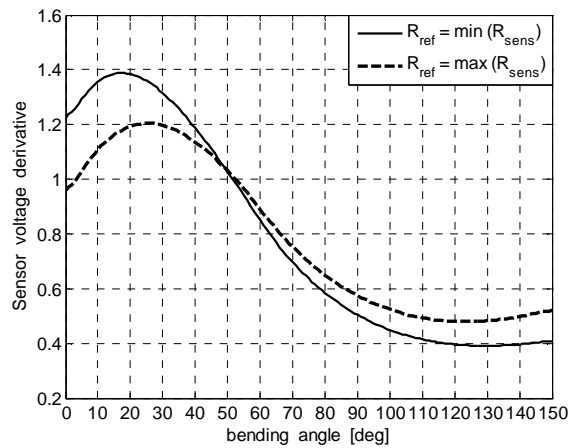


Fig. 5. Derivative of the sensor voltage from a resistive divider shows a sensitivity enhancement at low bending angles for a low value of reference resistance.

Dynamic measurements have been performed at different rotation rates through an LX.1746 impedance meter [12], connected to a PC through its USB interface, where it is controlled by the Visual Analyzer program, a free software of virtual instrumentation [13]. The measurement file data can be saved on a text file. This set-up allows to perform sensor resistance measurements with a great noise immunity. The set-up hardware and software interfaces are described by the block schematic in Fig. 6.

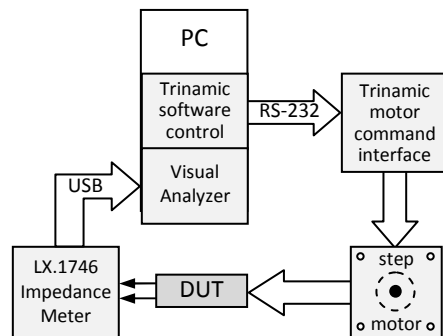


Fig. 6. Block schematic of the electrical characterization set-up.

III. ELECTRICAL MODELS

The most important manufacturers of commercial sensors do not provide any description of their technological process, and, in any case, this kind of investigation does not concern design engineers of sensor cognitive systems. From observation of sensor resistance response under fast bending rates, that is rotation speed, it has been observed a distortion of measured resistance waveform respect to that which should corresponds to the true forced rotations. If sensor displacement over the hinge has been carefully accomplished, avoiding any obstacle or friction which can hinder the sensor slide inside the hinge guide, this distortion can be accounted only to material relaxation delays. Authors suggest to model this behavior through an electrical model represented by a low-pass RLC circuit, shown in Fig. 7.

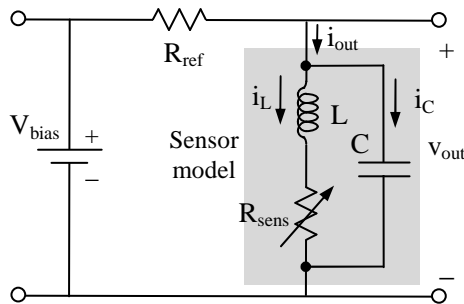


Fig. 7. Schematic representation of a resistive divider containing the sensor equivalent circuit to describe its dynamic behavior.

The resistance R corresponds to the static sensor resistance, corresponding to each bending angle. In order to hold linear analysis, R was represented as a piecewise-constant model, changing its value for each rotation degree. The sensor response was therefore obtained from an iterative routine, which performs linear circuit analysis computing successive step solutions, where the initial conditions at each step are the last values of the previous one. The global sensor response is obtained as a chain of successive solutions. The other two circuit parameters L and C can be represented by the resonant factor Q and frequency f_0 , which can be tuned in a reasonable range to fit the model simulation to the measured waveform, with no account on their physical meaning [14].

This approach has a twofold advantage: from one hand the model can predict the sensor performance for different bending ranges and rates, especially useful in that applications where high speed movements have to be monitored, from the other hand, a new method to recover the waveform corresponding to the true rotation can be developed.

IV. SIGNAL RECOVERY

Once the RLC electrical model parameters have been fit to the sensor dynamic measurement, the sensor performance can be yield either from sensor measurements with the impedance meter, or circuit model simulation from the equation

$$R_{mod}(t) = \frac{v_{out}(t)}{i_{out}(t)} \quad (1)$$

$$\text{being} \quad v_{out} = \frac{V_{bias} R_{mod}}{R_{ref} + R_{mod}} \quad (2)$$

$$i_{out} = \frac{V_{bias}}{R_{ref} + R_{mod}} \quad (3)$$

The method suggests to recover the ideal sensor resistance R_{sens} from simulation data derivatives, as developed in the following equations

$$i_C = C \frac{dv_{out}}{dt} \quad (4)$$

$$i_L = i_{out} - i_C \quad (5)$$

$$v_L = L \frac{di_L}{dt} \quad (6)$$

$$v_{sens} = v_{out} - v_L \quad (7)$$

$$\text{and finally} \quad R_{sens} = \frac{v_{sens}}{i_L} \quad (8)$$

Equation (8) provide the recovered sensor resistance waveform corresponding to the true bending degree of joint rotation. In order to avoid spurious spikes on simulated data derivatives, a twofold strategy has been followed: first of all selecting a model not only on the basis of error minimization but also continuity of second order derivatives, then adopting smoothing techniques based on derivative average and digital lowpass filtering. This approach has been also applied to different circuit topology, which here are not reported for sake of brevity.

This method has been applied to distorted sensor measurements, obtained from the test equipment setting the step motor speed for fast sawtooth rotations of the hinge where the sensor is lied, between 0 and 150 degrees, at 5 Hz cycle rate, which are, respectively, the maximum registered human joint rotation amplitude and speed. Look-up tables can map the sensor resistance response in the corresponding bending angles through interpolation of static characterization shown in Fig. 3. Results are plotted in Fig. 8, where it is evident that the suggested method has been succeeded to recover the signal waveform corresponding to the true hinge rotation, because the two traces are almost superimposed.

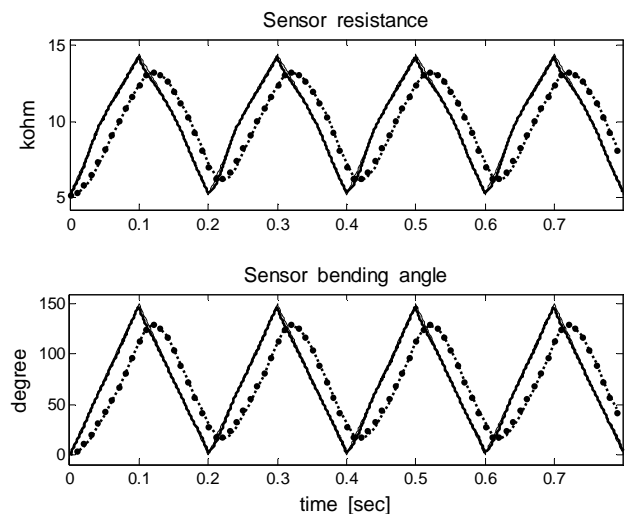


Fig. 8. Recovered sawtooth signal at 5 Hz of true joint rotation extracted from model fitted to dynamic measurements (•• meas, --- model, — true, — recovered).

In order to validate the method, the same modeling circuit has been used to recover the true hinge rotation from the simulated waveform with less distortion at a lower frequency (2 Hz). Results have been plotted in Fig. 9, which shows a perfect agreement between the true and recovered hinge rotation.

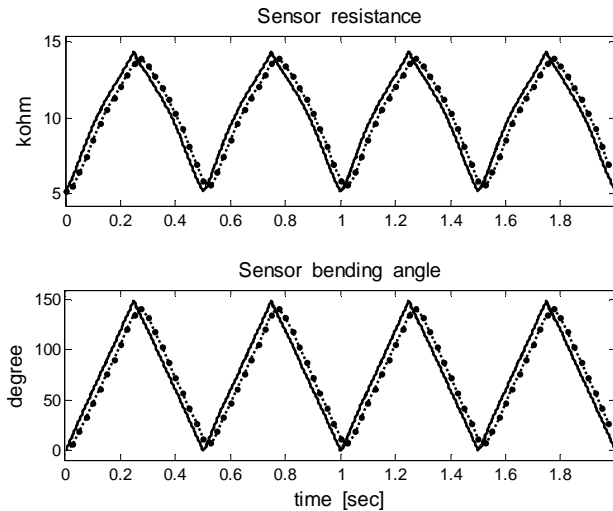


Fig. 9. Recovered sawtooth signal at 2 Hz of true joint rotation extracted from model fitted to dynamic measurements (••• meas, model, — true, — recovered).

Next developments of this method are foreseen where the true signal recovery will be performed in real time by digital signal processing routines, applied on input data stream from one or more bend sensors in a powered microcontroller or digital signal processor [15].

V. CONCLUSION

This paper aimed to demonstrate that resistive bend sensor can be applied for human posture and motion recognition. Even if static characterization has revealed that bend sensors change their resistance nonlinearly with bending rotation degrees, true bending angles would be correctly detected through corresponding look-up tables, if material relaxation delays would not cause signal distortion. Nevertheless, modeling the sensor behavior with appropriate circuit models, with no mind to the physical meaning of the circuit parameters, can lead to estimate the sensor performance for different rotation speed and amplitude, and to recover the original signal waveform which represents the true joint rotation from sensor measurements. The method has been successfully applied to track the fastest human joint rotation movements.

ACKNOWLEDGMENT

Acknowledgments are due to Dr. Alfredo Accattatis Ph.D., who designed the Visual Analyzer software and the Impedance Meter.

REFERENCES

[1] H. Zhou and H. Hu, "Human motion tracking for rehabilitation—A survey", Elsevier, Biomedical Signal Processing and Control, Volume 3, Issue 1, January 2008, pp. 1–18

[2] G. Latessa, F. Brunetti, A. Reale, G. Saggio, and A. Di Carlo, "Electrochemical synthesis and characterization of flexible PEDOT:PSS based sensors", *Sensors & Actuators: B. Chemical*, Elsevier, vol. B139, issue 2, pp. 304-309, June 2009.

[3] Images SI Inc., Staten Island NY, USA.

[4] Flexpoint Sensor Systems Inc., South Draper UT, USA.

[5] T. Giorgino, P. Tormene, F. Lorussi, D. De Rossi, and S. Quaglioni, "Sensor evaluation for wearable strain gauges in neurological rehabilitation", *IEEE Transactions on Neural Systems and Rehabilitation Engineering*, vol. 17, no. 4, pp. 409-415, August 2009.

[6] L. Dipietro, A. M. Sabatini, and P. Dario, "A survey of glove-based systems and their applications" *IEEE Transactions on Systems, Man, and Cybernetics-Part C: Applications and Reviews*, Vol. 38, No. 4, pp. 461-482, July 2008.

[7] L. Simone and D. Kamper, "Design considerations for a wearable monitor to measure finger posture", *J. NeuroEng. Rehab.* 2 (2005) 5.

[8] G. Saggio, S. Bocchetti, C. A. Pinto, and G. Orengo, "Wireless data glove system developed for HMI", 3rd Intern. Symp. on Applied Sciences in Biomedical and Communication Technologies (ISABEL), pp. 1-5, Rome, 10 November 2010.

[9] G. Saggio, P. Bisegna, G. Latessa, and S. Bocchetti, "Mechanical modeling of bend sensors exploited to measure human joint movements" *IEEE Intern. Symp. on a World of Wireless, Mobile and Multimedia Networks & Workshops*, pp 1-4, Kos (Greece) 2009.

[10] G. Orengo, G. Saggio, S. Bocchetti, and F. Giannini, "Advanced characterization of piezoresistive sensors for human body movement tracking", *IEEE International Symposium on Circuits and Systems (ISCAS)*, Paris, pp.1181-1184, May 2010.

[11] G. Saggio, M. De Sanctis, E. Cianca, G. Latessa, F. De Santis, and F. Giannini, "Long term measurement of human movements for health care and rehabilitation purposes", *Proc. of Wireless VITAE*, Aalborg, Denmark, pp.674-678, 17-20 May 2009.

[12] Nuova Elettronica, www.nuovaelettronica.it.

[13] <http://www.sillanumsoft.org>.

[14] G. Orengo, G. Saggio, S. Bocchetti, and F. Giannini, "Evaluating strain sensor performance for motion analysis", *International Conference on Biomedical Electronics and Devices (BIOSTEC-Biodevices)*, pp. 244-249, Rome, January 2011.

[15] G. Saggio, S. Bocchetti, C. A. Pinto, and G. Orengo, "Electronic interface and signal conditioning circuitry for data glove systems useful as 3D HMI tools for disabled persons", *International Conference on Health Informatics (BIOSTEC-Healthinf)*, pp. 248-253, Rome, January 2011.

SiC multilayer photonic structures:

A new active filter design

Manuela Vieira

Electronics Telecommunication and Computer Dept.
ISEL . CTS-UNINOVA, DEE-FCT-UNL,
Lisbon, Portugal.
mv@isel.ipl.pt

Manuel Vieira

Electronics Telecommunication and Computer Dept.
ISEL . CTS-UNINOVA,
Lisbon, Portugal.
mvieira@deetc.isel.ipl.pt

Paula Louro

Electronics Telecommunication and Computer Dept.
ISEL . CTS-UNINOVA,
Lisbon, Portugal.
plouro@deetc.isel.ipl.pt

Alessandro Fantoni

Electronics Telecommunication and Computer Dept.
ISEL . CTS-UNINOVA,
Lisbon, Portugal.
afantoni@deetc.isel.ipl.pt

Vitor Silva

Electronics Telecommunication and Computer Dept.
ISEL . CTS-UNINOVA,
Lisbon, Portugal
vsilva@isel.pt.

Abstract— Stacked layered pin a-SiC/a-Si devices based on a filter design are approached from a reconfigurable point of view. This paper shows that a double SiC/Si pin photodiode can be de-composed into two photonic active filters changeable in function. Reconfiguration is provided by optical control signals to the optoelectronic front and back pin building blocks. Depending on the wavelength and irradiation side of the external optical bias the device acts either as a short- and a long- pass band filter or as a band-stop filter, amplifying or rejecting a specific wavelength range. Particular attention is given to the amplification coefficient weights, which allow taking into account the wavelength background effects. We illustrate these effects in detail and discuss the filters transfer function characteristics. We present examples of filters and we propose a reconfigurable device for directed optical logic. An algorithm to decode the information is presented. An optoelectronic model supports the optoelectronic logic architecture.

Keywords—Optical filters, Photonics, multilayer devices, integrated filters

I. INTRODUCTION

Multilayered structures based on amorphous silicon technology are expected to become reconfigurable to perform WDM optoelectronic logic functions and provide photonic functions such as signal amplification and switching [1, 2]. They will be a solution in WDM technique for information transmission and decoding in the visible range [3]. The basic operating principle is the exploitation of

the physical properties of a nonlinear element to perform a logic function, with the potential to be rapidly biasing tuned. Amplification and amplitude change are two key functionality properties outcome of a balanced interaction between frequency and wavelength of the optical signal and background wavelength and placement within a WDM link. Any change in any of these factors will result in filter readjustments. Here, signal variations with and without front and back backgrounds move electric field action up and down in a known time frame. A numerical simulation support new optoelectronic logic architecture.

II. DEVICE CONFIGURATION AND OPERATION

The active device consists of a p-i'(a-SiC:H)-n/p-i(a-Si:H)-n heterostructure with low conductivity doped layers (Fig.1). The thicknesses and optical gap of the front i' (200 nm; 2.1 eV) and back i- (1000 nm; 1.8 eV) layers are optimized for light absorption in the blue and red ranges, respectively. Several monochromatic pulsed lights, separately ($\lambda_{R,G,B}$ input channels) or in a polychromatic mixture (multiplexed signal), at different bit rates illuminated the device from the glass side. Steady state optical bias with different wavelength are superimposed (400nm-800 nm) from the front or from the back sides and the generated photocurrent measured at -8 V. The device operates within the visible range using as input color channels (data) the wave square modulated light (external regulation of frequency and intensity) supplied by a red (R: 626 nm; 51 $\mu\text{W}/\text{cm}^2$), a green (G: 524 nm; 73 $\mu\text{W}/\text{cm}^2$) and a blue (B:

470 nm; 115 $\mu\text{W}/\text{cm}^2$) LED. Additionally, steady state red, green, blue and violet (background) was superimposed by LEDs driven at a constant current value (R: 625 $\mu\text{W}/\text{cm}^2$, G: 515 $\mu\text{W}/\text{cm}^2$, B: 680 $\mu\text{W}/\text{cm}^2$, V: 2800 $\mu\text{W}/\text{cm}^2$).

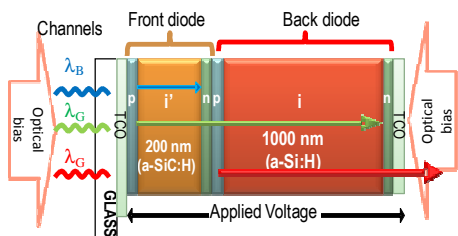


Figure 1. Device design and operation.

III. TRANSFER FUNCTION CHARACTERISTICS

The transfer function magnitude (or gain) allows to determine the ability of the optical filter to distinguish between signals at different wavelengths. The spectral sensitivity was tested through spectral response measurements under different frequencies, with and without steady state optical bias applied either from the front or back side (Fig.1).

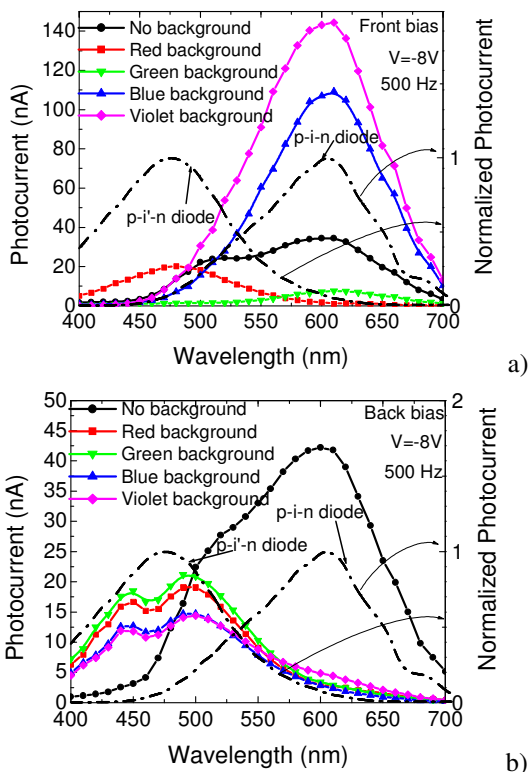


Figure 2. Photocurrent without and with front (a) and back (b) backgrounds. The current of the individual photodiodes are superimposed (dash lines).

In Fig. 2, at 500 Hz, the spectral photocurrent (symbols) is displayed under red, green, blue and violet background and without it. In Fig. 2a the steady state optical bias was applied from the front side and in Fig. 2b from the back side. For comparison the normalized spectral photocurrent for the front, p-i-n, and the back, p-i-n, photodiodes (dash lines) are superimposed.

Experimental data shows that the front and back building blocks, separately, presents the typical response of single p-i-n cells with intrinsic layers based on a-SiC:H or a-Si:H materials, respectively. The front diode cuts the wavelengths higher than 550 nm while the back one rejects the ones lower than 500 nm. The overall device presents an enlarged sensitivity when compared with the individual ones. Results show that under front irradiation the sensitivity is much higher than under back irradiation. Under front irradiation (Fig.2a) the violet background amplifies the spectral sensitivity in the visible range while the blue optical bias only enhances the spectral sensitivity in the long wavelength range (>550 nm) and quenches it in the others. Under red bias, the photocurrent is strongly enhanced at short wavelengths and disappears for wavelengths higher than 550 nm. Under green the sensitivity is strongly reduced in all the visible spectra. In Fig. 2b, whatever the wavelength of the backgrounds, the back irradiation strongly quenches the sensitivity in the long wavelength range (> 550nm) and enhances the short wavelength range. So, back irradiation, tunes the front diode while front irradiation, depending on the wavelength used, tunes the back one.

IV. OPTICAL BIAS AMPLIFICATION

In Fig. 3 the spectral gain, defined as the ratio between the spectral photocurrents under red (α^R), green (α^G) blue (α^B) and Violet (α^V) illumination and without it is plotted at 500 Hz and 3500 Hz. The optical bias is applied from the front side, in Fig. 3a and from the back side, in Fig. 3b.

Under front bias and red irradiation the gain is high at short wavelengths and strongly lowers for wavelengths higher than 550 nm, acting as a short-pass filter. Under green background and high frequencies, the device behaves as a band-stop filter that screens out the medium wavelength range (green) enhancing only the photocurrent for wavelengths outside of that range. Under blue and violet light the devices works as a long-pass filter for wavelengths higher than 550 nm, blocking the shorter wavelengths. Back light, whatever the frequency, leads to a short-pass filter performance. Experimental results show that by combining the background wavelengths and the irradiation side the short-, medium- and long- spectral region can be sequentially tuned.

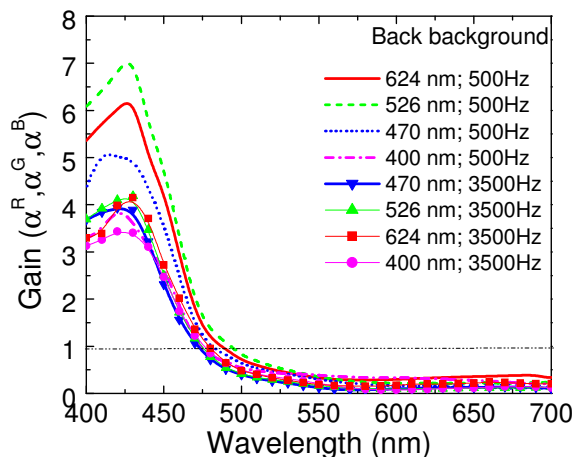
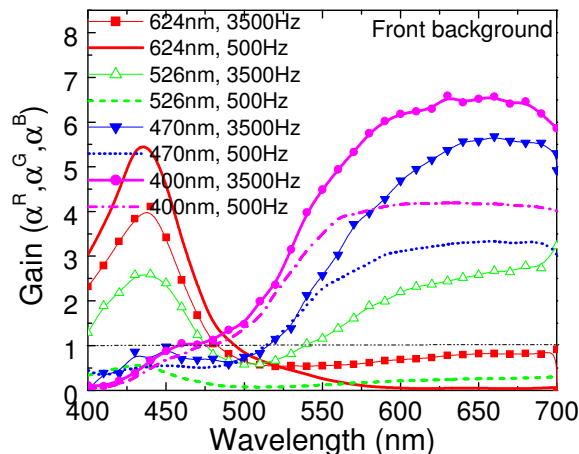


Figure 3. Spectral gain under red (α_R), green (α_G), and blue (α_B) optical bias, applied from the front (a) and the back (b) sides at different frequencies.

In Fig. 4 the front and back gains as a function of the frequency, at fixed wavelengths: 470 nm (blue channel), 526 nm (green channel) and as 624 nm (red channel) is plotted under 400 nm applied optical bias from the front (symbols) and back (lines) sides. Results show that, no matter what the irradiation side, the blue and green channel gain does not depend on the frequencies, while the red one increases under front illumination and is strongly reduced under back light. In Fig. 5 under front and back violet irradiation, it is displayed the spectral gain for three different frequencies.

Results show that, whatever the frequency, the device acts as an active long-pass filter under front irradiation and a low-pass filter under back irradiation. Under front bias the gain is higher than the unity for wavelengths above 500nm resulting in an amplification of the green and red spectral ranges. Back irradiation only amplifies the short wavelength range and extinguishes the others.

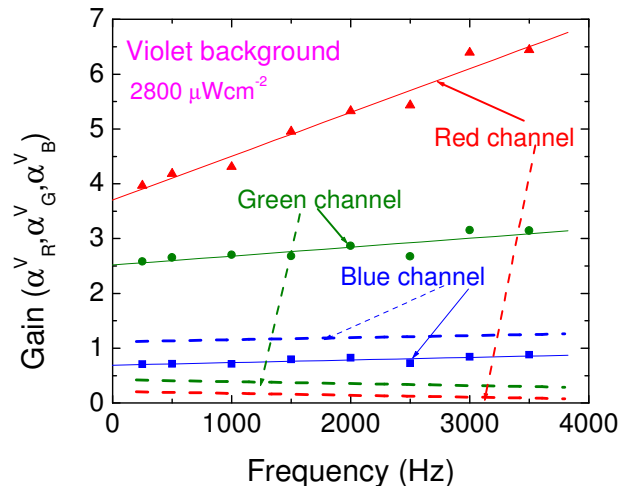


Figure 4. Input front (symbols) and back (lines) channel gains (α_R , α_G , α_B), as a function of the frequency.

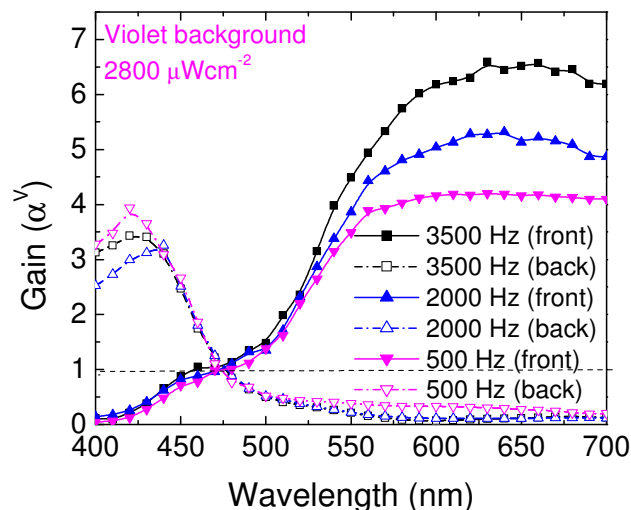


Figure 5. Spectral gain under violet optical bias (α^V) for different frequencies.

V. ENCODER AND DECODER DEVICE

To analyze the device under information-modulated wave and uniform irradiation, three monochromatic pulsed lights separately (red, green and blue input channels, Fig. 6a) or combined (multiplexed signal, Fig. 6b) illuminated the device at 6000 bps. Steady state violet optical bias was superimposed separately from the front (solid lines, pin_1) and the back (dash lines, pin_2) sides and the photocurrent generated measured at -8 V. The transient signals were normalized to their values without background. In Fig. 6b the multiplexed signal without and with background are displayed (solid lines). Here the input channels without optical bias (dash lines) are also superimposed. On the top of the figure the signals used to drive the input channels are shown.

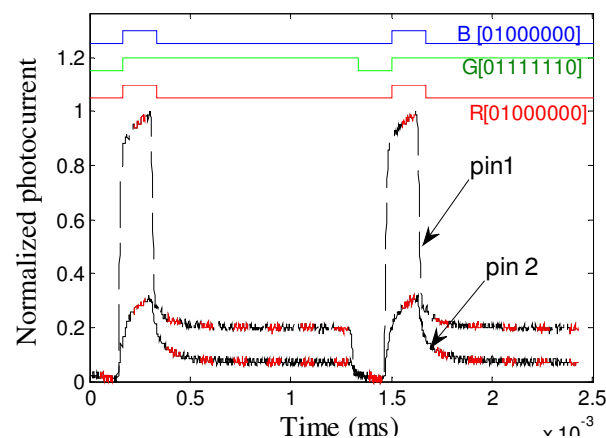
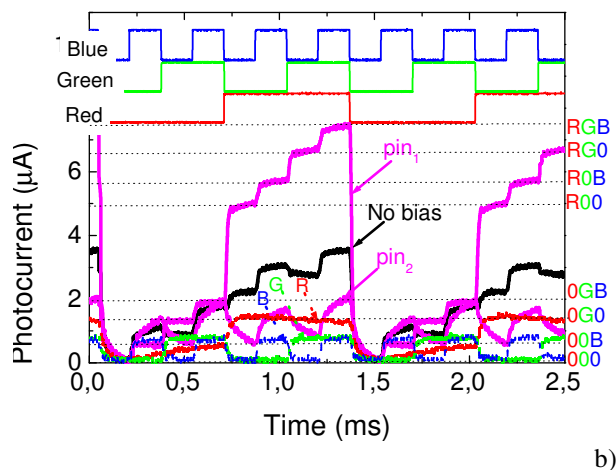
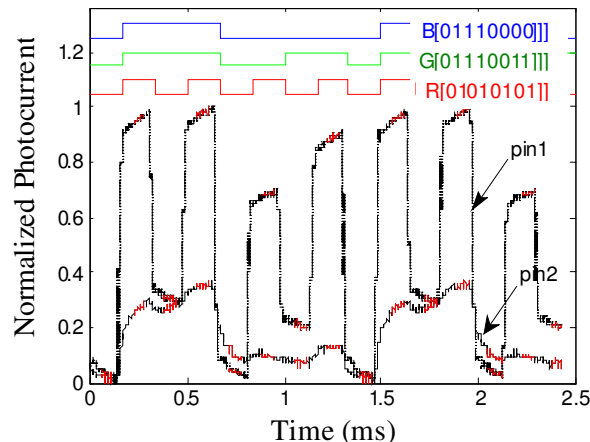
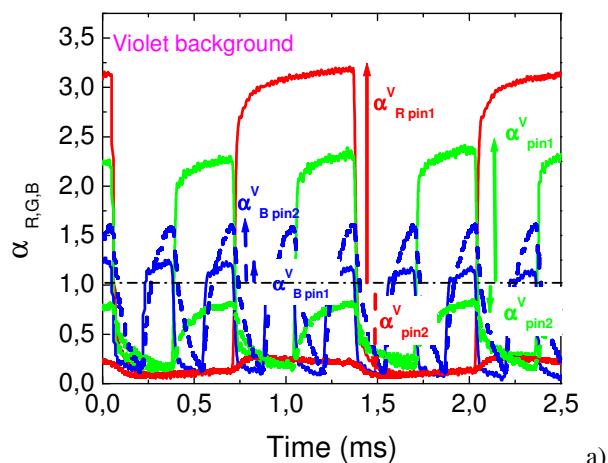


Figure 6. a) Normalized red, green and blue transient signals at -8V with violet (400 nm) steady state optical bias applied from the front side (apin1) and from the back side (apin2). b) Input R,G,B channels and multiplexed output without (no bias) and under front (pin1) and back (pin2) irradiation.

Figure 7. MUX signal under front and back irradiation. On the top the DEMUX signals obtained using the decoder algorithm is displayed as well as the binary bit sequences.

Even under transient conditions, as in Fig 3, the front background presents the same nonlinear dependence on the wavelength. It enhances mainly the light-to-dark sensitivity in the medium-long wavelength ranges. Violet radiation is absorbed at the top of the front diode, increasing the electric field at the least absorbing cell [4], the back diode, where the red and part of the green channels generate optical carriers. So the collection is strongly enhanced ($\alpha_{Gpin1}^V=2.2$, $\alpha_{Rpin1}^V=3.1$) while the blue collection stays near its dark value ($\alpha_{Bpin1}^V=1.1$).

Under back irradiation the small absorption depth of the violet photons across the back diode quenches the electric field and so, the red collection almost disappears ($\alpha_{Rpin2}^V=0.2$). Blue channel is absorbed across the front diode where the electric field is enhanced resulting in an increase collection of the blue channel ($\alpha_{Bpin1}^V=1.6$).

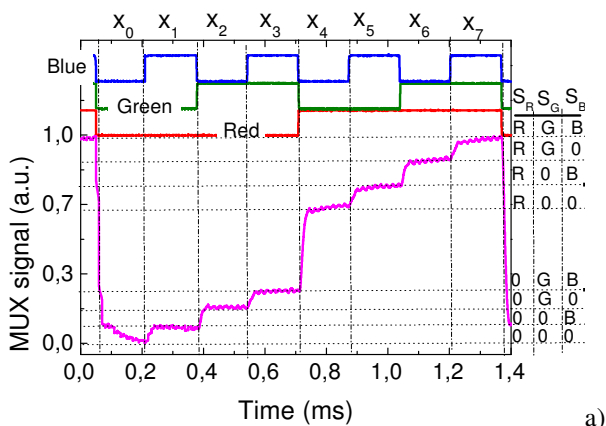
Since the green channel is absorbed across front and back diodes its collection is balanced by the increased collection in the front diode and its reduction at the back one ($\alpha_{Gpin2}^V=0.7$). Under front irradiation, the encoded multiplexed signal presents eight separate levels (2^3) each one related with an RGB bit sequence (right side of the Fig. 6b). Those levels can be grouped into two main classes due to the high amplification of the red channel under front irradiation. The upper four levels are ascribed to the presence of the red channel ON and the lower four to its absence allowing the red channel decoder. Since under front irradiation the green channel is amplified, the two highest levels, in both classes, are ascribed to the presence of the green channel and the two lower ones to its lack. Under back irradiation, the red channel is suppressed, the blue enhanced and the green reduced, so the encoded multiplexed signal presents only four main separate levels (2^2). The two higher levels correspond to the presence of the blue channel ON with or without the green ON respectively, and the other two to its absence. The blue channel is then decoded. We have used this simple algorithm to decode the multiplex signal.

The results are displayed in Fig. 7 for two different bit sequences. An excellent fit was obtained.

Results show that the pinpi'n multilayered structure become reconfigurable under front and back irradiation. They perform WDM optoelectronic logic functions providing photonic functions such as signal amplification, filtering and switching. So, by means of optical control applied to the front or back diodes, the photonic function is modified from a long- to a short-pass filter, giving a step reconfiguration of the device.

VI. PHOTONIC ACTIVE FILTERS

In the pi'n/pin device the morphology of filter system results from the interaction of the electric field under applied optical bias (red, green, blue, violet) and the transient electric field induced by the input channels. This interaction results in electric field lines that guides the photocarriers generated by the input channels. The flow rate of the optical carriers through those field lines towards the output depends on the on/off state of the color channels.



Inputs								MUX	Outputs			Y
x_0	x_1	x_2	x_3	x_4	x_5	x_6	x_7	DEMUX	S_2	S_1	S_0	
0	0	0	0	0	0	0	1		1	1	1	Red
0	0	0	0	0	0	1	0		1	1	0	Red
0	0	0	0	0	1	0	0		1	0	1	Red
0	0	0	0	1	0	0	0		1	0	0	Red
0	0	0	1	0	0	0	0		0	1	1	Green
0	0	1	0	0	0	0	0		0	1	0	Green
0	1	0	0	0	0	0	0		0	0	1	Blue
0	0	0	0	0	0	0	0		0	0	0	Blue

Figure 8. MUX signal outputs (a) and truth table (b) of the encoders that perform 8-to-1 multiplexer (MUX) function, under front violet irradiations.

In Fig. 8a an output MUX signal under front violet irradiation is displayed. On the top the signals used to drive the input channels are displayed showing the presence of all the possible 2^3 on/off states ($x_0...x_7$). Fig. 8b shows the truth table of an encoder that performs 8-to-1 multiplexer (MUX) function. In the inputs ($x_0...x_7$) the index of each bit is related with of the first (highest) nonzero logic input. To understand this mapping, in Fig. 8b, for the input x_7 and output S_2 , the first nonzero logic input is $7(2^2+2^1+2^0)$, which corresponds an output [111]. That OR gate is expressed as $S_2=x_7+x_6+x_5+x_4$. Under front violet irradiation, $\alpha^V_R \gg 1$, $\alpha^V_G > 1$ and $\alpha^V_B \sim 1$ (Fig. 5). So, the correspondence between the outputs S_2, S_1, S_0 and the on/off state of the input channels, S_R, S_G, S_B , is obvious.

The DEMUX, on the other hand, sends the input logic signal to one of its eight outputs ($y_s = x$), according to the optoelectronic demux algorithm.

To convert from a particular logic function (8-to-1 MUX) to another (FILTER), one needs only to redefine the input and output signals and to reconfigure the operation mode. Taking into account Fig. 5a, under back violet bias control, a step change in configuration occurs. Here, the encoded four level signal is grouped in two classes, the uppers two levels, where the blue channel is ON and the others where it is OFF (4-to-1 multiplexer; short-pass filter function).

VII. OPTOELECTRONIC MODEL

Based on the experimental results and device configuration an optoelectronic model, made out of a short-pass and a long-pass filter (see Fig. 4 and Fig. 5) and supported by the complete dynamical large signal Ebers-Moll model, was developed [5, 6]. The equivalent circuit, made out of a short-pass filter (front phototransistor, Q_1) and a long-pass filter (back phototransistor, Q_2) sections connected in parallel is displayed in Fig. 9a. The charge stored in the space-charge layers is modeled by the capacitor C_1 and C_2 . R_1 and R_2 model the dynamical resistances of the internal and back junctions under different dc bias conditions. To allow independent blue, red and green channels transmission four square-wave current sources with different intensities are used; two of them, $\alpha_1 I_B$ and $\alpha_2 I_R$, with different frequencies to simulate the input blue and red channels and the other two, $\alpha_1 I_{Gpin}$ and $\alpha_2 I_{Gpin}$, with the same frequency but different intensities, to simulate the green channel due to its asymmetrical absorption across both front and back phototransistors.

When the pi'n/pin device is reverse-biased, the base-emitter junction of both transistors are inversely polarized and conceived as phototransistors, taking, so, advantage of the amplifier action of adjacent collector junctions which are polarized directly. This results in a current gain proportional to the ratio between both collector currents. The amplifying elements, α_1 and α_2 , can provide gain if needed and attenuate unwanted wavelengths (<1) while amplifying (>1) desired ones. The values and the strategic placement of the resistors determine the basic shape of the output signals. So, the flow of current through the resistor connecting the two transistor bases, R_1 , is proportional to the difference in the voltages

across both capacitors (charge storage buckets). The device is formed by two reconfigurable building-blocks (the front and the back diodes) interconnected both optical and electrically, each of which has a distinct function. Depending on the side and wavelength of the optical bias control, the magnitude of the *signals* are changed by an α factor, and so the voltages across the front and the back or both photodiodes. The device behaves like an optoelectronic controlled transmission system that stores, amplifies and transports the minority carriers generated by the current pulses, through capacitors C_1 and C_2 .

To validate the model under front and back irradiation, in Fig. 9b, the experimental (solid lines) and the simulated (symbols) waveform under negative bias and violet front and back backgrounds is shown. The bit sequences to drive the channels are shown in the top of the figure to guide the eyes. To simulate the violet background, the current sources intensities that model the input channels (individual channels, Fig. 6b) were multiplied by the on/off ratio between the input channels with and without optical bias ($\alpha_{R,G,B}^{V_{pin1,2}}$, Fig. 6a). A good agreement between experimental and simulated data was achieved.

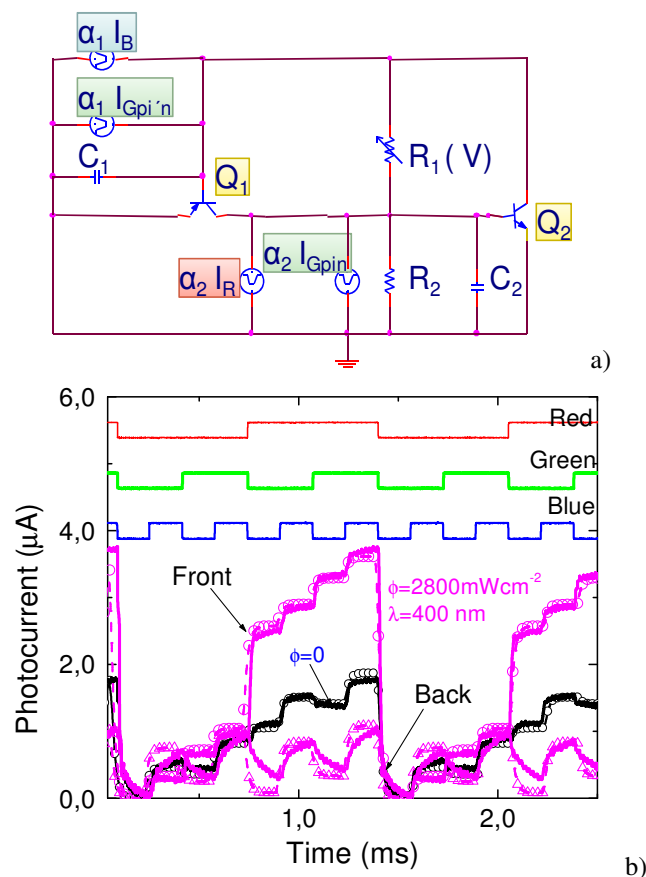


Figure 9. Simulated (symbols) and experimental (solid lines) multiplex signals under front and back violet background.

The device is formed by two reconfigurable building-blocks (the front and the back diodes) interconnected both optical and electrically, each of which has a distinct function. Depending on the side and wavelength of the optical bias control, the magnitude of the *signals* are changed by an α factor, and so the voltages across the front and the back or both photodiodes. Under front irradiation the expected optical amplification in the short wavelength range and quenching in the long ones is observed due to the effect of the active multiple-feedback filter when the back diode is light triggered. The opposite occurs under back irradiation.

VIII. CONCLUSIONS

Combined tunable converters based on SiC multilayer photonics active filters are analyzed. Results show that the light-activated pi-n/pin a-SiC:H devices combine the demultiplexing operation with the simultaneous photodetection and self amplification of an optical signal. The output waveform presents a nonlinear amplitude-dependent response to the wavelengths of the input channels. Depending on the wavelength of the external background it acts either as a short- or a long- pass band filter or as a band-stop filter. A two stage active circuit is presented and gives insight into the physics of the device.

ACKNOWLEDGMENT

This work was supported by FCT (CTS multi annual funding) through the PIDDAC Program funds and PTDC/EEA-ELC/111854/2009 and PTDC/EEA-ELC/120539/2010.

REFERENCES

- [1] C. Petit, M. Blaser, Workshop on Optical Components for Broadband Communication, ed. by Pierre-Yves Fonjallaz, Thomas P. Pearsall, Proc. of SPIE Vol. 6350, 63500I, (2006).
- [2] S. Ibrahim, L. W. Luo, S. S. Djordjevic, C. B. Poitras, I. Zhou, N. K. Fontaine, B. Guan, Z. Ding, K. Okamoto, M. Lipson, and S. J. B. Yoo, paper OWJ5. Optical Fiber Communications Conference, OSA/OFC/NFOEC, San Diego, 21 Mar 2010.
- [3] S. Randel, A.M.J. Koonen, S.C.J. Lee, F. Breyer, M. Garcia Larrode, J. Yang, A. Ng'Oma, G.J. Rijkenberg, and H.P.A. Boom. "ECOC 07 (Th 4.1.4). (pp. 1-4). Berlin, Germany, 2007.
- [4] M. Vieira, A. Fantoni, P. Louro, M. Fernandes, R. Schwarz, G. Lavareda, and C. N. Carvalho, Vacuum, 82, Issue 12, 8 August 2008, pp: 1512-1516.
- [5] M A Vieira, M. Vieira, M. Fernandes, A. Fantoni, P. Louro, M. Barata, Thin-Film Silicon Science and Technology — 2009, MRS Proceedings Volume 1153, A08-03.
- [6] M. A. Vieira, M. Vieira, J. Costa, P. Louro, M. Fernandes, A. Fantoni, Sensors & Transducers Journal, 9, Special Issue, December 2010, pp.96-120.

A Novel Flexure Parallel Micromanipulator Based on Multi-Level Displacement Amplifier

Dan Zhang^{1,2*}, Zhen Gao¹, Matteo Malosio³, Gianmarc Coppola¹

¹ Faculty of Engineering and Applied Science, University of Ontario Institute of Technology
Oshawa, ON, Canada, L1H 7K4

² Qingdao Technological University, Qingdao, Shandong, China

³ Institute of Industrial Technologies and Automation, National Research Council
Bassini 15, 20133 Milano, Italy

*Corresponding author, Email: Dan.Zhang@uoit.ca

Abstract-The conventional flexure parallel micromanipulators (FPM) usually suffer from small stroke. The performances of a FPM are highly related with the stroke of each actuated limb and the constraints including the non-actuated limbs. To conquer the drawbacks of the small workspace of the conventional FPM, the mechanism for displacement amplification would make a great contribution when it is imported into the design of the actuated limbs. This research is focused on a unique FPM based on multi-level displacement amplifier. Firstly, the structure modeling based on compact modular design is introduced. The macro/micro analysis of the displacement amplifier is conducted. Then, the comprehensive finite-element modeling including the strain and total deformation are implemented to examine the actual mechanical behavior of the proposed mechanism. The developed method and technology provide a promising solution to enhance the performance of the generic FPMs.

Keywords-Flexure parallel micromanipulator; multi-level displacement amplifier; finite-element analysis; symmetrical topology structure

I. INTRODUCTION

With the rapid and extensive development in both theories and applications in the past several decades, parallel manipulator has become a non-displaceable technology which reflect its merits in areas of machine tools [1-6], sensors and transducers [7-10], micro devices and MEMS systems [11-15], and motion platforms [16-18], majorly due to its distinct advantages including higher positioning precision, higher dynamic performance, higher stiffness, less accumulative error and easier for inverse kinematic modeling.

In the area of multi-axis micro-positioning, many scholars have developed different types of flexure parallel micromanipulators to achieve the expected goals [19-25]. In [20], a 3-limb 6-DOF parallel micromanipulator with 3PPSP structure was investigated. In each limb, there are two actuator joints which are integrated in a x-y plane attached to the base. In [21], the special materials including polyvinylidene fluoride and lead zirconium titanate were

utilized to develop the piezoelectric actuators for the vibration control of a planar compliant parallel manipulator. In [22], a nanopositioning parallel stage which has high bandwidth, high motion range and low cross-coupling was developed so that control strategies based on single-input single-output for trajectory tracking was available. In [23], a compliant positioned based on parallel kinematic structure was dually driven by six piezoelectric actuators and six piezoelectric ceramics. Through testing, it could be found that this structure simultaneously generated wide motion range and high precision. In [24], the pseudo rigid-body model was calculated for a 3-DOF flexure parallel micromanipulator in which three limbs are perpendicular to each other. In [25], the electromagnetic actuators with less than 0.1% full-scale position error were fabricated to drive a six-axis compliant parallel mechanism.

However, since every coin has its opposite side, especially for the case of parallel micromanipulators, the natural limitation of the small stroke of the traditional actuators restrict the workspace and the limb displacement in a small region. Regarding this, a unique FPM with 3-DOF based on multi-level displacement amplifier is designed for the potential application situations where large motion range is required in a micro- or nano- positioning environment. The proposed multi-level displacement amplifier based on a series of flexure hinges is integrated in each compliant limb as a monolithic structure which is driven by piezoelectric actuator.

The rest part of this paper is organized as follows: the conceptual designs and the kinematics modeling of the displacement amplifier and related planar/spatial flexure parallel micromanipulators are introduced Sections 2 and 3. In Section 4, the finite-element analysis is conducted to examine the static performance of the proposed FPM. Final section gives the conclusion.

II. CONCEPTUAL DESIGN

As the key part of the flexure parallel micromanipulators, the conceptual structure of the multi-level displacement

amplifier is illustrated in Fig. 1. The piezoelectric actuator will be placed in the middle of the mechanism between the two convex stages connected to the inner bars. The four free lower/upper ends are attached to a fixed base. Through multi-stage amplification of the original displacement, large workspace of the end-effector can be achieved.

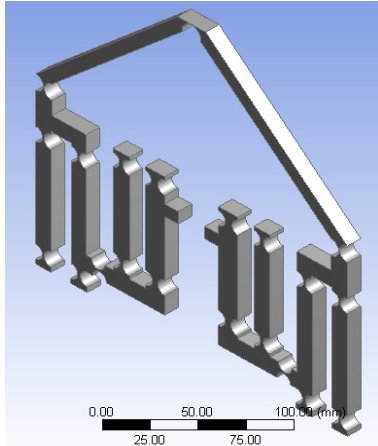


Figure 1. The CAD model of the proposed displacement amplifier

The following figure shows how to combine two multi-level displacement amplifiers to develop a high-precision XY positioning stage.

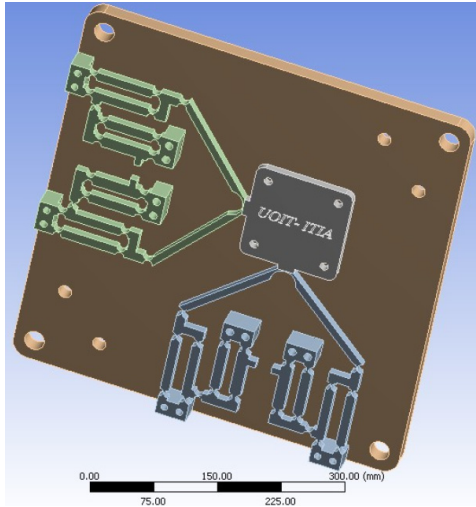


Figure 2. Planar flexure parallel micromanipulator based on displacement amplifier

Figure 3 displays a spatial FPM with large motion range for the potential application in micro positioning environment. The mechanism is utilized as the case study in this research to verify its characteristics.

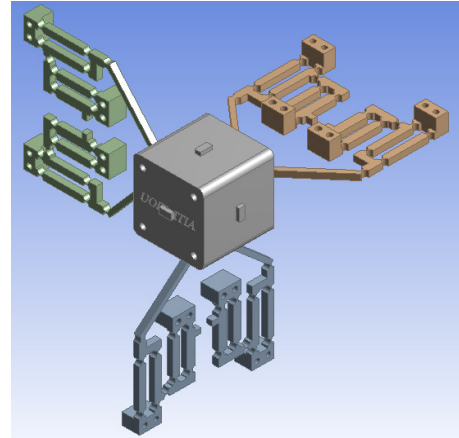


Figure 3. Spatial flexure parallel micromanipulator based on displacement amplifier

III. ANALYSIS OF THE DISPLACEMENT AMPLIFIER

A. Macro Analysis

In this subsection, it is focused on the amplification analysis of the proposed displacement amplifier based on the macro dimensions which are shown in Fig. 4.

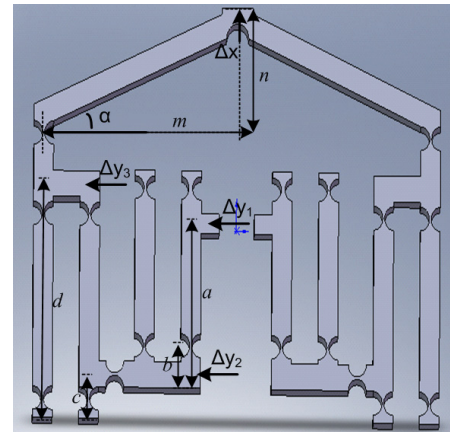


Figure 4. The macro dimensions of the proposed displacement amplifier

When the deformation Δy_1 occurs, it has

$$\Delta y_2 = \frac{b}{a} \Delta y_1 \quad (1)$$

$$\Delta y_3 = \frac{d}{c} \Delta y_2 \quad (2)$$

Then, the output displacement can be derived as,

$$\begin{aligned} \Delta x &= n - \sqrt{m^2 + n^2 - (m + \Delta y_3)^2} \\ &= n - \sqrt{n^2 - 2m \cdot \frac{b}{a} \cdot \frac{d}{c} \cdot \Delta y_1 - \left(\frac{b}{a} \cdot \frac{d}{c} \cdot \Delta y_1\right)^2} \end{aligned} \quad (3)$$

Thus, the amplification k is given as,

$$k = \frac{\Delta x}{\Delta y_1} = \frac{n - \sqrt{n^2 - 2m \cdot \frac{b}{a} \cdot \frac{d}{c} \cdot \Delta y_1 - \left(\frac{b}{a} \cdot \frac{d}{c} \cdot \Delta y_1\right)^2}}{\Delta y_1} \quad (4)$$

B. Micro Analysis

The circular flexure hinge can be expressed with the following compliance matrix,

$$\mathbf{C}_c = \begin{bmatrix} c_x^{F_x} & 0 & 0 & 0 & 0 & 0 \\ 0 & c_y^{F_y} & 0 & 0 & 0 & c_y^{M_z} \\ 0 & 0 & c_z^{F_z} & 0 & c_z^{M_y} & 0 \\ 0 & 0 & 0 & c_{\theta_x}^{M_x} & 0 & 0 \\ 0 & 0 & c_{\theta_y}^{F_z} & 0 & c_{\theta_y}^{M_y} & 0 \\ 0 & c_{\theta_z}^{F_y} & 0 & 0 & 0 & c_{\theta_z}^{M_z} \end{bmatrix} \quad (5)$$

As the most important element, $c_{\theta_z}^{M_z}$ is written as,

$$c_{\theta_z}^{M_z} = \frac{\theta_z}{M_z} = \frac{24R}{Ebt^3(2R+t)(4R+t)^3} [t(4R+t)(6R^2 + 4Rt + t^2) + 6R(2R+t)^2 \sqrt{t(4R+t)} \tan^{-1} \sqrt{1 + \frac{4R}{t}}] \quad (6)$$

where, R denotes the radius of circular arc. E is the elastic modulus of selected material. b represents the width of the hinge. t is the thickness of the thinnest part of the circular flexure hinge.

The elastic potential energy of the half part of a single displacement amplifier can be derived as,

$$E_e = \sum_{i=1}^9 \frac{1}{2c_{\theta_z}^{M_z}} \theta_{zi}^2 \quad (7)$$

The above equation can be rewritten as,

$$E_e = \sum_{i=1}^9 \frac{1}{48R} \cdot \frac{Ebt^3 \theta_{zi}^2 (2R+t)(4R+t)^3}{[t(4R+t)(6R^2 + 4Rt + t^2) + 6R(2R+t)^2 \sqrt{t(4R+t)} \tan^{-1} \sqrt{1 + \frac{4R}{t}}]} \quad (8)$$

IV. FINITE ELEMENT ANALYSIS

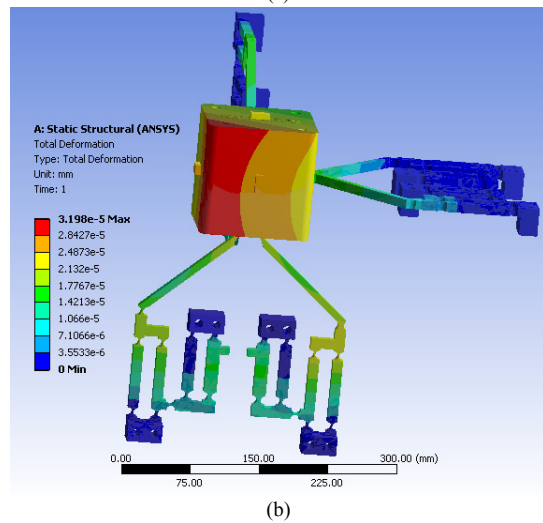
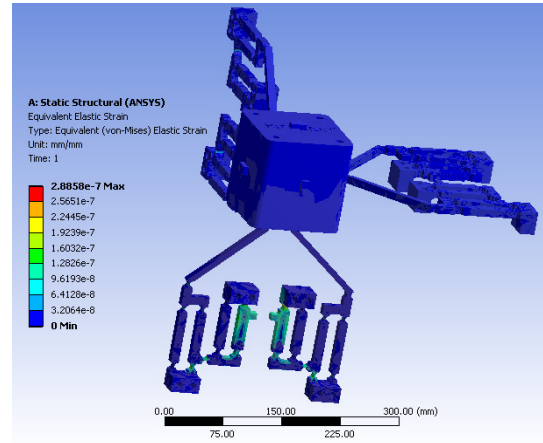
Finite element analysis (FEA) is a paramount method to test the performance of the flexure based compliant parallel manipulator. The different selection of materials also affects the practical characteristics. With a critical evaluation of design criteria based on various materials, stainless steel is chosen whose properties is described in Table 1.

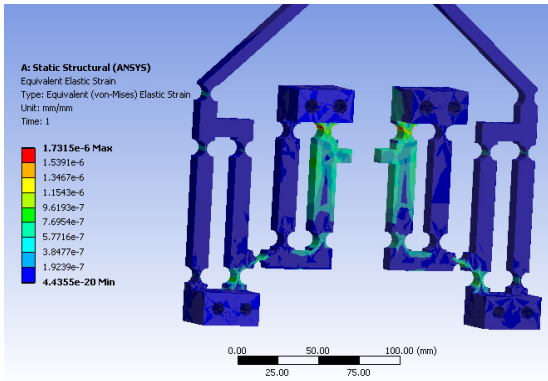
TABLE I. MATERIAL PROPERTIES

Density	7.85e-006 kg mm ⁻³
Coefficient of Thermal Expansion	1.2e-005 C ⁻¹
Specific Heat	4.34e+005 mJ kg ⁻¹ C ⁻¹

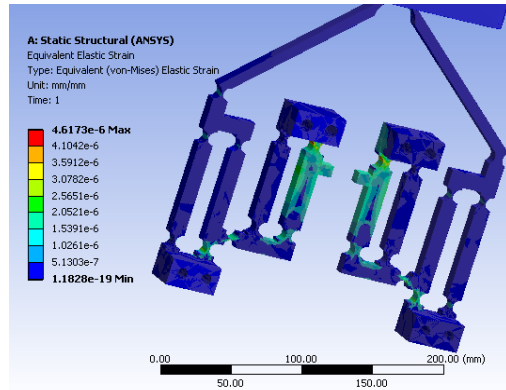
Thermal Conductivity	6.05e-002 W mm ⁻¹ C ⁻¹
Resistivity	1.7e-004 ohm mm

Figure 5 illustrates the strain and deformation results under external forces applied on one displacement amplifier. When $F = 1N$, the maximal/minimal equivalent elastic strain is $2.8858 \times 10^{-7} \text{ mm/mm}$ and 0 respectively, and the maximal total deformation is $3.198 \times 10^{-5} \text{ mm}$. When $F = 6N$, the maximal/minimal equivalent elastic strain is $1.7351 \times 10^{-6} \text{ mm/mm}$ and $4.4355 \times 10^{-20} \text{ mm/mm}$ respectively, and the maximal total deformation is $1.9188 \times 10^{-4} \text{ mm}$. When $F = 11N$, the maximal/minimal equivalent elastic strain is $3.1744 \times 10^{-6} \text{ mm/mm}$ and $8.1323 \times 10^{-20} \text{ mm/mm}$ respectively, and the maximal total deformation is $3.5178 \times 10^{-4} \text{ mm}$. When $F = 16N$, the maximal/minimal equivalent elastic strain is $4.6173 \times 10^{-6} \text{ mm/mm}$ and $1.1828 \times 10^{-19} \text{ mm/mm}$ respectively, and the maximal total deformation is $5.1168 \times 10^{-4} \text{ mm}$. When $F = 21N$, the maximal/minimal equivalent elastic strain is $6.0601 \times 10^{-6} \text{ mm/mm}$ and $1.5524 \times 10^{-19} \text{ mm/mm}$ respectively, and the maximal total deformation is $6.7158 \times 10^{-4} \text{ mm}$.

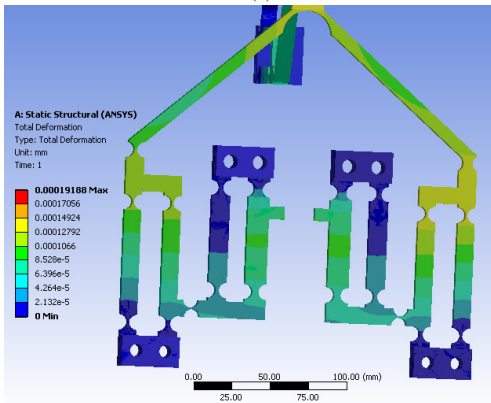




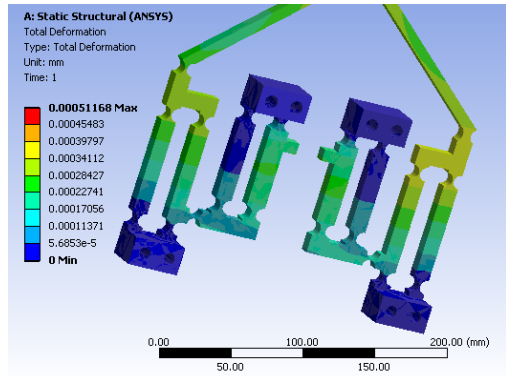
(c)



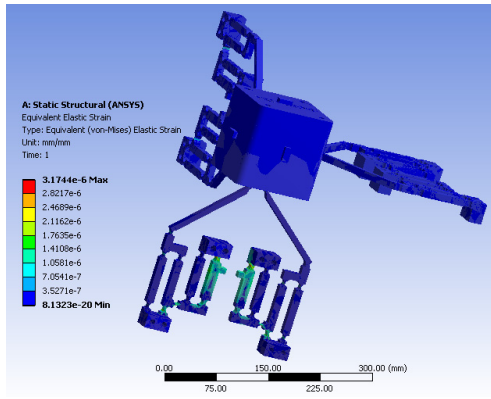
(g)



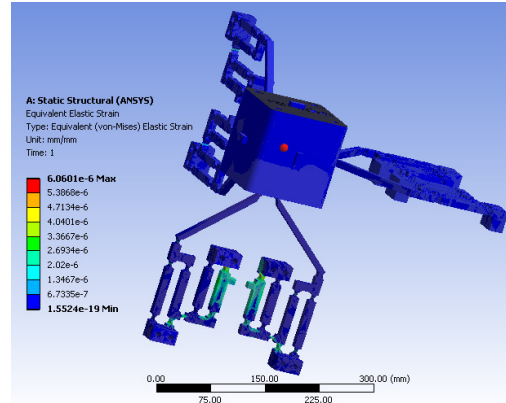
(d)



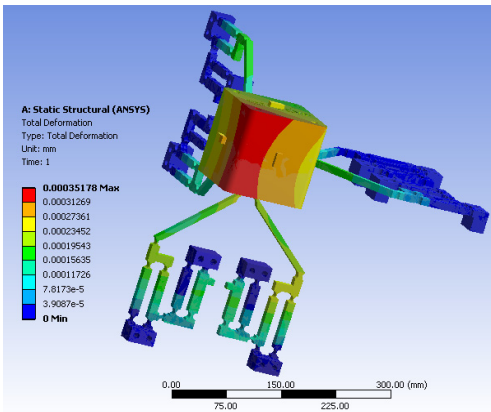
(h)



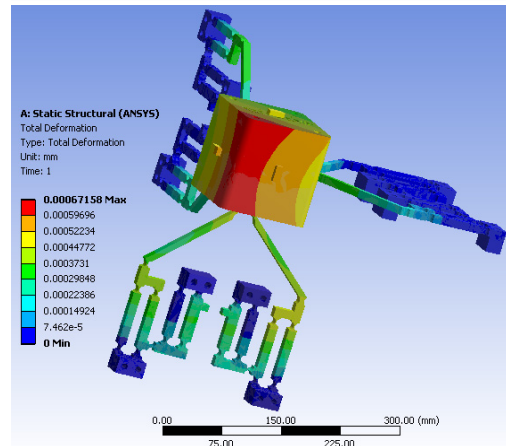
(e)



(i)



(f)



(j)

Figure 5. The strain and deformation results under external forces applied on one displacement amplifier

Figure 6 (a) shows the fitting curve of the maximal total deformation under different external forces. Figure 6 (b) and (c) describes the fitting curve of the maximal/minimal equivalent elastic strain under different external forces respectively. It can be found that the proposed FPM based on displacement amplifier has advantageous characteristics in terms of linearity and sensitivity.

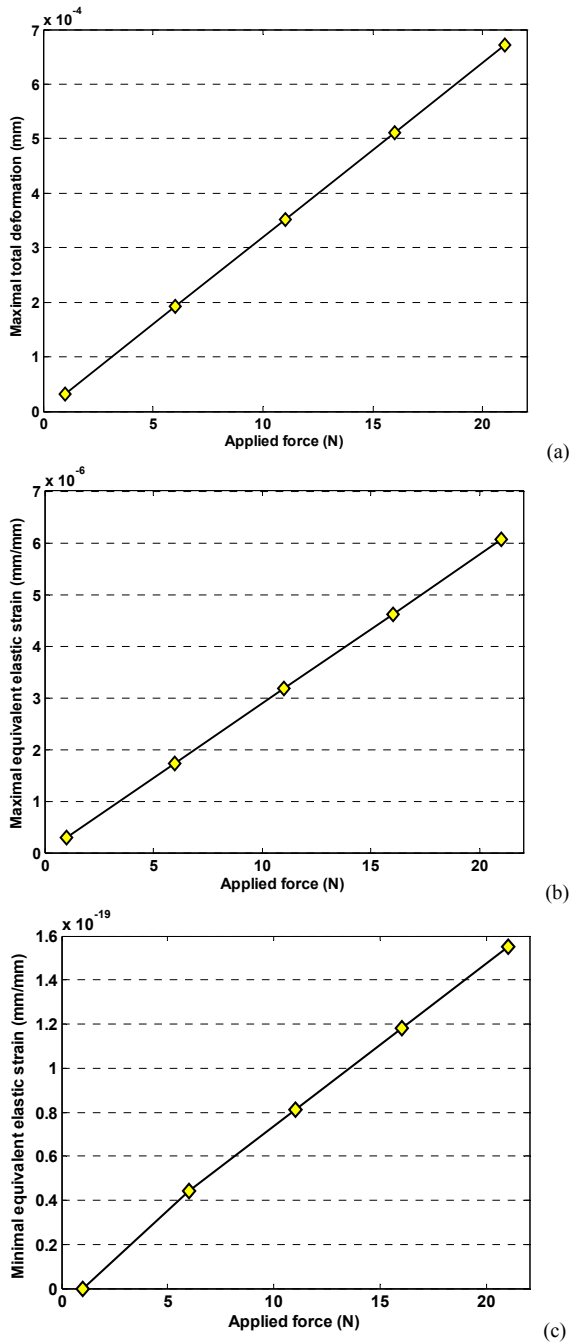


Figure 6. The fitting curve of the deformation and strain

The resonant frequency of FPM can be utilized for its modal analysis. The classic sample of a mechanical resonance is a discrete system consisting of a mass attached to a spring with a constant force. The proposed FPM based on displacement amplifier is more complicated than a simple spring, which implies that it may contain more than one resonance frequency. Through simulation, it can be found in Fig. 7 that there are at least four resonance frequencies. The total deformation under different frequency inputs are depicted in Fig. 8.

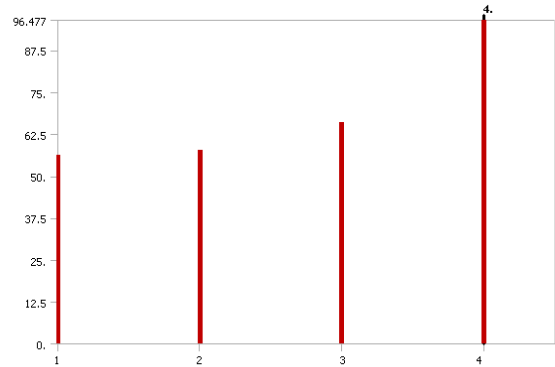
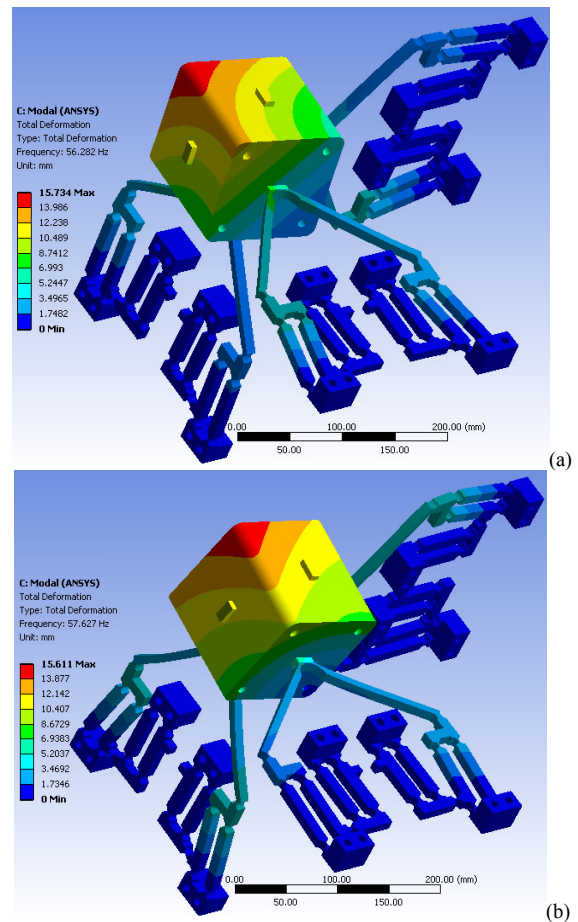


Figure 7. Mode and resonance frequency



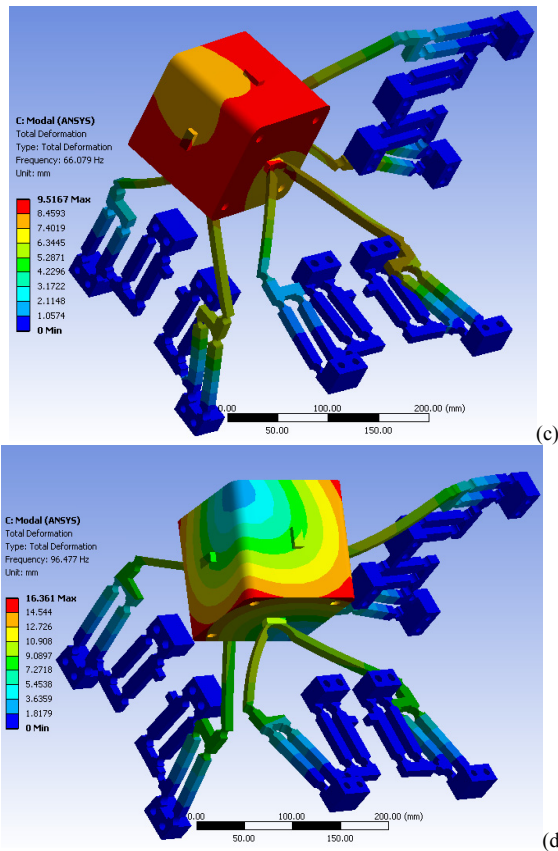


Figure 8. Modal analysis of the total deformation under different frequency conditions; (1) the first modal with the resonance frequency 56.282Hz, (2) the second modal with the resonance frequency 57.627Hz, (3) the third modal with the resonance frequency 66.079Hz, (4) the fourth modal with the resonance frequency 96.477Hz.

To analysis the forced vibrations and the steady-state response, harmonic response can be analyzed when the following assumptions are given: static structural modeling is implemented firstly and damping is neglected for modal analysis. Figure 9 reflects the frequency response of the directional deformation in z-axis, normal elastic strain and directional acceleration in z-axis. An external force of 10N is applied on the moving platform in z-direction.

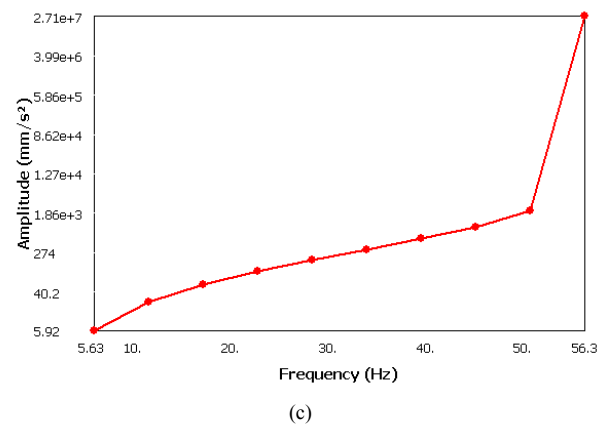
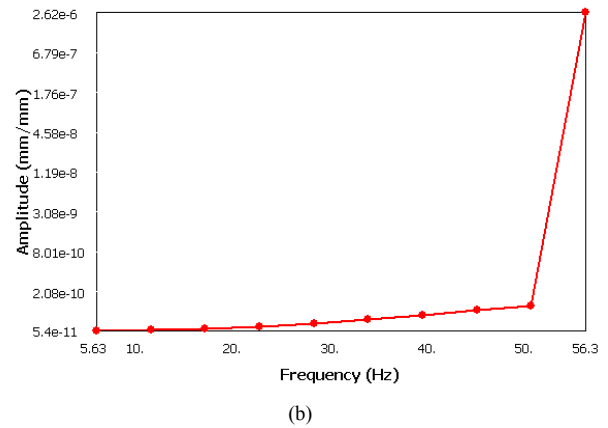
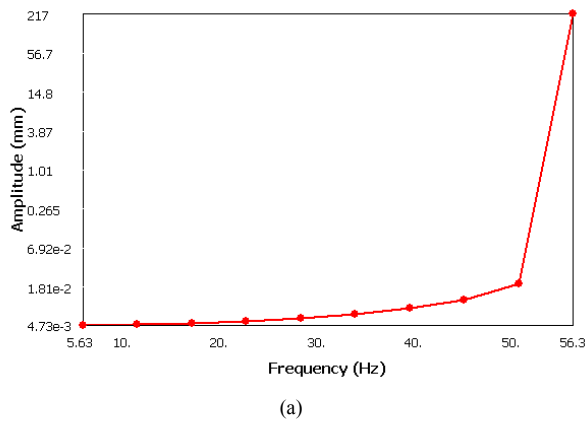


Figure 9. Frequency response when an external force of 10N is applied on the moving platform in z-direction when the first level mode 56.282 Hz is attached; a) directional deformation, b) normal elastic strain, c) directional acceleration

V. CONCLUSIONS AND FUTURE WORK

This research investigates on the conceptual design and performance analysis of a novel multi-level displacement amplifier based flexure parallel micromanipulator in which the stroke direction is perpendicular to the translation of the end-effector. The displacement amplifier is analyzed in macro and micro aspects. The finite element analysis proves the feasibility of the proposed design and it can be found that the proposed FPM has advantageous characteristics including high compliance, high linearity and high sensitivity. The proposed models and methods provide a new viewpoint for the development of compliant parallel micromanipulators. To eliminate the bending in undesired points, the improved symmetrical topology structures both in plane and in space will be developed for the future study. A physical prototype will be fabricated and tested. The experiments will be conducted to deeply explore the actual performances of the proposed design.

ACKNOWLEDGEMENTS

The authors would like to thank the financial support from the Natural Sciences and Engineering Research Council of Canada (NSERC). The authors gratefully acknowledge the financial support from Canada Research Chairs program, Early Researcher Award from Ministry of Research and Innovation of Ontario and the MITACS-NCE Research Project.

REFERENCES

- [1] D.A. Axinte, J.M. Allen, R. Anderson, I. Dane, L. Uriarte, and A. Olara, "Free-leg Hexapod: A novel approach of using parallel kinematic platforms for developing miniature machine tools for special purpose operations," *CIRP Annals - Manufacturing Technology*, Volume 60, Issue 1, 2011, pp. 395-398
- [2] H. Chanal, E. Duc, J.Y. Hascoët, and P. Ray, "Reduction of a parallel kinematics machine tool inverse kinematics model with regard to machining behavior," *Mechanism and Machine Theory*, Volume 44, Issue 7, July 2009, pp. 1371-1385
- [3] D. Zhang, Z. Bi, and B. Li, "Design and kinetostatic analysis of a new parallel manipulator," *Robotics and Computer-Integrated Manufacturing*, Vol. 25, pp. 782-791, 2009.
- [4] X. Ren, Z. Feng, and C. Su, "A new calibration method for parallel kinematics machine tools using orientation constraint," *International Journal of Machine Tools and Manufacture*, Volume 49, Issue 9, July 2009, pp. 708-721
- [5] Y. Li, J. Wang, X. Liu, and L. Wang, "Dynamic performance comparison and counterweight optimization of two 3-DOF parallel manipulators for a new hybrid machine tool," *Mechanism and Machine Theory*, Volume 45, Issue 11, November 2010, pp. 1668-1680
- [6] G. Gao, Y. Zhang, and L. Xue, "Sliding Mode Control with a Disturbance Observer for a Virtual Axis Machine Tool Parallel Mechanism," *Energy Procedia*, Vol. 13, 2011, Pages 610-616
- [7] R. Ranganath, P. S. Nair, T. S. Mruthyunjaya, and A. Ghosal, "A force-torque sensor based on a Stewart platform in a near-singular configuration," *Mechanism and Machine Theory*, Vol. 39, No. 9, pp. 971-998, 2004.
- [8] Z. L. Jin, F. Gao, and X. H. Zhang, "Design and analysis of a novel isotropic six-component force/torque sensor," *Sensors and Actuators A: Physical*, Vol. 109, pp. 17-20, 2003.
- [9] G. S. Kima, H. J. Shina, and J. W. Yoon, "Development of 6-axis force/moment sensor for a humanoid robot's intelligent foot," *Sensors and Actuators A: Physical*, Vol, 141, No. 2, pp. 276-281, 2008
- [10] Y. L. Hou, D. X. Zeng, J. T. Yao, K. J. Kang, L. Lu, and Y. S. Zhao, "Optimal design of a hyperstatic Stewart platform-based force/torque sensor with genetic algorithms," *Mechatronics*, Vol. 19, pp. 199-204, 2009
- [11] Y. Yue, F. Gao, X. Zhao, and Q. Ge, "Relationship among input-force, payload, stiffness and displacement of a 3-DOF perpendicular parallel micro-manipulator," *Mechanism and Machine Theory*, Volume 45, Issue 5, 2010, pp. 756-771
- [12] Tung-Li Wu, Jia-Hao Chen, and Shuo-Hung Chang, "A Six-DOF Prismatic-Spherical-Spherical Parallel Compliant Nanopositioner," *IEEE Transactions on Ultrasonics, Ferroelectrics, and Frequency Control*, vol. 55, no. 12, December 2008, pp. 2544-2551
- [13] D.S. Kang, T.W. Seo, Y.H. Yoon, B.S. Shin, X-J Liu, and J. Kim, "A Micro-positioning Parallel Mechanism Platform with 100-degree Tilting Capability," *CIRP Annals - Manufacturing Technology*, Volume 55, Issue 1, 2006, pp. 377-380
- [14] K. A. Jensen, C. P. Lusk, and L. L. Howell, "An XYZ micromanipulator with three translational degrees of freedom," *Robotica*, Vol. 24, No. 3, pp. 305-314, 2006.
- [15] J. Palmer, B. Dessent, J. F. Mulling, T. Usher, E. Grant, J. W. Eischen, A. Kingon, and P. Franzon, "The design and characterization of a novel piezoelectric transducer-based linear motor," *IEEE/ASME Transaction on Mechatronics*, Vol. 13, pp. 441-450, 2004
- [16] R. Franci, V. Parenti-Castelli, C. Belvedere, and A. Leardini, "A new one-DOF fully parallel mechanism for modelling passive motion at the human tibiotalar joint," *Journal of Biomechanics*, Volume 42, Issue 10, 22 July 2009, pp. 1403-1408
- [17] E. Ottaviano, M. Ceccarelli, and G. Castelli, "Experimental results of a 3-DOF parallel manipulator as an earthquake motion simulator," *ASME Conf. Proc. IDETC/CIE*, 2004.
- [18] R. Kelaiaia, O. Company, and A. Zaatri, "Multiobjective optimization of a linear Delta parallel robot," *Mechanism and Machine Theory*, Volume 50, April 2012, pp. 159-178
- [19] F. Mert Sasoglu, Andrew J. Bohl, Kathleen B. Allen, and Bradley E. Layton, "Parallel force measurement with a polymeric microbeam array using an optical microscope and micromanipulator," *Computer Methods and Programs in Biomedicine*, Volume 93, Issue 1, January 2009, pp. 1-8
- [20] L. Wang, W. Rong, M. Feng, T. Liu, and L. Sun, "Calibration of a 6-DOF parallel micromanipulator for nanomanipulation," *2010 3rd International Nanoelectronics Conference*, pp.38- 139
- [21] Bongsoo Kang and James K. Mills, "Study on Piezoelectric Actuators in Vibration Control of a Planar Parallel Manipulator," *Proceedings of the 2003 IEEE/ASME International Conference on Advanced Intelligent Mechatronics (AIM 2003)*, pp. 1268-1273
- [22] Y. K. Yong, S. Aphale and S. O. R. Moheimani, "Design, identification and control of a flexure-based XY stage for fast nanoscale positioning," *IEEE Trans. Nanotechnology*, vol. 8, no. 1, pp. 46-54, 2009.
- [23] W. Dong, L. N. Sun, and Z. J. Du, "Design of a precision compliant parallel positioned driven by dual piezoelectric actuators," *Sensors and Actuators A* 135 (2007) pp. 250-256
- [24] X. Tang, H.-H. Pham, Q. Li, and I.-M. Chen, "Dynamic analysis of a 3-DOF flexure parallel micromanipulator," in *Proc. IEEE Conf. on Robotics, Automation and Mechatronics*, pp. 95-100, 2004.
- [25] M. Culpepper and G. Anderson, "Design of a low-cost nano manipulator which utilizes a monolithic, spatial compliant mechanism," *Precision Engineering* 28 (2004) pp. 469-482

Improvement of the Diffusive Component of Dark Current in Silicon Photomultiplier Pixels

Roberto Pagano, Sebania Libertino, Domenico Corso, and Salvatore Lombardo

Istituto per la Microelettronica e Microsistemi,
Consiglio Nazionale delle Ricerche (CNR)
VIII Strada Z.I. 5, 95121, Catania, Italy
roberto.pagano@imm.cnr.it,
sebania.libertino@imm.cnr.it,
domenico.corso@imm.cnr.it,
salvatore.lombardo@imm.cnr.it

Giuseppina Valvo, Delfo Sanfilippo, Giovanni Condorelli, Massimo Mazzillo, Angelo Piana, Beatrice Carbone, and Giorgio Fallica

IMS-R&D
STMicroelectronics
Stradale Primosole, 50 95121 Catania, Italy
giusy.valvo@st.com, delfo.sanfilippo@st.com,
giovanni.condorelli@st.com,
massimo.mazzillo@st.com, angelo.piana@st.com,
beatrice.carbone@st.com, giorgio.fallica@st.com.

Abstract— The temperature behavior of dark current in SiPM pixels was studied for two fabrication technologies differing in the anode contact. The first (old) technology had the contact on the front, while the second (new) has the anode contact on the back. The layout changes allowed us to obtain a strong reduction of the dark current diffusive component thus strongly improving the device performances.

Keywords-Silicon Photomultipliers (SiPM); Dark Counts.

I. INTRODUCTION

Silicon Photomultipliers (SiPMs) are a very promising technology to complement or even replace conventional vacuum tube photomultipliers, given their strong advantages in terms of cost, mechanical robustness, reliability, and insensitivity to magnetic field [1-4]. These devices are the parallel connection of pixels, each one consisting in a p-n junction suitably doped in order to have avalanche breakdown in a well defined active area with a quenching resistance in series. The active area is formed by creating an enriched well, generally doped by ion implantation followed by thermal processing for dopant activation and defect annealing. This dopant local enrichment generates regions where the vertical junction electric field is higher, and these become the device active areas for photon detection [5]. The p-n junction devices are operated in Geiger mode [6], that is, they are biased above the junction breakdown voltage (BV). The single pixel operation is as follows: when the device is quiescent its active area is characterized by an electric field well above the breakdown field. In such a condition the absorption of a single photon in the active area will trigger, through the generation of an electron-hole pair, with a nearly 100% probability, the onset of the junction avalanche. The voltage drop across the series resistance, which decreases the voltage applied to the p-n junction, quickly quenches the avalanche. Therefore the photon arrival results in a current pulse which can then be easily measured by an external circuit. The avalanche quenching, moreover, restores the pixel to the original condition of electric field above BV,

rendering the pixel ready to the detection of a new photon [6]. The operation of the overall SiPM is simply the sum of the behaviors of the various pixels. Therefore, this device compared to the original design of the Single-Photon Avalanche Diode (SPAD) has the advantage of having a relatively large dynamic range response proportional to the flux of photons impinging on the detector at the same time [7].

The SiPM major drawback is the relatively large dark current, due to the combination of a diffusion current produced at the quasi-neutral regions at the boundaries of the device active region, and of generation of carriers due to point defects and/or metallic impurities in the active area depletion layer emitting carriers through the Shockley-Hall-Read (SHR) mechanisms, eventually boosted by the Poole-Frenkel effect [8].

In previous works [9-12], we investigated the dark current of SiPM devices produced by STMicroelectronics. After the first two work [9-10] that was essential to comprehend that the single pixel dark current in the first developed SiPM technology is due to the above two mentioned processes and that have different weight varying the temperature, we finally understood [12] that the first process, the diffusion of minority carriers, is relevant for temperatures below 10 °C and it is primary localized at the lateral border of the pixel, while the latter, the carriers generation through SHR mechanism, dominates at higher temperatures and is localized in the active area of the pixel. Hence, at 25 °C, the dark current is limited by the lateral diffusion of minority carriers. This is an intrinsic effect, due to the diffusion of minority carriers towards the p-n junction depletion layer, inversely proportional to the doping level and, therefore, larger at the perimeter of the active area, where the dopant concentration is lower. Being an intrinsic effect, one may conclude that the dark current levels of the above mentioned SiPM devices, at least at 25 °C, are the ultimate limit, which cannot be subjected to further improvements. In principle, however, this is not true, since

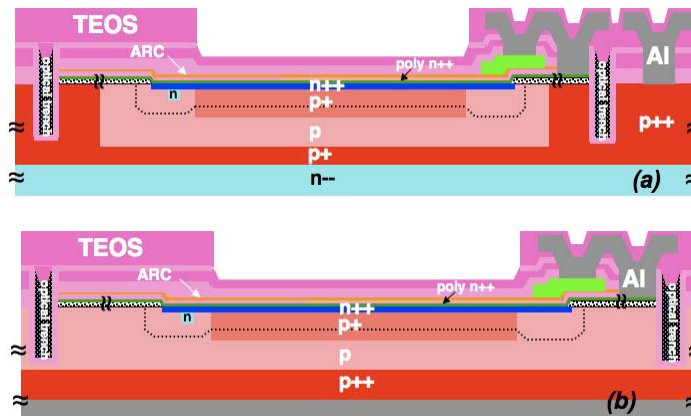


Figure 1. Schematic cross-section of a SiPM pixel (not in scale). (a) Old technology with double epitaxial layer, n-substrate and trenches crossing the sinker diffusion. (b) New technology with single epitaxial layer, p-substrate, and isolated sinker diffusion. Dotted black lines remark the depleted region extension.

the diffusion currents that leads to the dark current is expected to be also inversely proportional to the square root of minority carrier lifetime. Any strong improvement in the minority carrier lifetime would therefore translate into a dark current improvement.

In this paper, we show that a new device architecture, investigated in [11], does provide such a strong lifetime and the dark current improvement.

II. EXPERIMENTAL

The full device fabrication details can be found in [13]. In this paper, we want to focus our attention on similarities and differences between the two technologies in study. They have the same active part and guard ring of the device, fabricated and discussed in [9-13], thus producing the same BV (-28V at 25°C). The main difference between the two technologies is in the substrate: in the first technology a double epitaxial layer, first p⁺, then followed by a p⁻ is grown on a low doped n-type (100) oriented Si substrate [9,10,12]. In the second technology [11,13], only a single p⁻ epitaxial layer is grown on a highly doped p⁺ (100) Si substrate. In both cases deep optical trenches are realized for the optical and electrical isolation between the pixels. Figure 1 shows the schematic cross section of the device, not in scale, for the two technologies, old and new (Fig. 1a and b, respectively). A further difference in the two devices is that in the new technology is not needed the presence of the anode contact on the front, hence the p⁺ region between the active area and the optical trench has been removed (see Fig. 1).

Electrical characterization was performed at wafer level using a Cascade Microtech Probe Station 11000. The samples were cooled using a Temptronic TPO 3200A ThermoChuck that provide a stabilized temperature between -60°C and 200°C. Current vs. voltage measurements (I-V) were acquired using an HP 4156B precision semiconductor parameter analyzer using an integration time of 1s. The dark count was obtained using a Tektronix DPO 7104 Digital Oscilloscope with 1 GHz bandwidth and 20 Gsa/s. The I-V characteristics have been measured on more than 30 SiPM

pixels of old and new technologies, showing a very good uniformity.

III. RESULTS AND DISCUSSIONS

Dark currents of single SiPM pixels fabricated in the two different technologies were investigated with respect to voltage and temperature (from -25°C to 65°C). Figure 2 shows the dark currents as a function of voltage at three different temperatures, -25°C (circles), 25°C (triangles) and 65°C (squares) of a SiPM pixel fabricated in the old technology (filled symbols) compared to the dark current of a pixel in the new technology (open symbols). At -25°C the dark currents (circles) are of the same order of magnitude, while by increasing the temperature they show remarkable differences. At 25°C and at $V_{BIAS} = -32V$ (+ 4V overvoltage, OV) the dark current in the old technology is one order of magnitude higher than that of the new technology one. At 65°C the difference increases (two orders of magnitude of difference).

In order to understand the reason of such reduction, we extracted the activation energy of the dark current for the two devices as a function of the temperature. The Arrhenius plot of the dark current for a constant OV (+4V in Fig. 3) evidences a clear reduction of the diffusion component in the new technology. In particular, at low temperatures the dark current is dominated by SHR generation from mid-gap level defects of similar density in both technologies, as demonstrated by the measured activation energies, reported

TABLE I. MEASURED VALUE OF THE DC AT 25°C; ACTIVATION ENERGIES EXTRACTED FROM THE ARRHENIUS PLOT OF FIGURE 3; SOME OF THE PARAMETERS USED IN THE DC SIMULATION.

Technology	DC (s-1)	E_{A1} (eV)	E_{A2} (eV)	N_{DEF} (cm ⁻³)	$E_C - E_T$ (eV)	τ_n (s)
Old	600	0.57	1.18	10 ⁻⁹	0.55eV	10×10 ⁻⁶
New	4600	0.59	1.12	10 ⁻⁹	0.55eV	3×10 ⁻³

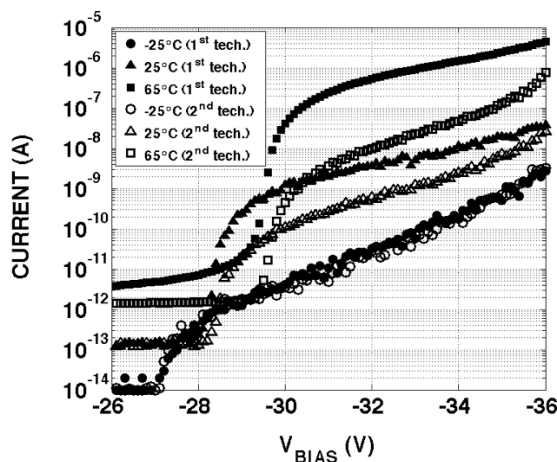


Figure 2. Dark currents at three different temperatures, -25°C (circles), 25°C (triangles) and 65°C (squares) of SiPM pixels fabricated in the old technology (filled symbols) and new technology (open symbols).

in Table I. At higher temperatures, the diffusion of minority carriers becomes the dominant mechanism of dark current. Note, however, that this mechanism becomes the leading effect at different temperatures for the two technologies. For the old one the diffusion mechanism dominates for temperatures above 10°C, while for the second one it prevails at temperatures above 40°C.

To get a further insight, the dark count (DC) rates for the two devices were measured as a function of temperature and bias voltage (Fig. 4). In general, it has been demonstrated that the DC rate in a pixel is well described by the following equation [10,12]:

$$DC = DC_{SHR} + DC_{DIFF} \quad (1)$$

The first term, DC_{SHR} , takes into account the SHR generation from mid-gap level defects located in the depleted active volume of the pixel p-n junction:

$$DC_{SHR} = N_{Def} \cdot A_{ACT} \cdot W \cdot \gamma_n \cdot \sigma_n \cdot T^2 \cdot \exp\left(-\frac{E_C - E_T}{kT}\right) \quad (2)$$

where N_{Def} is the defect concentration, W the depletion layer width, A_{ACT} the pixel active area, γ_n the universal constant for emissivity [14], σ_n the defect cross-section, $E_C - E_T$ the defect ionization energy [14], T the temperature, and k the Boltzmann constant.

The second term DC_{DIFF} is the component due to the minority carrier diffusion from the perimeter of the pixel active area into the active depleted volume, given by:

$$DC_{DIFF} = A_P \cdot \sqrt{\frac{D_n}{\tau_n}} \cdot \frac{n_i^2}{N_a} \quad (3)$$

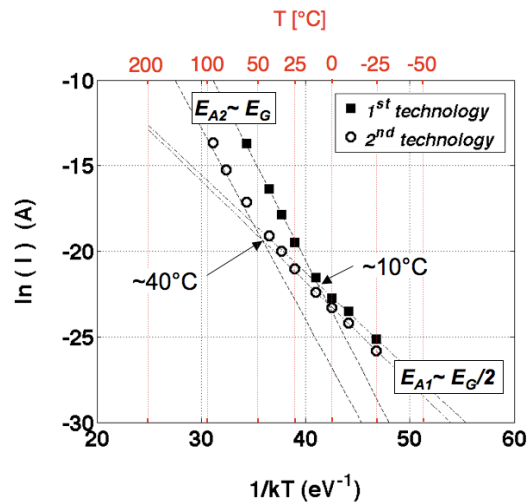


Figure 3. Arrhenius plot of the dark currents at constant +4 V overvoltage for a SiPM pixel fabricated in the old technology (filled squares) and in the new (open circles) technology.

where n_i is intrinsic carrier concentration, N_a is the dopant concentration of the epitaxial layer in the active area perimeter, D_n is the electron diffusivity, τ_n is the minority carrier lifetime and A_P the area of the perimeter zone surrounding the active area.

Figure 4 shows the comparison of the experimental (symbols) and the simulated DC rates (continuous and dashed line) using Eqs. (1), (2) and (3) for the old and the new technology respectively at different temperatures. The agreement between data and simulation is extremely good in the full temperature range explored. We modeled the experimental data by assuming $N_{Def} = 10^9 \text{ cm}^{-3}$, $E_C - E_T = 0.55 \text{ eV}$, $\sigma_n = 1.6 \times 10^{-15} \text{ cm}^2$, with the universal constant $\gamma_n = 1.78 \times 10^{21} \text{ cm}^{-2} \text{ s}^{-2} \text{ K}^{-2}$ for the SHR term (Eq. (2)) in both technologies. For the diffusion term (Eq. (3)) we assumed: $\mu_n = 1500 \text{ cm}^2/\text{Vs}$ and $N_a = 10^{15} \text{ cm}^{-3}$, that is the dopant concentration of the p- epitaxial layer. To explain the large difference in the DC rate in the diffusion regime, we have to assume drastically different values of minority carrier lifetime: $\tau_n = 10 \mu\text{s}$ for the old technology and $\tau_n = 3 \text{ ms}$ for the new technology. The large lifetime improvement results in a noticeable improvement of the DC rate diffusive component, as shown in Figs. 3 and 4. The reason for such radical improvement of both lifetime and DC rate in the diffusive regime may be ascribed to the different device architecture (see Fig. 1). In the old technology a large p-type dopant concentration in the device periphery, up to a B concentration of the order of $2 \times 10^{18} \text{ cm}^{-3}$, is present, while it is completely absent in the new technology. By considering that the Auger effect [15-16] for such a large dopant concentration becomes a relevant recombination mechanism, with lifetimes of the order of $1 \mu\text{s}$ in correspondence with the peak B concentrations at the periphery, we propose that the low effective minority carrier lifetimes observed in the old technology are due to Auger recombination occurring at the device periphery. Such effect disappears in the new technology, resulting in a noticeable improvement of lifetime

and, therefore, of *DC* rate in the diffusive regime. In the present new generation technology, the defect concentration is of the order of $10^9/\text{cm}^3$, hence the diffusive component dominates the *DC* rate at about 50°C and above. By further decreasing the concentration of SHR defects, the *DC* rate would be limited only by the diffusive regime also at room temperature (25 °C), which would result in a level of *DC* rate of a few tens of counts per second for our pixel size.

IV. CONCLUSIONS

In this paper, we have reported on the comparison of two SiPM pixel architectures: the first one has a double epitaxial layer p+/p on an n-type Si substrate and the anode contact is on the top of the structure; the second one has only a single p⁻ epitaxial layer grown on a highly doped p⁺ Si substrate with the anode contact at the bottom of the structure. In both cases deep optical trenches are realized.

The dark current behavior of SiPM pixels with respect to the temperature was studied for the two fabrication technologies. The realization of a back-side anode contact results in a major improvement of the minority carrier lifetime, probably due to the reduction and/or removal of Auger recombination at the device periphery taking place when a high B doping is used to provide the front side anode contact. This results in a noticeable improvement of the diffusive component of the *DC* rate and then to a reduction of the pixel *DC* for temperature higher than 10°C.

ACKNOWLEDGMENT

This work was partially supported by STMicroelectronics under Grant CDR.ST.CNR-IMM.MATIS.24.02.2010.002

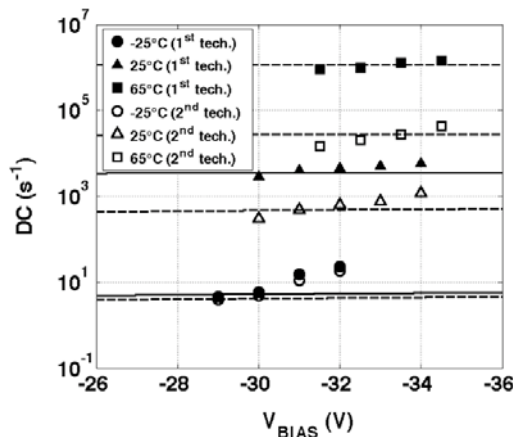


Figure 4. Comparison of DC at three different temperatures, -25°C (circles), 25°C (triangles) and 65°C (squares) of the two SiPM pixels fabricated in the old (filled symbols) and new (opens symbols) technologies. Continuous and dashed lines are the simulated DC as described in text for the old and the new technology respectively.

REFERENCES

[1] N. Otte, B. Dolgoshein, J. Hose, S. Kleminin, E. Lorentz, R. Mirzoyan, E. Popova, and M. Teshina, "The Potential of

SiPM as Photon Detector in Astroparticle Physics Experiments like MAGIC and EUSO", Nucl. Instr. and Meth. in Phys. B Proc. Suppl., vol. 150, 2006, pp. 144-149.

[2] V. D. Kovaltchouk, G. J. Lolos, Z. Papandreou, and K. Wolbaum, "Comparison of a silicon photomultiplier to a traditional vacuum photomultiplier", Nucl. Instr. and Meth. in Phys. A, vol. 538, 2005, pp. 408-415.

[3] P. Finocchiaro, A. Pappalardo, L. Cosentino, M. Belluso, S. Billotta, G. Bonanno, and S. Di Mauro, "Features of Silicon Photo Multipliers: Precision Measurements of Noise, Cross-Talk, Afterpulsing, Detection Efficiency, IEEE Trans. Nucl. Sci., vol. 56, 2009, 1033-1041.

[4] A. Del Guerra, N. Belcari, M. G. Bisogni, G. LLos, S. Marcatili, G. Ambrosi, F. Corsi, C. Marzocca, G. Dalla Betta, and C. Piemonte "Advantage and pitfalls of the silicon photomultiplier (SiPM) as photodetector for the next generation of PET scanners", Nucl. Instr. and Meth. in Phys. A, vol. 617, 2010, pp. 223-226.

[5] E. Sciacca, A. C. Giudice, D. Sanfilippo, F. Zappa, S. Lombardo, R. Consentino, C. Di Franco, M. Ghioni, G. Fallica, G. Bonanno, S. Cova, and E. Rimini, "Silicon Planar Technology for Single-Photon Optical Detectors" IEEE Trans. Elec. Dev., vol. 50, 2003, pp. 918-925.

[6] S. Cova, M. Ghioni, A. Lacaita, C. Samori, and F. Zappa, "Avalanche photodiodes and quenching circuits for single-photon detection", Appl. Opt., vol 35, 1996, pp. 1956-1976.

[7] D. Renker and E. Lorentz, "Advances in solid state photon detectors" J. Instrum., vol. 4, 2009, p.04004.

[8] S. Cova, A. Lacaita, and G. Ripamonti, "Trapping Phenomena in Avalanche Photodiodes on Nanosecond Scale" IEEE Electron Dev. Lett., vol. 12, 1991, pp. 685-687.

[9] R. Pagano, S. Libertino, G. Valvo, G. Condorelli, B. Carbone, A. Piana, M. Mazzillo, D. N. Sanfilippo, G.G. Fallica, G. Falci, and S. Lombardo, "Dark Count in Single Photon Avalanche Si Detectors", Proc. Of SPIE, vol. 7598, 2010, p. 75980Z-1-8.

[10] R. Pagano, S. Lombardo, S. Libertino, G. Valvo, G. Condorelli, B. Carbone, D. N. Sanfilippo, and G. Fallica, "Understanding dark current in pixels of silicon photomultipliers, proc. IEEE European Solid-State Device Research Conference, (ESSDERC 2010), IEEE press, Sept. 2010, pp. 265-268.

[11] R. Pagano, D. Corso, S. Lombardo, S. Libertino, G. Valvo, D. Sanfilippo, A. Russo, P. G. Fallica, A. Pappalardo, and P. Finocchiaro, "Optimized silicon photomultipliers with optical trenches", proc. IEEE European Solid-State Device Research Conference, (ESSDERC 2011), IEEE press, Sept. 2011, pp. 183-186.

[12] R. Pagano, D. Corso, S. Lombardo, G. Valvo, D.N. Sanfilippo, G. Fallica, and S. Libertino, "Dark current in SiPM pixel: data and model", IEEE Trans. Electron Dev. (in press).

[13] M. Mazzillo, G. Condorelli, D. Sanfilippo, G. Valvo, B. Carbone, G. Fallica, S. Billotta, M. Belluso, G. Bonanno, L. Cosentino, A. Pappalardo, and P. Finocchiaro, "Silicon Photomultiplier Technology at STMicroelectronics", IEEE Trans. Nucl. Sci., vol. 56, 2009, pp. 2434-2442.

[14] D. K. Schroder, *Semiconductor Material and Device Characterization 3rd ed.*, Wiley-Interscience, 2006, pp. 262-264.

[15] L. Passari and E. Susi, "Recombination mechanisms and doping density in silicon", J. Appl. Phys., vol. 54, 1983, pp 3935-3937.

[16] D. K. Schroder, "Carrier Lifetimes in Silicon", IEEE Trans. Electron Dev., vol. 44, 1997, pp. 160-170.

Impedance Measurements of Ethanol Sensing with Vanadium oxide / Porous Si / Si Structure

Katia Chebout

UDTS, 02 Bd Frantz Fanon B.P. 140 Algiers7
Merveilles (UDTS)
Algiers, Algeria
e-mail: Bouttondor@yahoo.fr

Aicha Iratni

LMMC, Faculty of engineering sciences. M'Hamed
Bougara University, 35000
Algiers, Algeria
e-mail: irataicha@yahoo.fr

Ahmed Bouremana, Kawthar M'hammedi

UDTS, 02 Bd Frantz Fanon B.P. 140 Algiers7
Merveilles (UDTS)
Algiers, Algeria
e-mail : ahmed.bouremana@gmail.com
e-mail : kawther_mhammedi@hotmail.fr

Hamid Menari, Aissa Keffous, Nouredine Gabouze *

UDTS, 02 Bd Frantz Fanon B.P. 140 Algiers7
Merveilles (UDTS)
Algiers, Algeria
e-mail: ngabouze@yahoo.fr
e-mail : keffousa@yahoo.fr
e-mail : menarih66@yahoo.fr

Abstract – The paper deals with a gas sensing device based on Vanadium oxide (V_2O_5)/ Porous Si (PS) /Si structure used to detect Ethanol gas at different concentration. The V_2O_5 thin films were deposited on porous silicon by the sol-gel (Dip-coating) technique. The Vanadium oxide has been produced from vanadium alcoxide precursor. Current-voltage and admittance characterizations show that the sensor characteristics are modified in the presence of gases. Conductance measurements at low frequencies indicate the presence of interface states.

Keywords- vanadium oxide; porous silicon; gas sensor.

I. INTRODUCTION

During the two last decades, the interest in environment issues, particularly in pollution, has become a major key factor in the industrial development. Recently, immense efforts have been done in the development of sensing devices based on porous silicon (PS) [1, 2]. Because of its high reactivity and high specific surface ($200-600 \text{ m}^2/\text{cm}^3$), porous silicon has been shown to be an interesting base material for gas sensing application [3, 4]. Porous silicon has been found highly sensitive against organic vapours such as methanol, ethane, propane or ethanol and acetone [3, 5-8]. However, PS-based sensors showed a relatively long response time, and a degradation of the structure due to porous silicon surface oxidation. Many recent efforts that are devoted to materials exploration for better sensor performance have appeared.

Metal oxides have been widely exploited as sensing elements in semiconductor gas sensors, because they provide featured active sites to adsorb gas molecules and catalyze reactions. Their surface states and chemical reducibility favor gas sensor operation at low temperatures.

Presently, only transition-metal oxides with d_0 or d_{10} electronic configurations (e.g., SnO_2 and ZnO with d_{10} ; TiO_2 and V_2O_5 with d_0) find their real gas sensor application [9]. Vanadium oxides have attracted attention because of their potential applications as chemical sensors and as the active components of various electrical and optical devices [10]. Thin films of vanadium oxides for ethanol sensor applications with the best sensitivity and selectivity were prepared by several authors [11, 12]; however, the mechanism sensing is not yet fully understood.

In the present work, we will present current-voltage, capacitance and conductance results of a gas sensing device based on Vanadium oxide (V_2O_5)/Porous Si (PS) /Si structure subjected to ethanol vapor.

II. EXPERIMENTAL

Porous silicon (PS) was obtained by electrochemical etching of p-type silicon wafer ($450 \mu\text{m}$ thickness, $1 - 10 \Omega\text{cm}$ resistivity). The etching solution was prepared by adding 50 vol. % of ethanol to 50 vol.% of HF aqueous solution (49 wt. %). Current density and etching time were varied to obtain porosity ranging from 40 to 75% and thickness of PS layer $2 - 15 \mu\text{m}$, respectively. Nanostructured vanadium pentoxide films deposited on PS surface were prepared by mixing vanadium (V) oxytriisopropoxide ($\text{VO}(\text{OPr}^i)_3$) (Sigma Aldrich) with isopropanol (Pr^iOH) in presence of acetylacetate. The obtained gel was deposited by dip coating technique and dried in air at room temperature.

Current-voltage and impedance spectroscopy are employed for electrical characterizations of the sensor in a controlled gas environment.

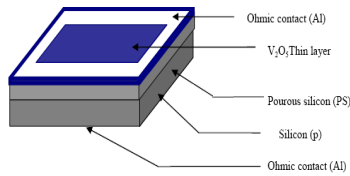


Figure 1. A schematic diagram of the V₂O₅/PS/Si sensor.

Sensor prototype structure of 5 mm x 5 mm cells was realized (Figure 1).

III. RESULTS AND DISCUSSION

III.1 Current-voltage characteristics

The current-voltage (I-V) characteristic of V₂O₅/PS/Si structure, shown in Figure 2, was measured in air environment and ethanol vapor environment. The current response of the devices shows generally that for bias potential values less than 1 V, an ideality factor of 1.72 is calculated. The value of the ideality factor n as obtained here could indicate that the current transport mechanism consists of both the trap-assisted tunneling and the thermionic emission [13, 14].

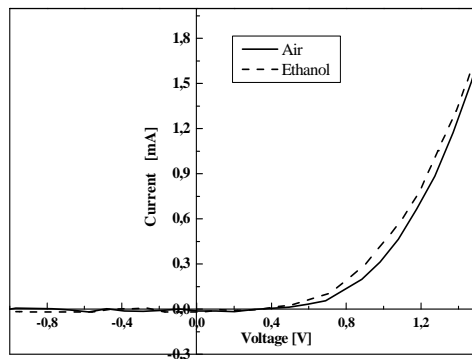


Figure 2. I-V characteristics of the structure against ethanol vapor at a concentration of 160 ppm.

A rectifying behavior is also observed when the ethanol vapor is in contact with the structure with no change in the shape of current-voltage curve, only a change in current magnitude at fixed potential is observed.

III.2 Capacitance and conductance measurements

The current-voltage characteristic does not provide sufficient information to model the device operation. Complementary information's can be obtained from the small signal impedance measurements. The measurements were made as a function of frequency in the range 1 Hz - 100 kHz.

Figure 3a which gives the variations of the capacitance versus bias (C-V) at constant frequency of 1 kHz shows that it behaves as Metal-Insulator-Semiconductor (MIS) structures as observed by several authors for Al/PS/Si structure [15]. The capacitance decreases monotonically and stabilizes at potential values lower than -1 V. When the gas is in contact with the ethanol vapor a large variation of the capacitance is observed, as shown in Figure 3b. For structure biased negatively C decreases monotonically with bias voltage.

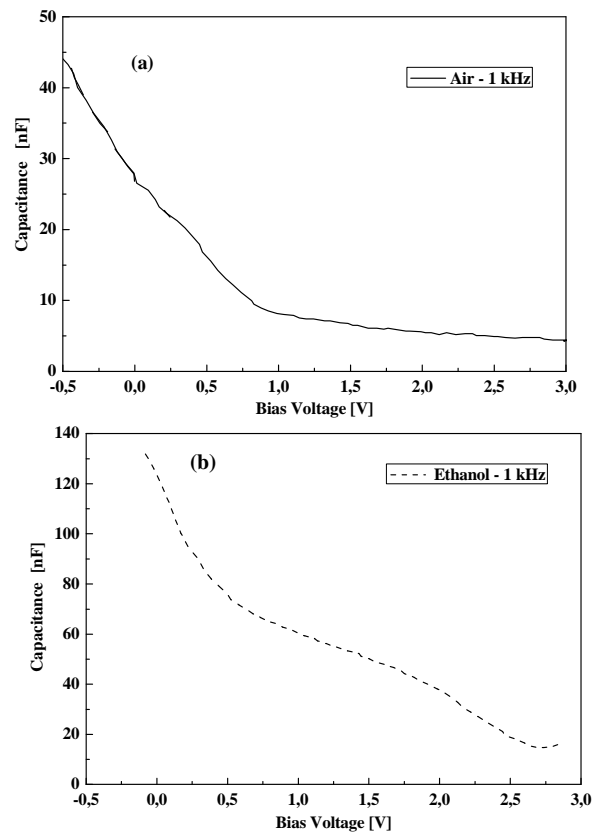


Figure 3. Variation of the capacitance vs. bias voltage at constant frequency of 1kHz, (a) under air, (b) ethanol vapor.

Figure 4 shows the dependence of the conductance on the voltage at 1 kHz frequency before and after introducing ethanol vapor. One can note that the introduction of ethanol vapor onto sensitive V₂O₅/PS surface causes, here again, changes in the conductance measurement. The conductance variations were seen to increase monotonically with negative

bias voltage when the gas is in contact with the device, the conductance value decreases with bias voltage. However a change in the variation shape of the conductance has been observed at low frequencies between 10 and 100 Hz, as shown in Figure 5, where it shows that in the potential range (0 - -1.5 V) the conductance presents a large “cavity” centered at about -0.4 V.

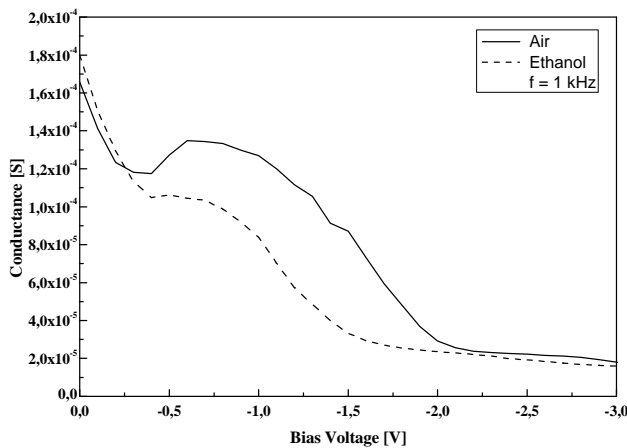


Figure 4. Variation of the conductance vs. bias voltage at constant frequency of 1 kHz under air and ethanol vapor.

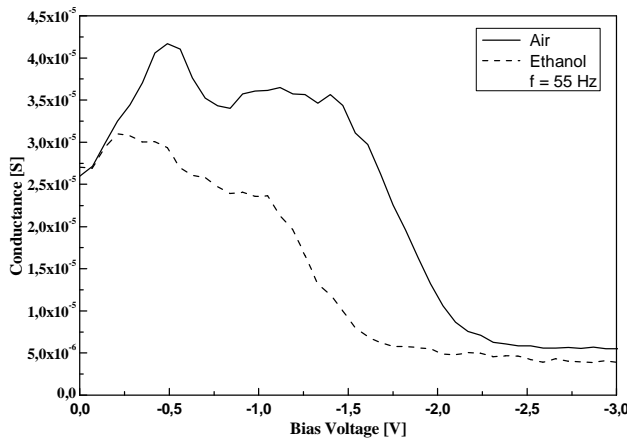


Figure 5. Dependence of the conductance on the voltage at constant frequency of 10 Hz.

This behavior could be related to the presence of interface states distributed in this bias potential range. This statement is confirmed by contacting the structure with the gas ethanol. In this case the interface states are filled with charges due to adsorption of ethanol vapor. In principle the evaluation of an interface density of states can be obtained from the dependence of the conductance G , divided by the frequency: G/ω as a function of ω . From the G/ω curve it is easy to calculate the density of the interface state [15, 16].

The capacitance and conductance as a function of frequency at a bias potential of -1 V are shown in Figure 6. It is shown that the capacitance is higher for very low frequencies then decreases monotonically to low values for higher frequencies (Figure 6a).

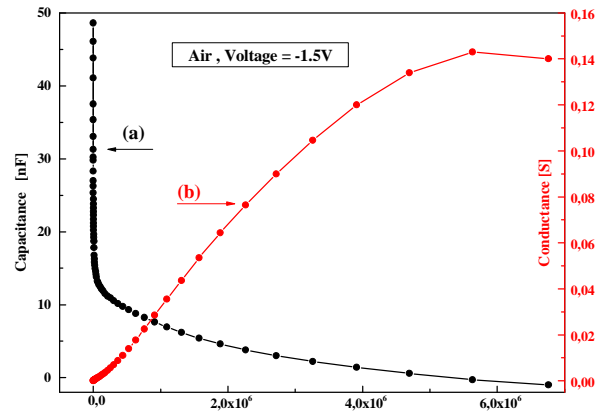


Figure 6. Capacitance and conductance of the $V_2O_5/PS/Si$ structure as a function of frequency.

The conductance is seen to increase linearly in the range 1 Hz to 1 kHz then tend to stabilize for higher frequency values (Figure 6b). It is clear that more results are needed in order to understand this behavior and elaborate an equivalent electrical circuit of the structure.

VI. CONCLUSION

In this work, we reported on the deposition of vanadium oxide on porous silicon and the application of $V_2O_5/PS/Si$ as structure for ethanol vapor sensing. Capacitance, conductance and current-voltage measurements show that the device response is modified by the ethanol vapor on the V_2O_5/PS surface. The results of impedance measurements at low frequency clearly demonstrate the presence of interface states at -0.4V.

REFERENCES

- [1] V. Mulloni, Z. Gaburro, and L. Pavesi, Porous silicon microactivities as optical chemical sensors, in: Proceedings of the Porous Semiconductors Science and Technology, Madrid Spain, 12-17 March (2000) 101.
- [2] S. Belhousse, H. Cheraga, N. Gabouze, and R. Outamzabet. Sensors and Actuators B: Chemical 100 (2004) 250.
- [3] S. J. Kim, S. H. Lee, and C.-J. Lee, J. Phys. D: Appl. Phys 34 (2001) 3505.
- [4] L. T. Canham, Properties of porous Silicon INSPEC (London) 1997, p. 44.

- [5] E. Galeazzo, H. E. M. Peres, G. Santos, N. Peixito, and F. J. Ramirez-Fernandez, *Sensors and Actuators B: Chemical* 93 (2003) 384.
- [6] H. K. Min, H. S. Yang, and S. M.Cho, *Sensors and Actuators B: Chemical* 67 (2000) 199.
- [7] K. Watanabe, T. Okada, I. Che, and Y. Sto, *Sensors and Actuators B: Chemical* 33 (1996) 194.
- [8] M. Archer, M. Christophersen, and P. M. Fauchet, *Sensors and Actuators B: Chemical* 106 (2005) 347.
- [9] G. Korotcenkov / *Materials Science and Engineering B* 139 (2007) 1.
- [10] M.H. Lee and M.G. Kim, *Thin Solid Films* 286 (1–2) (1996) 219.
- [11] E. Strelcov, Y. Lilach, and A. Kolmakov, Gas sensor based on metal-insulator transition in VO₂ nanowire thermistor. *Nano Lett.* 2009, 9, 2322.
- [12] R.R. Andronenko and A.T. Nakusov, *Glass Physics and Chemistry*, vol. 33, no. 4, (2007) 411.
- [13] S. Altindal, S. Karadeniz, N. Tugluoglu, and A.Tataroglu, *Solid State Electronics* 47 (2003) 1847.
- [14] T. Nagatomo, M. Ando, and O. Omoto, *Jpn J Appl Phys* 18 (1979) 1103.
- [15] Card HC, Rhoderick EH. *J.Phys D4* (1971) 1589.
- [16] N. Gabouze, Thèse de l'Université Pierre & Marie Curie, Paris VI, 1988.
- [17] A.J .Simons, T.I. Cox, A. Loni, P.D.J. Calcott, M.J.Uren, and L.T.Canham, MRS Boston, USA, December 1996.

Wireless and Passive Sensors for High Temperature Measurements

Bruno Francois*, Denny Richter[†], Holger Fritze[†], Zacharis J. Davis[‡], Christophe Droit[§],
Blandine Guichardaz*, Valérie Petrini*, Gilles Martin*, Jean-Michel Friedt[§] and Sylvain Ballandras*

*FEMTO-ST, time and frequency department, Besancon, France

Email: ballandr@femto-st.fr

[†]TU Clausthal, Institut für Energieforschung und Physikalische Technologien, Clausthal, Germany

Email: denny.richter@tu-clausthal.de

[‡]Danish Technological Institute, Taastrup, Denmark

Email: zjd@teknologisk.dk

[§]SENSeOR SAS, Besancon, France

Email: jmfriedt@femto-st.fr

Abstract—Surface acoustic waves have been studied for more than 50 years and are mainly used as passive components (resonators, frequency filters, sensors, etc.) for signal processing, and more specifically. As demonstrated by Bao et al, surface acoustic wave devices can operate without on-board power supply using a dedicated interrogation unit. Using appropriate design considerations, these devices are sensitive to external conditions including temperature, pressure, strain or chemical/biological mass loading. Therefore, the unique characteristics of such devices allows for an effective implementation providing new opportunities for remote control of physical and chemical parameters.

Keywords—Surface acoustic wave; high temperature; sensor; langasite; quartz; aging; radiofrequency; reader; passive.

I. INTRODUCTION

The work presented in this paper has been achieved within the SAWHOT European project frame [1], devoted to the development of sensor and interrogation system for an unprecedented temperature range (from cryogenic conditions to temperature in excess of 650°C). In the following, the development of temperature sensors operating from room to high temperature is described, the application concerning high temperature furnace monitoring, turbine operation control. Two different types of substrate have been used for the fabrication of SAW (Surface Acoustic Wave) sensors to assess first the possibility for accurate measurements using a differential structure, second to reach temperatures in excess of 700°C using a single resonator sensor to demonstrate the capability of these devices to withstand such operation conditions. Quartz [2] and Langasite-based [3] solutions have been respectively implemented in that purpose [4].

The first part of the paper briefly recalls the principle of wireless SAW sensors. Design rules are subsequently reported considering the specific problem of temperature robustness. Particularly, the specific problem of packaging and antenna assembly is discussed. The final sections are devoted to effective temperature measurements in the above-mentioned ranges. As a conclusion, the capability of LGS-

based sensors to reach temperature in excess of 700°C is discussed.

II. WIRELESS SAW SENSOR INTERROGATION PRINCIPLE

SAW sensors are based either on delay lines on Lithium Niobate operating in the Industrial-Scientific-Medical (ISM) 2.45 GHz band or on resonators working at lower frequencies, i.e. ISM bands centered in 434, 868 or 915 MHz. For the later case, the basic principle of the interrogation strategy is a combination of a frequency-sweep network analyzer used to identify the resonance frequencies of the device, and a monostatic pulse-mode RADAR strategy [5] for improving the isolation between emission and reception stages. The whole interrogation system is usually called reader as it actually reads the resonance frequencies. A radio-frequency pulse gates a carrier at variable frequencies within the ISM band. If the emitted pulse spectrum overlaps the bandpass of one resonator, the acoustic device stores the energy. Once the antenna of the interrogation unit switched from the emission to the reception stages of the reader, the resonator restores the loaded energy at its own resonance frequency, shifting with the variation of the physical parameter measured by the resonator [6]. This pulse is received by the interrogation unit using a wideband power detector. The returned power vs frequency curves allows for the identification of the resonance frequency [7].

III. SAW SENSOR DESIGN FOR HIGH TEMPERATURE MEASUREMENTS

An important knowledge has been developed for 20 years based on work devoted to the simulation and computation of surface acoustic wave devices (SAW), [8]. The two mainly exploited methods are FEM (Finite Element Method) [9] and BEM (Boundary Element method) [10], both combined to accurately represent effective SAW boundary conditions. FEM is used to account for the inhomogeneous part of the transducer whereas of BEM is used to represent the contribution of the substrate. This later function is achieved

using Green’s function of any layered substrates (Fig. 1) assuming flat interface between each layer of the stack. These computations are used to derive mixed-matrix or Coupling-Of-Mode (COM) parameters necessary to simulate the electrical response of actual devices.

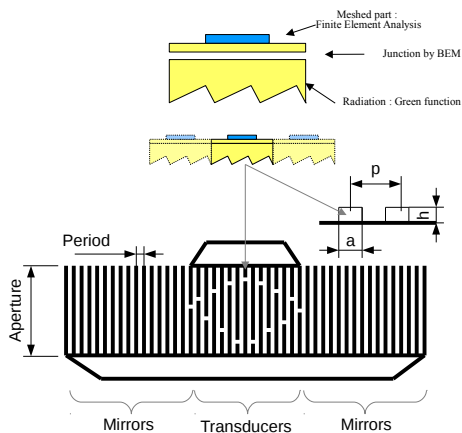


Figure 1. FEM/BEM synoptic.

Two high temperature ranges are targeted, below and over 500°C. For “low temperature”, sensors based on Quartz are used with aluminum-copper electrodes allowing for high quality factor resonances (≥ 10000) [11]. Regarding the Curie temperature of Quartz, this material can not be used at temperature higher than 573°C (limited to 540°C in practice); therefore Langasite (lanthanum gallium silicate) substrate [12] has been chosen for temperature measurement over 500°C [13], [14].

Quartz sensors used for first tests are TSEAS10 (5x5 mm², Fig. 2) from SENSEOR (Mougins, France), this device uses two resonators for differential measurements reducing the influence of correlated noise and aging effect on the response. SAW devices based on Quartz with Al-Cu electrodes provide high Q factor as required for wireless interrogation considering the capability of the sensor to store energy from the RF wave, and to restore it at its own frequency depending of environmental physical parameters [15].

Fig. 2 shows a quasi-perfect match between the simulation and the experiment for this type of sensor (association of quartz substrate with aluminum for interdigital transducers, IDT).

IV. PACKAGING OF SAW DEVICES FOR HIGH TEMPERATURE

Packaging is one key-point of the project. The device must be mounted on a carrier to avoid applying any stress on the device. Therefore, package and substrate materials require coefficients of thermal expansion as close one another as possible. The whole package is composed of a standard SMD ceramic case with tungsten/molybdenum pads (Ky-

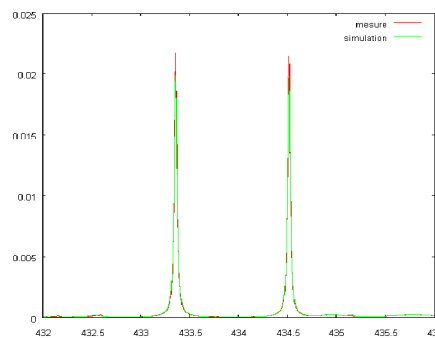


Figure 2. Comparison between computation and measurement of the TSEAS10 double resonators sensor.

ocera 7.1*9.1 mm² A440), connected to device by gold wire-bonding (Fig. 3).

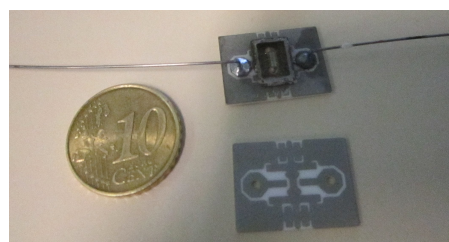


Figure 3. The different stages of the packaging process.

At the moment, devices are sealed using another upside-down package as lid. The case is connected to an alumina plate with patterned connection, this footprint is realized in AgPb alloy to avoid the migration of the solder, stainless steel antennas and case are connected to the pattern thanks to tin solder.

An additional conditioning is required to preserve the device integrity when exposed to high temperature. The corresponding process is currently under patent application process and will be described when presented at the conference.

V. TEMPERATURE MEASUREMENTS WITH SAW SENSORS BASED ON QUARTZ

The first experiment helps us to understand what happens to Quartz-based sensor between 25 °C and 250 °C.

The interrogator includes adapted SAW filters yielding operating in the 434MHz-centered ISM frequency band (434 MHz \pm 0.85MHz). The algorithm used by the reader is based on the separation of the above 1.7MHz band in two equilibrated frequency sub-bands. Each resonance of the differential sensor is located in one of the band for the whole temperature excursion. The problem in our case is that the sensor is used out of its specifications (room temperature to 250°C instead of -15°C to 165°C); therefore

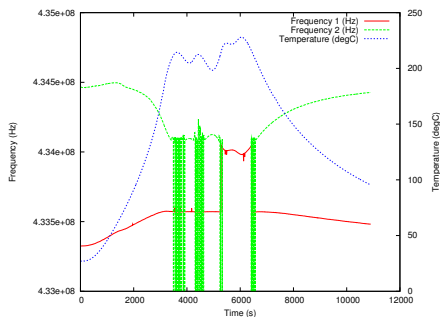


Figure 4. Behavior of resonator at intermediate temperatures, exhibiting the crossing of the higher frequency resonance (starting as the green curve) into the low-frequency band between dates 500 and 600, for temperatures above 180°C.

the resonance frequencies are overlapping over 180°C. With this algorithm, the first band begins at 433.05MHz and finishes at 433.89MHz, while the second band starts at 433.89MHz and stops at 434.83MHz. Each band is used to measure only one frequency. if two resonance frequencies arise in the same band, the measured signal is the one with the largest amplitude. On Fig. 4, the first frequency (green curve) is leaving the upper band to penetrates the second one (>434 MHz), the power received by the reader corresponding to this resonance is larger than for the other one (red curve).

The second experiment aims at using Quartz sensor at temperature up to 450°C without frequency band program of the reader (the contrary of the last experiment), providing the flexibility needed to measure SAW sensors out of their specifications.

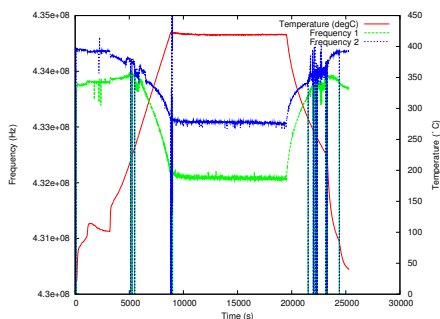


Figure 5. Behavior of resonator at intermediate temperature (around 450°C).

The sensor is based on differential measurements, but the two corresponding resonators do not exhibit the same behavior versus temperature. The 434 MHz frequency (blue between 0 and 5000s) is the reference mode exhibiting less frequency variation than the sensor mode (433 MHz) corresponding to the sensor mode. The turnover of the reference mode is situated in the temperature range from

room temperature to 200°C, then, the frequency is dramatically decreasing as shown from 5000s to 10000s. The turnover of the other mode is situated at higher temperature, therefore the frequency shift of this mode versus temperature is less important than for the reference mode. The higher frequency is crossing the other resonance between 5000s and 7500s, then both frequencies have changed their places in the frequency band when the oven stopped to heat up at 22500s. With this later algorithm, the reader is able to measure frequencies, which are separated from at least 200 kHz (depending of the averages number performed and the frequency band measured, considering 150 steps in a 4 MHz wideband, each “valid” measure separated by 7 steps). More experiments have been led on Quartz-based sensors to evaluate if a solution with this substrate can be an alternative to high temperature substrate at intermediate temperatures (room temperature to 500°C). As shown on Fig. 6, this resonator suffered 50h at 450°C without visible damages.

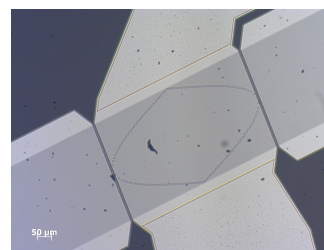


Figure 6. Picture of the IDT of TSEAS10 sensor used during 50 hours at 450°C while measured by wireless interrogator. IDT are polluted after the opening of the ceramic package using milling tools.

VI. AGING AND TEMPERATURE MEASUREMENTS WITH SAW SENSORS BASED ON LANGASITE

The first steps of the experiments are focusing on the evaluation of the efficiency of the wireless sensor at intermediate (Fig. 8), and then at high temperature (Fig. 13). Moreover, the frequency measurements of the devices will help understanding and evaluating the frequency variations of the resonators. The necessity of a “preaging” process for Langasite sensors then will be emphasized.

For the first experiment, the resonator was placed in a ceramic oven (able to warm up up to 1200°C, Fig7).

The resonator has been submitted at a temperature of 500°C during 50h. Meanwhile, its resonance frequency has been wirelessly monitored with a refreshing rate of about one measurement per second.

As expected, the temperature cycle applied to the resonator did operate as an aging process and the frequency of the resonator has evolved. As shown on Fig. 8, a difference of 300 kHz is observed at room temperature before and after the 50h-500°C cycle (at dates 50000s and 320000s). The frequency is shifting along time (during the 500°C heating process), showing a difference of 50 kHz between the dates



Figure 7. High temperature bench : ceramic oven with non-metallic back for RF wireless measurement associated with oscilloscope for debugging signal issue from reader unit, another temperature probe is used to measure temperature as close as possible of the device.

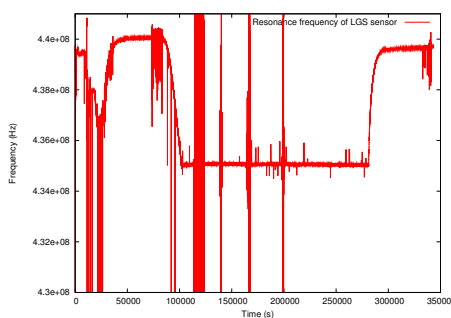


Figure 8. Wireless measurement of the sensor at 500°C during 50h. Between 0s and 50000s, the sensor is packaged (Fig3) and placed in the oven for a first preliminary cycle (100°C for 2h, 270°C for 2h and 360°C for 2h). Between 80000s and 280000s, the sensor withstands a temperature of 500°C.

100000s and 280000s. The observed variance at short term of the measured frequency is 10 kHz.

The resonator then is used at 700°C to push ahead the experiment (Fig. 9) and to continue to estimate the observed shift of the frequency.

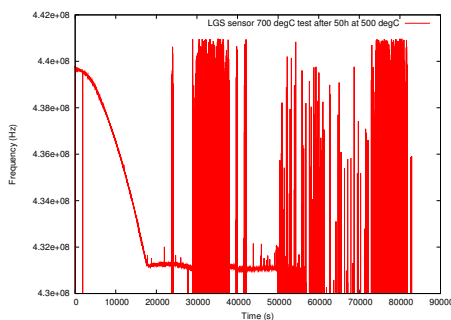


Figure 9. Wireless measurement of the sensor at 700°C. Between 0s and 18000s, the oven is warming up. The sensor is then operating at 700°C during 36000s (from 18000s to 54000s), then the sensor does not operate anymore.

After 10h of measurements, the interrogator does not

measure any response. In order to determine the origin of the failure, the package has been opened and it was identified a break of the wire-bonding induced by the deformation of the metallization used for the connection pad of the case. Concerning data acquired during these 10h of operation, the signal is too noisy to determine the frequency shift. As a conclusion, this resonator was able to operate during 50h at 500°C and then 10h more at 700°C. The noise measured during both experiments (Fig. 8 and Fig. 9) is related to the laboratory activities. Note that the resonator was still operating when probed with tips.

In parallel, another resonator was used for stabilizing a temperature controlled oscillator based on a Collpits-like structure. The device was placed in the oscillation loop once dicing process performed without any preaging. This resonator (Fig. 10) showed a Q factor of 5000 with a coupling factor of 0.04%. The temperature of the system was locked at 50°C. This test was performed to estimate aging effects of LGS resonators used at room temperature to corroborate the need for pre-aging process application in general.

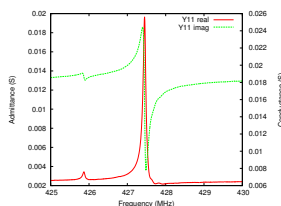


Figure 10. Reponse of the resonator used in the oscillator loop.

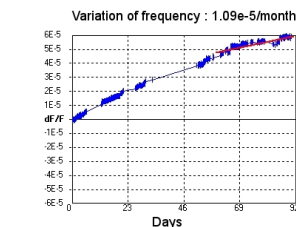


Figure 11. Variation of frequency of the oscillator over time (1.09×10^{-5} for LGS versus 10^{-7})

Regarding the frequency variation curve (Fig. 11) and the frequency variation at intermediate temperature (Fig. 8), the langasite based devices would need the development of a “preaging” process to reduce as much as possible the frequency shift of the sensor in harsh environments.

For the second experiment, a different resonator is used for life time tests, regarding the low (10-20 cm) range induced by its “low” coupling coefficient (0.19%, low compared to the other devices issued of the same wafer) and its low Q factor (<500), it is not possible to use this sensor for wireless measurement. The resonator is placed in the oven with another case up and down as hood, this package will protect the resonator against a direct contact with high temperature environment (as it will be in packaged device for wireless measurements).

The sensor is measured using tip-prober between each successive cycle to evaluate the impact of the temperature on the response of the device. The temperature cycle used in this experiment is composed of a 5h warming from room temperature to 700°C, and then keeping the temperature constant during 10h.

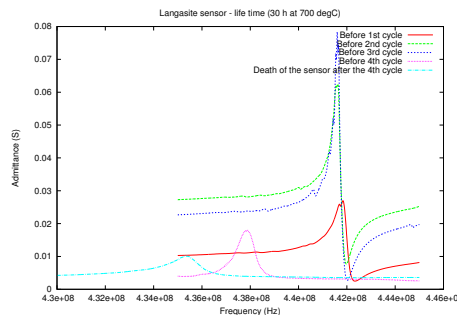


Figure 12. Life time test: temperature cycles are performed from room temperature to 700°C during 10h, showing a life time of 30 hours.

As shown on Fig. 12, the dynamics of the resonator admittance is changing along cycles. The coupling coefficient of the device remains constant despite successive cycle application. However, after 4 cycles, no more response is measured.

The third experiment aims at using langasite sensors in high temperature environment (>500 °C). The goal of this experiment is to observe the evolution of the resonance frequency at 700°C (Fig13) and to evaluate the effect of operating in harsh environment on the response of the device.

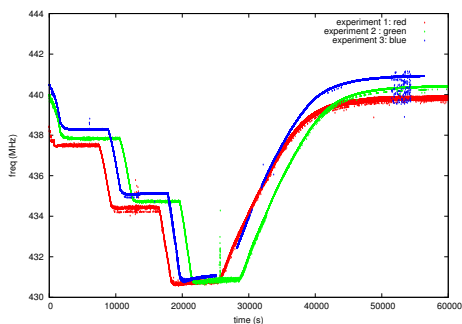


Figure 13. Behavior of a langasite sensor. The experiment cycle is divided in 3 steps, 300 °C, 500 °C and 700 °C for 2h at each temperature.

Considering the used resonator, the frequency band of the reader had to be adapted and a wide band interrogator was used (440 MHz ± 10 MHz instead of classical configuration 434 MHz ± 0.85 MHz). As expected, the frequency band needed to measure the behavior of the Langasite sensor was around 10 MHz (441 MHz at room temperature versus 430.5 MHz at 700°C). The frequency of the resonator decreases by 300 kHz after each step at 700°C, as shown in Fig. 13, the frequency is only shifting at “low” temperature (room, 300°C, 500°C), the evolution of the frequency at 700°C after each process is less significant (50 kHz). After this last experiment, the sensor was not able to operate anymore. The package has been opened to analyzed what happened to the device (Fig. 14 and Fig. 15). It appears that the fail

is coming from the destruction of the IDT induced by a too long exposure at high temperature [16], [17], [18].



Figure 14. State of langasite resonator : picture of the IDT.



Figure 15. State of langasite resonator : picture of the mirrors.

VII. CONCLUSION AND FUTURE WORK

In the frame of the SAWHOT project, SAW devices for wireless passive high temperature measurements have been developed. Two main operating range have been identified, from room temperature to 500°C and beyond 500°C. For both ranges of temperature, sensors have been developed, starting from basic design operation (using FEM/BEM and mixed-matrix-based tools) to characterization in oven using wireless measurements. Simulated results did match with devices behavior when measured via tip-probing. Quartz-based sensors were found suitable for intermediate temperature measurements (<500°C). This type of sensor shows that this range of temperature can be measured using Al-Cu electrode on SAW Quartz resonators, with numerous degree-of-freedom for optimizing specifications such as sensitivity, frequency range and the number of resonators (differential measurements or not). The algorithm for resonance frequency tracking prevents the overlapping of both measured resonators. For high temperature (>500°C), Langasite-based sensors were found to operate up to 700°C. The firsts experiments have been done using a wideband reader, according to the frequency/temperature range. The results show that the sensors can be actually measured at 700°C using SENSEOR’s interrogator with a 30 cm range interrogation distance (across the oven back). The resonance frequency of the sensor is evolving at high temperature, showing a decrease of 300 kHz of the frequency after each cycle at room temperature, 300°C, 500°C. At 700°C, the shift of frequency is reduced and is around 50 kHz. Moreover, the langasite device has been able to operate at this temperature for 30h, during this period, the dynamic admittance is increasing, while the coupling coefficient remains constant.

Further works are currently performed, focusing on the upgrading of the sensor parameters (Q factor, coupling coefficient), the life time of sensor at high temperature and the aging process for the devices.

ACKNOWLEDGMENT

This work was performed within the SAWHOT project [1], funded in the framework of the European Communitys Seventh Framework Program ([FP7/2007-2013]) under grant agreement n°[NMP4-SL-2009-247821].

The authors wish to thank the partners of the SAWHOT project for fruitful discussions and technical exchanges.

REFERENCES

- [1] "Sawhot project," <http://www.sawhot-project.com/>, 2009.
- [2] D. Ballantine, *Acoustic wave sensors: theory, design, and physico-chemical applications*. Academic Pr, 1997.
- [3] W. Buff, M. Binhack, S. Klett, M. Hamsch, R. Hoffmann, F. Krispel, and W. Wallnofer, "Saw resonators at high temperatures," in *Ultrasonics, 2003 IEEE Symposium on*, vol. 1. IEEE, 2003, pp. 187–191.
- [4] D. Damjanovic, "Materials for high temperature piezoelectric transducers," *Current Opinion in Solid State and Materials Science*, vol. 3, no. 5, pp. 469–473, 1998.
- [5] A. Pohl, F. Seifert, L. Reindl, G. Scholl, T. Ostertag, and W. Pietsch, "Radio signals for saw id tags and sensors in strong electromagnetic interference," in *Ultrasonics Symposium, 1994. Proceedings., 1994 IEEE*, vol. 1. IEEE, 1994, pp. 195–198.
- [6] L. Reindl, G. Scholl, T. Ostertag, C. Ruppel, W. Bulst, and F. Seifert, "Saw devices as wireless passive sensors," in *Ultrasonics Symposium, 1996. Proceedings., 1996 IEEE*, vol. 1. IEEE, 1996, pp. 363–367.
- [7] J.-M. Friedt, C. Droit, G. Martin, and S. Ballandras, "A wireless interrogation system exploiting narrowband acoustic resonator for remote physical quantity measurement," *Review of Scientific Instruments*, vol. 81, no. 1, p. 014701, 2010. [Online]. Available: <http://link.aip.org/link/?RSI/81/014701/1>
- [8] J. Garcia, T. Laroche, W. Daniau, E. Carry, G. Martin, S. Ballandras, and J. Friedt, "2-and-3d analysis of temperature effects on periodic transducers using a fea/bem approach," in *Frequency Control Symposium, 2009 Joint with the 22nd European Frequency and Time forum. IEEE International. IEEE, 2009*, pp. 424–429.
- [9] W. Daniau, M. Lenczner, T. Laroche, J. Garcia, E. Carry, and S. Ballandras, "On the convergence of 2d and 3d finite element/boundary element analysis for periodic acoustic waveguides," in *Frequency Control Symposium, 2009 Joint with the 22nd European Frequency and Time forum. IEEE International. IEEE, 2009*, pp. 430–434.
- [10] S. Ballandras, R. Lardat, M. Wilm, T. Pastureaud, A. Reinhardt, N. Champavert, W. Steichen, W. Daniau, V. Laude, R. Armati *et al.*, "A mixed finite element/boundary element approach to simulate complex guided elastic wave periodic transducers," *Journal of Applied Physics*, vol. 105, no. 1, pp. 014911–014911, 2009.
- [11] X. Bao, W. Burkhard, V. Varadan, and V. Varadan, "Saw temperature sensor and remote reading system," in *IEEE 1987 Ultrasonics Symposium*. IEEE, 1987, pp. 583–586.
- [12] E. Forsen, D. Nilsson, W. Daniau, B. Francois, and S. Ballandras, "Fabrication of saw resonators on quartz and langasite using nano-imprint lithography," in *Ultrasonics Symposium (IUS), 2010 IEEE*. IEEE, 2010, pp. 2091–2094.
- [13] J. Thiele and M. da Cunha, "High temperature surface acoustic wave devices: fabrication and characterisation," *Electronics Letters*, vol. 39, no. 10, pp. 818–819, 2003.
- [14] J. Hornsteiner, E. Born, G. Fischerauer, and E. Riha, "Surface acoustic wave sensors for high-temperature applications," in *Frequency Control Symposium, 1998. Proceedings of the 1998 IEEE International*. IEEE, 1998, pp. 615–620.
- [15] W. Bulst, G. Fischerauer, and L. Reindl, "State of the art in wireless sensing with surface acoustic waves," *Industrial Electronics, IEEE Transactions on*, vol. 48, no. 2, pp. 265–271, 2001.
- [16] S. Firebaugh, K. Jensen, and M. Schmidt, "Investigation of high-temperature degradation of platinum thin films with an in situ resistance measurement apparatus," *Microelectromechanical Systems, Journal of*, vol. 7, no. 1, pp. 128–135, 1998.
- [17] M. da Cunha, R. Lad, T. Moonlight, G. Bernhardt, and D. Frankel, "High temperature stability of langasite surface acoustic wave devices," in *Ultrasonics Symposium, 2008. IUS 2008. IEEE*. IEEE, 2008, pp. 205–208.
- [18] D. Richter, S. Sakharov, E. Forsén, E. Mayer, L. Reindl, and H. Fritze, "Thin film electrodes for high temperature surface acoustic wave devices," *Procedia Engineering*, vol. 25, pp. 168–171, 2011.

Modeling and Comparing the Linear Performance of Non-uniform Geometry Bend Sensors

Giancarlo Orengo, Antonino Lagati, Giovanni Saggio

Department of Electronics Engineering
Tor Vergata University
Rome – Italy

orengo@ing.uniroma2.it, antonino.lagati@istruzione.it, saggio@ing.uniroma2.it

Abstract— Resistive bend sensors have been increasingly used in different areas for their interesting property to change their resistance when bent. They can be employed in those systems where a joint rotation has to be measured, such as in biomedical systems to measure human joint static and dynamic postures. In spite of their interesting properties the commercial bend sensors have a resistance vs. bent angle characteristic which is not actually ideal as a linear function, to measure bend angles, would be. In this work, we have developed a way to calculate the sensor resistance for different bending angles with a generalized strip contour, in order to predict how shaping it with different non-uniform geometries changes the resistance dependence on bending angles, and investigate what kind of strip geometry can lead to a more linear behavior.

Keywords– bend sensor; gesture recognition.

I. INTRODUCTION

In order to measure human body kinematics, it is convenient to adopt sensors, which can measure bending angles with good precision despite a low cost.

Commercial bend sensors are usually made of a few micrometer thick resistive material deposited onto a thicker plastic insulating substrate. The resistive strip is screen printed with a special carbon ink, to be applied on virtually any custom shape and size film [1]. Normally, however, as well as the overall sensor, it has a rectangular geometry, with one side somewhat larger than the other. The ink's resistance value changes with bending due to an applied external force. The overall thickness is anyway negligible compared to the total largeness and lengthiness. All sensor materials, however, must be able to bend repeatedly without failure for the sensor to work. This kind of sensors are available on the market (Images SI Inc. [2], Flexpoint Sensor Systems Inc. [3]).

These devices can be adopted as sensors when placed on different kind of joints with the larger side bent according to the joints. They can be applied to body joint as electronic goniometers, to realize goniometric sock for rotation assessment of body segments in human posture recognition [4,5,6].

From a characterization point of view, the model which takes into account the mechanical aspect of the sensor predicts a linear behavior of the electric resistive variation with the bending angle [7]. Nevertheless the sensor resistance has increasing derivatives, especially for small angles, which result in non linear characteristics, as provided by the electrical characterization of the sensors.

The idea developed in this paper is to change the regular (rectangular) geometry of the sensor, cutting some part of it, in order to increase or decrease its resistance value, obtaining a linearization of its intrinsic non linear behavior. To this aim, the change of sensor resistance with bending angle has been modeled for a generalized resistive strip contour.

II. EXPERIMENTAL APPARATUS

The apparatus employed for this analysis was designed to emulate, in a controlled environment, the behavior of commercial bend sensors, when applied to body joints to track segment rotations. Figure 1 provides a photo of a sensor strip sample.



Fig. 1. Photograph of a resistor sensor sample (Flexpoint Sensor Systems Inc. South Draper UT, USA) in 1:1 scale.

Figure 2 shows a schematic of the experimental set-up. The sensor sample was laid as a cantilever beam on a metal hinge. In order to bend the sensor from 0 to +90 degrees, the sample side connected to the electrodes was locked in a stationary clamp, fixed to a rotating platform operated by a step motor. The other side of the sensor was put in a sliding clamp to avoid the sample stretching. For this kind of sensors the resistive material must be external with respect to the rotation. Bending angle step amplitude was changed reliably with one degree resolution from a Labview interface serial connected to a PC. The step motor is a PD-109-57 sample from Trinamic, connected to the PC through a RS-232 cable. The sensor resistance measurement against different bending angles was obtained connecting a digital multimeter to the Labview setup [8].

We measured the characteristic of several commercial bend sensors. In particular, we investigated the behavior of 2 inches long Flexpoint non encapsulated sensors, polyester encapsulated sensors and polyimide encapsulated sensors, when bent on a 8 mm hinge.

Measurements results, reported in Fig. 3, demonstrated the non linear mentioned characteristic. In particular the resistance variation is greater for non encapsulated sensors stands their higher flexibility, whereas the polyester one

exhibits better linearity. These imply that the resistive material must be non isotropic and must present non-uniform variation when bent.

The idea developed in this paper is to investigate how the change of a regular (rectangular) sensor geometry, cutting some part of it, increases its resistance value, obtaining a linearization of its intrinsic non linear behavior. In order to predict how shaping sensor resistive strip with different non-uniform geometries changes the resistance dependence on bending angles, this dependence has been calculated for a generalized resistive strip contour in the next section [9].

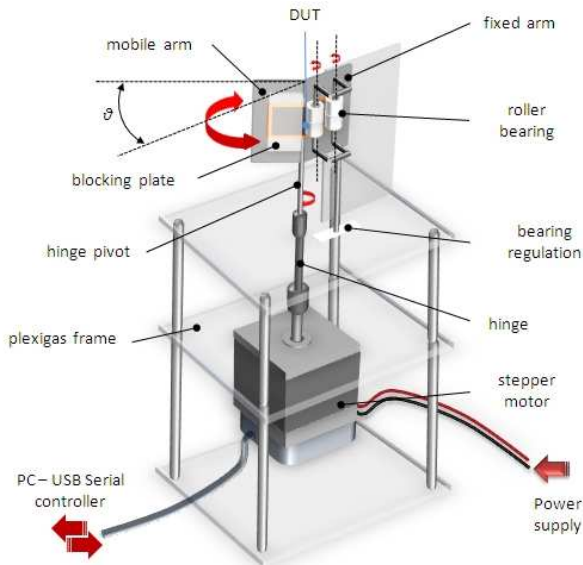


Fig. 2. Schematic of the experimental set-up.

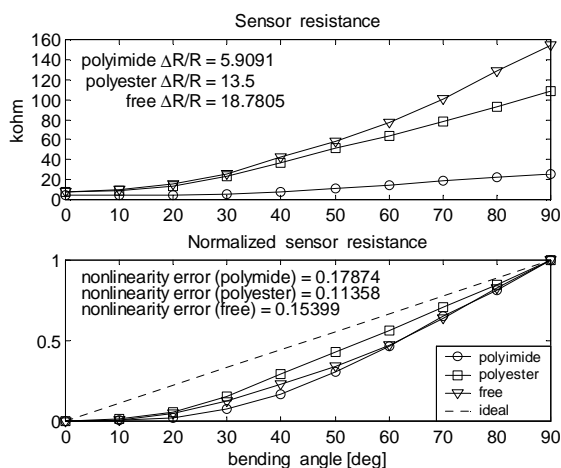


Fig. 3. Resistance variation vs bending angle for three different Flexpoint sensors

III. SENSOR RESISTANCE MODELING

For a flat rectangular sensor of size $L \times W$, where L is the length and W the width of the resistive strip, its

constant sheet resistance or resistance per square $R_{sheet}^{0^\circ}$ and its total resistance $R_S^{0^\circ}$ are linked by the equation

$$R_S^{0^\circ} = R_{sheet}^{0^\circ} \frac{L}{W} \quad (1)$$

If the resistive strip has not a rectangular contour, say not a constant width given by the function $w(x)$, the total resistance can be numerically calculated from the equation

$$R_S^{0^\circ} = R_{sheet}^{0^\circ} \sum_{i=1}^N \frac{\Delta x_i}{w(x_i)} \quad (2)$$

where the strip length have been divided into N uniform or non-uniform segments of length Δx_i for numerical integration.

As previously affirmed, when the polyester or polyimide substrate is bent, the material of its resistive strip is stretched, and the sheet resistance increases around the bending rotation axis. Although it is rather difficult to physically model this phenomenon, an abstract model can be still attempted with a general Gaussian function centered on the rotation axis, supposed at a known distance L_R from the strip longitudinal edge at $x=0$. Assuming then

$$G(x) = \frac{I}{\sqrt{2\pi\sigma^2}} e^{-\frac{x^2}{2\sigma^2}} \quad (3)$$

the sheet resistance results from

$$R_{sheet}(x, \phi) = R_{sheet}^{0^\circ} + K(\phi) G(x - L_R) \quad (4)$$

where the unknown parameters are the calibration factor $K(\phi)$, scaling the sheet resistance with the bending angle, and the variance σ which determines the longitudinal extension of the region around the bending axis where resistivity increases. To this parameter, it has been arbitrarily assigned a starting value $\sigma = d/2$, where d is the hinge diameter. However, by comparison of model simulation and experimental measurements this value can be adjusted, although a constant value seems to fit better than one changing with the bending angle.

As a consequence, the resistance variation of a rectangular sensor with the bending angle can be calculated as

$$\begin{aligned} R_S(\phi) &= \frac{I}{W} \sum_{i=1}^N R_{sheet}(x_i, \phi) \Delta x_i = \\ &= R_S^{0^\circ} + \frac{K(\phi)}{W} \sum_{i=1}^N G(x_i - L_R) \Delta x_i \end{aligned} \quad (5)$$

from which results

$$R_S(\phi) = R_S^{0^\circ} + \frac{K(\phi)}{W} \quad (6)$$

standing that, if the Gaussian function is almost comprised inside the strip length, results

$$\sum_{i=1}^N G(x_i - L_R) \Delta x_i \approx I \quad (7)$$

Equation (6) allows to determine the calibration factor $K(\phi)$ from measurements of the sensor resistance variation with bending angle for a rectangular sensor.

$$K(\phi) = W [R_{S_meas}(\phi) - R_S^{0^\circ}] \quad (8)$$

It is worth to note that the calibration factor, even if calculated for a rectangular strip, is independent from the strip geometry. Then, the response of a non-uniform geometry can be calculated from the equations

$$R_S(\phi) = \sum_{i=1}^N \frac{R_{sheet}(x_i, \phi)}{w(x_i)} \Delta x_i \quad (9)$$

$$\begin{aligned} R_S(\phi) &= R_{sheet}^{0^\circ} + K(\phi) \sum_{i=1}^N G(x_i - L_R) \frac{\Delta x_i}{w(x_i)} = \\ &= R_S^{0^\circ} + K(\phi) \cdot H_{geom} \end{aligned} \quad (10)$$

where H_{geom} is a constant factor dependent on sensor geometry, but independent from the bending angle. As a consequence, since $K(\phi)$ is linearly dependent from $R_{S_rect}(\phi)$ as result from (8), even with non-uniform geometry the normalized sensor resistance is the same of that of a rectangular one given by (5). In other words, no linearity enhancement can be yield from non-uniform geometry in this case.

So far, it has not been taken into account that, when the sensor is bent, the sample side not connected to the electrodes slides in a clamp of an amount equal to the arc of the hinge (diameter d) corresponding to the rotation angle, and the rotation axis moves away from the locked edge ($x=0$) of half this quantity, namely

$$s(\phi) = \frac{1}{2} \frac{\phi}{180^\circ} \frac{\pi d}{2} \quad (11)$$

from which the sheet resistance results

$$R_{sheet}(x, \phi) = R_{sheet}^{0^\circ} + K(\phi) \cdot G[x - L_R - s(\phi)] \quad (12)$$

To keep the rotation axis in the central region of the strip, a good practice would be to set

$$L_R = 0.5(L - s_{max}) \quad (13)$$

Calculating the total sensor resistance

$$R_S(\phi) = R_S^{0^\circ} + K(\phi) \sum_{i=1}^N G[x_i - L_R - s(\phi)] \frac{\Delta x_i}{w(x_i)} \quad (14)$$

it can be also expressed as

$$R_S(\phi) = R_S^{0^\circ} + K(\phi) \cdot H_{geom}(\phi) \quad (15)$$

where this time the geometric factor H_{geom} is dependent on the bending angle. In this case, the normalized sensor resistance has a different behavior between uniform and non-uniform geometry. This fact will be exploited in the next section to investigate if particular geometries can lead to a linearization of its intrinsic non linear behavior.

IV. SENSOR PERFORMANCE SIMULATION

The question which now arises, of course, is whether it would be possible to optimize the resistive strip geometry to yield a linear behavior with bending angle. However it is to note that the highest non linearity is observed for small angles, where the sheet resistance has a little increase. As a consequence, the modulation of the sensor width has a little influence on its performance for small angles. Nevertheless, a contour optimization has been attempted investigating different simple geometries, in particular trials have been performed on rectangular, triangular and circular contours, where dimensions have

been randomly optimized, on the basis of the rms error between the normalized sensor performance and an ideal linear one (nonlinearity error). This approach has been attempted on the 2 inch polyester sensor from Flexpoint, where the strip size has been set to 36×5.6 mm, with a double width respect to the standard one, to allow safe shrinking of the sensor width do not compromise the sensor capability to bend repeatedly without failure.

Being the squared contour a particular case of the triangular one, results have been presented only for the last one. Random iterations have been tried sweeping three geometry parameters in the following ranges: $W/2 < W_1 < W, 0 < L_1 < L, 0 < L_2 < L - L_1$. Fig. 4 plots the results either for sensor resistance and its normalized value, showing difference performance in dynamic ($\Delta R/R$) and linearity (nonlinearity error), either for the rectangular contour and the triangular cut.

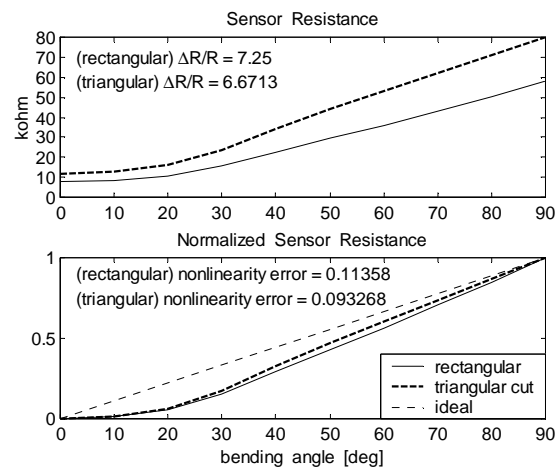


Fig. 4. Resistance and its normalized value variation vs bending angle comparison between rectangular and randomly optimized triangular contours for the most linear sensor resistance.

The result of random optimization of strip contour dimension is reported in Fig. 5, where calibrated sheet resistance Gaussian functions and their shift with bending angle has been superimposed. It can be noted that optimization suggests an almost square and deepest allowed cut as the best performing geometry.

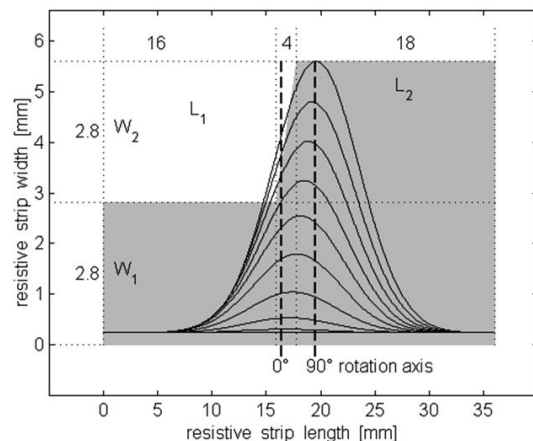


Fig. 5. Randomly optimized resistive strip triangular contour for the most linear sensor resistance.

Finally, the same random optimization can be also tried to enhance the linearity of a resistive divider, shown in Fig. 6, where the sensor is inserted in many applications, when it is the voltage across the sensor rather than its resistance that has to be processed.

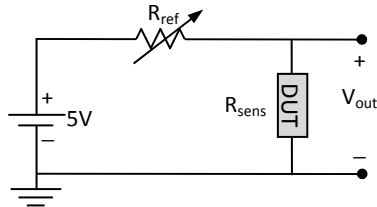


Fig. 6. Resistive divider to read the sensor voltage.

Results have been plotted in Figs. 7 and 8, where the same optimization has been applied this time to a circular contour. Moreover, at each iteration corresponding to a particular contour, the reference resistance R_{ref} has been swept inside the sensor resistance dynamic to yield the most linear behavior. Although not all results have been included in this paper for sake of brevity, it has been demonstrated that a square cut in sensor contour lets to achieve the best linearity performance, especially with a larger sensor width and deeper cuts, either for sensor resistance and voltage.

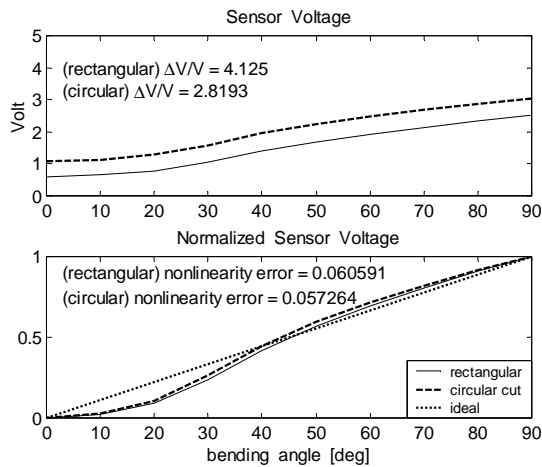


Fig. 7. Resistance and its normalized value variation vs bending angle comparison between rectangular and randomly optimized circular contours for the most linear sensor voltage.

V. CONCLUSION

The linearization of the bend sensor’s characteristic leads to undeniable advantages in joint rotation assessment. In this work a method to calculate resistance variation with bending angle for any resistive strip geometry has been proposed, and different contour geometry have been compared from the linearity point of view. Results have demonstrated, from one hand, that the best results can be obtained with a square cut, from the other hand, that the larger is the sensor width and deeper the cut in resistive strip contour, the more relevant is the

enhancement in linearity performance, either for sensor resistance and voltage across it when inserted in a resistive divider.

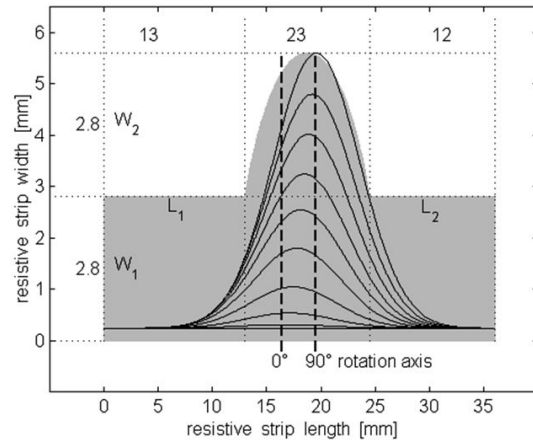


Fig. 8. Randomly optimized resistive strip circular contour for the most linear sensor voltage.

REFERENCES

- [1] G. Latessa, F. Brunetti, A. Reale, G. Saggio, and A. Di Carlo, “Electrochemical synthesis and characterization of flexible PEDOT:PSS based sensors”, *Sensors & Actuators: B. Chemical*, Elsevier, vol. B139, issue 2, pp. 304-309, June 2009.
- [2] Images SI Inc., Staten Island NY, USA.
- [3] Flexpoint Sensor Systems Inc., South Draper UT, USA.
- [4] R. Gentner and J. Classen, “Development and evaluation of a low-cost sensor glove for assessment of human finger movements in neurophysiological settings” *Journal of Neuroscience Methods* 178 (2009) 138–147.
- [5] L. Dipietro, A. M. Sabatini, and P. Dario, “A survey of glove-based systems and their applications” *IEEE Transactions on Systems, Man, And Cybernetics—Part C: Applications and Reviews*, Vol. 38, No. 4, July 2008.
- [6] LK. Simone, N. Sundarajan, X. Luo, Y. Jia, and D. G. Kamper, “A low cost instrumented glove for extended monitoring and functional hand assessment” *J Neurosci Methods* 2007;160:335–348.
- [7] G. Saggio, P. Bisegna, G. Latessa, and S. Bocchetti, “Mechanical modeling of bend sensors exploited to measure human joint movements” *1st IEEE International WoWMoM Workshop on Interdisciplinary Research on E-Health Services and Systems, IREHSS 2009, Kos (Greece) 2009.*
- [8] G. Saggio, M. De Sanctis, E. Cianca, G. Latessa, F. De Santis, and F. Giannini, “Long term measurement of human movements for health care and rehabilitation purposes”, *Proc. of Wireless VITAE’09 conf., Aalborg (DK), 2009.*
- [9] G. Saggio, S. Bocchetti, C. A. Pinto, G. Latessa, and G. Orenco, “Non uniform geometry bend sensors exploited for biomedical systems”, *International Conference on Bio-inspired Systems and Signal Processing, (BIOSTEC-Biosignals)*, pp. 389-392, Rome, January 2011.

Heat Balanced Bolometer with Sigma-Delta Interface

Matthieu Denoual,
 Mathieu Pouliquen,
 Gilles Allègre
 GREYC-ENSICAEN
 University of Caen
 Caen, France
 initialname@ensicaen.fr

Damien Brouard,
 Arthur Veith
 ENSICAEN, Caen, France
 name@ecole.ensicaen.fr

Olivier de Sagazan
 IETR
 University of Rennes
 Rennes, France
 name@univ-rennes1.fr

Patrick Attia
 NXP-Semiconductors
 Colombelles, France
 name@nxp.com

Abstract—This paper presents a single-loop 2nd order sigma-delta interface circuit for a bolometer operating in closed-loop mode. Switched capacitor circuitry is developed to implement the sigma-delta structure. The sigma-delta modulator acts both as digital readout circuit and as a mean of heat feedback. The design approach of the sigma-delta structure and the feedback shaping is explained. The circuit is designed for a realization in AMS CMOS 0.35µm technology.

Keywords-bolometer; sigma-delta modulator; electrical substitution; frequency sensor.

I. INTRODUCTION

Uncooled resistive bolometers are part of the thermal infrared detector’s category. In 2010, uncooled resistive bolometers represented 95% of the market of infrared imaging system [1]. Their operating principle is based on the measurement of temperature variations due to the incident optical power. In parallel to research work trying to improve the sensitivity of the bolometers through material or geometry optimization, other research work has focused on the development of feedback techniques to operate the bolometers in closed-loop mode as constant temperature bolometric detectors [2, 3]. All the proposed techniques are based on the Electrical Substitution principle that assumes that optical power can be substituted by electrically produced power. For integration and simplicity reasons, heat feedback is produced by Joule effect, considering that heat electrically produced can be used to equivalently stimulate the sensing resistor of the bolometer. This assumption is the basis of the Electrical Substitution (ES) principle also called Electric Equivalence principle [3, 4]. The advantages of closed-loop operation are numerous, including improvement of bandwidth and reduction of spatial noise. In 2009, a new configuration has been proposed for the closed-loop operation of resistive bolometers [5]. The so-called Capacitively Coupled Electrical Substitution (CCES) configuration exhibits the advantages of previous configurations without their limitations in terms of additional material required or stability issues. Proofs of principle of the CCES configuration have been demonstrated through successive analogous and digital implementations with discrete components [5, 6]. Digital implementation, besides the implicit digital measurement output, exhibit extra performance compared to analogous implementation because of linearization of the system [4, 5]. Recently, smart-

functions using a digital implementation of the CCES configuration with a microcontroller have been experimentally demonstrated [7].

In this work, we aim at integrating the electronic circuitry of the CCES configuration for closed-loop operation of resistive bolometers and for smart-functions implementation. With a view toward integration of lines or matrixes of pixels, digital solution using a sigma-delta core is preferred to solution using a microcontroller. Consequently, for the first time to our knowledge, an integrated sigma-delta interface for a bolometer is developed. The sigma-delta modulation is attractive because it provides a digital output, linearizes the heat feedback path and can be easily implemented in high-density CMOS technology. Such device will inherit the advantages and performance of the previous discrete realizations and will be the first step toward fully integrated smart infrared imagers.

The paper is organized as follows. The second section describes the principle of the digital closed-loop operation of resistive bolometers. The third section presents the design of the sigma-delta interface associated with the bolometer. Finally, the result section exhibits simulation results that illustrate the expected behavior and performance.

II. DESCRIPTION OF THE SYSTEM

The system is a heat balanced bolometer using heat feedback through electrical substitution means. It is composed of a resistive bolometer, its readout electronics, and a sigma-delta modulator with a feedback shaping block for the implementation of the CCES configuration.

A. Uncooled resistive bolometers

Resistive bolometers are composed of a sensing resistor on a surface thermally insulated from the substrate by suspension legs, as illustrated in Fig. 1.

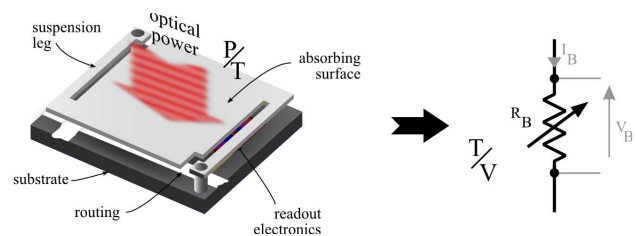


Figure 1. Top view of a bolometer pixel and equivalent electrical model

The operating principle is the following: the optical infrared (IR) power absorbed onto the surface of the bolometer rises the temperature of the sensing resistor (P/T conversion). If the sensing resistor (R_B) is current biased (I_B), then the voltage across the resistor (V_B) measures the temperature variations (T/V conversion). The material of the sensing resistor is chosen for its high Temperature Coefficient of Resistance (TCR).

The responsivity of a bolometer characterizes the variations of the output voltage signal (V_B) depending on the infrared input optical power (P_{opt}) [8]. It is expressed by

$$R(s)[V/W] = \frac{V_B(s)}{P_{opt}(s)} = \frac{\alpha \eta I_B R_B}{G_{eff} (1 + s\tau_{eff})} \quad (1)$$

where α is the TCR of the sensing resistor, η is the absorption coefficient of the absorbing surface, G_{eff} and τ_{eff} are the effective thermal conductance and the effective thermal constant respectively [8]. τ_{eff} depends on the heat capacity C_{th} of the bolometer as follows: $\tau_{eff} = C_{th}/G_{eff}$. The equation (1) indicates that the more the bolometer is thermally insulated, *i.e.* G_{eff} small, the higher the responsivity is. However, the more the bolometer is thermally insulated, the higher the time constant is, *i.e.* the slower the bolometer is. This is the traditional tradeoff between responsivity and time constant of resistive bolometers. Usually, the thermal conductance is designed to match the time constants required for imaging applications and therefore the responsivity is not optimized. Such tradeoff can be released by operation in closed-loop mode.

B. Closed loop operation of uncooled resistive bolometers

Like for every sensor and generally speaking system, closed-loop configuration has advantages over open-loop configuration, including reduced time response and linearization. Closed-loop operation of resistive bolometers enables other interesting characteristics such as operation around a user defined operating point and simple selection of the measurement range. In the case of matrixes of bolometer pixels, since the output response in closed-loop is quite independent from the nominal resistance value of the sensing resistor, the spatial noise due to process discrepancies is intrinsically cancelled.

Closed-loop operation requires heat feedback since the incoming signal is power. Fig. 2 illustrates the closed-loop configuration of a resistive bolometer. The system is controlled in temperature to a dynamic set point defined by a bias voltage V_{Bias} . G is the gain of the conditioning electronics and V_T the amplified voltage. The absorbed incoming optical power, ηP_{opt} , is considered as a perturbation compensated by the Joule power P_J . The closed-loop system maintains the temperature of the bolometer constant by keeping the total amount of power constant. The total power corresponds to the Joule power initially applied prior to exposure to optical power to elevate the temperature

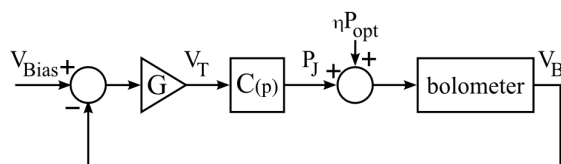


Figure 2. Schematic of electrical substitution feedback loop

of the bolometer. This initial power sets the static thermal working point. A controller $C(p)$ is inserted in the loop to adjust the performance of the closed-loop system (bandwidth, robustness, noise rejection, ...). As usually $R(s).G$ is large, a simple controller $C(p)=1$ can be used in a first try.

Bolometers operating in closed-loop mode have been developed either with analog or digital feedback implementations. Digital implementation is interesting in that the feedback path is linearized in a simple way if pulsed modulated signals are used [4, 5] and in that the output signal is directly digital. The digital pulsed signals can be modulated in width (PWM, pulsed width modulation) or in density (sigma-delta modulation). The major drawback of previously proposed digital implementation [6] is the need for a microcontroller with an ADC for the digital feedback path. We propose here to use a sigma-delta modulator both for the digital conversion and the feedback signal generation. This approach is somehow comparable to that of micro-accelerometers operating in closed-loop mode with sigma-delta modulators. In the case of lines or matrixes of bolometer pixels, this approach should lead to a solution better suited for integration.

The schematic of the sigma-delta feedback loop for the bolometer is illustrated in Fig. 3, with a controller $C(p)=1$.

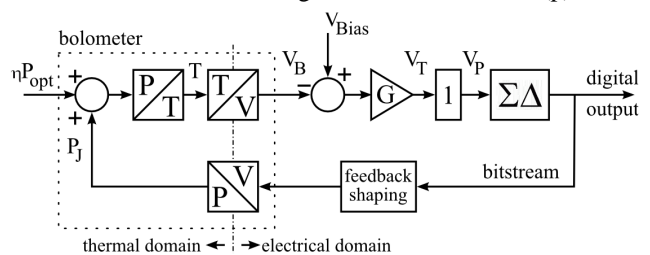


Figure 3. Schematic of sigma-delta feedback loop for the bolometer

The output bitstream corresponding to the measurement at the output of the sigma-delta modulator would have to be treated by digital filters and decimators to get the output signal with the format resolution allowed by the oversampling rate.

The feedback shaping is here to implement the capacitively coupled electrical substitution (CCES) that enables easy setting of the system. In the case of the CCES implementation, the pulsed modulated signal is shifted to high frequencies by modulation with a carrier and then capacitively coupled onto the sensing resistor of the bolometer. The objective is to dissociate the electrical and thermal working points according to a frequency basis. It uses a high frequency modulated signal for the heat feedback voltage applied to the sensing resistor. This implementation can be applied to any kind of uncooled resistive bolometer.

The sigma-delta interface for heat balanced bolometer using CCES configuration requires two main functional blocks:

- (1) a sigma-delta modulator,
- (2) a feedback shaping block.

III. DESIGN OF THE CIRCUIT

The design is for AMS 0.35 μm CMOS technology.

A. Sigma-Delta ($\Sigma\Delta$) modulator

For stability, linearity and resolution reasons, a single-loop, single-bit, 2nd order sigma delta architecture was chosen for the sigma-delta modulator [9]. The resulting architecture is illustrated in Fig. 4. It is composed of two integrators with gain a and b respectively -0.5 and -2.0, of a comparator and of a 1-bit digital-to-analog converter. Compared to classical architectures, here an extra input on the first integrator is used to add a component to the signal. The role of this input is to set the static thermal working point, *i.e.* the Joule power applied in absence of optical signal. The oversampling ratio (OSR) is 256 to ensure at least the 98 dB signal-to-noise ratio required for a 16-bit resolution according to [9]

$$\text{SNR}_{\text{dB}} = 10 \log \left[\frac{3\pi}{2} (2^B - 1)^2 (2n + 1) \left(\frac{\text{OSR}}{\pi} \right)^{2n+1} \right] \quad (2)$$

where B is the number of bits of the quantizer, n is the order of the modulator.

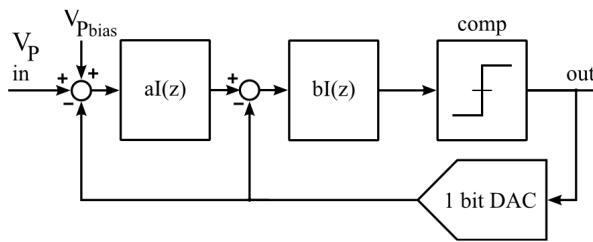


Figure 4. Block diagram of the 2nd order single loop 1-bit $\Sigma\Delta$ modulator

For integration reasons, switched capacitor circuitry was chosen leading to the classical fully-differential structure illustrated in Fig. 5. The sigma-delta modulator is clocked at 5 MHz for an input bandwidth of 10 kHz. Non-overlapping two-phase clock signals with delayed outputs are used and double sampling correlation is implemented to reduce the flicker noise contribution of the OTA [10]. The capacitors are 500fF minimum to ensure a kT/C noise small enough compared to the quantization noise.

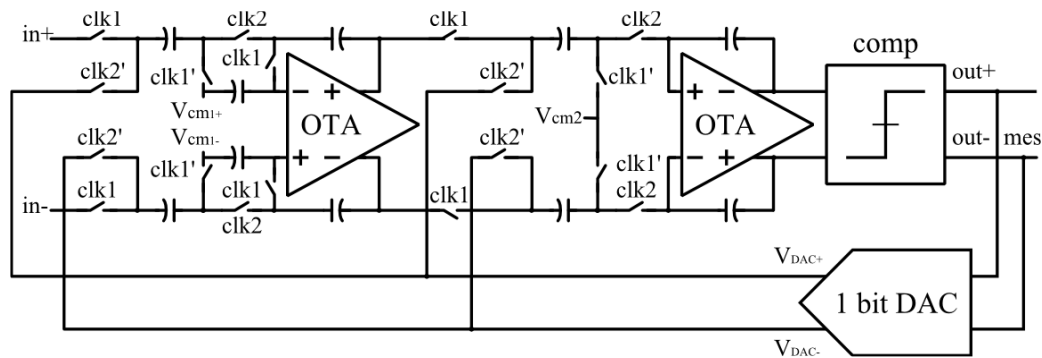


Figure 5. Schematic of the 2nd order sigma-delta modulator

The integrators are built around folded-cascode OTA with gain above 60 dB to ensure the chosen resolution [11]. Folded-cascode OTA with switched-capacitor common mode feedback circuitry was chosen for stability reasons and for its high gain-bandwidth product, here over 100 MHz.

The common mode voltages of the first integrator, $V_{\text{cm}1+}$ and $V_{\text{cm}1-}$, are used to set the static thermal working point; they correspond to the V_{Pbias} signal of Fig. 4. These inputs can also be used as built-in stimuli useful for self-test, self-calibration or self-identification as illustrated in [12], *i.e.* useful to upgrade the bolometer into a smart-bolometer. The common mode voltage of the second integrator, $V_{\text{cm}2}$, is unique and is set at half the supply voltage.

B. Feedback shaping block

The role of the feedback shaping block is to translate to high frequency the pulse-density modulated bitstream of the sigma-delta modulator output. The feedback shaping block involves a Voltage Controlled Oscillator (VCO), a mixer and a programmable attenuator as illustrated in Fig. 6.

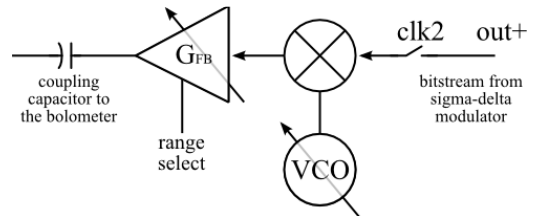


Figure 6. Feedback shaping

The VCO is a chain of inverters forming a ring topology whose frequency can be tuned between 70 MHz and 800 MHz. The mixer consists in a transmission gate controlled by the pulse-density modulated bitstream signal from the sigma-delta modulator. The programmable attenuator is a ladder of cascaded transmission gates with different ON resistances. The selected gain, G_{FB} , defines the measurement range of the closed-loop system. An 8-bit selection word allows changing the measurement range over more than two orders of magnitude. The feedback is only applied during the integration phase (clk2) not to disturb the sampling phase.

IV. SIMULATION RESULTS, EXPECTED PERFORMANCE

Simulations performed to verify that the design fulfills the requirements are time consuming, therefore, once the performance validated, the blocks are modeled to carry out top-level simulations. The top-level simulations of the complete system are performed using Simulink®.

C. Sigma-Delta simulation

The electrical simulation results confirm the expected performances of the 2nd order sigma-delta modulator. The density of the pulses of the bitstream varies linearly according to the input signal (Fig. 7).

Since the voltage to power conversion (V/P) is linear with this type of modulation, the feedback path is entirely linear.

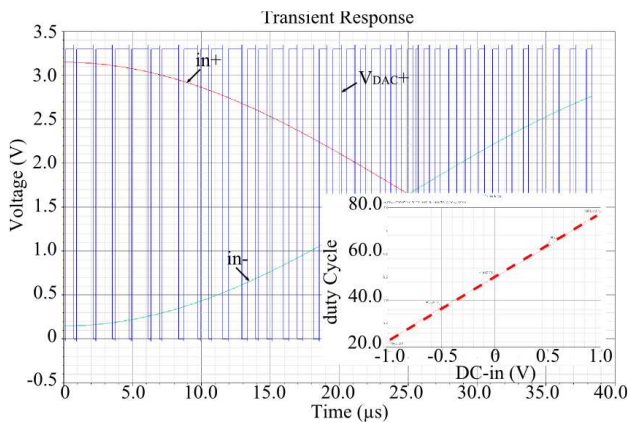


Figure 7. Transient simulation of the sigma-delta modulator. Inset, duty cycle versus DC input from transient simulations

D. Complete system

The top-level simulations illustrate the expected behavior of the system and its expected noise performance. The models developed in [13] are used for the integrators of the sigma-delta modulator and for the noise considerations. Typical characteristics taken from [14] are used for the bolometer (7 ms time constant and 5×10^{-8} W/K thermal conductance). Fig. 8(a) illustrates the step response of both the bolometer in open-loop (output V_T) and in closed-loop mode when the bolometer is heat-balanced with the sigma-delta interface directly looped (output corresponding to the bitstream after filtering). The input step is $1 \mu\text{W}$. The closed-loop operation is interesting in that the output is directly proportional to the incoming power and the time response is much faster, *i.e.* response time (5% final value) below 1 ms.

Fig. 8(b) illustrates the expected performances in terms of noise taking into account the noise sources of sigma-delta interface (quantization noise, kT/C noise, clock jitter noise, and OTA noise). The noise floor is 100 dB below the $50 \mu\text{W}$ reference signal, this means that the sigma-delta interface does not negatively impact the noise performance of the system, *i.e.* the noise performance will still be limited by the noise of the bolometer.

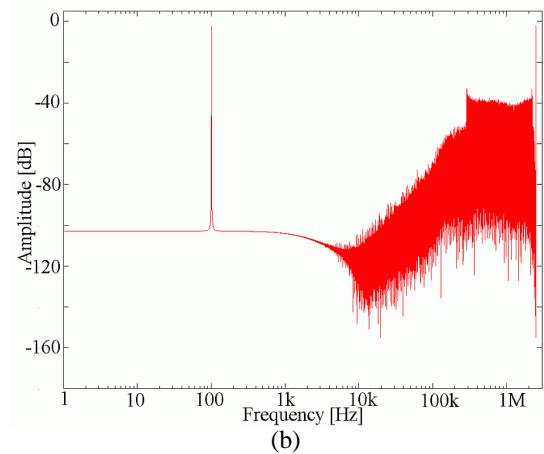
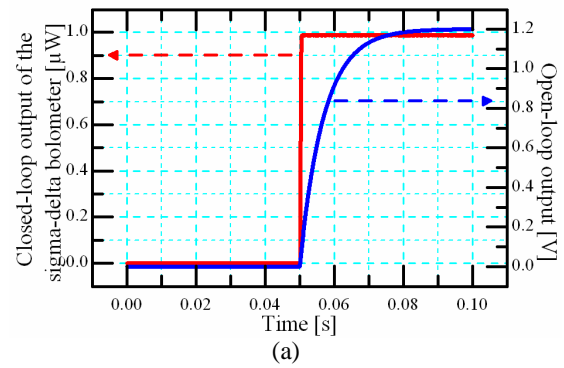


Figure 8. (a) Step response of the bolometer in open-loop and in closed-loop when heat balanced with the sigma-delta interface. (b) Expected noise performance of the sigma-delta interface, with a $50 \mu\text{W}$ input reference signal at 100 Hz

IV. CONCLUSION AND FUTURE WORK

In this paper, the design of a sigma-delta interface for a heat balanced bolometer is presented. This interface enables an integrated implementation of the capacitively coupled electrical substitution configuration for uncooled resistive bolometers. By enclosing the bolometer in a one-bit feedback loop, simultaneous heat feedback and analog-to-digital conversion is achieved. The feedback path enables built-in stimulus to be applied and the resulting device is a pulsed digital output infrared detector part of so-called frequency sensors, with configuration capabilities upgrading it into a smart bolometer. Future work will involve the characterization and test of the realized prototypes and next development will focus on the integration of lines and matrixes of pixels.

ACKNOWLEDGMENT

The planned foundry of the integrated circuit in July 2012 is funded by the PSOC-INS2I program (n°78518). The author would like to thank Aziz Doukkali, Jean-Robert Tourret and Philippe Vallerand for fruitful help during the design.

REFERENCES

- [1] Yole Développement, Uncooled IR Cameras & Detectors for Thermography and Vision, Tech. & Market Report, 2010.
- [2] C. D. H. Williams, An appraisal of the noise performance of constant temperature bolometric detector systems, *Meas. Sci. Technol.*, 1990, vol. 1(322), pp. 322-328.
- [3] M. Galeazzi, An external electronic feedback system applied to a cryogenic micro-calorimeter, *Rev. Sci. Instr.*, 1998, vol. 69(5), pp. 2017-2023.
- [4] R. C. S. Freire, S. Y. C. Catunda, and B. A. Luciano, Applications of Thermoresistive Sensors Using the Electric Equivalence Principle, *IEEE Trans. Instr. Meas.*, 2009, vol. 58(6), pp. 1823-1830.
- [5] M. Denoual, G. Allègre, S. Delaunay, and D. Robbes, Capacitively coupled electrical substitution for resistive bolometer enhancement, *Meas. Sci. Technol.*, 2009, vol. 20, doi: 015105.
- [6] M. Denoual, S. Lebargy, and G. Allègre, Digital implementation of the capacitively coupled electrical substitution for resistive bolometers, *Meas. Sci. Technol.*, 2010, vol. 21, doi: 015205.
- [7] M. Denoual, O. de Sagazan, P. Attia, and G. Allègre, Smart Bolometer: Toward Monolithic Bolometer with Smart Functions in Bolometers, *INTECH publisher, A. G. Unil Perera Editor*, 2012, ISBN: 978-953-51-0235-9, pp. 171-196.
- [8] Kruse, P.W. (2001). Uncooled Thermal Imaging: Arrays, Systems and Applications, SPIE Optical Engineering Press, Bellingham, WA, ISBN: 0-8194-4122-8.
- [9] L. Yao, M. Steyaert, and W. Sansen, Low-Power Low-Voltage Sigma-Delta Modulators in Nanometer CMOS, *The Springer International Series in Eng. and Comp. Sc.*, 2006, Vol. 868, ISBN 978-1-4020-4139-6.
- [10] C. Enz and G. Temes, Circuit techniques for reducing the effects of op-amp imperfections: autozeroing, correlated double sampling, and chopper stabilization, *Proc of IEEE*, 1996, vol.84(11), pp. 1584-1614.
- [11] K. Onodera and A. Abo, A second-order sigma-delta A/D converter, EE290Y project June 1995, citeseerx.ist.psu.edu/viewdoc/summary?doi=10.1.1.115.3182 [retrived: July, 2012].
- [12] M. Denoual and P. Attia, Top-Level Simulation of a Smart-Bolometer Using VHDL Modeling», *Sens. & Trans.*, 2012, vol. 14-1, pp. 48-64.
- [13] P. Malcovati, S. Brigati, F. Francesconi, F. Maloberti, P. Cusinato, and A. Baschiroto, Behavioral modeling of switched-capacitor sigma-delta modulators, *IEEE Trans. Circuits and Systems-I*, 2003, Vol. 50, N° 3, pp. 352-364.
- [14] B. Fièque, J.L. Tissot, C. Trouilleau, A. Crastes, and O. Legras, Uncooled microbolometer detector : Recent developments at Ulis, *Infrared Physics & Technology*, 2007, vol. 49, pp. 187-191.

Optical Characterisation of $\text{La}_{0.7}\text{Sr}_{0.3}\text{MnO}_3$ Thin Film Based Uncooled Bolometers

Ammar Aryan^{1,2,3,*}, Jean-Marc Routoure^{1,2,3,+}, Bruno Guillet^{1,2,3,+}, Pierre Langlois^{1,2,3,+}, Cédric Fur^{1,2,3,+}, Julien Gasnier^{1,2,3,+}, Carolina Adamo^{4,#}, Darrell G. Schlom^{4,5,##} and Laurence Méchin^{1,2,3,+}

¹ Université de Caen Basse-Normandie, UMR 6072 GREYC, F-14032 Caen, France

² ENSICAEN, UMR 6072 GREYC, F-14050 Caen, France

³ CNRS, UMR 6072 GREYC, F-14032 Caen, France

⁴ Department of Materials Science and Engineering, Cornell University, Ithaca, New York 14853-1501, USA

⁵ Kavli Institute at Cornell for Nanoscale Science, Ithaca, New York 14853, USA

⁺ Email addresses: first-name.name@unicaen.fr

[#] Email address: ca259@cornell.edu

^{##} Email address: schlom@cornell.edu

* Corresponding author: ammar.aryan@unicaen.fr

Abstract— This paper reports the potentialities of the manganese oxide $\text{La}_{0.7}\text{Sr}_{0.3}\text{MnO}_3$ (LSMO) for the realization of uncooled thermal detectors. Close to room temperature, LSMO exhibits a metal-to-insulator transition, where a large change of electrical resistance versus temperature occurs. The tested sample is a 100 nm thick epitaxial LSMO thin film deposited on a SrTiO_3 buffered Si substrate. The optical responsivity and electrical noise were measured in a frequency range of 1 Hz-100 kHz, thus enabling the estimation of specific detectivity. It is shown that due to the very low $1/f$ noise level, in this epitaxial film deposited on silicon wafer, LSMO thermal detectors can exhibit competitive performances at room temperature.

Keywords- Bolometer; manganite; thermal detector.

I. INTRODUCTION

Uncooled infrared (IR) detectors have been studied in recent years due to a variety of applications such as thermal cameras, night vision cameras, thermal sensors, surveillance, etc. The IR detectors are generally sorted in two types: photon detectors and thermal detectors. The photon detectors have high signal to noise ratio and very fast response, but require generally a cooling system, which is heavy and expensive. In comparison with photon detectors, most of thermal detectors operate at room temperature, thus reducing the cost of operation. Even its response time is still larger than that of photon detectors, it has no limitation on the wavelength response band. Thus makes it possible to be used for hand-held infrared applications.

Thermal detectors are based on three different approaches, namely, bolometers, pyroelectric and thermoelectric effects. Uncooled microbolometers take a large part of infrared imaging application business [1]. A bolometer is a thermal detector whose electrical resistance R changes as a function of radiant energy. So, the larger the resistance changes, the higher the

Temperature Coefficient of Resistance ($\beta=1/R \times dR/dT$ expressed in K^{-1}), and the higher the responsivity. Many materials such as metals (Au, Pt, Ti, etc.) [2][3], and semiconductors (VO_x , amorphous silicon, etc.) [4][5] have been used as thermometer in uncooled bolometers.

The rare earth manganese oxides may find important applications such as magnetic random access memories and magnetic sensors [6][7]. It has been realized that these materials have a promising potential for bolometric infrared detection [8][9]. The large change of their electrical resistance R at the metal-to-insulator transition, which takes place in the 300-350 K range, makes them potential materials for the fabrication of uncooled thermal detectors. Ideal materials would present, at the desired operating temperature T close to 300 K, a high β and a low noise level.

Even if it does not exhibit the highest β values at room temperature, compared to other possible manganite compositions, we study $\text{La}_{0.7}\text{Sr}_{0.3}\text{MnO}_3$ (LSMO) because it shows low $1/f$ noise and no excess noise at the metal-to-insulator transition [9]-[15]. In addition, we use a good quality LSMO films deposited on silicon substrates, which enables the compatibility with silicon microelectronic fabrication process and possible development of more complex systems.

In section II we will describe the sample fabrication details together with the measurement setup. The third section is dedicated to the theoretical principle of operation of bolometer, and to the definitions of figures of merits. Then, in the fourth section, we will show detailed electrical and optical characterizations of the tested sample, with comparison to other uncooled bolometers. Finally, a conclusion section is devoted to show the potentialities of LSMO/STO/Si thin films as promising uncooled thermal detector.

II. EXPERIMENTAL DETAILS

A. Sample preparation

The sample consists in a 100 nm thick epitaxial LSMO thin film deposited on SrTiO₃ (20 nm thick) buffered Si (001) substrates by reactive molecular beam epitaxy [16]. After gold deposition, the film was patterned using standard UV photolithography and argon ion milling. Ultrasonic bonding was used to connect the gold contacts to the sample holder.

Our sample, shown in Fig. 1, has a meander line shape with the overall pixel dimension of 150×230 μm². The meander line width is 50 μm. The meander filling factor (defined as the ratio of the area occupied by the LSMO meander to the device nominal area) is equal to 91%.

B. Measurement setup

A semiconductor laser diode (635 nm, 5 mW) electronically modulated at different frequencies was used to optically heat the device. The laser beam was collimated and passed through a 1:1 beam splitter with one beam incident on a photodiode and the other incident on the studied sample. Thus, by knowing the transmission coefficient of all optical elements, the power of the incident light on the sample can be directly obtained by measuring the photodiode output signal. The laser diode spot has an elliptical shape, with dimensions of 128 μm × 186 μm estimated at Full Width Half Maximum.

The sample was glued to a copper plate, having a heating element, then fixed into a vacuum chamber equipped with an optical window. The chamber is evacuated by a mechanical pump, and no cooling system was used. A temperature controller was used to maintain temperature stability of 15 mK during measurements at fixed temperature. The controller, also, provides the possibility of heating the sample in the range 300-350 K.

The LSMO sample was current biased using a quasi-ideal DC current source, which exhibits very high output impedance and a negligible noise contribution [17]. A standard four-probe technique was used to provide bias current and measure the voltage signal of the LSMO sample. The output voltage of the sample was read out by a homemade voltage amplifier. The dynamic optical response and electrical noise measurements were carried out using a spectrum analyser (HP3562A). The measurement setup is equipped with personal computer with GPIB interface to read and store the measured values.

III. BOLOMETER BACKGROUND

A. Principle of operation

When the bolometer material absorbs an amount Q of radiated power from a light source, a temperature change ΔT occurs: $\Delta T = \eta Q / G_{\text{eff}}$, where G_{eff} is the effective thermal conductance of bolometer material (expressed in

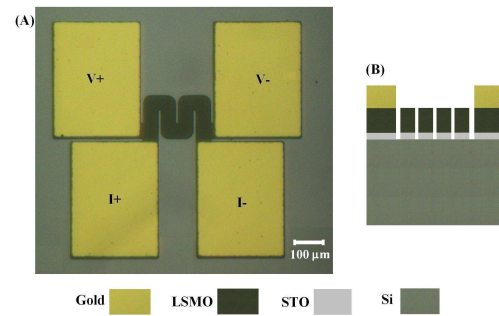


Figure 1. (A) Optical photograph of the tested sample with the two current probes [I+, I-] and two voltage probes [V+, V-]. (B) Schematic cross-section of the sample.

$W \cdot K^{-1}$), and η is the absorption coefficient (dimensionless). G_{eff} is related to the self-heating effect and given by the relation: $G_{\text{eff}} = G - I_b^2 \times (dR/dT)$, where G is the geometrical thermal conductance of the bolometer. The variation of the temperature causes a change in the electrical resistance R of the bolometer material:

$$\Delta R = \beta R \times \Delta T = \beta R \times \eta Q / G_{\text{eff}} \quad (1)$$

So, when using a bias current I_b through such a bolometer, a voltage change can be measured:

$$\Delta V = (I_b \beta R \eta Q) / G_{\text{eff}} \quad (2)$$

B. Figures of merit

The performance of bolometers is expressed in terms of device figures of merit such as optical responsivity (\mathfrak{R}_v), Noise Equivalent Power (NEP), specific detectivity (D^*), and β [18].

The optical responsivity (\mathfrak{R}_v) of a bolometer is defined as the output voltage per radiated power when bias current I_b is applied to the bolometer device, and is written as:

$$\mathfrak{R}_v(\omega) = \frac{\Delta V}{\Delta Q} = \frac{\eta I_b}{G_{\text{eff}}(1 + \omega^2 \tau_{\text{eff}}^2)^{1/2}} \frac{dR}{dT} \quad [V \cdot W^{-1}] \quad (3)$$

where $\tau_{\text{eff}} = C / G_{\text{eff}}$ is the effective thermal time constant, and C is the thermal capacitance of the bolometer.

The NEP (expressed in $W \cdot Hz^{-1/2}$) is defined as the incident power on a pixel that generates a signal-to-noise ratio equal to unity in a 1 Hz output bandwidth. The NEP of the bolometer is calculated as the ratio of the square root of the voltage noise spectral density ($S_v^{1/2}$) over the bolometer responsivity (\mathfrak{R}_v).

The D^* (expressed in $cm \cdot Hz^{1/2} \cdot W^{-1}$) provides information that is equivalent to NEP, but with the possibility to compare bolometer pixels of different areas. It is calculated as the ratio of the square root of effective surface of bolometer (expressed in cm^2) over the NEP.

Another important figure of merit is the impulse detectivity [19], which is defined as $D^*/\tau_{\text{eff}}^{1/2}$ (expressed in $\text{cm}\cdot\text{J}^{-1}$). This parameter illustrates the necessary compromise between optical responsivity and effective time thermal constant.

IV. RESULTS AND DISCUSSION

A. Electrical characteristics

The electrical resistance versus temperature (R-T) data of the LSMO sample was measured using a standard four-point technique. Then the R-T data were fitted with a smooth equation and then the dR/dT and β data were calculated and plotted as seen in Fig. 2 and Fig. 3. The maximum β value obtained is $2.7 \times 10^{-2} \text{ K}^{-1}$, which is a typical value for the LSMO material [10][11]. We can estimate the electrical resistivity of about $2.4 \times 10^{-5} \Omega\cdot\text{m}$ at 300 K, which is close to literature value for this material [20].

The R-T plot presents a non linear shape. So, in order to get maximum responsivity, the sample should be characterised at a temperature where we have the maximum of dR/dT (Fig. 3). The maximum dR/dT value equals $85 \Omega\cdot\text{K}^{-1}$ at 318 K, so the sample will be optically characterised at this temperature (and not at the temperature where β is maximal).

B. Optical responsivity

In order to identify whether the optical responsivity is bolometric (thermal), we have compared it with dR/dT as a function of the temperature (Fig. 3). It is found that the dependence of optical responsivity (\mathfrak{R}_v) at 1 Hz on the temperature follows well the variation of dR/dT versus temperature, and they reach a maximum value at the same temperature 318K. This suggests that the major component of the response at 1 Hz is bolometric.

C. Dynamic characterisations

Figure 4 shows the dependence of the optical responsivity as a function of the laser power modulation frequency for different bias currents. We have an optical responsivity of $0.65 \text{ V}\cdot\text{W}^{-1}$ at 1 Hz for the bias current equals to $400 \mu\text{A}$.

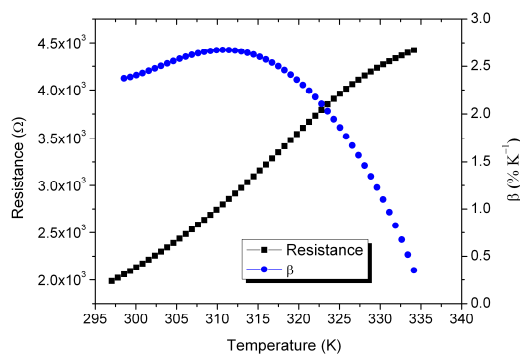


Figure 2. Sample's electrical resistance and β versus temperature

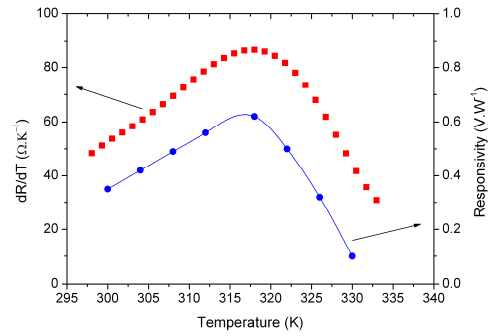


Figure 3. Optical responsivity \mathfrak{R}_v , at bias current $400 \mu\text{A}$ and frequency 1 Hz and dR/dT versus temperature curves.

Three different behaviours can be observed in Fig. 4. From 1 Hz up to the cut-off frequency (around 1 kHz), the optical responsivity is almost constant, whatever is the value of I_b . In the 1-10 kHz decade, we observe a low-pass behaviour and then an increasing of the optical responsivity as function of frequency. Equation (3) can be used to identify the plateau and the low pass filtering. Inset of Fig. 4 shows that the optical responsivity increases linearly with increasing the bias current, according to (3).

We do not observe a constant plateau in our experiment. One possible explanation could be the heat diffusion across the substrate. The increasing optical responsivity at higher frequencies (more than 1 kHz) could be related to the contribution of photo-induced effects in LSMO or in the LSMO/STO/Si heterostructure [8][21]. Further studies are in progress to characterize this non-bolometric component.

An optical step of incident power light was applied at the sample, and then the output voltage time-response of sample was measured. Thus, we can extract the effective thermal time constant τ_{eff} of the sample by using the fitting of sample's time-response as a first order system. We found that τ_{eff} is of the order of $180 \mu\text{s}$, which is consistent with the measured cut-off frequency (Fig. 4). This effective thermal time constant is quite short for a thin film bolometers [8][21][22].

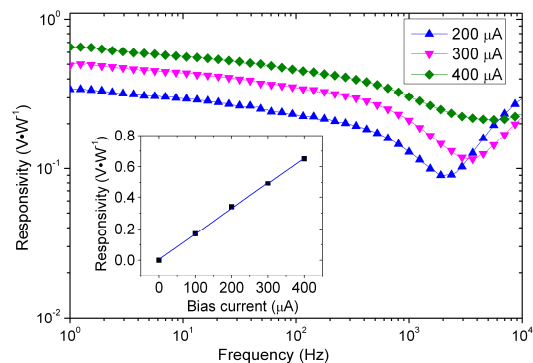


Figure 4. Optical responsivity versus laser modulation frequency at different bias currents at 318 K. The inset shows optical responsivity versus bias current at 1 Hz and 318 K

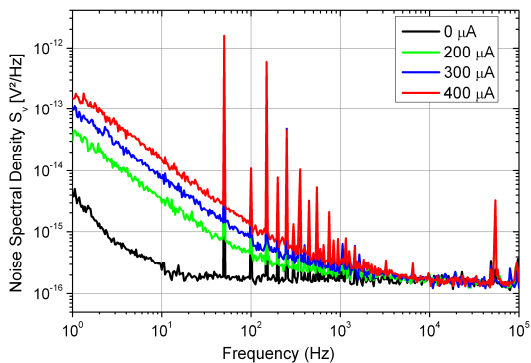


Figure 5. Noise spectral density measured in the four probe configuration at different bias currents at 318K.

We can also estimate $G = 47 \times 10^{-3} \text{ W} \cdot \text{K}^{-1}$ by using (3) in the pass-band frequencies, and using the value of absorption $\eta=85\%$ from earlier measurements on this material [9][20]. We found that $G_{\text{eff}} = G$ at bias current equals $400 \mu\text{A}$. By knowing the thermal time constant and the thermal conductance, we can estimate the thermal capacitance of our sample $C=8.5 \times 10^{-6} \text{ J} \cdot \text{K}^{-1}$.

D. Noise, NEP and D^*

The voltage noise spectral density (S_v) of the sample was measured using the four-probe configuration for different values of the bias current at 318 K, as shown in Fig. 5.

As expected, the white noise level does not depend on the bias current and the $1/f$ noise increases with bias current. Measurement results give a value of S_v equals to $4.4 \times 10^{-15} \text{ V}^2 \cdot \text{Hz}^{-1}$ at 30 Hz, for bias current equals to $400 \mu\text{A}$. Using the value of the optical responsivity, we can estimate the value of NEP and D^* . The measured NEP and D^* value at 318 K, $400 \mu\text{A}$ and 30 Hz, are $1.1 \times 10^{-7} \text{ W} \cdot \text{Hz}^{-1/2}$ and $1.7 \times 10^5 \text{ cm} \cdot \text{Hz}^{1/2} \cdot \text{W}^{-1}$ respectively.

Table I presents a comparison with other manganite material bolometer [23]. We notice that our sample present better optical responsivity at the same bias current ($1.95 \text{ V} \cdot \text{W}^{-1}$ at 1.2 mA , using (3)) even it has a smaller surface. So, in terms of optical responsivity, LSMO bolometer presents a better performance than LPSMO. Also, even if our sample has smaller D^* , it presents a smaller effective time constant (τ_{eff}). So, in terms of impulse detectivity, which includes both parameters, our sample achieves same value as that of [23], but with a decrease of about 4 factor in Joule heating.

The summary of results of the tested bolometer, with comparison of other uncooled bolometers, is shown in Table II. We can note that the D^* of our sample is still limited compared to these bolometer materials, like Poly-SiGe [24] and VOx [25], but our sample present better time response. It is also still limited in terms of impulse detectivity. This is mainly related to the fact that other bolometers used suspended structures, which decrease the thermal conductance (about $10^{-7} \text{ W} \cdot \text{K}^{-1}$), thus

enhancing the specific detectivity by about 4 orders of magnitude.

V. CONCLUSION

In this paper, the potentialities of LSMO thin films as thermal detector at room temperature have been reported. We have fabricated and characterized the LSMO/STO/Si sample at an operating temperature of 318 K. The sample showed high β ($24 \times 10^{-3} \text{ K}^{-1}$) and low electrical noise.

The sample presents a very good quality LSMO film deposited on Si substrate. This proves the compatibility with silicon microelectronic fabrication process, and gives the opportunity to the integration of LSMO as uncooled thermal detector with the readout electronics.

Figures of merits of bolometer have been measured and analyzed. It showed that due to a thermal conductance of $47 \times 10^{-3} \text{ W} \cdot \text{K}^{-1}$, the device performance is limited to a D^* of $1.7 \times 10^5 \text{ cm} \cdot \text{Hz}^{1/2} \cdot \text{W}^{-1}$ at 30 Hz and $400 \mu\text{A}$. Though, a small effective thermal time constant of $180 \mu\text{s}$ was measured.

Further studies are in progress to optimize the geometrical parameters of the sample, like size and number of lines in the meander, and on different substrates in order to achieve maximal performance of this promising material as thermal detector.

TABLE I. COMPARISON WITH OTHER MANGANITE BOLOMETERS

	This work	Ref. [23]
Film/Substrate	LSMO/STO/Si	LPSMO*/LaAlO ₃
Pixel pitch size ($\mu\text{m} \times \mu\text{m}$)	150×230	2500×3000
β ($\% \text{K}^{-1}$)	2.4 @318K	5.5 @300K
G ($\text{W} \cdot \text{K}^{-1}$)	47×10^{-3}	3×10^{-3}
I_b (mA)	0.4	1.2
$R \cdot I_b^2$ (mW)	0.34	1.58
\mathfrak{R}_v ($\text{V} \cdot \text{W}^{-1}$)	0.65	0.60
τ_{eff}	180 μs	500 ms
NEP at 30Hz ($\text{W} \cdot \text{Hz}^{-1/2}$)	1.1×10^{-7}	3.0×10^{-8}
D^* at 30Hz ($\text{cm} \cdot \text{Hz}^{1/2} \cdot \text{W}^{-1}$)	1.7×10^5	9.0×10^6
$D^*/\tau_{\text{eff}}^{1/2}$ ($\text{cm} \cdot \text{J}^{-1}$)	1.3×10^7	1.3×10^7

*LPSMO : $\text{La}_{0.7}(\text{Pb}_{0.65}\text{Sr}_{0.37})_{0.3}\text{MnO}_3$

TABLE II. COMPARISON WITH OTHER UNCOOLED BOLOMETERS

	This work	Ref. [24]	Ref. [25]
Film/Substrate	LSMO/STO/Si	Poly-SiGe/Si	VO _x /Si
Structure	not suspended meander	suspended microbridge	suspended microbridge
Pixel pitch size (μm×μm)	150×230	50×60	50×60
Resistance at 300K (kΩ)	2.13	350	50
β at 300K (%K⁻¹)	1.9	-1.9	-2.1
G (W.K⁻¹)	47 × 10 ⁻³	1 × 10 ⁻⁶	1 × 10 ⁻⁵
R·I_b² (mW)	0.34	0.45	0.50
τ_{eff}	180 μs	16.6 ms	3 ms
D* at 30Hz (cm·Hz^{1/2}·W⁻¹)	1.7 × 10 ⁵	7.5 × 10 ⁸	2 × 10 ⁸
D*/τ_{eff}^{1/2} (cm·J⁻¹)	1.3 × 10 ⁷	5.8 × 10 ⁹	3.7 × 10 ⁹

ACKNOWLEDGMENTS

The authors would like to thanks the CIMAP laboratory at ENSICAEN for providing optical equipment.

REFERENCES

[1] J.L. Tissot, "IR detection with uncooled sensors", *Infrared Phys. Techn.*, 46, pp. 147-153, 2004.

[2] K.C. Liddard, "Thin-film resistance bolometer IR detectors", *Infrared Phys.*, pp. 57-64, 1984.

[3] A. Tanaka, S. Mastsumoto, N. Tsukamoto, S. Itoh, and K. Chiba, "Infrared focal plane array incorporating silicon IC process compatible bolometer", *IEEE Trans. Electron. Dev.*, vol. 43, pp. 1844-1850, 1996.

[4] H. Jerominek, F. Picard, N. Swart, M. Renaud, and M. Levesque, "Micromachined uncooled VO₂-based IR bolometer arrays", *Proceedings of SPIE*, vol. 2746, p. 60, 1996.

[5] E. Mottin, A. Bain, J.L. Martin, J.L. Ouvrier-Buffet, S. Bisotto, J.J. Yon, and J.L. Tissot, "Uncooled amorphous silicon technology enhancement for 25-μm pixel pitch achievement", *Proceedings of SPIE*, vol. 4820, pp. 200-207, 2003.

[6] T. Venkatesan, M. Rajeswari, Z.-W. Dong, S. B. Ogale, and R. Ramesh, "Manganite-based devices: opportunities, bottlenecks and challenges", *Phil. Trans. R. Soc. Lond. A*, vol. 356, no. 1742, pp. 1661-1680, 1998.

[7] S. Wu, D. Fadil, S. Liu, A. Aryan, B. Renault, J. -M. Routoure, S. Flament, P. Langlois, L. Méchin, and B. Guillet, "La_{0.7}Sr_{0.3}MnO₃ Thin films for magnetic and Temperature Sensors at Room Temperature", *Sensors & Transducers Journal*, vol. 14-1, pp. 253-265, 2012.

[8] M. Rajeswari, C. H. Chen, A. Goyal, C. Kwon, M. C. Robson, R. Ramesh, T. Venkatesan, and S. Lakeou, "Low-frequency optical response in epitaxial thin films of La_{0.67}Ca_{0.33}MnO₃ exhibiting colossal magnetoresistance", *Appl. Phys. Lett.*, vol. 68, p. 3555 1996.

[9] L. Méchin, J.-M. Routoure, B. Guillet, F. Yang, S. Flament, D. Robbes, and R. Chakalov, "Uncooled bolometer response of a low noise La_{2/3}Sr_{1/3}MnO₃ thin film," *Appl. Phys. Lett.*, vol. 87, p. 204103, 2005.

[10] B. Raquet, J. Coey, S. Wirth, and S. von Moln'ar, "1/f noise in the half-metallic oxides CrO₂, Fe₃O₄, and La_{2/3}Sr_{1/3}MnO₃," *Phys. Rev. B*, vol. 59, no. 19, pp. 12435-12443, 1999.

[11] A. Lisauskas, S. Khartsev, and A. Grishin, "Studies of 1/f Noise in La_{1-x}M_xMnO₃ (M= Sr, Pb) Epitaxial Thin Films," *J. Low Temp. Phys.*, vol. 117, no. 5, pp. 1647-1651, 1999.

[12] A. Palanisami, R. Merithew, M. Weissman, M. Warusawithana, F. Hess, and J. Eckstein, "Small conductance fluctuations in a second-order colossal magnetoresistive transition," *Phys. Rev. B*, vol. 66, no. 9, p. 92407, 2002.

[13] L. Méchin, J.-M. Routoure, S. Mercone, F. Yang, S. Flament, and R. Chakalov, "1/f noise in patterned La_{0.7}Sr_{0.3}MnO₃ thin films in the 300-400 K range," *J. Appl. Phys.*, vol. 103, p. 083709, 2008.

[14] K. Han, Q. Huang, P. Ong, and C. Ong, "Low-frequency noise in La_{0.7}Sr_{0.3}Mn_{1-x}Fe_xO₃ thin films," *J. Phys. Condens. Matt.*, vol. 14, p. 6619, 2002.

[15] F. Yang, L. Méchin, J.-M. Routoure, B. Guillet, and R. A. Chakalov, "Low-noise La_{0.7}Sr_{0.3}MnO₃ thermometers for uncooled bolometric applications," *J. Appl. Phys.*, vol. 99, no. 2, p. 024903, 2006.

[16] L. Méchin, C. Adamo, S. Wu, B. Guillet, S. Lebargy, C. Fur, J.-M. Routoure, S. Mercone, M. Belmeguenai, and D. G. Schlom, "Epitaxial La_{0.7}Sr_{0.3}MnO₃ thin films grown on SrTiO₃ buffered silicon substrates by reactive molecular-beam epitaxy", in press in *Phys. Status Solidi A*, DOI/10.1002/ ppsa. 201127712, 2012.

[17] J.-M. Routoure, D. Fadil, S. Flament, and L. Méchin, A low-noise high output impedance DC current source, in *Proceedings of the 19th International Conference on Noise and Fluctuations; ICNF 2007*, AIP Conference Proceedings, vol. 922, no. 1, pp. 419-424, 2007.

[18] P. L. Richards, "Bolometers for infrared and millimeter waves", *J. Appl. Phys.*, vol. 76, p. 1, 1994.

[19] I. A. Khrebtov, "Superconductor Infrared and Submillimeter Radiation Receivers", *Sov. J. Opt. Technol.*, vol. 58, p. 261, 1991.

[20] Y. Okimoto, T. Katsufuji, T. Ishikawa, T. Arima, and Y. Tokura "Variation of electronic structure in La_{1-x}Sr_xMnO₃ (0≤x≤0.3) as investigated by optical conductivity spectra", *Phys. Rev. B*, vol. 55, p. 4206, 1997.

[21] J. H. Hao, X. T. Zeng, and H. K. Wong, "Optical response of single-crystal (La,Ca)MnO₃ thin films", *J. Appl. Phys.* vol. 79, p. 1810, 1996.

[22] J. H. Hao, X. Mao, C. H. Chen, and D. X. Lu, "Room Temperature Bolometric Applications Using Manganese Oxide Thin Films", *Int. J. Infrared Millim. Waves*, vol. 20, pp. 2113-2120, 1999.

[23] A. Lisauskas, S. I. Khartsev, and Alex Grishin, "Tailoring the colossal magnetoresistivity: La_{0.7}(Pb_{0.63}Sr_{0.37})_{0.3}MnO₃ thin-film uncooled bolometer", *Appl. Phys. Lett.*, vol. 77, p. 756 (2000)

[24] L. Dong, R. Yue, and L. Liu, "An uncooled microbolometer infrared detector based on poly-SiGe thermistor", *Sens. Actuators A*, vol. 105, pp. 286-292, 2003.

[25] H. Wang, X. Yi, G. Huang, J. Xiao, X. Li, and S. Chen, "IR microbolometer with self-supporting structure operating at room temperature", *Infrared Phys. Techn.*, vol. 45, pp. 53-57, 2003.

Identification of Yarn Periodical Errors Using Signal Processing Techniques Based on Capacitive and Optical Sensors Measurements

Vítor Carvalho^{1,2}, Filomena Soares¹
¹Dept. Industrial Electronics and Computers
¹Minho University, ²IPCA-EST
¹Guimarães, ²Barcelos, Portugal
 (vcarvalho, fsoares)@dei.uminho.pt

Michael Belsley³, Rosa Vasconcelos⁴
³Dept. Physics, ⁴Dept. Textile Engineering
 Minho University
³Braga, ⁴Guimarães, Portugal
 belsley@fisica.uminho.pt, rosa@det.uminho.pt

Abstract—This paper presents a study to identify the type and location of yarn periodical errors applying three different signal processing approaches based on FFT – Fast Fourier Transform, FWHT-Fast Walsh-Hadamard Transform and FDFI – Fast Impulse Frequency Determination. The errors determination is applied for the mass measurement of yarn using a capacitive sensor and for the measurement of yarn diameter/hairiness based on optical sensors. Commercial equipment uses exclusively a FFT approach which is not able to clearly detect other types of common periodical yarn errors, especially impulse errors, as well as an inferior resolution than the 1mm used in this work. The theoretical description of each signal processing technique is presented, as well as their application to several simulated errors, namely, sinusoidal, rectangular, pulse and impulse errors, showing proper results and a more complete analysis of periodical errors.

Keywords- capacitive sensors; optical sensors; periodical errors; yarn mass; yarn hairiness; yarn diameter; fast walsh-hadamard; fast impulse frequency determination; fft.

I. INTRODUCTION

The existence of yarn irregularities occurring with a constant frequency is a dominant source of imperfections in fabrics. These defects appear as high energy peaks in the frequency analysis [1-3] of yarn characteristics. So, with spectral analysis, it is possible to detect periodic errors in the yarn production process. Hairiness [4-7] (protruding fibers released from the main body of the yarn) (Figure 1) and irregularities (thin and thick places and neps) [1-3] (Figure 2a), are the major yarn parameters to be analyzed for the occurrence of periodical errors. However, there are two other types of errors [3, 8, 9]. The first type (Figure 2b) typically occurs due to the accumulated dirt at the stretching rollers in the drafting systems, or the displacement of the roller axis, producing a sinusoidal imperfection in the spun yarn diameter. The second type (Figure 2c) is generally due to imperfections in the surface of the rollers, generating a periodic impulse fault (imperfections in the raw material are seldom periodic).



Figure 1. Yarn hairiness

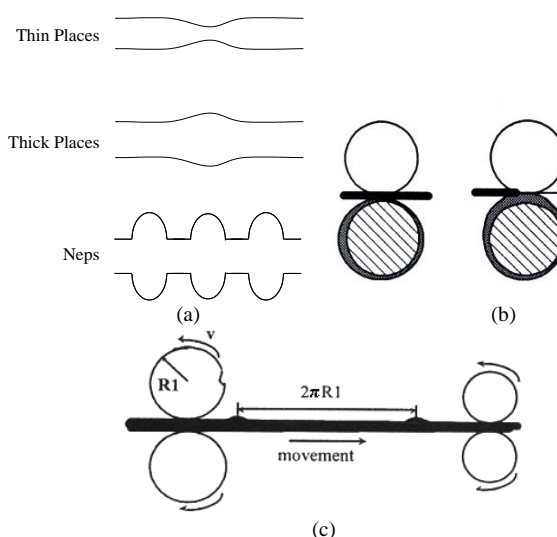


Figure 2. (a) Yarn irregularities (b) Accumulated dirt error (c) Imperfection in the surface rollers error

To detect these yarn errors we have employed three different signal processing (SP) approaches [3] based on FFT (Fast Fourier Transform), FWHT (Fast Walsh-Hadamard Transform) and FDFI (Fast Impulse Frequency Determination), instead of a single strategy, based on FFT, as is the case for all current commercial solutions [1-3]. As most of the yarn periodical errors are sinusoidal they are easily detected by the FFT. It is our intention to explore the use of the FWHT, as an alternative to the FFT, as it has the advantage of requiring a lower computational effort when compared to the others. The FDFI detects impulse errors, as they are not clearly identified by the other techniques. So, as

impulse errors could appear regularly, it was of major importance to present a viable solution for their detection.

This paper contains the following structure: the present Section I- identifies the problem and objectives of the paper; Section II - describes the sensors and the electronic/optical hardware employed for signals capture; Section III- describes the signal processing approaches used; Section IV- presents the results and Section V- presents the conclusions and future work developments.

II. THE MEASUREMENT SOLUTIONS DEVELOPED

To measure yarn irregularities, a parallel plates capacitive sensor was employed to detect yarn mass variations [3, 10, 11], while a coherent optical signal processing technique based on Fourier analysis together with an optical sensor was used to measure yarn hairiness [4-7]. The measurement of yarn irregularities can also be performed considering the yarn diameter variation [12-14]. All employed systems have a sample resolution of 1 mm (Figure 3).

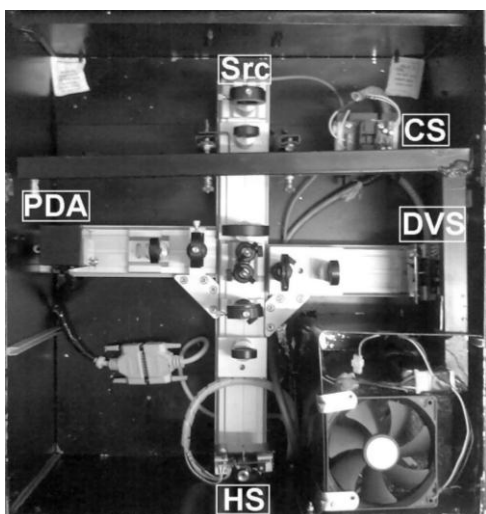


Figure 3. Measurement systems (PDA - Photodiode Array (Diameter Characterization Sensor), DVS - Photodiode (Diameter Variation Sensor), HS - Photodiode (Hairiness Sensor), CS - Capacitor (Mass Variation Sensor), Src - Laser Source)

A. Yarn Mass Variation System

The yarn mass variation system employed uses a 1 mm parallel plate capacitive sensor based on the integrated circuit MS3110 from Irvine Sensors, allowing direct yarn mass measurements over sample lengths of 1 mm. The sensor adopts a differential configuration to assure a higher robustness to variations in temperature, air humidity and pressure. It integrates transducer amplification and signal conditioning, as shown in Figure 4 [15]. This sensor has a resolution of capacity superior to 4 aF/rtHz, difficult to find in other commercial solutions, being compatible with the measurements of resolution in the order of aF needed for proper yarn mass quantification and variation.

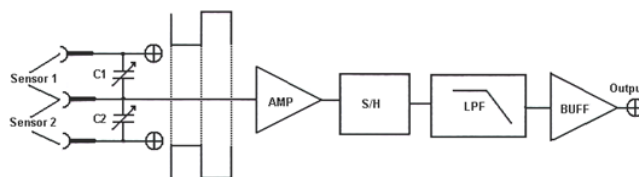


Figure 4. Capacitive sensor configuration (C1,C2 – Adjustable capacitors to calibrate the sensors, AMP – Capacity to voltage converter and amplifier, S/H – Sample and hold, LPF – Two pole low pass filter, and BUFF – Output buffer)

B. Yarn Diameter and Hairiness Quantification

The yarn diameter and hairiness quantification, based on two single photodiodes (S1227-1010BR from Hamamatsu) configured for a 1 mm sample length analysis, uses an optical setup with a low-pass spatial filter, to perform the diameter measurement (eliminating the influence of hairiness, Figure 5a), as well as with a high-pass spatial filter, to perform the hairiness measurement (eliminating the influence of the light which is not blocked by the yarn, Figure 5b) [15-18]. Figure 5c presents the optical hardware employed to determine yarn diameter and hairiness. A coherent optical imaging technique is employed to obtain an optical signal proportional to the amount of hairiness present on the yarn being sampled.

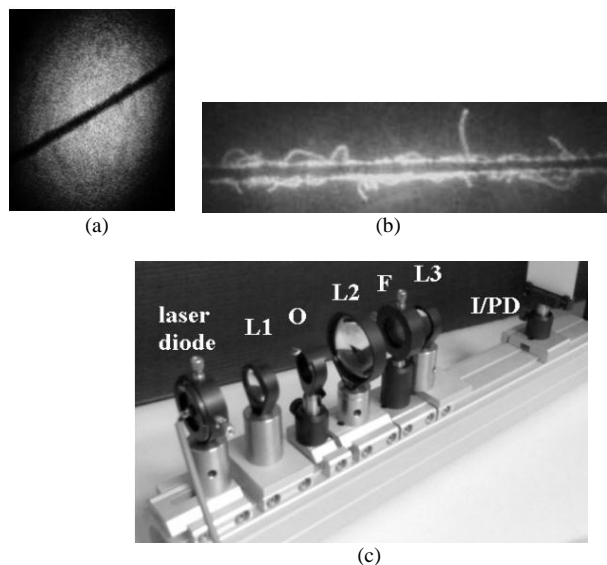


Figure 5. Example of an image resulting from the application of a (a) low-pass spatial filter, (b) high-pass spatial filter, (c) Custom developed optical yarn measurement hardware for a single direction

A diode laser (Eudyna FLD6A2TK) was used as an illumination source. This laser emits light at 685 ± 10 nm in both a single transverse and single longitudinal mode, with an especially low aspect ratio of 1.3. Emitting in a single longitudinal mode, the coherence length of the laser light is expected to be greater than several metres. The light from this laser was collimated using a single plano-convex lens of 40 mm focal length (L1). After illuminating the sample under study (O), the light passes through a 60 mm focal

length, 50 mm diameter plano-convex lens (L2) used to obtain the spatial Fourier transform of the object in its principal focal plane. A roughly 1 mm diameter opaque target (F) placed in the Fourier plane, blocks all spatial frequencies below 10 mm^{-1} , corresponding to a characteristic size of 100 microns or larger in the object plane. The filter is chosen to pass all of the relevant information regarding the small fibres, while almost entirely eliminating the nearly constant background light due to laser light that is not incident on the sample. However, the amount of light transmitted by the spatial filter is relatively small, roughly 3 to 4 orders of magnitude less than the full power emitted by the laser. A third plano-convex lens of 60 mm focal length (L3) is used to form a final filtered image (position of the photo detector in Figure 5c) (I/PD), which then highlights the sharp transitions in the object, basically the core boundary of the fibre and any small protruding hairs from the yarn core, allowing the measurement of hairiness. All lenses are 1 inch in diameter, except for the Fourier lens, L2, which is 2 inches in diameter. The lenses are carefully aligned to have a common optical axis. For the diameter measurements, basically the same optical hardware is used, with the exception that the high-pass spatial filter is replaced by a low-pass spatial filter, corresponding to a roughly 1mm diameter circular aperture, i.e., the complement of the high pass spatial filter. This filter blocks all spatial frequencies above 10 mm^{-1} , resultant to a characteristic size of 100 microns or less in the object plane. Afterwards, in order to obtain a voltage proportional to the brightness of the final image, a conditioning circuit was developed for yarn hairiness/diameter quantification. A high precision current to voltage converter based on a Burr-Brown operational amplifier OPA277P [19] was used between the output of the photodiode and the sampling board. Considering the hairiness and diameter measurement, the presented optical configuration overcomes the referred drawbacks of most available commercial methods [5, 20, 21]. The system also integrates a photodiode array (PDA in Figure 3), S8378-256Q from Hamamatsu, to allow a precise characterization of diameter and hairiness.

III. SIGNAL PROCESSING APPROACHES FOR DETECTION OF YARN PERIODICAL ERRORS

This section describes the signal processing techniques employed for detection of yarn periodical errors in diameter variation, mass variation and hairiness variation. In order to detect these errors, three different approaches are applied, namely, the FFT approach for sinusoidal errors, the FWHT approach for rectangular errors and the FDFI approach for impulse errors. The results obtained are shown in terms of wavelengths ($\lambda(\text{m})$), calculated according to (1) [2], as they give a more perceptive result to the yarn producer.

$$\lambda = L_{\text{sample}} \frac{f_a}{1000 f_d} \quad (1)$$

where, L_{sample} is the sample length (mm), f_a is the acquisition frequency (Hz) and f_d is the detected faults frequencies (Hz).

A. FFT Approach

The first approach is based on the FFT transform [11-13] with a narrow bands definition to aggregate the harmonics, due to the highly concentrated information of the spectrum. This can be considered a periodogram. All the wavelengths detected at the corresponding energy band, are added and then multiplied by the number of detected wavelengths, obtaining the final value of the energy band (2) [1, 10].

$$e(j) = k_e \sum_{w=1}^{w=k_e} \lambda(w) \quad (2)$$

where, k_e is the number of detected wavelengths in the band, w is the index of the detected wavelength and λ is the wavelength amplitude at the index w .

B. FWHT Approach

The Walsh functions create an ordered set of rectangular waves presenting only two possible amplitudes, +1 and -1 [14, 15]. Walsh functions are commonly classified using a notation in terms of odd and even symmetries. Two series are presented, the CAL series (even) and the SAL series (odd), which are very similar to the trigonometric series COSIN and SIN, respectively. The Hadamard order is the one used in this work, as it is computationally the most efficient. The Walsh Hadamard transform is given by (3).

$$FWHT = [X(0) \ X(1) \ \dots \ X(n_s - 1)]^{n_w} WH \quad (3)$$

where, X is the array of signal variation $(0, \dots, n_s - 1)$, n_s is the number of samples, n_w is the order of the WH matrix.

C. FDFI Approach

The FFT and FWHT do not achieve good results in detecting impulse errors: the FFT cannot detect them and the FWHT do not distinguishes them from other errors. So, a new approach, Fast Impulse Frequency Determination (FDFI) [1, 8-10] was considered. In the impulse error presented in Fig. 2, if there are stretching rollers in addition to those responsible for the error, the error will be extended, causing an impulse error with a longer width. The FDFI Transform was developed [1, 8-10] to detect this kind of fault, following an approach which consists of the multiplication of an error signal by a coefficient matrix. The error signal is obtained comparing each sample with a predefined threshold. If the sample amplitude is outside the threshold, the error signal takes the '1' value, otherwise, it takes the value '0'. Afterwards, a matrix is generated, where all the admissible error periods and phases (initial points) are tested (from $n_s / 2$ to $(n_s / 4) + 1$). As the $n_s / 4$ period is multiple of the $n_s / 2$ period, it is not necessary to test it.

IV. RESULTS OF SIGNAL PROCESSING TECHNIQUES WITH SIMULATED ERRORS

A study on the application of signal processing techniques to simulated periodical errors in a hairiness variation signal [10] is presented. Periodical errors tested: sinusoidal error with amplitude of 20 % (Figure 6a); positive periodic rectangular error with amplitude of 40 % (Figure 6b); a pulse error with amplitude of 100 % (Figure 7a) and a periodic impulse error with amplitude of 400 % every 384 samples (Figure 7b).

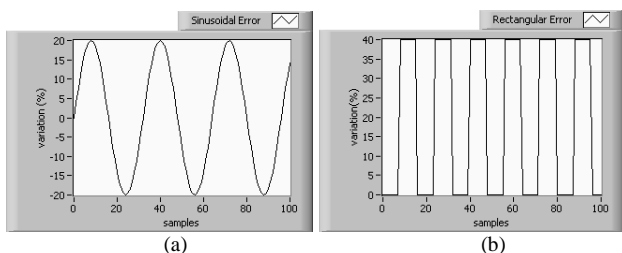


Figure 6. (a) Zoomed sinusoidal error and (b) positive rectangular error added to the original signal (Figure 8)

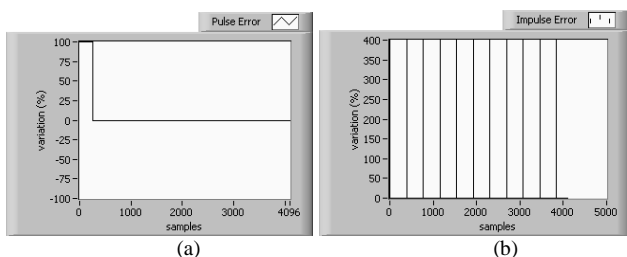


Figure 7. (a) Pulse errors and (b) periodic impulse error added to the original signal (Figure 8)

A. Original Signal

In order to test the signal processing approaches it was considered a real acquired signal: Figure 8 - original signal, is based on the signal of hairiness of a 100% cotton yarn measured by the photodiode DS (Figure 3). It considers the variation (%) of each sample of 1mm in reference to the average of hairiness measured. The results of FFT and FWHT of Figures 9-16 present normalized results in the Y-axis.

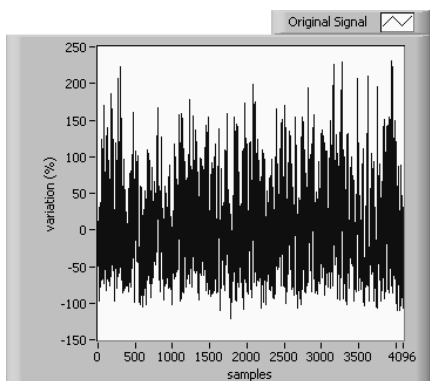


Figure 8. Original signal

B. Original Signal with a Sinusoidal Error Added Analysis

Figures 9 and 10 present the results of FFT and FWHT approach for this situation, respectively.

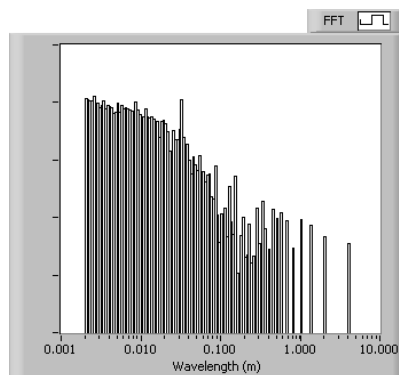


Figure 9. FFT result for the original signal with the sinusoidal error

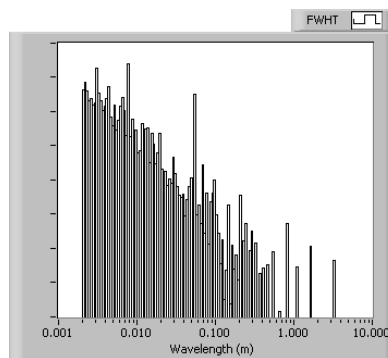


Figure 10. FWHT result for the original signal with the sinusoidal error

Analysing Figure 9 (FFT), it is verified that a relevant protruding peak is now observed around 3 cm, detecting as expected, a clear sinusoidal error at this wavelength. The FWHT spectrogram Figure 10 also presents, mainly, two new protruding peaks around 3 mm and 6 cm. So, as expected, it can be verified that a sinusoidal error is also detected by the FWHT, but in several narrow bands. As known when an error does not match a tested waveform of the applied signal processing technique, it is reflected over several waveforms at different (usually harmonic) wavelengths (decomposition).

C. Original Signal with a Rectangular Error Added Analysis

Figures 11 and 12 present the results of FFT and FWHT approach for this situation, respectively.

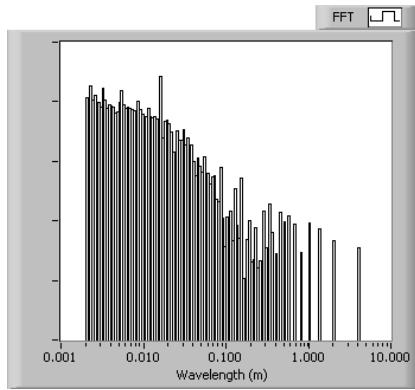


Figure 11. FFT result for the original signal with the rectangular error

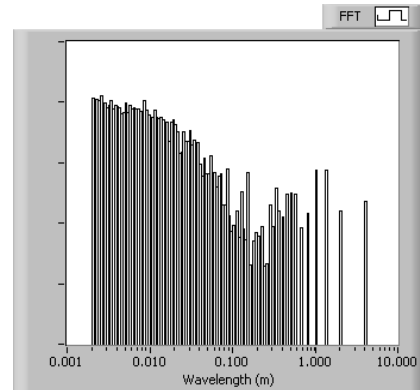


Figure 13. FFT result for the original signal with the pulse error

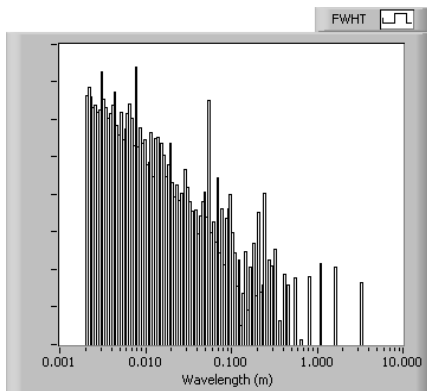


Figure 12. FWHT result for the original signal with the rectangular error

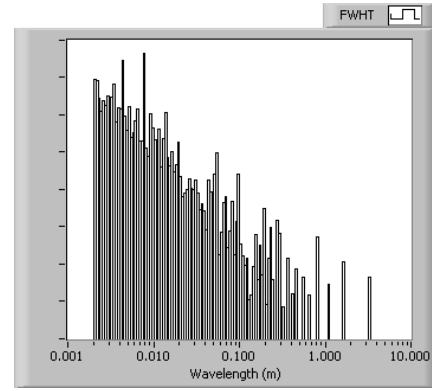


Figure 14. FWHT result for the original signal with the pulse error

Figure 11 (FFT) contains a relevant protruding peak at around 2 cm and three others peaks, with minor amplitudes at wavelengths near 2 mm, 3 mm and 5 mm. As expected, it can be verified that a rectangular error is also detected by the FFT over several narrow bands in which the main error component clearly protrudes over the spectrogram. The FWHT spectrogram (Figure 12) also presents several new protruding peaks around 3 mm and 5 mm, 3, 5, 7, 10, 25 cm. However, the more relevant new protruding peaks are at wavelengths 3 mm, 5 cm and 25 cm. So, it can be verified that a periodic rectangular error is also detected over several bands by the FWHT as in the FFT, probably because the added rectangular error does not completely match a tested FWHT waveform. However, in the FWHT the protruded peaks which are also detected in the FFT have higher amplitudes, due to its close similarity to the FWHT waveforms.

D. Original Signal with a Single Pulse Error Added Analysis

Figures 13 and 14, present the results of FFT and FWHT approach for this situation, respectively.

No new protruding peaks are observed in Figure 13 (FFT), highlighting that this technique is not at all sensitive to pulse errors. This situation was expected because it is a non-periodic error. In FWHT (Figure 14) a new protruding peak is observed around 5 mm probably because the simulated error matched a tested waveform of the FWHT technique. It can be concluded that the FWHT could be useful to detect pulse errors.

E. Original Signal with a Periodical Impulse Error Added Analysis

Figures 15 and 16 present the results of FFT and FWHT approach for this situation, respectively. As no new protruding peaks are observed in Figure 15 (FFT), this technique seems to be unhelpful to detect impulse errors. In FWHT (Figure 16), several alterations are observed: the main protruding peak of the spectrogram around 8 mm as well as several other, were severely reduced while a new protruding peak is observed around 2.5 mm. Finally, a reinforcement of the amplitude of the protruding peak around 8 cm occurred. It can be concluded that although the FWHT detects this type of error, it is impossible to distinguish it, in the spectrogram, from the pulse error. So the use of the FDFI is now considered.

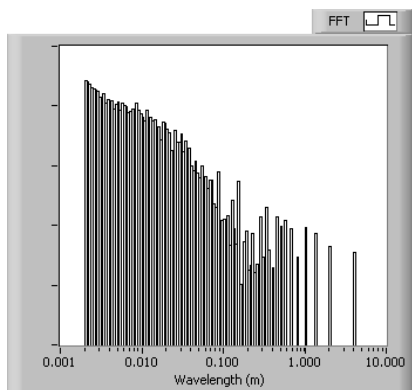


Figure 15. FFT result for the original signal with the impulse error

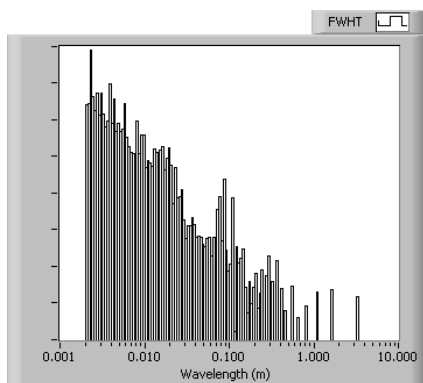


Figure 16. FWHT result for the original signal with the impulse error

Table I presents the signal processing results based on FDFI, tested for impulse errors with a threshold of 300 % showing their initial position, period and number of impulses

TABLE I. DESCRIPTION OF THE DETECTED IMPULSE ERRORS

100 % error row	Initial position (sample)	Period (samples)	Number of impulses
254016	0	1920	3
254400	384	1920	2
254784	768	1920	2
255168	1152	1920	2
255552	1536	1920	2
917760	0	1536	3
918144	384	1536	3
918528	768	1536	3
918912	1152	1536	2
1434048	0	1152	4
1434432	384	1152	4
1434816	768	1152	3

As it can be seen in Table I, it is verified that the signal error is decomposed in 12 error rows, with initial positions in indexes 0, 384, 768, 1152 and 1536, containing periods of 1152, 1536 and 1920 samples, resulting in a number of impulses between 2 and 4.

V. CONCLUSION AND FUTURE WORK

Different signal processing techniques based on FFT, FWHT and FDFI were tested using an experimental hairiness spectrogram for error detection. Artificial sinusoidal, rectangular, pulse or periodical impulse errors were added to the original signal. The previously described analysis allows us to conclude that: periodic sinusoidal errors are clearly distinguished using the FFT approach over a narrow band and in the FWHT over several bands where the main components are visible in the spectrum; periodic rectangular error is distinguished in the FFT approach over several bands, where the main error component clearly extends above the spectrum and in the FWHT, also over several bands, if the error does not match the tested waveforms of the technique (if a match is verified a clearly narrow band will protrude); pulse or periodic impulse errors are not detected by the FFT approach but are detected by the FWHT over a narrow band, considering the pulse error and over several bands considering the periodic impulse error. However, it is difficult to distinguish, an impulse error from a pulse error. For this it is more suitable to use an FDFI analysis; periodic impulse errors are clearly detected by the FDFI approach.

The performance allowed by the FWHT in comparison to the FFT, is supported by the computational effort reduction associated to the less complex calculation of rectangular square waves in comparison to sinusoidal waves.

For a complete analysis of given yarn with unknown error, we recommend the use of all three signal processing techniques as they are in many sense complementary.

Future work will include the development of new optimized FDFI algorithms in order to reduce the associated computational effort as well as studies that allow the use of the FWHT in replacement of the FFT.

ACKNOWLEDGMENT

The authors are grateful to the Portuguese Foundation (FCT) for funding through the scholarship (BD/ 19028/ 2004).

REFERENCES

- [1] V. Carvalho, "Parametrização de Fio Têxtil Baseada na Análise de Massa", Msc Thesis, Minho University, Guimarães, 2004 (in Portuguese).
- [2] R. Furter, "Evenness Testing in Yarn Production: part I", The Textile Institute and Zellweger Uster AG, Manchester, 1982.
- [3] J. Neves, "A Irregularidade dos Fios Têxteis, Sua Origem, Medição e Análise", Oporto, 1968.
- [4] B. Goswami, J. Martindale, and F. Scardino, "Textile Yarns: Technology, Structure and Applications", 2nd Edition, John Wiley & Sons, New York, 1977.
- [5] V. Carvalho, P. Cardoso, M. Belsley, R. Vasconcelos, and F. Soares, "Yarn Hairiness Parameterization Using a Coherent Signal Processing Technique", Sensors and Actuators A: Physical, Vol. 145 (1), 2008, pp. 217-224.
- [6] V. Carvalho, P. Cardoso, M. Belsley, R. Vasconcelos, and F. Soares, "Optical Yarn Hairiness Measurement System", INDIN 2007, 5th IEEE Conference on Industrial Informatics, 23-27 July, Vienna, Austria, 2007.

- [7] V. Carvalho, P. Cardoso, M. Belsley, R. Vasconcelos, and F. Soares, "Yarn Irregularity Parameterization Using Optical Sensors", *Fibres and Textiles in Eastern Europe*, Vol. 17, N.º 1 (72), 2009, pp. 26-32.
- [8] J. Monteiro, "Sistema Distribuído de Análise da Regularidade de Fios Têxteis", PhD Thesis, Minho University, Braga, 1990 (in Portuguese).
- [9] J. Monteiro and C. Couto, "Pulse Frequency Calculation and Estimation in Yarn Evenness Analysis", IEEE Industrial Electronics Society, Orland, USA, 1995.
- [10] V. Carvalho, P. Cardoso, M. Belsley, R. Vasconcelos, and F. Soares, "Optical Yarn Hairiness Measurement System", INDIN 2007, 5th IEEE Conference on Industrial Informatics, 23-27 July, Vienna, Austria, 2007.
- [11] V. Carvalho, "Automatic Yarn Characterization System", PhD Thesis, Minho University, Braga, 2008.
- [12] V. Carvalho, M. Belsley, R. Vasconcelos, and F. Soares, "Automatic Yarn Characterization System: Design of a Prototype", IEEE Sensors Journal, Vol. 9 (8), 2009, pp. 987-993.
- [13] V. Carvalho, J. Monteiro, R. Vasconcelos, and F. Soares, "Yarn Mass Analysis With 1 mm Capacitive Sensors", ISIE2004, 4-7 May, Ajaccio, France, 2004.
- [14] V. Carvalho, M. Belsley, R. Vasconcelos, and F. Soares, "Yarn Periodical Errors Determination Using Three Signal Processing Approaches", (submitted for publication in *Journal of Signal Processing Systems*).
- [15] V. Carvalho, M. Belsley, R. Vasconcelos, and F. Soares, "Automatic Yarn Characterization System", IEEE Sensors 2008, 7th IEEE Conference on Sensors, 26-29 October, Lecce, Italy, 2008.
- [16] V. Carvalho, P. Cardoso, M. Belsley, R. Vasconcelos, and F. Soares, "Yarn Diameter Measurements Using Coherent Optical Signal Processing", IEEE Sensors Journal, Vol. 8 (11), 2008, pp. 1785-1793.
- [17] A. Barella, "Yarn Hairiness", *Textile Progress Journal*, Vol. 13 (1), 1981, pp. 1-57.
- [18] V. Carvalho, P. Cardoso, M. Belsley, R. Vasconcelos, and F. Soares, "Yarn Hairiness Characterization Using Two Orthogonal Directions", IEEE Trans. Instrumentation & Measurement, Vol. 58 (3), 2009, pp. 594-601.
- [19] [url:http://pdf1.alldatasheet.com/datasheet-pdf/view/56757/BURR-BROWN/OPA277.html](http://pdf1.alldatasheet.com/datasheet-pdf/view/56757/BURR-BROWN/OPA277.html) (access in June 2012)
- [20] V. Carvalho, P. Cardoso, M. Belsley, R. Vasconcelos, and F. Soares, "Yarn Diameter Measurements Using Coherent Optical Signal Processing", IEEE Sensors Journal, Vol. 8(11), 2008, pp. 1785-1793.
- [21] V. Carvalho, P. Cardoso, M. Belsley, R. Vasconcelos, and F. Soares, "Yarn Diameter Characterization Using Two Orthogonal Directions", *Journal Experimental Techniques*, Vol. 35 (5), 2011, pp. 7-15.

TCR, Responsivity, and Noise Properties of Carbon Nanotube-polymer Bolometric IR Detectors

Will Riedel, Gustavo E. Fernandes, Jin Ho Kim, Jimmy Xu

School of Engineering
Brown University
Providence, RI 02912 USA

william_riedel@brown.edu, gustavo_fernandes@brown.edu, jin_ho_kim@brown.edu, jimmy_xu@brown.edu

Abstract—We investigate the temperature coefficient of resistance and noise properties of polymer-infiltrated carbon nanotube membranes and their applications to infrared detection. In agreement with previous work the noise is found to be dominated by a $1/f$ contribution. We found, however, that small bolometric time constants, of ~ 10 ms, are achievable in this system in reasonably large “pixels” of $50\ \mu\text{m} \times 50\ \mu\text{m}$, which is beneficial to future applications. Contrary to our expectations, the polymer-nanotube system did not exhibit a large temperature coefficient of resistance. The possible reasons are discussed.

Keywords—Bolometer; Infrared Detection; Carbon Nanotube; polymer.

I. INTRODUCTION

Bolometric detection relies on the fact that the resistance of an object is a function of its temperature [1]. When a sensing element absorbs radiation, it heats up, increasing its temperature and changing its resistance. For short enough wavelengths (e.g., visible and near IR) conventional band gap photodetectors offer better sensitivity and speed, and are thus the preferred platform. As the wavelength increases (and the required band gap decreases), cryogenic cooling becomes a requirement for such band gap photodetectors. Bolometers, on the other hand, can operate in uncooled mode typically with wide operating temperature ranges (although they can too benefit from cooling).

There are two contributions to the resistance of a random network of carbon nanotubes (CNTs): the resistance down the length of a nanotube (i.e., the single nanotube resistance), and the contact resistances between neighboring nanotubes [2]. Because of the large conductivity of individual CNTs, the CNT network resistance is dominated by the contact resistances. Such contact resistances depend on the probability of electron tunneling between adjacent nanotubes. In a simple approximation the intertube electron tunneling probability can be modeled in the framework of a thermal activation process, i.e., it is found to be proportional to $\exp(-E/k_B T)$, where E is an activation energy corresponding to the mean potential energy of the intertube contact gaps and T is the temperature [3]. According to this simplified picture, the CNT network conductivity is proportional to $\exp(-E/k_B T)$ and its reciprocal, the resistivity, to $\exp(E/k_B T)$. The temperature coefficient of

resistance (TCR), which is given by $d\ln(R)/dT$, where R is the sample resistance, becomes proportional to $-E/(k_B T^2)$ and is thus also directly proportional to the activation energy. In principle, thus, the CNT network TCR could be increased via engineering of the activation energy E .

Various recent works have explored CNT bolometers [4-7], and found TCR values in the neighborhood of $\sim -0.5\%/K$ at room temperature. Such small TCR suggests that E is rather small for an unmodified CNT network.

However, polymers may present a readily available possibility for boosting the TCR and thus the performance of CNT bolometers. It is well known that certain polymers can be well incorporated into CNT networks [2]. Passivation of the CNTs by the polymer chains can also readily be achieved. In the latter case the polymer may infiltrate between the intertube gaps, thus providing a means to boost the intertube activation energy E . This may be expected to occur via a number of different processes including residual trapping of charges in the polymer, alteration of the intertube distances via thermal expansion, and changes in the dielectric permittivity in the intertube tunneling gap, all of which effectively change the shape and height/width of the intertube potential barriers.

In this paper, we test a simple CNT bolometric system consisting of 20 nm thin membranes of randomly oriented overlapping CNTs embedded in a polymer medium (Fig. 1). Among other bolometric parameters, we characterize its TCR, responsivity and noise figures and compare with values obtained after a hydrogel polymer is applied onto the membrane. We find that for reasonably small device sizes ($50\ \mu\text{m} \times 50\ \mu\text{m}$) very short time constants are achievable with the fabrication strategies employed here and discuss its potential implications to bolometric detection. No significant boost is observed in the TCR however, the reasons for which are discussed and believed to be related with the fabrication procedure employed. The noise figure of the CNT-polymer system shows a strong $1/f$ contribution, which is consistent with previous reports and indicates that the presence of polymer does not change the noise characteristic of the system.

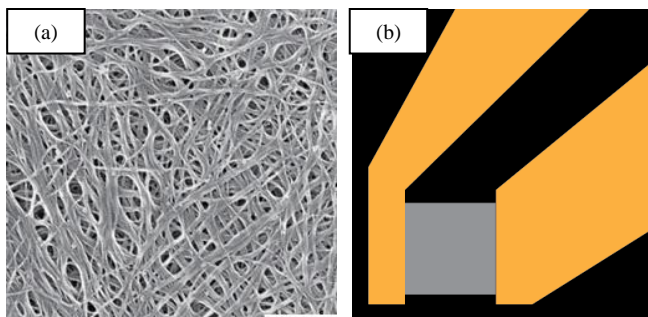


Figure 1. (a) Scanning electron microscope image of a 20 nm thick CNT membrane used in this work. The scale bar is 300 nm. (b) top-view schematic of a single device, with gold electrical contacts (orange) connected to each side of the CNT-polymer composite pixel (gray).

II. EXPERIMENTAL

A. Sample Fabrication

Square pixels of size $50\ \mu\text{m} \times 50\ \mu\text{m}$ and $200\ \mu\text{m} \times 200\ \mu\text{m}$ were fabricated as follows. First, a 20 nm thick film of carbon nanotubes was made by filtration through a membrane filter of a water-dispersed CNT solution. The commercially available CNT solution consists of sodium dodecyl sulfate (SDS) functionalized CNTs dispersed in water. The films were then transferred to a glass substrate via contact printing [8], and metallic contacts were defined directly atop the CNT film by photolithography. We used Shipley S1818 photoresist spun at 2000 rpm for 30 seconds which was exposed for 3 minutes using a Karl-Suss mask aligner. The exposed samples were then developed for 1 minute in MF-321 developer. After development, a 6 nm adhesion layer of titanium was evaporated using electron beam evaporation, followed by 75 nm of gold by thermal evaporation without breaking vacuum. Lift-off was performed in acetone to complete the contacts. Finally, a second photolithography process identical to the first was used to define the CNT pixels in the region between contacts. The remainder of the CNT membrane was etched away by plasma using a Trion reactive ion etch system. The input gas flows were 9 standard cubic centimeters per minute (sccm) argon and 13 sccm oxygen, at a pressure of 50 millitorr and input power of 100 W for 45 seconds. Next, the photoresist was removed in acetone. Wires were bonded to the contact pads using silver paste. Finally, approximately one $1\ \mu\text{L}$ drop of an aqueous poly(Nisopropylacrylamide) hydrogel solution (10 mg/mL) mixed with 1% SDS was applied to each pixel using a micropipette and the samples were annealed at $80\ ^\circ\text{C}$ for several hours to remove residual moisture from the polymer. Measurements were then repeated on the samples with polymer.

B. TCR Measurement

The sheet resistances of the samples were measured in a sealed environmental chamber kept steady at room temperature ($\sim 22\ ^\circ\text{C}$) and 1 atm. The relative humidity

(RH) value inside the measurement chamber was controlled by adjusting the flow of wet and dry N_2 (wet N_2 was obtained by flowing dry N_2 through a water bubbler) and monitored with a hygrometer. For this work the RH was fixed at 80% for all measurements, to enable partial hydration of the hydrogel medium at lower temperatures and thus to enhance the effect of hydrogel addition. The samples were mounted on a thermoelectric heater/cooler plate inside the chamber which allowed the sample temperature to be varied. Sheet resistance measurements were taken at sample temperatures between 2 and $45\ ^\circ\text{C}$ in increments of $1\ ^\circ\text{C}$. Two source measure units (Model 236, Keithley) were used for the electrical measurements. The sample temperature was adjusted and controlled via a temperature controller (LDC 3722B, ILX Lightwave) and monitored by a thermocouple that was mounted onto the Al block that served as sample stage in the chamber.

C. Responsivity Measurement

The photoresponse was measured at constant current by measuring the voltage drop across the films with a lock in amplifier (SRS830, Stanford Research). Two-point measurements were deemed adequate based on negligible contact resistance found through four-point measurements in previous studies. Illumination was provided by a 650 nm laser diode with a power intensity $3\text{W}/\text{cm}^2$. The measurements were performed at room pressure with the atmosphere in the environmental chamber kept at a constant temperature of $22\ ^\circ\text{C}$. The sample temperature was controlled independently.

Previous measurements showed that the Seebeck coefficient for CNT's is $\sim 30\ \mu\text{V}/\text{K}$ [10]. With an estimated temperature change in the sample of less than 1 K at DC, the resulting potential is too small to affect the measurement, so no adjustment was made for the Seebeck voltage.

From this data, one can construct plots of the responsivity as a function of the modulation frequency of the laser diode, from which the thermal conductance and capacitance of the sample through non-linear curve fitting, as described below.

III. RESULTS AND DISCUSSION

Fig. 2 shows the resistance and TCR for the $50\ \mu\text{m}$ sample of as a function of temperature. The resistance varies nearly linearly with temperature, and the TCR fluctuates near $-0.2\%/^\circ\text{C}$, which is similar to results for pure carbon samples [4-6]. The behavior is consistent over the entire measured temperature range. We note that the negative TCR obtained indicated that the conductivity in these CNT membranes is indeed dominated by contact effects (instead of by the $2/3$ metallic CNTs traditionally present in such membranes). However, the addition of polymer did not significantly improve the TCR compared with previous studies on CNT films [4-6]. The choice of high relative humidity for the measurement was made so that the hydrogel would

experience hydration and swelling, especially at the lower temperatures (i.e., at or below the dew point temperature), and thus significantly alter the intertube distances. However, no signature of such a process was observed.

The photoresponse also did not show any major enhancements. Fig. 3 shows the measured responsivity as a function of modulation frequency for the 50 μm sample at 15 °C. The device exhibits behavior that conforms to the well known responsivity formula [1]:

$$\mathfrak{R} = \frac{i_b R \alpha \eta}{G \sqrt{1 + \omega^2 \tau^2}} \quad (1)$$

where i_b is the bias current, α is the TCR, η is the absorption coefficient, G is the thermal conductance and $\tau = C/G$, where C is the thermal capacitance. However, the drop off is more gradual than that of the model. In this case the model was weighted to fit the low frequency behavior more closely so as to not underestimate the time constant. The obtained values of G can C for both samples are given in Table 1.

The time constants obtained from fitting (Table I) are very fast for a bolometric system. Although the response speed is partially the result of high thermal conductance due to the direct contact of the devices with the substrate, there is much room for design adjustment in our structures to improve the poor responsivity while still maintaining an effective time constant. For example, in order to improve the responsivity, the substrate thermal conductivity could be reduced, or alternatively the thermal coupling between film and substrate could be modified by addition of a thin thermally insulating film between the substrate and the CNT membrane.

To complete our analysis, we investigate the noise behavior of these bolometers. The plots of the predicted and measured noise levels for the 50 μm device are plotted vs. frequency in Fig. 4. The magnitude of noise decreases with frequency, indicating that 1/f noise is indeed the dominant source. Additionally, the measured noise agrees reasonably well with the empirical formula previously established by Snow [9] for pure CNT devices:

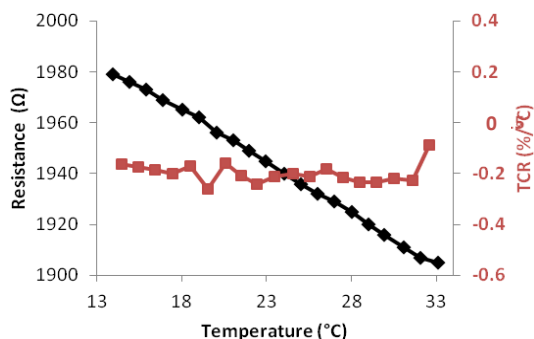


Figure 2. Resistance (black) and TCR (red) vs. Temperature for device of side length 50 μm.

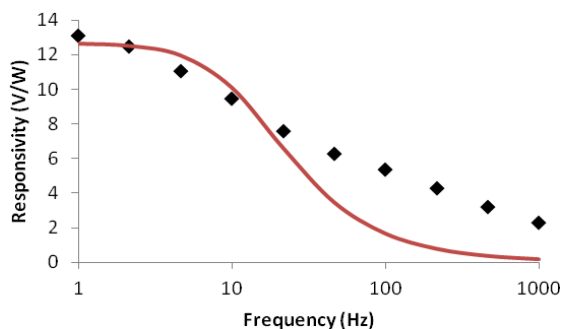


Figure 3. Responsivity vs. Frequency for device of side length 50 μm. Black dots are the measured values, red line is the modeled behavior using parameters estimated by curve fitting. Here the time constant $\tau = 12$ ms.

$$V_{1/f}^2 = (9 \cdot 10^{-11}) \frac{RV^2}{L^{1.3}f} = (9 \cdot 10^{-11}) \frac{R^3 i_b^2}{L^{1.3}f} \quad (2)$$

where L is the side length of the sample, V is the applied voltage bias, and f is the frequency of modulation. The addition of the polymer does not appear to have a substantial effect on the noise levels in the system. Near DC, the signal-to-noise ratio of the detector is only about 10, contributing to poor performance at this frequency. At higher frequencies, however, this ratio improves, and the NEP and detectivity improve as well.

Interestingly, when the photoresponse measurements are made using only a standard resistor, 1/f noise still dominates the system at low frequencies, although the magnitude is lower.

TABLE I. MEASURED DEVICE CHARACTERISTICS

	200 μm sample	50 μm sample
Thermal Conductance (μW/K)	422	38
Thermal Capacitance (μJ/K)	14	0.46
Time Constant τ (ms)	34	12
Responsivity (V/W)	1.1	12.6

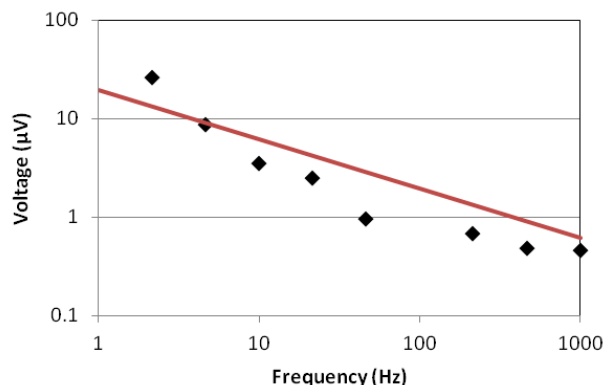


Figure 4. Noise voltage vs. Frequency for devices of side length 50 μm . The black data points indicate measured values, and the red line indicates the empirical formula given by Snow et al.

IV. CONCLUSION AND FUTURE WORK

CNT-polymer composite bolometric detectors as small as 50 μm x 50 μm were fabricated and characterized. Measurements revealed that the polymer does not have a significant impact on the TCR or time constant of the devices. Short time constants near 10 ms were achieved, suggesting the potential for use in high speed bolometric imaging applications, which are sought after.

Contrary to our expectations, the inclusion of a humidity absorbing polymer did not lead to large TCR or indeed any dramatic changes in behavior of these bolometers compared to previous reports on CNT bolometers. We hypothesize that this may have been a result of our device fabrication strategy. Although aqueous solutions of CNT were used to fabricate the CNT membranes, the subsequent processing with acetone and the liftout procedure may have stripped the surfactants (SDS) off the CNTs thus rendering them hydrophobic, which may ultimately have prevented the water based polymer solution from infiltrating into the membrane and indeed filling the intertube contact gaps.

Further work is thus necessary in order to make the fabrication procedure compatible with polymer addition. Possibly, soaking the patterned devices with SDS just prior to polymer application may improve polymer infiltration into the CNT membrane. The sensitivity could also be improved through suspension of the devices, but this will inevitably come at a cost in terms of response time.

ACKNOWLEDGMENT

The development of the composite material was made possible by a grant from AFOSR (P.M. L. Lee) and the exploration of its potential for bolometric IR detection was supported by DARPA (P.M. N. Dhar) and ARL (P.M. M. Dubey).

REFERENCES

- [1] K. C. Liddiard, "Thin-Film resistance bolometer IR detectors," *Infrared Physics*, vol. 24, pp. 57-64,
- [2] D. H. Zhang, K. Ryu, X. Liu, E. Polikarpov, J. Ly, M. E. Tompson, C. Zhou, "Transparent, conductive, and flexible carbon nanotube films and their application in organic light-emitting diodes," *Nano Letters* 6, 1880-1886, (2006)
- [3] Cite P. Sheng, E. K. Sichel, J. I. Gittleman, *Phys. Rev. Lett.* 1978, 40, 1197
- [4] M. E. Itkis, F. Borondics, A. P. Yu, and R.0020C. Haddon, "Bolometric infrared photoresponse of suspended single-walled carbon nanotube films," *Science*, vol. 312, pp. 413-416, 2006.
- [5] R. T. Lu, Z. Z. Li, G. W. Xu, and J. Z. Wu, "Suspending single-wall carbon nanotube thin film infrared bolometers on microchannels," *Applied Physics Letters*, vol. 94, p. 163110, 2009.
- [6] A. E. Aliev, "Bolometric detector on the basis of single-wall carbon nanotube/polymer composite," *Infrared Physics & Technology*, vol. 51, pp. 541-545, 2008.
- [7] M. B. Jakubinek, M. A. White, M. F. Mu, and K. I. Winey, "Temperature dependence of thermal conductivity enhancement in single-walled carbon nanotube/polystyrene composites," *Applied Physics Letters*, vol. 96, pp. 083105-083108, 2010.
- [8] Z. C. Wu, Z. H. Chen, X. Du, J. M. Logan, J. Sippel, M. Nikolou, K. Kamaras, J. R. Reynolds, D. B. Tanner, A. F. Hebard, and A. G. Rinzler, "Transparent, conductive carbon nanotube films," *Science*, vol. 305, pp. 1273-1276, 2004.
- [9] E. S. Snow, J. P. Novak, P. M. Campbell, and D. Park, "Random networks of carbon nanotubes as an electronic material," *Applied Physics Letters*, vol. 82, pp. 2145-2147, 2003.
- [10] S. Jung, K. B. Kim, G. Fernandes, J. H. Kim, F. Wahab, J. M. Xu. "Enhanced thermoelectric power in nanopatterned carbon nanotube film," *Nanotechnology*, vol. 23, 2012.

Application of a Conductive Polymer Electronic-nose Device to Identify Aged Woody Samples

Alphus Dan Wilson

Forest Insect and Disease Research
 USDA Forest Service, Southern Hardwoods Laboratory
 Stoneville, MS, USA
 e-mail: dwilson02@fs.fed.us

Abstract— The identification of aged woody samples is often a difficult task as a result of weathering and physical deterioration over time which removes or obscures distinguishing anatomical features and characteristics required for visual taxonomic determinations. Fortunately, the chemical characteristics of aged woods usually are preserved better than physical characteristics if the wood remains dry in storage. All wood types, determined by the particular plant species from which woody samples are derived, produce and release a unique complex of volatile organic compounds that distinguish individual wood types when headspace volatiles (containing these unique chemical mixtures) are collectively analyzed using an electronic gas-sensing device such as an electronic nose. The advantage of electronic-nose devices over conventional analytical-chemistry instruments, typically used in laboratory chemical analyses, is that the woody source (plant species) from which headspace volatiles are derived may be identified without having to identify individual chemical compounds present in the headspace analyte mixture. Methods were developed for a conductive polymer type electronic nose gas-sensing device, the Aromascan model A32S, to accurately identify aged woody samples derived from wood pieces held in dry storage for long periods of time. An aroma library was developed using diagnostic aroma profile databases (electronic aroma signature patterns) from known woods of numerous tree species. The A32S electronic nose was capable of distinguishing between 44 wood types, providing correct identification determinations at frequencies ranging from 92-99%. The distribution of aroma class components, defined by wood type for each sample analyzed, also could be determined to indicate the relatedness of volatile aroma components that each sample analyte had in common with individual wood aroma classes. This information was useful for determining the taxonomic relatedness of wood types (plant species) based on the headspace volatiles that were produced. Furthermore, principal component analysis provided precise statistical numerical values (quality factors of significance) that indicated the chemical relatedness between wood volatiles based on pairwise comparisons of organic chemical mixtures from individual wood types.

Keywords- *electronic aroma detection; e-nose technologies; volatile organic compounds; wood identification*

I. INTRODUCTION

There are numerous situations where the identity of wood types must be known for many commercial or industrial

applications, scientific research, or forensic analyses. Conventional methods used for the determination of wood type identities involve examinations of macroscopic and microscopic anatomical characteristics of wood tissues. The identification of wood types becomes more difficult if the wood is exposed to adverse environmental conditions (such as weathering) that result in physical deterioration of the wood, masking or diminishing diagnostic anatomical characteristics required for visual taxonomic determinations. By contrast, most chemical characteristics of wood are not lost during aging or weathering as long as the wood is stored in a dry state, even over extended periods of time. Traditional chemical and microscopic methods used for wood identification hitherto are cumbersome and less reliable because they often require extensive and expensive sample preparation and time-consuming analyses. Thus, there is a need for an analytical device that quickly identifies organic samples such as wood types without the high cost of conventional chemical analyses.

Electronic-nose devices are designed to produce digital electronic signatures of volatile organic compounds (VOCs) released from any source [1-3]. Unlike other analytical instruments, these devices have the capability of identifying organic samples from the VOCs they release without having to identify individual chemical compounds present in volatile mixtures [4-6]. A variety of different sensor types have been developed for various applications including optical sensors [7], metal oxides [8, 9], semiconductive polymers [10-13], and conductive polymers [14-15]. The agricultural and food industries have utilized electronic aroma detection (EAD) technologies to evaluate food quality and product aromas [16-18], food storage life and freshness [19-20], detect industrial wastes [21-22], diagnose plant diseases [23], and for many other applications requiring gas-detection technologies [24-27].

The purposes of this study were to 1) determine if an electronic-nose (e-nose) device, the conductive polymer (CP)-type Aromascan A32S e-nose, has the capability of identifying and distinguishing between dried aged specimens of various temperate North American wood types based on headspace volatiles (given the reduced amount of volatiles released from aged wood), to 2) evaluate the effectiveness (accuracy) of wood-type determinations, and to 3) assess whether e-nose aroma data outputs provide indications of

taxonomic-relatedness between aged specimens of various hardwood and conifer wood types.

II. MATERIALS AND METHODS

A. Collection and storage of woody samples

Aged wood blocks (4 cm long \times 2 cm wide \times 2 cm thick), over 20 years old and derived from an archival reference collection of temperate North American wood types stored in the pathology herbarium collection at the Southern Hardwoods Laboratory (SHL), were utilized in this study. A subset of the collection selected for e-nose analysis included 44 wood types (plant species) from 16 genera, representing both hardwood and conifer tree species. These archival wood blocks were highly desiccated while in storage. Each sample was rehydrated by soaking (complete submersion) in sterile distilled water for 15 min, followed by blotting with Kimwipes tissue paper (Kimberly-Clark Inc., Roswell, GA) to remove any free moisture from the wood surfaces immediately prior to e-nose analysis.

B. Sample preparation and prerun procedures

Wood blocks from each wood type were analyzed separately in a 500 ml Pyrex sampling bottle no. 1395 (Corning Inc., Corning, NY) fitted with reference air, sampling, and exhaust ports on a polypropylene bottle cap. Reference air entered the sampling bottle through a 3 mm polypropylene tube extending to just above the bottom of the sampling bottle. The sampling bottle was maintained at a constant air temperature of 25 C and was purged with filtered, moisture-conditioned reference air for 2 min prior to building headspace volatiles. The sampling bottle was sealed and volatiles from each wood type sample were allowed to build headspace and equilibrate for 30 min prior to each run. Reference air was maintained at 4% RH at 25 C. The sampling bottle was purged with conditioned reference air between runs to remove volatiles from the previous sample.

C. Instrument configuration and run parameters

All e-nose analyses were conducted with an Aromascan A32S (Osmetech Inc., Woburn, MA) CP e-nose instrument with 32 sensors in the sensor array and 15 V across sensor paths. The response sensitivities of individual sensors, measured as percent changes in electrical resistance response across sensor paths relative to base resistance ($\% \Delta R/R_{base}$), varied with the type of plastic polymer used in the sensor matrix coating, the type of ring substitutions used to modify its conductive properties, and the type of metal ions used to dope the matrix to improve and modulate sensor response. Detailed analyses containing calibration data for the sensor array were reported previously [23]. The block temperature of the sensor array was maintained at a constant 30 C. Reference air was preconditioned by passing room air sequentially through a carbon filter, silica gel beads, inline filter, and Hepa filter to remove organic compounds, moisture, particulates, and microbes, respectively, prior to humidity control and introduction into the sampling bottle. The flow rate (suction) of sample air at the sampling port was maintained at -702 ml/min using a calibrated ADM 3000

flow meter (Agilent Technologies, Wilmington, DE). Sensor surfaces were purged between runs using a 2% isopropanol wash solution. The instrument was interfaced with a personal computer via an RS232 cable and controlled with Aromascan Version 3.51 software. The instrument plumbing was altered from conventional architecture and specifically configured for static sampling of the headspace by allowing air flow, maintained at 605 ml/min flow rate, coming out of the external vent port of the instrument during analytical runs, and closing the exhaust port on the sampling bottle so that headspace volatiles were taken from a homogeneous static air mass within the sampling bottle.

D. Data acquisition parameters and run schedules

Data from the sensor array were collected at 1 s intervals using a 0.2 detection threshold (y-units), a 15–20 y-max graph scale, and with a pattern average of five data samples taken per run during data acquisition. A uniform run schedule was used consisting of reference air 20 s, sampling time 90 s, and wash 20 s, followed by 90 s of reference air for a total run time of 220 s. A 2 min reference air purge was completed between runs after each sample was removed from the sampling bottle.

E. Construction of reference libraries and validation

An aroma signature reference library was constructed from wood types of known reference woods of angiosperm and gymnosperm species included in this study. All database files were linked to specific (designated) aroma classes defining each sample type or category. The following recognition network options (neural net training parameters) were used for each training session: training threshold = 0.60, recognition threshold = 0.60, number of elements allowed in error = 5, learning rate = 0.10, momentum = 0.60, error goal = 0.010 (P = 0.01), hidden nodes = 5, maximum iterations (epochs) = 10,000, using normalized input data, not actual intensity data. Some parameters were modified for improvement of recognition accuracy. A typical training required 2–35 min, depending on the size of the database applied, using an IBM-compatible personal computer with a minimum of 64 mb of RAM and 350 MHz run speed. Neural net trainings were validated by examining training results that compare individual database files for compatibility or by similarity matches to each specific odor classes by test-assigned odor class distributions among related odor classes included in each library. The specific detailed analytical methods used for identification of unknowns, data processing, and statistical determinations followed the procedures and specifications indicated by Wilson et al. [28].

F. Principal component analysis

Detailed comparisons of relatedness of odor classes (wood types) were determined using principal component analysis (PCA) algorithms provided by Aromascan 3.51 software. Three-dimensional PCA was used to distinguish between wood headspace volatiles released from 12 woody conifer plant species. The mapping parameters for three-dimensional PCA were: iterations = 30, units in Eigen values (%), and use of normalized input data.

III. RESULTS

A. Identification of wood sample types

The A32S conductive polymer e-nose correctly identified the vast majority of the 44 wood types tested based on differences in the aroma profiles of headspace wood volatiles derived from woody samples from the SHL archival wood collection. Correct identifications of unknown wood samples were determined at rates well above 90% (range 92-99%) for all wood types tested except for *Pseudotsuga menziesii*. Wood samples of this tree species were determined to be unknown, indicating that the e-nose could not assign the aroma profile to a specific aroma class, present in the aroma reference library, because the majority of the aroma components within the volatiles from this species did not fall into a single aroma class. The aroma components of *P. menziesii* were distributed more evenly among several aroma classes. However, none of the wood sample identifications were determined to be incorrect or ambiguous, defined as determinations for different wood samples of the same type that were assigned to different aroma classes or wood-identification types in separate runs.

B. Discrimination between wood types

The A32S e-nose also effectively discriminated between the headspace volatiles (aroma profiles) of most wood types tested among twelve conifer species. The aroma profiles of each wood type were further evaluated by neural net training validation during the process of creating a diagnostic aroma library for conifer woods. Following neural-net training, analysis of data for each aroma class (defined by the principal components present in aroma profiles from each wood type) provided a precise breakdown of the aroma class distribution of these principal aroma components present in volatiles among the twelve coniferous wood types as summarized in Table I. The aroma class distribution indicates (on a percentage bases) the proportion of aroma components, present in the headspace volatiles from each wood type, that are in common with principal aroma elements of volatiles from other wood types present in the reference library. Thus, the degree of overlap among principal aroma elements from volatiles of each wood type provides an indication of relatedness between plant species based on the chemical nature of volatiles released from individual wood types. All of the wood types that were identified correctly among the 12 conifer woods had a majority proportion of the aroma profile that was assigned to the principal aroma element characteristic of each individual wood type or plant species. The range of aroma class distributions attributed to an individual principal aroma element characteristic of each wood type ranged from 79.7% in *Abies concolor* to 95.8% in *Pinus ponderosa*. Only aged wood from *Pseudotsuga menziesii* (Douglas fir) had an exceptionally low proportion (15.8%) of aroma components that were attributed to its principal aroma element. Consequently, *P. menziesii* was determined as an unknown aroma profile and could not be identified. The proportion of secondary aroma elements attributed to aroma classes besides the principal aroma element ranged from <1% with

several species to as high as 15.3% in *Tsuga heterophylla* with *Abies concolor* aroma elements and 18.1% in *Abies concolor* with *P. menziesii* aroma elements.

Intensity differences, using the difference-mode software option for displaying aroma signature patterns, between sensor outputs of individual sensors in the sensor array provided clues to differences in VOCs that distinguish headspace volatiles of different wood types. For example, a comparison of the differences in sensor outputs in response to volatiles from *Quercus alba* and *Tsuga canadensis* woods may indicate differences in the types of chemical constituents that are present in one wood type, but not the other (Fig. 1). These differences can be deduced from the chemical classes of VOCs that individual sensors in the array are known to be most sensitive to – as determined by direct comparison tests using single-chemical e-nose analyses. The organic chemical classes that individual sensors (within the A32S sensor array) are most sensitive to were determined and reported previously [23]. The strong positive differences between sensor output responses for sensors 1-3 indicate that *Q. alba* wood volatiles may contain short-chain alcohols, carboxylic acids, or aliphatic amines that are absent in *T. canadensis* wood volatiles. Similar deductions are possible to a lesser extent for sensors 4-16 with the exception of sensors 10-12. The strong negative difference between sensor output responses of sensors 20, 23, and 24 indicate that *T. canadensis* wood volatiles may contain long-chain alcohols, short- or long-chain esters, aliphatic ketones, or aromatic hydrocarbons that are absent in *Q. alba* wood volatiles. Further deductions also may be inferred for negative differences observed for sensors 25-32 with the exception of sensors 29 and 31.

C. Principal component analysis

An analysis of seven pine (*Pinus*) species using PCA by pairwise comparisons of headspace wood volatiles in all possible combinations provided greater details of chemical relatedness between species within a single woody plant genus. The results of relatedness of wood volatiles between these pine species were measured using a statistical algorithm called quality factor (QF) analysis that determines the distance between aroma profiles using Euclidean distance units of measurement. The greater the QF value determined from pairwise comparisons of volatiles, the greater the difference (or distance) between the aroma signature profiles of the two aromas being compared. In terms of statistical determinations, a QF value of 2.0 is roughly equivalent to a statistical difference at $P = 0.10$ level of significance. The relatedness among the seven pine taxa varied greatly based on Euclidean distance as indicated in Table II. QF values ranged from 0.1 to >70, indicating a very wide range of chemical relatedness between individual pine species. Among the seven species compared, a QF of 0.1 indicated a very close chemical relationship between *P. strobus* and *P. contorta*, whereas a QF >70 indicated a very wide difference between the volatile VOCs from woods of *P. palustris* compared with *P. lambertiana*. Relatively low levels of relatedness were found between *P. strobus*, *P. resinosa*, and *P. palustris* as a group. Intermediate levels of chemical

TABLE I. DISTRIBUTION OF ELECTRONIC-NOSE AROMA CLASS COMPONENTS AMONG TWELVE CONIFER WOOD TYPES

Wood Type	Aroma Class Distribution (%) ^a											
	Wood Types (Plant species abbreviations)											
	Acon	Cdec	Claw	Jvir	Locc	Pgla	Ppon	Pmen	Ssem	Tdis	Tocc	Thet
<i>Abies concolor</i>	79.7	–	10.4	4.7	7.1	4.6	–	18.1	–	–	0.1	12.8
<i>Calocedrus decurrens</i>	–	85.0	7.1	–	–	1.3	5.3	–	6.9	–	5.5	12.8
<i>Chamaecyparis lawsoniana</i>	10.1	7.6	88.8	–	–	2.2	3.6	–	4.3	–	3.2	–
<i>Juniperus virginiana</i>	3.1	–	–	94.3	0.9	3.6	1.8	3.4	2.7	2.3	–	3.8
<i>Larix occidentalis</i>	9.0	–	3.5	1.1	87.0	–	8.5	14.9	8.1	1.5	5.5	–
<i>Picea glauca</i>	–	1.4	2.4	3.7	1.3	91.0	–	6.9	3.9	–	–	–
<i>Pinus ponderosa</i>	–	0.7	3.4	0.9	1.6	–	95.8	3.4	–	–	–	–
<i>Pseudotsuga menziesii</i>	11.5	–	–	–	6.8	2.7	0.1	15.8	–	6.3	7.1	4.9
<i>Sequoia sempervirens</i>	–	11.7	3.3	5.4	6.8	5.1	–	–	86.9	10.5	–	–
<i>Taxodium distichum</i>	–	–	–	–	0.9	3.3	3.0	14.7	8.4	85.6	6.5	7.8
<i>Thuja occidentalis</i>	0.6	4.9	–	–	4.4	3.0	0.9	10.9	–	12.8	88.3	–
<i>Tsuga heterophylla</i>	12.0	15.3	–	4.6	–	2.4	3.5	10.9	–	8.5	–	80.9

a. Mean percent aroma class distributions indicated for each wood type; read from left to right (by row), not top to bottom. Plant species abbreviations correspond to wood types (column 1).

relatedness were found between *P. strobus*, *P. monticola*, *P. lambertiana*, and *P. ponderosa*, but not between *P. monticola* and *P. lambertiana* that are fairly closely related chemically based on wood volatiles.

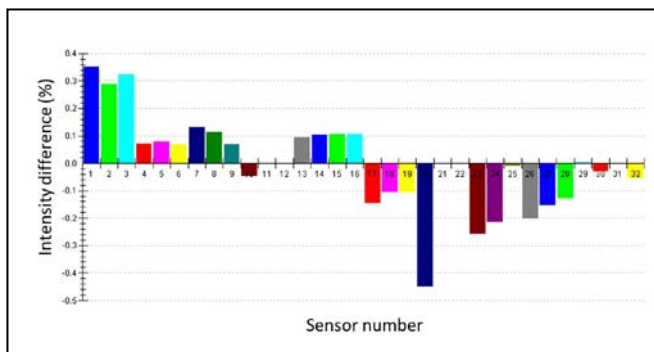


Figure 1. Percentage differences in e-nose sensor output intensity between wood volatiles of *Quercus alba* and *Tsuga canadensis* species.

The relatedness between aroma profiles of wood volatiles from the seven *Pinus* species, based on 3-dimensional CPA, was graphed in the form of an aroma map that indicates Euclidean distances among the seven pine species (Fig. 2). The percentages of the total variance for this analysis, accounting for the variability explained by each orthogonal principal component (PC), are as follows: PC 1 = 54.5%; PC 2 = 31.8%; and PC 3 = 13.4%, representing the x-, y-, and z-axis of the aroma map, respectively. A high proportion (86.3%) of the variation was explained by the first two principal components (PC 1 and PC 2). Notice that the data

points for *P. strobus* are very close to one of the *P. contorta* points and indicate a close chemical relationship based on wood volatiles. *Pinus resinosa* is also fairly closely related to *P. strobus* and *P. contorta*. However, there are very large chemical differences between *P. lambertiana* and *P. palustris*, and between *P. palustris* and *P. contorta*.

IV. DISCUSSION AND CONCLUSIONS

An electronic-nose correct-identification rate above 90% generally is considered quite acceptable for unknown sample sizes greater than n=30 for any one aroma class. The rate of correct identifications can be significantly increased through neural net training to a higher level of specificity and thus lower error rate for e-noses that provide neural net training features in their operating software. The level of discrimination is largely determined by how long the neural net training is allowed to proceed before it is terminated. Specific levels of error rates may be specified and set via training parameters prior to training to reach specific target levels of discrimination for different applications. For example, sample types that have relatively small variations in aroma profiles must be trained to higher levels of discrimination to achieve effective differences between sample types. However, too much training specificity can result in the inability to determine distinctions between sample types. The level of discrimination desired for sample identifications is defined and specified by the specific reference aroma library used for sample identifications which are defined by the level of neural net training used to create each aroma library.

TABLE II. RELATEDNESS OF SEVEN PINE (*PINUS* SPP.) WOOD TYPES BASED ON 3-DIMENSIONAL PCA OF WOOD VOLATILES

Aroma class	Aroma class	QF value ^a
<i>P. strobus</i>	<i>P. monticola</i>	17.5***
	<i>P. lambertiana</i>	15.3***
	<i>P. resinosa</i>	4.6*
	<i>P. palustris</i>	5.1*
	<i>P. ponderosa</i>	10.3**
	<i>P. contorta</i>	0.1
	<i>P. monticola</i>	<i>P. lambertiana</i>
<i>P. monticola</i>	<i>P. resinosa</i>	6.0*
	<i>P. palustris</i>	20.7***
	<i>P. ponderosa</i>	18.6***
<i>P. ponderosa</i>	<i>P. contorta</i>	5.9*
	<i>P. resinosa</i>	9.2**
	<i>P. palustris</i>	> 70****
<i>P. lambertiana</i>	<i>P. ponderosa</i>	37.7
	<i>P. contorta</i>	3.8*
	<i>P. resinosa</i>	4.2*
<i>P. resinosa</i>	<i>P. palustris</i>	22.2***
	<i>P. ponderosa</i>	5.3*
	<i>P. contorta</i>	66.5****
<i>P. palustris</i>	<i>P. ponderosa</i>	4.6*
	<i>P. contorta</i>	14.9***
	<i>P. ponderosa</i>	<i>P. contorta</i>

a. Quality factor significant difference levels between aroma classes: * = P < 0.05; ** = P < 0.01; *** = P < 0.001; **** = P < 0.0001. The percentages of the total variance, accounting for the variability explained by each orthogonal principal component (PC), are as follows: PC 1 = 95.26%; PC 2 = 4.27%; and PC 3 = 0.43%.

Because none of the wood sample identifications in this study were determined to be incorrect or ambiguous, the absence of false positives is an advantage for a diagnostic gas-sensing analysis method. Generally, e-noses are set to a level of specificity that preclude false positives and result in unknown determinations for samples that cannot be recognized or that have aroma profiles that are missing from the reference aroma library. The diagnostic specificity can be improved even further by building e-nose methods and libraries that are specific to particular sample types so that false positive determination are exceedingly rare.

The results of e-nose analyses of wood types in the current study were similar to those obtained in other related studies, but with fresh wood samples and similar or different e-nose technologies based on several different gas-sensing principles [28, 29]. Wilson et al. [28] identified and distinguished between twenty-three different angiosperm and gymnosperm wood types using fresh tree cores frozen at -20 C and thawed immediately prior to analysis with a A32S CP e-nose. Baietto et al. [29] utilized and compared the

performance of three different e-nose instruments, including the PEN3 metal-oxide (MOS) e-nose, the LibraNose quartz microbalance (QMB) e-nose, and the Aromascan A32S CP e-nose to effectively discriminate between different healthy wood types and wood decayed by various wood-rot fungi.

Aroma data profiles from e-nose analyses that provide some indications of chemical relatedness between plant species may be a new tool and means for studying chemotaxonomic relationships between woody plants based on their wood volatiles as well as relationships between non-woody plants based on leaf, stem, or floral volatiles.

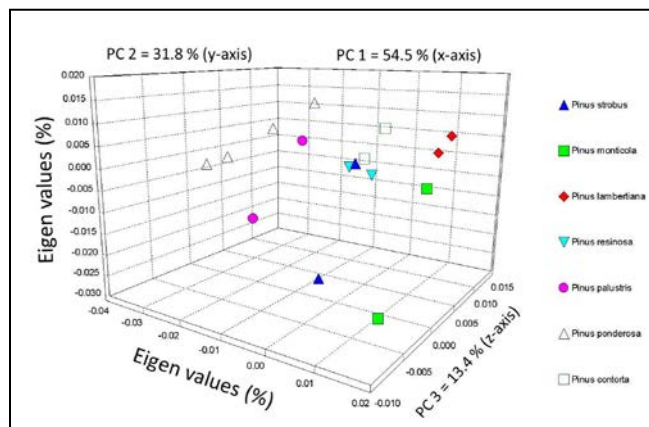


Figure 2. Aroma map showing the relatedness of wood volatiles from seven *Pinus* spp. using conductive polymer analysis (CPA).

Some possible reasons why the *P. menziesii* wood type could not be identified may include insufficient wood volatiles for analysis, the lack of sufficient principal components in adequate quantities to make up a representative aroma signature profile for this particular wood type, or the presence of particular wood VOCs to which the A32S e-nose sensors were not sufficiently sensitive, thus unable to generate a distinctive pattern of sensory outputs. This problem would no doubt be resolved with a fresher sample, but applying moisture to the sample surface and building headspace volatiles longer might help generate enough wood VOCs for analysis.

This study has demonstrated that a CP e-nose has the capability of identifying and discriminating wood types even when wood samples are aged in storage for long periods of time. The critical treatment of aged woods during sample preparation that made e-nose analysis possible was to wet the surface of the wood for a minimum of 15 min (followed by blotting) to facilitate the release of wood volatiles. Without wetting the wood sample surfaces, insufficient volatiles were generated to build headspace for an effective e-nose analysis. However, the wetting procedure should have no effect on the accuracy of results as long as sufficient volatiles are released to produce a sensory output (pattern) from the sensor array.

ACKNOWLEDGMENT

The author thanks Drs. Manuela Baietto and Daniele Bassi (Dipartimento di Produzione Vegetale, Università

degli Studi di Milano, Italy), as well as Dr. Francesco Ferrini (Dipartimento di Ortoflorofruitticoltura, Università di Firenze, Sesto Fiorentino (FI), Italy) for their collaborative research investigations of electronic-nose technologies with the author that facilitated the development of new international e-nose applications.

REFERENCES

- [1] G. Dodd and K. C. Persaud, "Analysis of discrimination mechanisms in the mammalian olfactory system using a model nose," *Nature*, vol. 299, pp. 352–355, Sept. 1982.
- [2] S. G. Shirley and K. C. Persaud, "The biochemistry of vertebrate olfaction and taste," *Sermm. Neurosci.*, vol. 2, pp. 59–68, 1990.
- [3] K. C. Persaud, "Electronic gas and odor detectors that mimic chemoreception in animals," *Trend. Anal. Chem.*, vol. 11, pp. 61–67, Feb. 1992.
- [4] J. W. Gardner, "Detection of vapours and odours from a multisensor array using pattern recognition: principal component and cluster analysis," *Sens. Actuators*, vol. 4, pp. 109–115, May 1991.
- [5] F. A. M. Davide, C. D. Natale, and A. D'Amico, "Self-organizing sensory maps in odour classification mimicking," *Biosens. Bioelectron.*, vol. 10, pp. 203–218, 1995.
- [6] M. C. Lonergan, E. J. Severin, B. J. Doleman, S. A. Beaber, R. H. Grubbs, and N. S. Lewis, "Array-based vapor sensing using chemically sensitive, carbon black-polymer resistors," *Chem. Mater.*, vol. 8, pp. 2298–2312, Sept. 1996.
- [7] J. White, J. S. Kauer, T. A. Dickinson, and D. R. Walt, "Rapid analyte recognition in a device based on optical sensors and the olfactory system," *Anal. Chem.*, vol. 68, pp. 2191–2202, July 1996.
- [8] H. V. Shurmer, J. W. Gardner, and H. T. Chan, "The application of discrimination techniques to alcohols and tobacco using tin oxide sensors," *Sens. Actuators*, vol. 18, pp. 359–369, July 1989.
- [9] H. Nanto, H. Sokooshi, and T. Kawai, "Aluminum-doped ZnO thin film gas sensor capable of detecting freshness of sea foods," *Sens. Actuators*, vol. 14, pp. 715–717, June 1993.
- [10] M. Egashira and Y. Shimizu, "Odor sensing by semiconductor metal oxides," *Sens. Actuators*, vol. 13, pp. 443–446, May 1993.
- [11] M. E. Meyerhoff, "Polymer membrane electrode based potentiometric ammonia gas sensor," *Anal. Chem.* vol. 52, pp. 1532–1534, Aug. 1980.
- [12] H. S. Yim, C. E. Kibbey, S. C. Ma, D. M. Kliza, D. Liu, S. B. Park, C. E. Torre, and M. E. Meyerhoff, "Polymer membrane-based ion-, gas- and bio-selective potentiometric sensors," *Biosens. Bioelectron.*, vol. 8, pp. 1–38, 1993.
- [13] A. M. Pisanelli, A. A. Qutob, P. Travers, S. Szyszko, and K. C. Persaud, "Applications of multi-array polymer sensors to food industries," *Life Chem. Rep.*, vol. 11, pp. 303–308, 1994.
- [14] J. V. Hatfield, P. Neaves, P. J. Hicks, K. C. Persaud, and P. Tavers, "Toward an integrated electronic nose using conducting polymer sensors," *Sens. Actuators*, vol. 18, pp. 221–228, Mar. 1994.
- [15] H. Bai, C. Li, F. Chen, and G. Shi, "Aligned three-dimensional microstructures of conducting polymer composites," *Polymer*, vol. 48, pp. 5259–5267, Aug. 2007.
- [16] T. Aishima, "Discrimination of liqueur aromas by pattern recognition analysis of responses from a gas sensor array," *Anal. Chim. Acta*, vol. 243, pp. 293–300, 1991.
- [17] S. Hanaki, T. Nakamoto, and T. Moriizumi, "Artificial odor recognition system using neural network for estimating sensory quantities of blended fragrance," *Sens. Actuators*, vol. 57, pp. 65–71, Oct. 1996.
- [18] P. N. Bartlett, J. M. Elliott, and J. W. Gardner, "Electronic noses and their applications in the food industry," *Food Technol.*, vol. 51, pp. 44–48, 1997.
- [19] C. Di Natale, F. A. M. David, A. D'Amico, G. Sberveglieri, P. Nelli, G. Faglia, and C. Perego, "Complex chemical pattern recognition with sensor array: the discrimination of vintage years of wine," *Sens. Actuators*, vol. 25, pp. 801–804, Apr. 1995.
- [20] C. Di Natale, J. A. J. Brunink, and F. Bungaro, "Recognition of fish storage time by a metalloporphorins-coated QMB sensor array," *Meas. Sci. Technol.*, vol. 7, pp. 1103–1114, Aug. 1996.
- [21] P. J. Hobbs, T. H. Misselbrook, and B. F. Pain, "Assessment of odours from livestock wastes by a photoionization detector, an electronic nose, olfactometry, and gas chromatography–mass spectrometry," *J. Agric. Eng. Res.*, vol. 60, pp. 137–144, Feb. 1995.
- [22] K. C. Persaud, S. M. Khaffaf, P. J. Hobbs, T. H. Misselbrook, and R. G. Sneath, "Application of conducting polymer odor sensing arrays to agricultural malodour monitoring," *Proc. International Conference on Air Pollution from Agricultural Operations*, Midwest Plan Service, Kansas City, MO, 1996, pp. 249–253.
- [23] A. D. Wilson, D. G. Lester, and C. S. Oberle, "Development of conductive polymer analysis for the rapid detection and identification of phytopathogenic microbes," *Phytopathology*, vol. 94, pp. 419–431, May 2004.
- [24] J. Ouellette, "Electronic noses sniff out new markets," *Ind. Phys.*, vol. 5, pp. 26–29, 1999.
- [25] B. Yea, R. Konishi, T. Osaki, and K. Sugahara, "The discrimination of many kinds of odor species using fuzzy reasoning and neural networks," *Sens. Actuators*, vol. 45, pp. 159–165, Nov. 1994.
- [26] A. D. Wilson and M. Baietto, "Applications and advances in electronic-nose technologies," *Sensors*, vol. 9, July 2009, pp. 5099–5148, doi:10.3390/s90705099.
- [27] A. D. Wilson and M. Baietto, "Advances in electronic-nose technologies developed for biomedical applications," *Sensors*, vol. 11, Jan. 2011, pp. 1105–1176, doi:10.3390/s110101105.
- [28] A. D. Wilson, D. G. Lester, and C. S. Oberle, "Application of conductive polymer analysis for wood and woody plant identifications," *For. Ecol. Managem.*, vol. 209, pp. 207–224, May 2005.
- [29] M. Baietto, A. D. Wilson, D. Bassi, and F. Ferrini, "Evaluation of three electronic noses for detecting incipient wood decay," *Sensors*, vol. 10, Jan. 2010, pp. 1062–1092, doi:10.3390/s100201062.

A Methanol Sensor Incorporating Nanostructured ZnO and Integrated Microheater on Thermally Isolated Planar MEMS Platform

Sudhir Chandra, Hardik Jeetendra Pandya, Anoop Lal Vyas

Indian Institute of Technology Delhi, Hauz Khas

New Delhi-110016, India

schandra@care.iitd.ernet.in, hjpele@yahoo.com, alvyas@iddc.iitd.ac.in

Abstract—A sensor incorporating nanostructured zinc oxide film on planar and thermally isolated MEMS platform is reported for detecting methanol vapours. An innovative technique for fabricating sensor having integrated microheater with improved mechanical strength is presented. The proposed innovation facilitates the sensor to achieve desired temperature on the chip at lower power. The sensors are capable of detecting methanol vapours at 50 °C and at room temperature (30 °C) with slightly reduced sensitivity. To achieve the operating temperature of 50 °C and 30 °C, the sensor requires only 40 and 20 mW of power respectively. The lower operating temperature has been achieved due to the use of nanostructured material as sensing layer. The sensor is capable of giving detectable response for concentrations of methanol vapor as low as 5 ppm.

Keywords- Nanostructured ZnO; Thermal evaporation; MEMS Platforms; Methanol sensor.

I. INTRODUCTION

In many industries, gases and volatile organic compounds (VOCs) are increasingly being used as raw materials and for this reason, it has become very important to develop highly sensitive detectors for these compounds. It is desirable that such devices should continuously monitor the VOCs and gases in the environment in quantitative and selective manner [1]. However, many of these devices have not yet reached commercial viability because of problems associated with the production worthiness of the gas sensing technologies. Selectivity, power consumption on account of heating requirements of the sensing layer and reliability are some of the issues which have not been adequately resolved for these sensors to be deployed on a large scale [2]. With the increasing demand for better gas sensors of higher sensitivity and greater selectivity, intense efforts are being made to find more suitable materials with the required surface and bulk properties for use in gas sensors. Detection and quantification of gaseous species in air as contaminants (polluting gases) at low cost is also becoming important.

The metal oxides have been explored and used as sensing layers in gas / VOC sensors for more than a decade [3, 4-10]. ZnO is one of the prominent metal oxide materials, which has been extensively investigated for gas/VOC sensors. This arises because of the high mobility of conduction electrons and good chemical and thermal

stability under the operating conditions. The use of nanostructured materials for the sensing device is envisaged to further improve the sensitivity of these devices at lower operating temperature [1-2, 11]. This is attributed to enormously increased surface to volume ratio compared to their thin films.

The sensors based on metal oxide materials operate at elevated temperatures (~ 300 °C) which results in higher power consumption [4, 8, 10]. To reduce the heat loss and thus power consumption, the thickness of the substrates is selectively reduced [12]. The thinning of the substrate results in reduced mechanical strength of the substrate. As a result, extra care is required during packaging. The yield also becomes an important issue.

In the present work, the sensors are fabricated using two different techniques: (a) on suspended diaphragm of SiO₂ (~2 μm) and (b) thermally isolated planar platform. The proposed innovation facilitates the sensor to achieve desired temperature on the chip at lower power. The sensing film in both the cases is nanostructured ZnO. The sensors are capable of detecting the methanol vapours in the range of 5-50 ppm at fairly low operating temperature of 50 °C. Furthermore, the power consumption is also considerably reduced without compromising the mechanical strength of the substrate in the planar type thermally isolated platform presented here. To the best of our knowledge, this type of performance is not reported in the published literature.

II. EXPERIMENTAL WORK

A schematic drawing of the sensor on suspended diaphragm is shown in Fig. 1 and the corresponding process flowchart is shown in Fig. 2. The sensor was fabricated using 7-masks process sequence and used a combination of bulk-surface micromachining technique [13]. The starting silicon wafers were 280 μm thick, n-type, having 5–10 Ω-cm resistivity and (100) orientation. A layer of SiO₂ (1 μm) was grown by thermal oxidation process. A window was opened on front side of the wafer by lithography technique (mask #1) and a pit (2.5 mm x 2.5 mm and 5 μm depth) was formed using bulk micromachining which was carried out in 40% KOH solution at a temperature of 80 °C. ZnO was then deposited as sacrificial layer using RF magnetron sputtering technique and its thickness was chosen to be somewhat more than the pit depth [13, 14].

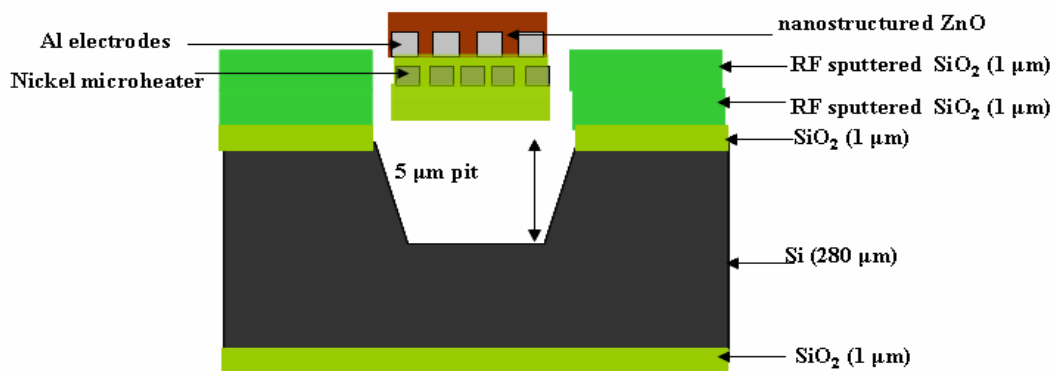
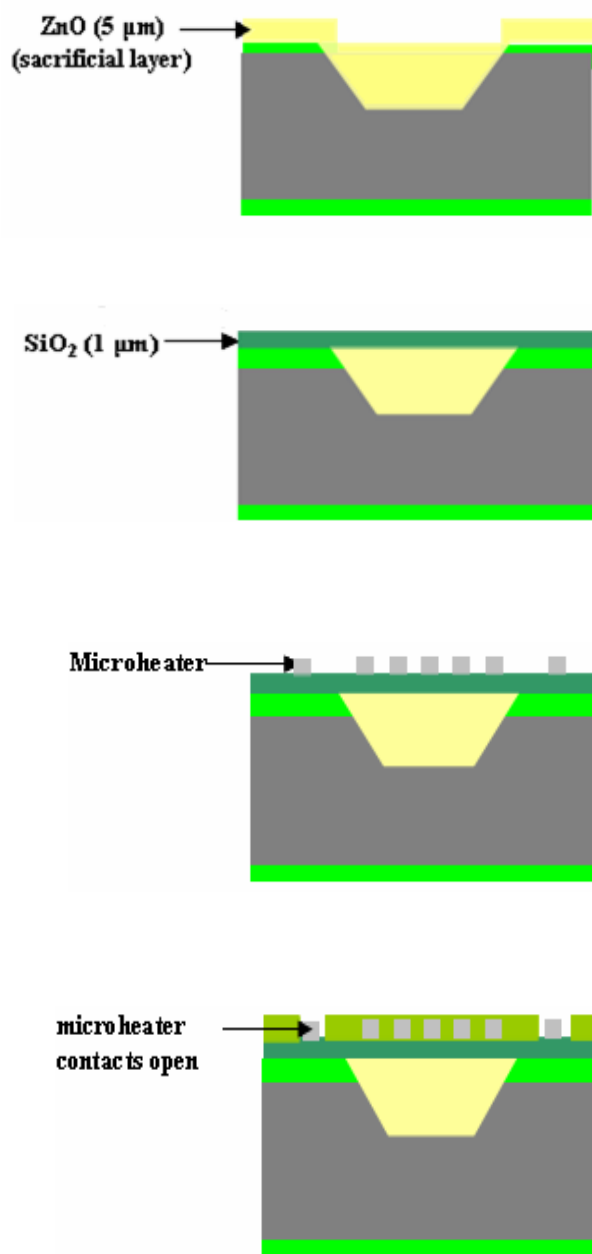


Figure 1. A schematic diagram of the MEMS gas sensor on a suspended platform.

The pit was planarized using lithography process (mask #2) followed by chemical mechanical planarization (CMP). Silicon dioxide layer (1 μm) was then sputter deposited on the wafer in the next step. A layer of nickel (0.3 μm thickness) was then deposited using RF diode sputtering over this SiO₂ layer. The Ni layer was then patterned using photolithography to form the microheater (mask #3). Over this, a layer of SiO₂ (1 μm) was again sputter deposited. The purpose of this layer was to electrically isolate the heater and the aluminum inter-digital electrodes to be formed in the next step. The SiO₂ from the microheater contacts was removed (mask #4). The aluminum layer of 0.8 μm was then deposited by thermal evaporation and patterned to form the sensing inter-digital electrodes (mask #5). A Zn film (0.3 μm) was selectively deposited using lift-off technique (mask #6) and annealed at 300 °C for 12 h in air ambient. The lift-off technique was used for patterning Zn as the etchant for Zn [HCl-DI water solution (1:100 by volume)] affects the Al. As the last step, the sacrificial layer was etched to complete the fabrication. The sacrificial layer etching was accomplished through lateral etching initiated from four windows formed outside the sensor area using photolithography (mask #7), as illustrated in the Fig. 2 and Fig. 5.



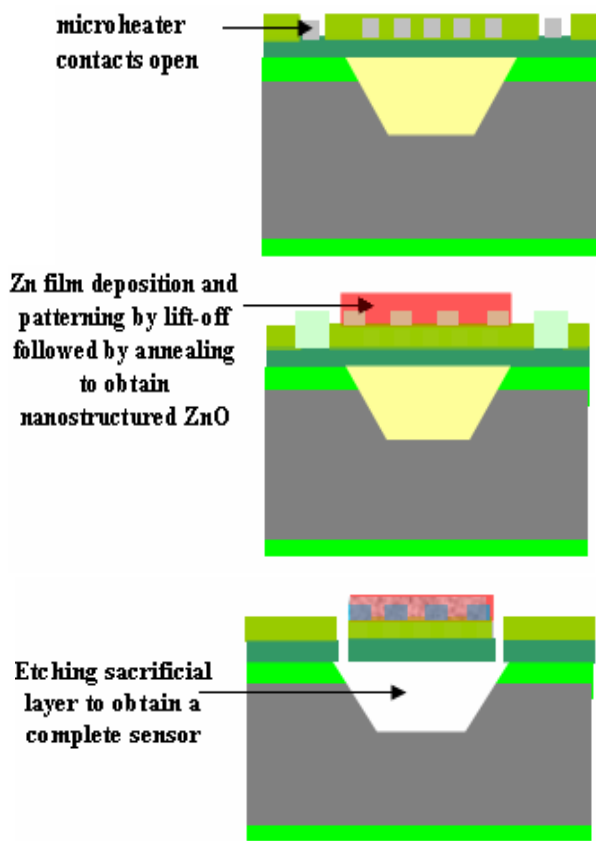


Figure 2. Process flowchart of sensor fabricated on suspended diaphragm.

In the second approach, the sensor was fabricated on a thermally isolated planar platform without using a suspended diaphragm. The blown-up diagram of the sensor fabricated using this technique is shown in Fig. 3 and the corresponding process flow is shown in Fig. 4.

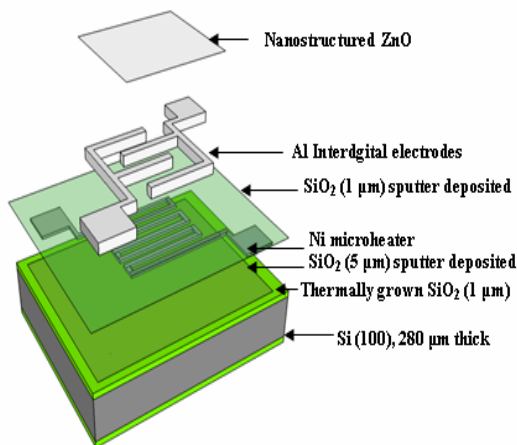


Figure 3. Blown-up diagram of the sensor fabricated on thermally isolated planar platform.

The sensor fabrication requires a 6-mask process sequence. The starting silicon wafers used were 280 μm thick, n-type, having 5–10 Ω-cm resistivity and (1 0 0) orientation. A layer of SiO₂ (1 μm) was grown by thermal oxidation process.

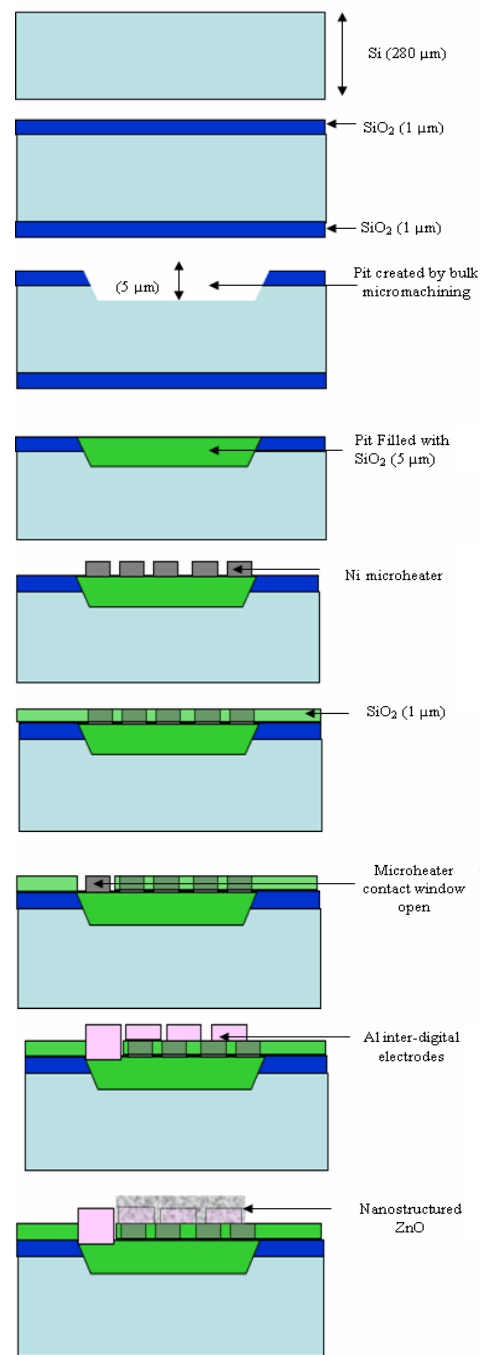


Figure 4. Process flow for sensor fabrication on thermally isolated planar platform and corresponding optical photographs at different steps.

A window was opened on front side by lithography technique (mask #1) and a pit (5mm x 5mm and 5 μm depth) was formed using bulk micromachining which was carried out in 40% KOH solution at a temperature of 80 °C. The pit was filled by SiO₂ deposited by RF magnetron sputtering process. The pit was planarized using photolithography (mask #2) and CMP. The rest of the process steps are identical to those used in the previous design. The advantage of fabricating sensor using the above mentioned process is that the complete sensor is fabricated on silicon substrate using trench formation, backfill and CMP. Thus there is no diaphragm or hanging structure. The mechanical strength of the substrate is retained in this approach. The optical photographs of the sensors fabricated on suspended diaphragm (2 μm) and on thermally isolated platform are shown in Fig. 5.

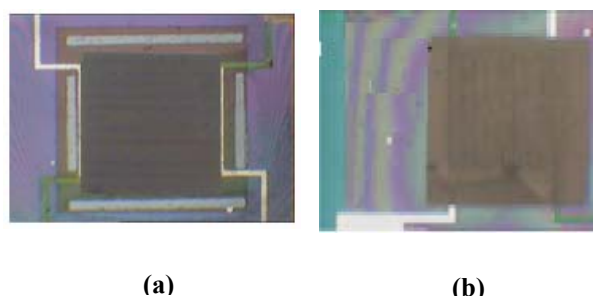


Figure 5. Optical photograph of sensor fabricated on (a) diaphragm (2 μm) and (b) using thermally isolated platform technology.

III RESULTS AND DISCUSSION

Fig. 6 shows the plot of power consumption versus temperature for the sensors fabricated on suspended diaphragm (2 μm) and sensor fabricated using thermally isolated platform.

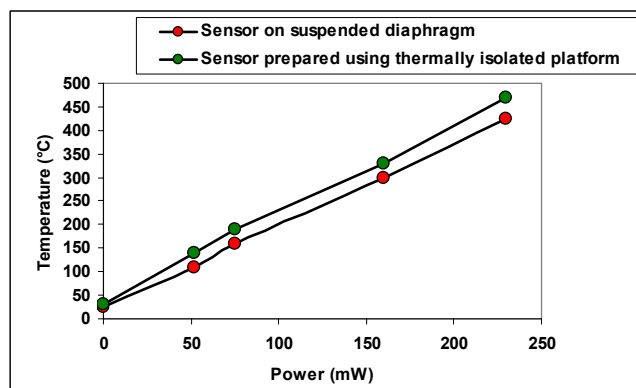


Figure 6. Power versus temperature plot of microheater fabricated on suspended diaphragm (2 μm) and sensor fabricated using thermally isolated platform technology.

It can be concluded that the electrical power required to raise the temperature of the sensing layer to required level is

considerably reduced because of improved thermal isolation of the sensor fabricated on suspended diaphragm. For example, a temperature of 175 °C is reached at a power of 80 mW for a sensor prepared on suspended diaphragm and same temperature is achieved at a power of 90 mW for sensor fabricated using thermally isolated platform technology. In contrast, the power consumption for the same operating temperature of the sensor made on conventional silicon substrate has been simulated and measured to be about 235 mW. The advantage of using thermally isolated planar platform technology is that the mechanical strength of the substrate is not compromised while the power consumption is also very low.

The SEM image of nanostructured ZnO film is shown in Fig.7. The VOC sensing results of the sensors fabricated on thermally isolated platform are now presented. The sensor was tested for methanol vapors in a closed chamber [15]. The sensor was heated to different temperatures by applying power to the integrated heater. The methanol vapors were introduced in the chamber by bubbling N₂ through the methanol maintained at room temperature (20 °C). The desired concentration of the vapors was obtained in the chamber by controlling the flow rate of N₂ through methanol and adding pure air through a separate gas line [15].

The flow rates were measured and controlled using precision flow meters. The concentration of methanol vapors was calculated using the following equation [16].

$$C = \frac{\frac{P^* \times L}{760 - L}}{\frac{P^* \times L}{760 - L} + L + L^*} \times 10^6 \quad (1)$$

where, L and L* are gas flow rates of N₂ (through the bubbler) and air respectively. P* is the vapor pressure of the methanol (in mm of Hg) at room temperature (20 °C).

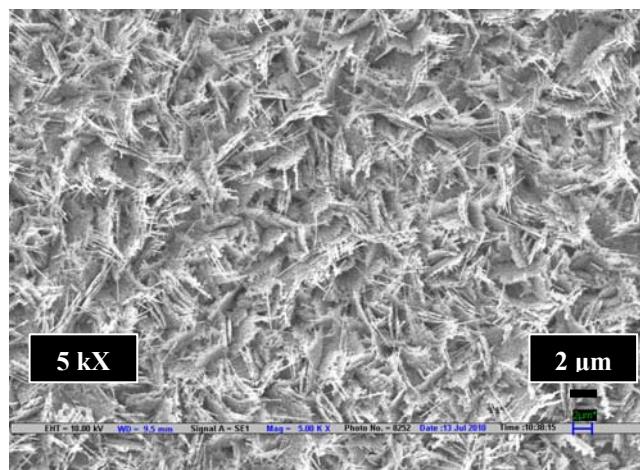


Figure 7. SEM image of ZnO nanocombs obtained after annealing Zn film (300 nm) at 300 °C for 12 h.

The focus of the present work is to develop energy efficient sensors that can operate near room temperature. This is an important consideration for the sensors to be deployed at remote places and are battery operated. The power consumption becomes an important issue. Accordingly, one of the primary aims of the present work is to develop the sensor, which can give appreciable response at lower operating temperatures. This will result in lower power consumption of integrated microheater thereby prolonging the life of the battery. It was observed that at 50 °C, the power consumption of the microheater was significantly less as compared to the corresponding value at 150 °C. Also, the sensor response at 50 °C is appreciable. A comparison of the sensor response at 30, 50, 100 and 150 °C is presented in Fig. 8 to illustrate this point.

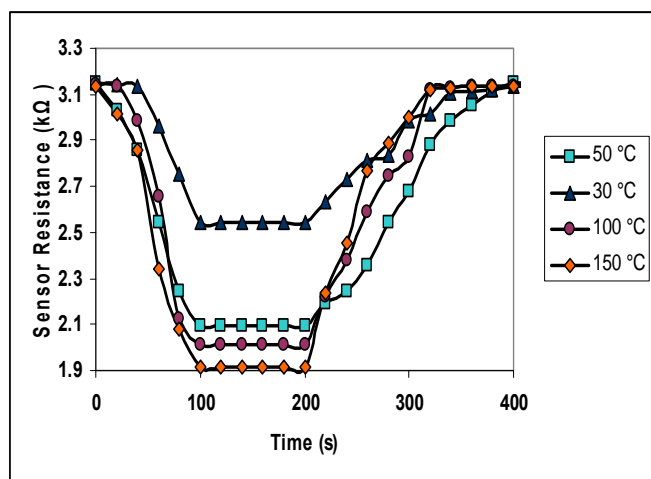


Figure 8. Response of the sensor to 50 ppm of methanol vapors at different operating temperatures.

The response of the sensor at 50 °C for other VOCs is shown in Fig. 9. It can be clearly observed that the sensor shows detectable change in resistance at such a low operating temperature. It was observed that at 50 °C, the change in sensor resistance is significant for methanol vapors as compared to other VOCs. This shows that at operating temperature of 50 °C, the sensor is somewhat selective to methanol. The power required to achieve a temperature of 50 °C is only about 40 mW.

The dynamic response of the sensor to different concentrations of methanol vapors at 50 °C operating temperature is shown in Fig. 10. The sensor is capable of detecting methanol vapors down to 5 ppm level. The sensor showed repeatable response with response time of 80 s and recovery time of about 120 s. The large values of response and recovery times are attributed to the large size of the chamber used for testing and does not represent the inherent response time of the sensor [15].

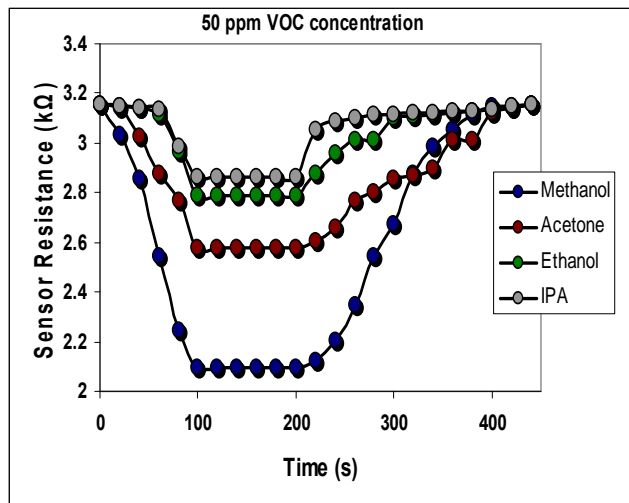


Figure 9. Response of the sensor to different VOCs at 50 °C operating temperature.

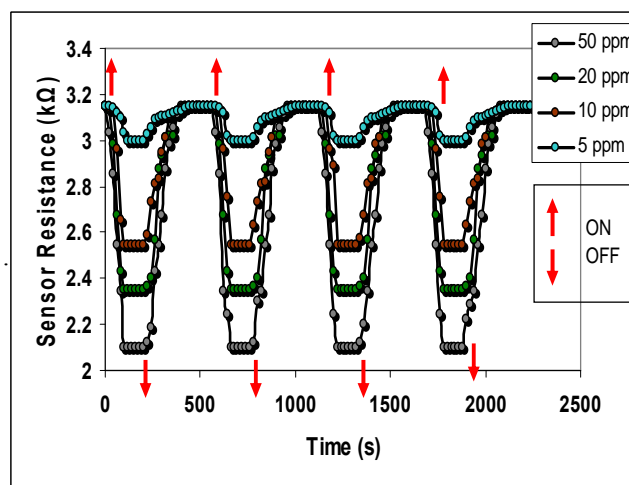


Figure 10. Dynamic response of the sensor for different concentration of methanol vapors at operating temperature of 50 °C. The arrows indicate the switching ON and OFF of N₂ flowing through the bubbler containing methanol.

From these studies, it can be inferred that, if at a given time, several VOCs are present, then the sensor developed in the present work cannot distinguish these individually. However, one can use this sensor in application such as electronic nose where there is an array of sensitive sensors and the response can be given to artificial neural network for training and testing purpose. Identifying a particular VOC in presence of several other VOCs continues to be a challenge.

IV. CONCLUSION

The aim of the present work was to develop energy efficient sensors, which are capable of operating at considerably reduced temperatures. For this purpose, nanostructured ZnO was synthesized using a catalyst-free process and the same was integrated with MEMS processing. To reduce the power consumption of the microheater integrated with the sensor, an innovative technique for fabricating the sensors on a planar and thermally isolated MEMS platform is presented. It has been demonstrated that the fabricated sensors are energy-efficient. The sensor is prepared using low cost materials and is capable of detecting methanol vapors at 50 °C utilizing only 40 mW of power. The sensor showed quite a large change in its resistance on exposure to methanol at 50 °C. The concept of a thermally isolated oxide platform is implemented using technologies which are standard processes in integrated circuit and MEMS manufacturing. The mechanical strength of the silicon substrate is not compromised in the present technology, as is the case when similar levels of power reduction is achieved by creating a cavity by partial etching of silicon from the back side or making a sensor on a suspended diaphragm. The standard packaging techniques can be used for the innovative sensors developed in the present work as the silicon wafer has no cavities in it. The proposed process does not require any modification in mask design, when the substrate thickness changes because of wafers of different diameter. Double-side polished wafer is also not needed in the present work. The issues of compatibility of sensing layer material with etchants used for the formation of sensing electrode of aluminum are completely resolved by using lift-off process for patterning the Zn film.

ACKNOWLEDGEMENT

Hardik Jeetendra Pandya acknowledges the financial support received from NAIP, ICAR Project Number C10125 (Component-4).

An Indian Patent application (1802/DEL/2012 dated 12 June 2012) has been filed covering some of the innovations presented here.

REFERENCES

- [1] A. Mandeles and C. Christofides, "Physics, Chemistry and Technology of Solid State Gas Sensor Devices" (John Wiley & Sons, Inc., New York, 1993).
- [2] D. M. Wilson and S. P. DeWeerth, "Signal Processing for Improving Gas Sensor Response Time", *Sensors Actuators, B*, 41, pp. 63–70, 1997.
- [3] R. Mukhopadhyay, "Don'tWaste Your Breath", *Analytical Chemistry*, pp.273-276, 2004.
- [4] M. Stankova, X. Vilanova, J. Calderer, E. Llobet, J. Brezmes, I. Gr'acia, C. Can'e and X. Correig, "Sensitivity and Selectivity Improvement of RF Sputtered WO₃ Microhotplate Gas Sensors", *Sensors Actuators B*, vol. 113, pp. 241–248, 2006.
- [5] J. P. Viricelle, A. Pauly, L. Mazet, J. Brunet, M. Bouvet, C. Varenne and C. Pijolat, "Selectivity Improvement of Semi-Conducting Gas Sensors by Selective Filter for Atmospheric Pollutants Detection", *Mater. Sci. Eng., C*, 26, pp. 186–195, 2006.
- [6] S. R. Morrison, "Selectivity in Semiconductor Gas Sensors", *Sensors Actuators, B*, 12, pp. 425–440, 1987.
- [7] R. Ionescu and E. Llobet, "Wavelet Transform-Base Fast Feature Extraction from Temperature Modulated Semiconductor Gas Sensors", *Sensors Actuators, B*, 81, pp. 289–295, 2002.
- [8] N. Yamazoe, G. Sakai and K. Shimanoe, "Oxide Semiconductor Gas Sensor", *Catal. Surv. Asia*, 7, pp.63–75, 2003.
- [9] M. E. Franke, T. J. Koplín and U. Simon, "Metal and Metal Oxide Nanoparticles in Chemi-resistors: Does the Nanoscale matter?", *Small*, 2, pp. 36–50, 2006.
- [10] Q. Wan, Q. H. Li, Y. J. Chen, T. H. Wang, X. L. He, J. P. Li and C. L. Lin, "Fabrication and Ethanol Sensing Characteristics of ZnO Nanowire Gas Sensors", *Appl. Phys. Lett.*, 84, pp.3654–3656, 2004.
- [11] E. Comini, G. Faglia, G. Sberveglieri, Z. Pan and Z.L. Wang, "Stable and highly sensitive gas sensors based on semiconducting oxide nanobelts", *Appl Phys Lett*, 81, pp. 1869–1871, 2002.
- [12] K.D. Mitzner, J. Strnhagen and D.N. Glipeau, "Development of micromachined hazardous gas sensor array", *Sensors Actuators B*, 93, pp. 92–99, 2003.
- [13] V. Bhatt and S. Chandra, "Planar Microstructures Using Modified Surface Micromachining Process", *Sensor Letters*, 5, pp.387-391, 2007.
- [14] V. Bhatt, Prem Pal and S. Chandra, "Feasibility Study of RF Sputtered ZnO Film for Surface Micromachining", *Surface and Coating Technology*, 198, pp.304-308, 2005.
- [15] H.J. Pandya, Sudhir Chandra and A.L.Vyas, "Fabrication and characterization of ethanol sensor based on RF sputtered ITO films", *Sensors and Transducers*, 10, pp. 141-150, 2011.
- [16] C.B. Lim, J.B. Yu, D.Y. Kim, H.G. Byun, D.D. Lee and J.S. Huh, "Sensing characteristics of nano-network structure of polypyrrole for volatile organic compounds (VOCs) gases", *IEEE Sensors*, pp. 695-698, 2006.

Development of Au Nano-particles Cladding-doped Optical Fiber for Surface Plasmon Resonance Sensor Applications

Seongmin Ju, Seongmook Jeong,
Youngwoong Kim, Poram Jeon,
and Won-Taek Han

*School of Information and
Communications/Department of
Photonics and Applied Physics,
Gwangju Institute of Science and
Technology,
Gwangju, South Korea
e-mail: jusm@gist.ac.kr,
seongmook@gist.ac.kr, kyw@gist.ac.kr,
porams@gist.ac.kr, wthan@gist.ac.kr*

Seongjae Boo

*Solar Center,
Korea Institute of Industrial
Technology,
Gwangju, South Korea
e-mail: sboo@kitech.re.kr*

Pramod R. Watekar

*Sterlite Optical Technologies,
E1, E2, E3, MIDC, Waluj,
Aurangabad, India
e-mail: pramod.watekar@sterlite.com*

Abstract — A novel optical fiber having its cladding doped with Au nano-particles was developed by modified chemical vapor deposition process. Absorption peaks of the optical fiber preform and the fiber appearing at 585 nm and 428 nm, respectively were due to surface plasmon resonance (SPR) of the incorporated Au nano-particles in the cladding. The measured peak wavelength of the SPR was found to increase from 480.9 nm to 505.5 nm with refractive index (n) from 1.406 to 1.436 and the SPR sensitivity was estimated to be 820 nm/RIU.

Keywords - nano-particles; cladding-doped optical fiber; absorption; surface plasmon resonance.

I. INTRODUCTION

Recently, optical fiber sensors based on surface plasmon resonance (SPR) have gained attraction of scientists and engineers due to their all-optical remote sensing capability to measure various chemical, physical, and biological quantities [1-11]. SPR sensing phenomenon of the optical fiber can be divided into two categories, a propagating SPR and a localized SPR. The former can be obtained from thin metal coating onto the surface of optical fiber and a surface plasmon comes from extended charge waves traveling on the interface of metal and glass that are excited when dispersion of output light matches with that of incident light. Therefore, it is evanescent electromagnetic waves bounded by metal-glass interfaces induced by oscillations of the conduction electrons in the metal [12-14]. The latter is usually observed by confined colloidal, periodic, nano-systems [6][14-25], and a localized surface plasmon gets resonantly excited when the wavelength of incident light is equal to the characteristic wavelength of metal nano-particles [11-14]. It comes from confined conduction electrons oscillating in resonance with the electromagnetic field. In general, the excitation of surface plasmon is known to occur when the wave vector of the propagation constant of evanescent wave exactly matches with that of the surface plasmon of similar frequency and

state of polarization. This occurs at a particular angle of incidence and the corresponding resonance condition for surface plasmons. The sharp absorption peak is observed at resonance angle because of reduction in the energy of the reflected light due to its energy transfer to surface plasmons. The resonance angle is very sensitive to variation in the refractive index of the sensing layer [1-5][8-11].

Optical fiber sensors based on SPR usually use thin metal film or nano-particles of Au or Ag because these noble metals present a sharp and intense plasmonic band in their internal reflectance spectrum when excited in the Kretschmann configuration of SPR [1-5][12-14]. To increase the sensitivity of optical fiber based SPR sensor, various configurations of optical fiber such as polished fiber, tapered fiber, grating fiber and coated fiber have been suggested [1-8][10-12][16]. Also, to improve the SPR sensing performance, effect of size, thickness, shape, and composition of plasmonic materials have been studied [4-6][25-28]. Despite all the efforts, however, optical fiber SPR sensors with controlled coating parameters have limitations: handling difficulty, difficulty of mass production, and high manufacturing cost.

In this paper, we developed a novel optical fiber incorporated with Au nano-particles (NPs) in cladding region, which is the first in the world to the best of our knowledge, allowing simple fabrication process due to no metal coating needed, mass production and compatibility with the existing SPR probe. Optical fiber sensor based on SPR of the fabricated fiber was demonstrated and in particular effect of environmental refractive index change on the SPR characteristics was investigated.

II. EXPERIMENTAL

The optical fiber incorporated with Au NPs in cladding region was fabricated by using the modified chemical vapor deposition (MCVD) and the fiber drawing processes. The

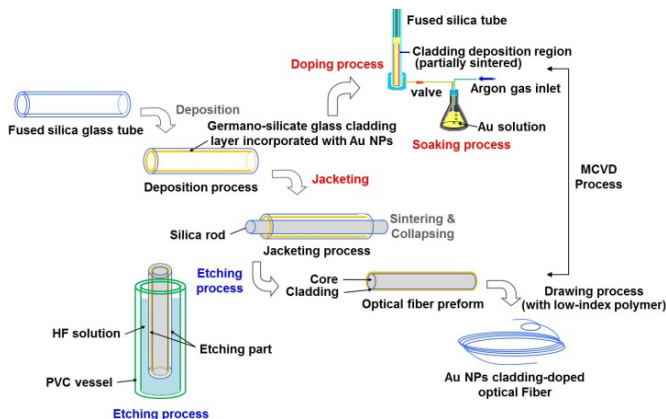


Figure 1. Schematic flow diagram of the fabrication process of the optical fiber incorporated with Au NPs in cladding region.

doping solution was prepared by dissolving 0.025 mole of reagent grade $\text{Au}(\text{OH})_3$ powder (Aldrich Chem. Co. Inc., 99.9 %) in nitric acid solution (Junsei Co., 70 %). To make a solid glass rod, known as a preform, the porous germano-silicate layers were deposited onto the inner surface of a silica glass tube by using primarily silicon tetrachloride (SiCl_4) and germanium tetrachloride (GeCl_4) in MCVD process. To incorporate Au NPs, the porous deposition layers were soaked with Au doping solution for two hours and the tube was dried and sintered. Then a silica glass rod (refractive index, $n = 1.4571 @ 633 \text{ nm}$) was inserted in the tube and consolidated into a rod to obtain a fiber preform. To reveal the doped layers to surface of the rod as a cladding, the outer part of the glass rod that was the silica glass tube, was etched off using hydrofluoric acid solution (J. T. Baker, 49%). The final preform consisted of the cladding doped with Au NPs in germano-silicate glass and the core of pure silica glass. Finally, the fiber preform was drawn into a fiber with $124.3 \mu\text{m}$ in diameter using the draw tower at $2150 \text{ }^\circ\text{C}$. During the drawing process, the fiber was coated with lower refractive index polymer (EFIRON UVF PC-375, $n = 1.3820$) than that of the germano-silicate glass of the cladding to

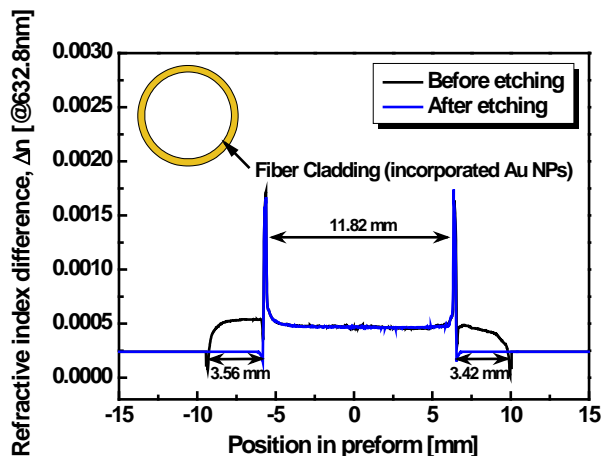


Figure 2. Measured refractive index profile of the fiber preform incorporated with Au NPs in cladding region (Inset: cross-section of the preform).

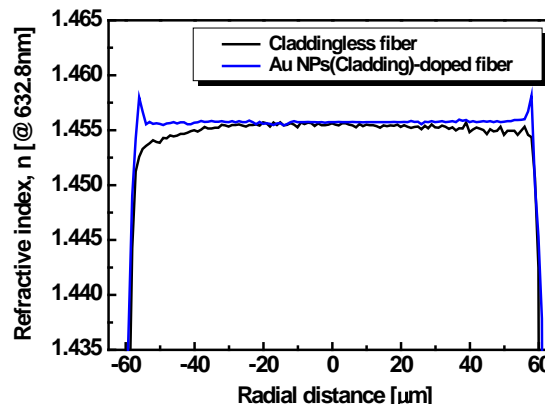


Figure 3. Measured refractive index profile of the optical fiber incorporated with Au NPs in cladding region.

induce total internal reflection for light transmission. A process flow steps to fabricate the optical fiber incorporated with Au NPs in cladding region are shown in Figure 1.

Figure 2 and Figure 3 show the measured refractive index profile of the fabricated optical fiber preform before and after the etching process and the optical fiber incorporated with Au NPs in cladding region, respectively. Successful removal of the silica glass tube by the etching process was indicated by the measured indices of the preform and the fiber as shown in Figure 2 and Figure 3, respectively. The refractive index difference between the core and cladding was about 0.00125, enabling light signal to propagate into the cladding region not into the core, as shown in Figure 4. The cladding width and total diameter of the optical fiber were $2.6 \mu\text{m}$ and $124.3 \mu\text{m}$, respectively. To confirm formation of Au NPs in the cladding, the optical fiber preforms were examined by transmission electron microscope (TEM, FEI Tecnai G2 F30 S-TWIN) and UV-VIS spectrophotometer (Varian, Cary500Scan). Optical absorption of the optical fibers was also measured to confirm the propagation of light and the existence of Au NPs by the cut-back method using the Optical Spectrum Analyzer (Ando AQ 6315B). Then, to characterize SPR sensing property, optical absorption of the fiber was measured by putting small drops of the refractive index matching oil with various refractive indices ($n = 1.406 - 1.436$) on the surface of the fiber. The total and detector length of the fiber used for the SPR measurement are 50 cm and 5 cm, respectively, as shown in Figure 5.

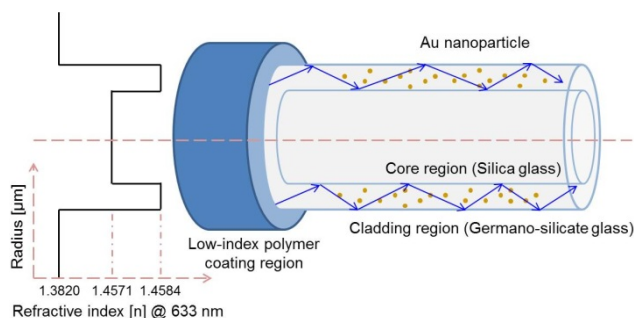


Figure 4. Refractive index and the propagation of light through the cladding of the fiber doped with Au NPs.

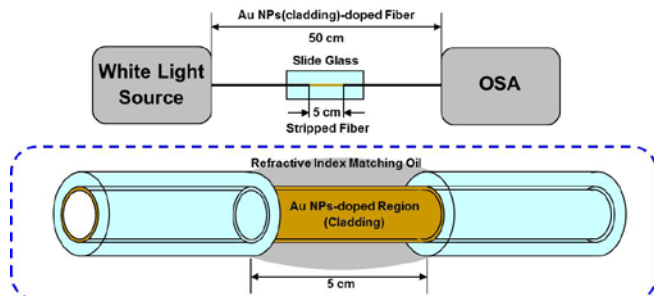


Figure 5. Schematic of the SPR measurement set-up using the optical fiber incorporated with Au NPs in cladding region.

III. RESULTS AND DISCUSSION

Figure 6 compares the UV-VIS spectra of the optical fiber preform incorporated with and without Au NPs. The absorption band centering at 585 nm was found to appear after the incorporation of Au NPs and it was attributed to Au NPs in the cladding region of the preform [29-31]. The existence and size distribution of Au NPs of the preform was verified by the TEM morphology of the fiber preform, as shown in Figure 7. The Au NPs was found to be crystalline and the rather spherical particles were dispersed homogeneously without agglomeration. The average

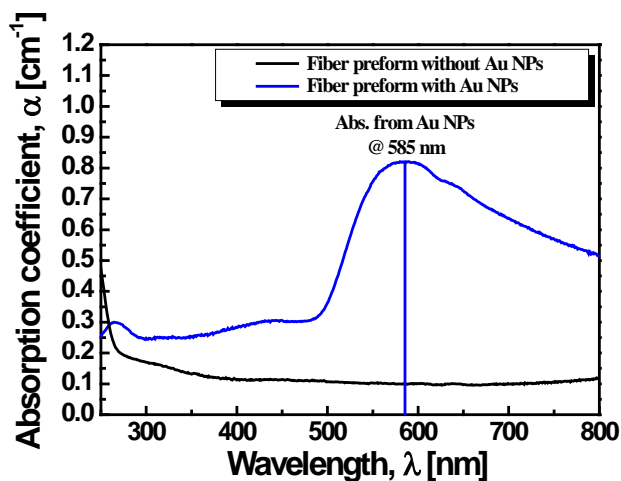


Figure 6. UV-VIS spectra of the optical fiber preform incorporated with and without Au NPs in cladding region.

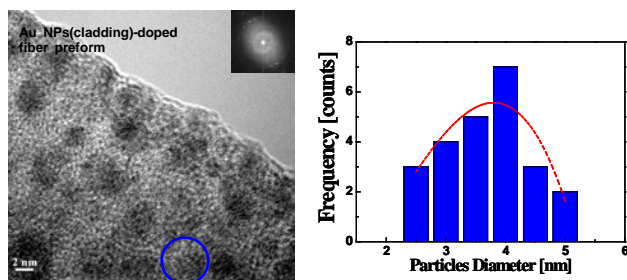


Figure 7. TEM image and the size distribution of Au NPs incorporated in the cladding of the optical fiber preform.

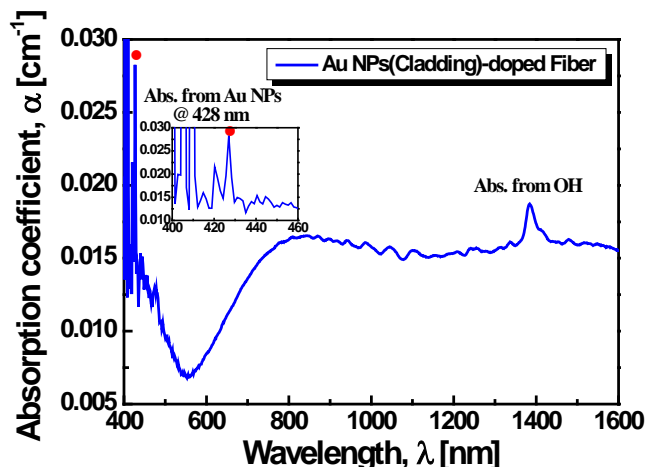


Figure 8. Absorption spectrum of the optical fiber incorporated with Au NPs in cladding region.

diameter of Au NPs was ~ 3.8 nm (2.5 nm \sim 5.2 nm). Note that peak position of the optical absorption is known to depend on the particle size of Au metals [31-33].

In the case of optical fiber, which was drawn from the fiber preform incorporated with Au NPs, the existence of Au NPs was verified by optical absorption spectra, as shown in Figure 8. Absorption peaks appeared at 428 nm and 1380 nm and they are due to surface plasmon resonance from Au NPs and OH impurities, respectively [30-34]. Note that to extract the absorption peak from the detector noise, we performed the spectral decomposition and denoising by using the OriginPro-8.6 code, which clearly distinguishes the absorption peak at 428 nm as shown in Figure 9.

As per earlier reported work, the Au NP related absorption peak has been observed at around 520 nm; however we measured the absorption peak at 585 nm in the optical fiber preform. Moreover, the absorption peak due to Au NPs was found to shift to shorter wavelength of 428 nm in the optical fiber as compared to 585 nm peak in the

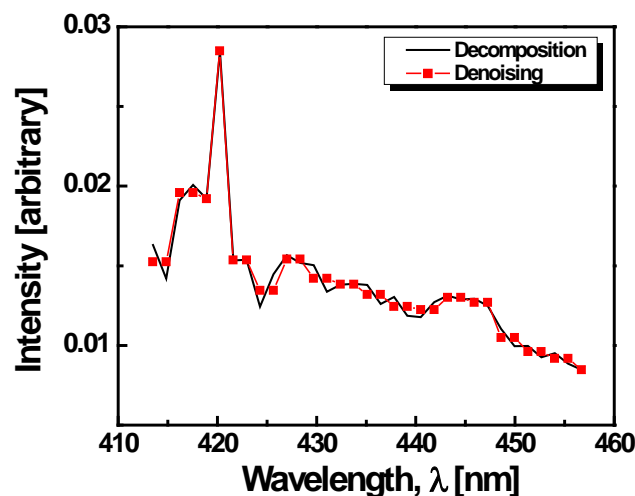


Figure 9. Resolving the absorption peak in the optical fiber incorporated with Au NPs in cladding region.

preform. As we needed to heat the fiber preform at 2150 °C to draw the fiber, Au NPs size would increase due to the growth of Au NPs after the high temperature drawing process. Thus, our sample showed the blue-shift of Mie resonance absorption peak with increment in the size of nano-particles, which is quite opposite behavior where increment in nano-particles size gives red shift in the absorption peak [35-37].

The blue-shift of SPR peak with the increase of nano-particles size is not a new behavior, it has been already reported for Au particles in Au-alumina composite film [38] and Au NPs dispersed within pores of porous silica [31-33]. The peak position from Mie resonance is almost independent of the size of Au particles in the range from 4 to 25 nm (by using the dielectric constant of Au [31][39][40]). The blue-shift can be thought to be due to association with the boundary coupling (interface interaction) between Au particles within the pores and pore walls of porous silica [31]. Usually, a small lattice contraction yields to the high surface-to-volume ratio and, hence, high surface energy (surface tension) for metal NPs. The lattice dilatation in [31-33], it is probably related to the decreased surface energy of Au particles via boundary coupling. It is well known that at the surface of small particles, there exist many dangling bonds (unsaturated bonds). In other words, the extension of electronic wave function outside particles surface becomes significant for small particles. Thus, interactions at the particles' surface are inevitable due to the high activity, and charge transfer from metal particles to the matrices occurs during interface interaction. This charge transfer can induce a decrease of the free electron density in metal particles. Therefore, the blue-shift occurs with the increase of Au particle size due to the electron charge transfer from Au particles to the silicate glass host at the interface.

Figure 10 shows the absorption spectra of the optical fiber after dropping the index matching oils ($n = 1.406 - 1.436$) to confirm the SPR and its dependence of environmental change. Because of noisy behavior of the output spectrum, FFT (Fast Fourier Transform) filtering method was adopted to locate peaks. The SPR band was found to occur at a particular wavelength around 500 nm for the corresponding refractive indices, increased with the increase of the index [1, 3][8-11]. The measured peak wavelength of the SPR band were at 480.9 nm, 483.3 nm, 494.4 nm, and 505.5 nm with refractive indices (n) 1.406, 1.416, 1.426, and 1.436, respectively as shown in Figure 11. The observed red-shift of the SPR band with the increase of the refractive index of matching oils is related to the angle of incident light, increased with the increase of refractive index [1-3][8-11]. The shift of the Au plasmon peak towards a longer wavelength with the increase of the medium refractive index can be understood by the well-known Mie theory. It is noted that the absorption peak of the fiber coated with low-index polymer ($n=1.382$) appearing at 428 nm due to surface plasmon resonance from Au NPs was also found to shift to ~ 500 nm after dropping the index matching oils, which is basically an extension phenomenon by the Mie theory. The SPR sensitivity (wavelength/RIU), which is the slope of Figure 11, of the optical fiber incorporated with Au

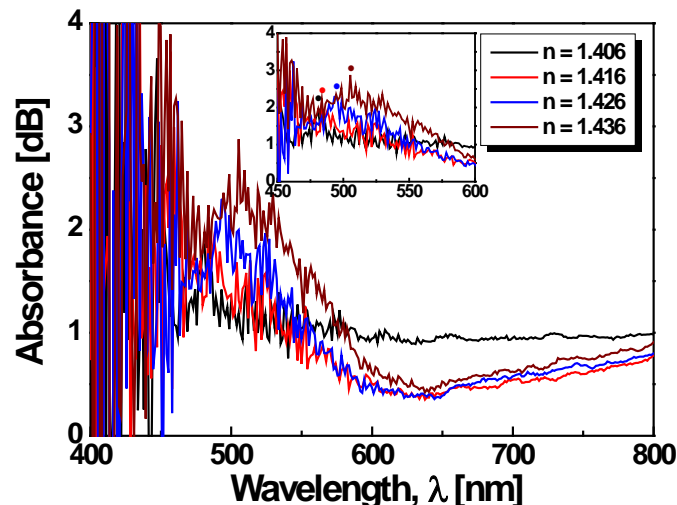


Figure 10. Absorption spectra of the Au NPs(doped) optical fiber covered with the index matching oils of different refractive indices ($n = 1.406 - 1.436$).

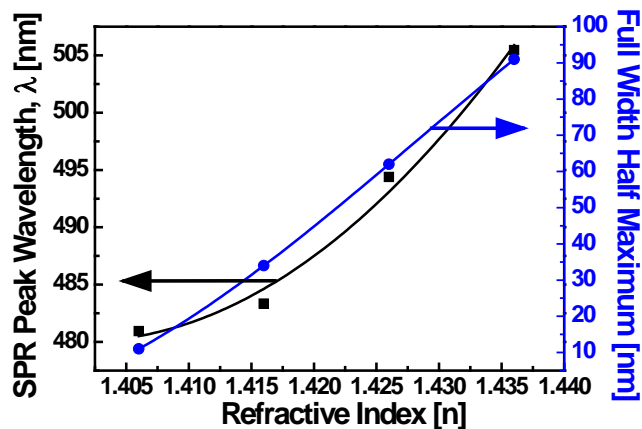


Figure 11. Peak and width change of the surface plasmon resonance (SPR) peak of the Au NPs(doped) optical fiber covered with the index matching oils of different refractive indices ($n = 1.406-1.436$).

NPs was estimated to be 820 nm/RIU. Indeed, the SPR sensitivity of optical fiber sensor based on glass optical fiber incorporated with Au NPs in the cladding region is smaller than that of the conventional Au thin film based optical fiber SPR sensor, which has about 9,630 nm/RIU [41]. However, 820 nm/RIU is still a valuable level to identify the possibility of a new type fiber SPR sensor for its advantage of mass production. In this paper, we have focused on the fabrication of specialty optical fiber incorporated with Au NPs in cladding region for SPR sensor applications, which is the first in the world to the best of our knowledge. Increase of the sensitivity of the sensor is under progress and will be communicated in future.

It is noted that the increase in intensity and width of the SPR absorption band was also found to be 1.5 dB and 91 nm (after baseline correction), respectively with the increase of the refractive index from 1.406 to 1.436. The broadening of the SPR absorption may be due to the spatial spreading and scattering of the conduction electrons [42].

The proposed fiber sensor based on optical fiber incorporated with Au NPs in the cladding region has the clear advantages over the conventional Au thin film based optical fiber SPR sensor such that the bulk metal film coating is not necessary after post-processings of fiber polishing and tapering to satisfy the phase matching criterion for excitation. Since no metal coating is needed for the sensor, mass production with simple fiber fabrication is possible and compatibility with the existing SPR probe is secured.

IV. CONCLUSION

We developed and demonstrated specialty optical fiber incorporated with Au NPs in cladding region for SPR sensor applications. The optical fiber incorporated with Au NPs in cladding region was fabricated by using the modified chemical vapor deposition (MCVD) and the fiber drawing process. Porous germano-silicate layers were deposited onto the inner surface of a silica glass tube and the layers were soaked with Au doping solution to incorporate Au NPs followed by drying and sintering. Then a silica glass rod (refractive index, $n = 1.4571 @ 633 \text{ nm}$) was inserted in the tube and consolidated into a rod and the outer silica glass was etched off to obtain a fiber preform incorporated with Au NPs in cladding region. Finally, the fiber preform was drawn and coated with the lower refractive index polymer (EFIRON UVF PC-375, $n = 1.3820$) than that of the cladding to obtain a fiber with the cladding width of $2.6 \mu\text{m}$ and total diameter of $124.3 \mu\text{m}$.

The measured SPR absorption band centered at 585 nm of the optical fiber preform was attributed to the large concentration of the Au NPs with the average diameter of 3.8 nm . In the case of the fiber, the SPR absorption peak due to Au NPs was found to shift to 428 nm as compared to 585 nm of the preform. This blue-shift is due to the increase of the particle size through the growth of the Au NPs during the fiber drawing process at $2150 \text{ }^\circ\text{C}$, the absorption band of Au NPs within pores of porous silica yielded the significant blue-shift, which was interpreted in terms of interface interactions between Au NPs and silica glass host. The blue-shift of the absorption band in the present study may originate from the electron transfer from Au particles to the silica host during interfacial interaction.

The SPR absorption peak due to Au NPs in the bare optical fiber was found to appear at 428 nm . When the index matching oils was dropped onto the fiber, the SPR was found to occur at a particular wavelength around 500 nm . The measured peak wavelength of the SPR increased from 480.9 nm to 505.5 nm with refractive index (n) from 1.406 to 1.436 . The SPR sensitivities of the optical fiber incorporated with Au NPs in cladding region was estimated to be 820 nm/RIU .

ACKNOWLEDGMENTS

This work was supported partially by the Ministry of Science and Technology, the NRF through the research programs (No. 2008-0061843 and No. 20100020794), the New Growth Engine Industry Project of the Ministry of Knowledge Economy, the Core Technology Development

Program for Next-generation Solar Cells of Research Institute of Solar and Sustainable Energies (RISE), the Brain Korea-21 Information Technology Project, and by the (Photonics2020) research project through a grant provided by the Gwangju Institute of Science and Technology in 2012, South Korea.

REFERENCES

- [1] J. Homola, S. S. Yee, and G. Gauglitz, "Surface plasmon resonance sensors: review," *Sens. Actuators B*, vol. 54, pp. 3-15, September 1999.
- [2] C. van Trigt, "Visual system-response functions and estimating reflectance," *JOSA A*, vol.14, pp. 741-755, April 1997.
- [3] A. K. Sharma, R. Jha, and B. D. Gupta, "Fiber-optic sensors based on surface plasmon resonance: A comprehensive review," *IEEE Sens. J.*, vol. 7, pp. 1118-1129, August 2007.
- [4] B. D. Gupta and R. K. Verma, "Review article: Surface plasmon resonance-based fiber optic sensors: Principle, probe designs, and some applications," *J. Sens.*, vol. 2009, pp. 1-12, June 2009.
- [5] C. R. Yonzon, E. Jeoung, S. Zou, G. C. Schatz, M. Mrksich, and R. P. V. Duyne, "A comparative analysis of localized and propagating surface plasmon resonance sensors: The binding of concanavalin A to a monosaccharide functionalized self-assembled monolayer," *J. Am. Chem. Soc.*, vol. 126, pp. 12669-12676, September 2004.
- [6] S. Singh and B. D. Gupta, "Simulation of a surface plasmon resonance-based fiber-optic sensor for gas sensing in visible range using films of nanocomposites," *Meas. Sci. Technol.*, vol. 21, pp. 115202, September 2010.
- [7] A. K. Sharma and B. D. Gupta, "Simulation of a localized surface-plasmon-resonance-based fiber optic temperature sensor," *Opt. Soc. Am.*, vol. A 27, pp. 1743-1749, July 2010.
- [8] Y. Lin, Y. Zou, and R. G. Lindquist, "A reflection-based localized surface plasmon resonance fiber-optic probe for biochemical sensing," *Biomed. Opt. Express*, vol. 2, pp. 478-484, March 2011.
- [9] A. S. Yeri, L. Gao, and D. Gao, "Mutation screening based on the mechanical properties of DNA molecules tethered to a solid surface," *J. Phys. Chem. B*, vol. 114, pp. 1064-1068, January 2010.
- [10] R. Slavík, J. Homola, J. Čtyroký, and E. Brynda, "Novel spectral fiber optic sensor based on surface plasmon resonance," *Sens. Actuators B*, vol. 74, pp. 106-111, April 2001.
- [11] M. Mitsushio, S. Higashi, and M. Higo, "Construction and evaluation of a gold-deposited optical fiber sensor system for measurements of refractive indices of alcohols," *Sens. Actuators A*, vol. 111, pp. 252-259, March 2004.
- [12] B. Liedberg, C. Nylander, and I. Lunström, "Surface plasmon resonance for gas detection and biosensing," *Sens. Actuators*, vol. 4, pp. 299-304, May-June 1983.
- [13] H. Reather, *Surface plasmons on smooth and rough surfaces and on gratings* (Springer-Verlag: Berlin, 1988).
- [14] F. Yu, S. Ahl, A.-M. Caminade, J.-P. Majoral, W. Knoll, and J. Erlebacher, "Simultaneous excitation of propagating and localized surface plasmon resonance in nanoporous gold membranes," *Anal. Chem.*, vol. 78, pp. 7346-7350, October 2006.
- [15] T. R. Jensen, G. C. Schatz, and R. P. Van Duyne, "Nanosphere lithography: Surface plasmon resonance spectrum of a periodic array of silver nanoparticles by

- ultraviolet-visible extinction spectroscopy and electrodynamic modeling," *J. Phys. Chem. B*, vol. 103, pp. 2394-2401, February 1999.
- [16] J. M. Steele, Z. Liu, Y. Wang, and X. Zhang, "Resonant and non-resonant generation and focusing of surface plasmons with circular gratings," *Opt. Express*, vol. 14, pp. 5664-5670, June 2006.
- [17] N. Nath and A. Chilkoti, "Label-free biosensing by surface plasmon resonance of nanoparticles on glass: Optimization of nanoparticle size," *Anal. Chem.*, vol. 76, pp. 5370-5378, August 2004.
- [18] S. H. Chang, S. K. Gray, and G. C. Schatz, "Surface plasmon generation and light transmission by isolated nanoholes and arrays of nanoholes in thin metal films," *Opt. Express*, vol. 13, pp. 3150-3165, April 2005.
- [19] J. Aizpurua, P. Hanarp, D. S. Sutherland, M. Kall, G. W. Bryant, and F. J. G. de Abajo, "Optical properties of gold nanorings," *Phys. Rev. Lett.*, vol. 90, pp. 057401, February 2003.
- [20] J. Fu, B. Park, and Y. Zhao, "Nanorod-mediated surface plasmon resonance sensor based on effective medium theory," *App. Opt.*, vol. 48, pp. 4637-4649, August 2009.
- [21] J. Kim, G. L. Liu, Y. Lu and L. P. Lee, "Spectral tuning of localised surface plasmon-polariton resonance in metallic nano-crescents," *IEE Proc.-Nanobiotechnol.*, vol. 153, pp. 42-46, June 2006.
- [22] Z. W. Liu, Q. H. Wei, and X. Zhang, "Surface plasmon interference nanolithography," *Nano. Lett.*, vol. 5, pp. 957-961, April 2005.
- [23] N. Halas, "Playing with plasmons. Tuning the optical resonant properties of metallic nanoshells," *MRS Bull.*, vol. 30, pp. 362-367, May 2005.
- [24] P.-Y. Chung, T.-H. Lin, G. Schultz, C. Batich, and P. Jiang, "Nanopyramid surface plasmon resonance sensors," *Appl. Phys. Lett.*, vol. 96, pp. 261108, July 2010.
- [25] L. S. Live, O. R. Bolduc, and J.-F. Masson, "Propagating surface plasmon resonance on microhole arrays," *Anal. Chem.*, vol. 82, pp. 3780-3787, March 2010.
- [26] G. P. Anderson, J. P. Golden, L. K. Cao, D. Wijesuriya, L. C. Shriver-Lake, and F. S. Ligler, "Development of an evanescent wave fiber optic biosensor," *IEEE Eng. Med. Biol. Mag.*, vol. 13, pp. 358-363, June-July 1994.
- [27] T.-C. Peng, W.-C. Lin, C.-W. Chen, D. P. Tsai, and H.-P. Chiang, "Enhanced sensitivity of surface plasmon resonance phase-interrogation biosensor by using silver nanoparticles," *Plasmonics*, vol. 6, pp. 29-34, September 2011.
- [28] K.-S. Lee and M. A. El-Sayed, "Gold and silver nanoparticles in sensing and imaging: sensitivity of plasmon response to size, shape, and metal composition," *J. Phys. Chem. B*, vol. 110, pp. 19220-19225, September 2006.
- [29] J. Matsuoka, R. Mizutani, S. Kaneko, H. Nasu, K. Kamiya, K. Kadono, T. Sakaguchi, and M. Miya, "Sol-Gel processing and optical nonlinearity of gold colloid-doped silica glass," *J. Ceram. Soc. Jpn.*, vol. 101, pp. 53-58, January 1993.
- [30] S. Ju, N. V. Linh, P. R. Watekar, B. H. Kim, C. Jeong, S. Boo, C. J. Kim, and W.-T. Han, "Fabrication and optical characteristics of a novel optical fiber doped with the Au nano-particles," *J. Nanosci. Nanotechnol.*, vol. 6, pp. 3555-3558, November 2006.
- [31] H. Shi, L. Zhang, and W. Cai, "Preparation and optical absorption of gold nanoparticles within pores of mesoporous silica," *Mater. Res. Bull.*, vol. 35, pp. 1689-1691, December 2000.
- [32] W. Cai, H. Hofmeister, T. Rainer, and W. Chen, "Optical properties of Ag and Au nanoparticles dispersed within the pores of monolithic mesoporous silica," *J. Nanopart. Res.*, vol. 3, pp. 443-453, June 2001.
- [33] A. E. Badger, W. Weyl, and H. Rudow, "Effect of heat-treatment on color of gold-ruby glass," *Glass Ind.*, vol. 20, pp. 407-414, November 1939.
- [34] J. Stone, "Reduction of OH absorption in optical fibers by OH \rightarrow OD isotope exchange," *Ind. Eng. Chem. Prod. Res. Dev.*, vol. 25, pp. 609-621, December 1986.
- [35] S. Link and M. A. El-Sayed, "Spectral properties and relaxation dynamics of surface plasmon electronic oscillations in gold and silver nanodots and nanorods," *J. Phys. Chem.*, vol. 103, pp. 8410-8426, September 1999.
- [36] M.-C. Daniel and D. Astruc, "Gold nanoparticles: assembly, supramolecular chemistry, quantum-size-related properties, and applications toward biology, catalysis, and nanotechnology," *Chem. Rev.*, vol. 104, pp. 293-346, January 2004.
- [37] S. J. Oldenburg, R. D. Averitt, S. L. Westcott, and N. J. Halas, "Nanoengineering of optical resonances," *Chem. Phys. Lett.*, vol. 288, pp. 243-247, March 1998.
- [38] Y. Hosoya, T. Suga, T. Yanagawa, and Y. Kurokawa, "Linear and nonlinear optical properties of sol-gel-derived Au nanometer-particle-doped alumina" *J. Appl. Phys.*, vol. 81, pp. 1475-1480, October 1997.
- [39] C. F. Bohren and D. R. Huffman, *Absorption and scattering of light by small particles; Chapter. 12* (John Wiley & Sons, New York, 1983).
- [40] M. Otter, "Optische konstanten massiver metalle," *Z. Physik*, vol. 161, pp. 163-178, April 1961.
- [41] S. Ju, S. Jeong, Y. Kim, P. Jeon, H. S. Kim, M.-S. Park, J.-H. Jang, and W.-T. Han "Surface Plasmon Resonance of Au/Ti Coated Tapered Optical Fiber," in *Proceedings of The 5th International Conference on Surface Plasmon Photonics*, (Academic, Busan, Korea, 2011), TUP-72, May 2011.
- [42] Y. Zhang, A. H. Yuwono, J. Li, and J. Wang, "Highly dispersed gold nanoparticles assembled in mesoporous titania films of cubic configuration," *Micropor. Mesopor. Mater.*, vol. 110, pp. 242-249, June 2007.

A Smartphone System: Providing a Shoe-Embedded Interface

Kaname Takauchi, Kazuhiro Watanabe, Kazumasa Takami
 Information System Technology Department
 Graduate School of Engineering, Soka University
 Hachioji-shi, Tokyo, Japan
 {e10m5222, kazuhiro, k_takami}@t.soka.ac.jp

Abstract— Although a handsfree man-machine interface is useful when the user’s hands are not free, existing handsfree input devices are not the type of device that are normally worn by people. We focus on a shoe as an input device because people normally wear it when they go out, and propose a shoe-embedded interface. The input device is a sensor shoe. Weight sensors are attached at three positions on a sole: the first metatarsal, the fifth metatarsal, and the calcaneal tuberosity. These positions have been selected based on the characteristics of the human foot skeleton. Two types of foot operation have been used: tap and push. By combining these operations, 10 commands have been defined. The sensor shoe houses an insole with hetero-core optical fiber sensor elements attached to it. These elements are sensitive to weight. We have built an experimental system that runs on a smartphone and provides the shoe-embedded interface, and conducted experiments with three test subjects to evaluate the system. The average rate of successful command identification was 89%.

Keywords- shoe-embedded interface; heterocore optical fiber sensor; handsfree interface

I. INTRODUCTION

In the field of human-computer interaction, there are intensive studies on a man-machine interface [1]-[6]. A handsfree interface is useful for people who are in a public space and whose hands are not free, such as passengers holding baggage in an airport, parents holding small children, and golf players. Most handsfree interfaces with practical products already available use speech recognition. Speech recognition has been widely implemented in mobile information devices, such as smartphones, tablet terminals, and laptop PCs. Handsfree interfaces generally consist of an input device and a processing terminal. In cases where speech recognition is used, the input device is either built in a mobile information device or a microphone connected to the input port of a mobile information device, and the processing terminal is the mobile information device itself. The processing terminal conveys the user’s intention to a given application by extracting a word from the waveforms sent from the input device, and identifying a pre-defined command that matches the word.

In cases where the user is in a public space and his/her hands are not free, a problem with conventional human interfaces is that the user needs to wear an input device just for the purpose of acquiring this interface whether the input device is an earphone-equipped microphone or a headset for

voice input, a head-mounted display or eye-glass-like device for eye-tracking input, a cap-shaped input device for a brain-machine interface, or a camera to recognize a gesture or a motion. When the user does not need this interface, he/she has no need to wear such devices.

We have focused on a shoe because people always wear it when they go out. Specifically, we have chosen to use a shoe-embedded interface because it is suitable for use in a public space. The input device is a sensor shoe with a hetero-core optical fiber sensor element built in it [7]-[13]. The processing terminal is a smartphone. Section II gives an overview of the shoe-embedded interface. Section III describes three aspects of implementing the shoe-embedded interface: sensor shoe design, command input method, and command definition. Section IV describes the experimental system we have developed based on the proposed method. Section V reports on the experiment carried out using the experimental system, and evaluates the proposed method based on the experiment result. Finally, Section VI provides the conclusions and future work.

II. SHOE-EMBEDDED HUMAN INTERFACE

The shoe-embedded human interface is a wearable handsfree human interface. It consists of a sensor shoe and a processing terminal. A sensor shoe is a shoe with weight sensors. The weight sensors are attached to the insole of the user’s shoe. The user puts his/her weight on the sensors to input an operation. The sensors are so thin that the shoe appears to be a normal shoe. The processing terminal identifies the user’s operation from the weights measured by the sensors. The weight data is sent to the processing terminal using wireless communication. A smartphone is used as the processing terminal. Advantages of the proposed interface include resistance to noise, mobility and invisibility. The interface is highly resistant to noise because the user operates the sensor with his/her weight. It provides high mobility because the sensor shoe is not wired to the processing terminal. It is invisible to others because it requires only a sensor shoe and a smartphone. The user can use it without worrying about how he/she looks.

One of the criteria generally used to assess the ease of using a man-machine interface is usability. Usability is defined in ISO9241-11[14]-[16] as “extent to which a product can be used by specified users to achieve specified goals with effectiveness, efficiency and satisfaction in a

specified context of use.” ISO9241-11 goes on to define effectiveness as “accuracy and completeness with which users achieve specified goals,” efficiency as “resources expended in relation to the accuracy and completeness with which users achieve goals,” and satisfaction as “freedom from discomfort, and positive attitudes towards the use of the product.” Ishikawa [17] states that “usability is often evaluated in terms of the achievement of specified goals. In other words, it is evaluated with a defined evaluation task.” However, it is difficult to generalize the functions of the potential device that will be operated by the user. Therefore, we focus on the simple task of selecting a function when the user is in a public space and his/her hands are not free.

Figure 1 shows an example of the function selection task. In this example, the user in an airport selects the service of checking information about his/her reserved boarding pass from a list of services available. The user attaches his/her smartphone on the strap of his/her bag, and can see the display screen of the smartphone simply by looking down. First of all, the user inputs a start command to shift the system’s state from the walking state to the input state. Then, the processing terminal sends to the server an inquiry about services that are available at the airport, obtains a list of available services from the server, and displays it for the user. A unique command identifier is associated with each service. The user can recognize the associations between services and command identifiers from the positions of the identifiers on the screen. When the user inputs the command identifier associated with checking information about the reserved boarding pass, the processing terminal identifies it, and conveys this request to the server. In this case, effectiveness can be evaluated in terms of the probability at which the processing terminal correctly recognizes the command identifier for the service wanted by the user, or simply in terms of the rate of successfully identifying the intended command. Efficiency can be evaluated in terms of the amount of labor required to operate the user interface, or simply in terms of the number of input attempts. Since it is difficult to evaluate satisfaction in a general term, it is not addressed in this paper.

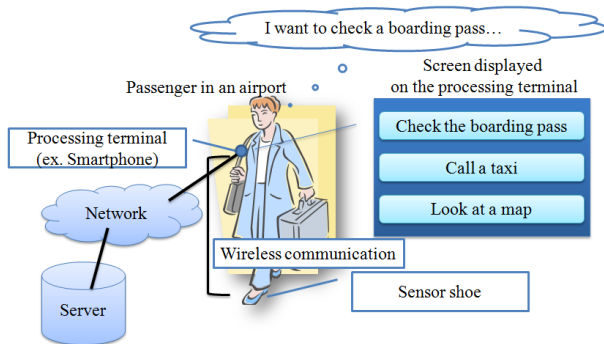


Figure 1. Example of the Use of the Proposed System.

III. PROPOSALS

A. Design of the Sensor Shoe

A sensor shoe has three weight sensors attached to the positions shown in Fig. 2. These positions have been determined based on the structure of the human foot skeleton. According to Noda [18], the plantar arch, a characteristic feature of the human foot skeleton, is made up of three arches linking three points: the first metatarsal (the base of big toe), the fifth metatarsal (the base of the little toe), and the calcaneal tuberosity (the heel area that touches the ground). Noda also states that, when the entire sole is touching the ground, the weight is distributed on the three points at the ratios of 2 on the first metatarsal, 1 on the fifth metatarsal, and 3 on the calcaneal tuberosity. The selection of the sensor positions is based on this finding.

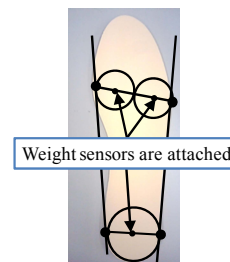


Figure 2. Positions of Weight Sensors.

B. Tap and Push Operation

The user’s operations are defined using variations in the user’s weight. Weight sensors handle only two types of data: duration in when the weight is measured and the weight value. Operations can be defined in terms of either duration or weight. In a method focusing on duration, a threshold is defined regarding the weight value to determine whether the user has intended to make certain operation or not. Multiple types of operation can be defined depending on the duration in which the user continues this operation. In a method focusing on weight, a point in time, such as 5000 ms after the transition to the input waiting state, is selected for the identification of the user’s intention. Multiple types of operation can be defined depending on the weight measured at that time. However, this method requires delicate control of the weight the user applies. Controlling the weight is more difficult than controlling the duration. Therefore, we have adopted a method focusing on duration.

A command is defined by a combination of two types of operations: a tap operation and a push operation. A tap operation is tapping the sole of the user’s shoe on the ground. In this operation, the change in weight is expected to show a triangular wave, as shown in Fig. 3. By setting a threshold on the weight, it is possible to detect this operation through two steps:

- Step 1: Measure the weight that exceeds the threshold value
- Step 2: Measure the weight when it is below the threshold value over a certain duration.

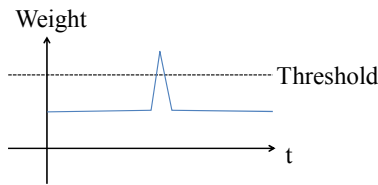


Figure 3. Change in Weight at the Time of Tap Operation.

A push operation is applying weight on the sensor casing as if the user is pressing the sensor. In this operation, the weight changes in the form of a trapezoidal wave, as shown in Fig. 4. By setting a threshold, it is possible to detect this operation through three steps:

- Step 1: Measure the weight that exceeds the threshold value
- Step 2: The weight continues to exceed the threshold value for more than a certain time
- Step 3: Measure the weight when it is below the threshold value

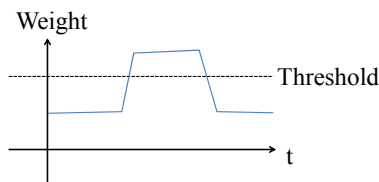


Figure 4. Change in Weight at the Time of Push Operation.

C. Definition of Commands

Ten commands have been defined by combinations of tap and push operations, as shown in Fig. 5. A unique command identifier is associated with each command.

Command ID	Operation Patterns
1	Push A -> Push A
2	Push A -> Push B
3	Push A -> Push C
4	Push B -> Push A
5	Push B -> Push B
6	Push B -> Push C
7	Push C -> Push A
8	Push C -> Push B
9	Push C -> Push C
10	Tap

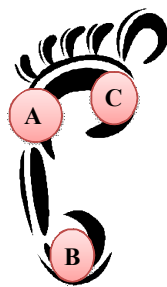


Figure 5. Definition of Commands.

Nine commands are represented by a push operation, and one command by a tap operation. The reason for defining the commands in this manner is as follows. Ishikawa [17] states that the task of selecting a function can be expressed as a hierarchical menu in a tree structure chart. If the number of commands to be defined for the task of selecting a function is small, the number of layers that must be crossed to reach the goal becomes large, resulting in an increased burden on the user because he/she needs to make a large number of input operations. Conversely, if the number of commands is

large, it becomes a burden for the user to learn the required operations. One of the quantitative expressions of human's short memory capacity is Miller's Magical Number Seven, Plus or Minus Two [19][20]. He argues that the number of objects an average human can hold in working memory is around 7. This implies that if the number of commands used to select a function exceeds two digits, the burden of learning is large. Since such a burden reduces the efficiency of using the interface, it is necessary to minimize the number of commands. In the case of selecting one out of 50 functions, the relations between the number of commands and the calculated number of inputs are as shown in Table I. P stands for a "push operation," and T for a "tap operation." If the number of commands of push operation is 2, a tree that expresses 50 elements needs to have 6 layers. Just passing through each node requires one push operation (selection) and one tap operation (selection done). Therefore, to go through the 6 layers, a total of 12 operations are required. We have also studied other numbers of commands and found that, in cases where three weight sensor elements are attached to a sensor shoe, the number of required input operations is the smallest (i.e., the input operation is the most efficient) when the number of commands is 9. This is the reason why 9 commands are based on a push operation in this paper.

TABLE I. COMPARISON OF DIFFERENT NUMBERS OF COMMANDS IN TERMS OF EFFICIENCY

Number of commands for selecting functions	Required operations	Number of inputs	Burden of learning
2	(P→T)×6 times	12	Small
3	(P→T)×4 times	8	Small
4	(P:2 times→T)×3 times	9	Small
8	(P:3 times→T)×2 times	8	Small
9	(P:2 times→T)×2 times	6	Small
16	(P:4 times→T)×2 times	10	Large
27	(P:3 times→T)×2 times	8	Large

IV. IMPLEMENTATION

We have built an experimental system based on the method proposed in Section III. As shown in Fig. 6, the system consists of a sensor shoe, an optical measurement instrument, and a user operation detection application running on a smartphone[21][22].

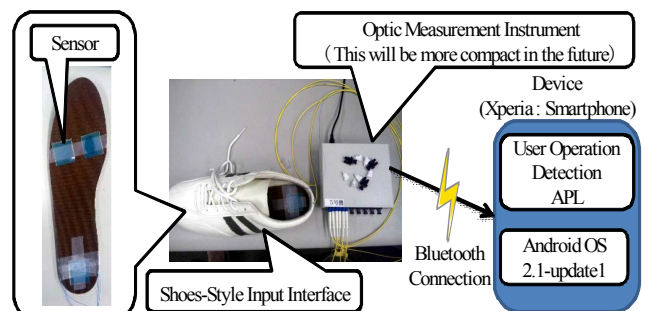


Figure 6. Structure of the Experimental System.

The sensor shoe is an insole. The parts of the insole where weight sensors are to be attached were removed and replaced with sensor casings. A hetero-core optical fiber weight sensor was used as a weight sensor. As shown in Fig. 7, a hetero-core optical fiber is composed of an optical fiber of a uniform core diameter with a small fiber segment with a different core diameter inserted. When the hetero-core optical fiber is bent, its optical loss increases. The hetero-core optical fiber weight sensor uses this property. It is highly sensitive to bending. When a weight is applied on the sensor casing, the fiber is bent, increasing its optical loss. The sensor detects how big the applied weight is by measuring the optical loss. The weight is actually measured by the optical measurement instrument. An LED/PD (Light Emitting Diode / Photo Diode) power meter was used as this instrument. The experimental system measures optical loss (in mV) and sends the measured value to the processing terminal every 33 ms. Since weight is expressed as optical loss, the larger the weight, the lower the level of the optical signal.

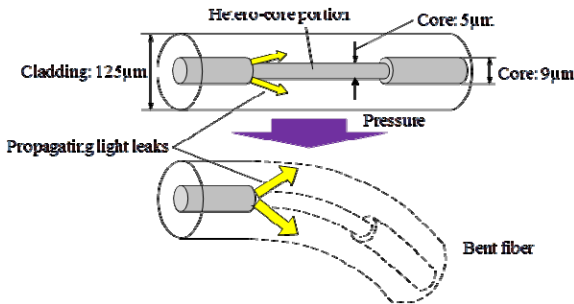


Figure 7. Hetero-core Optical Fiber.

The operation detection application software is configured as shown in Fig. 8, and is implemented on a smartphone. This application performs three functions: setting parameters for the experiment, calibration and operation detection. By calibration is meant the processing to equalize differences in users' weights and in sensors' sensitivities. The calibration was performed as follows. A push operation was applied to each element for 3 seconds a number of times, and the maximum and the minimum measurements were recorded. The difference between the maximum and the minimum values was multiplied by the value of a parameter we call a weight ratio. This value is subtracted from the maximum value. The result is used as the weight threshold. The $p_{threshold}$ can be expressed as

$$p_{threshold} = p_{max} - \{ Weight Ratio \times (p_{max} - p_{min}) \} \quad (1)$$

The other parameters used are the detection duration for a tap operation and that for a push operation.

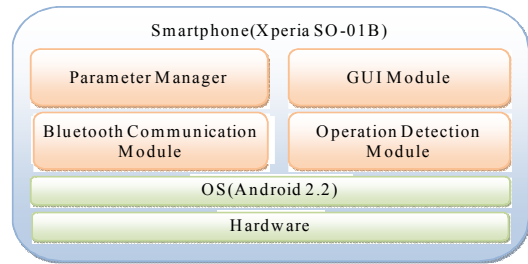


Figure 8. Configuration of the Operation Detection Application.

V. EXPERIMENT AND EVALUATION

A. Detection Duration of a Tap Operation, that of a Push Operation, and Threshold Value

Experiments were carried out using the experimental system. Parameters were set before starting the experiment. We measured changes in weights measured respectively by elements A, B and C in Fig. 5 when a tap operation and a push operation were respectively applied in order to determine the duration needed to detect an operation successfully. As shown in Fig. 9, 85% to 90% of the measured weight data concentrated on either the range where the optical measurement value was between the maximum value and that minus 25% or the range where it was between the minimum value and that plus 25%. We found that the weight fell in one of these ranges only when an operation was applied, and therefore, it is possible to detect an operation by setting the weight threshold in the middle of these two ranges. When the threshold was calculated with the weight ratio at 0.7, it took 100 ms to 200 ms for the user to perform a tap operation, as shown in Fig. 10, and 600 ms to 1100 ms to perform a push operation, as shown in Fig. 11. Therefore, we decided that operations can be detected correctly if we set the detection duration for a tap operation to around 200 ms, and the detection duration for a push operation to slightly below 600 ms.

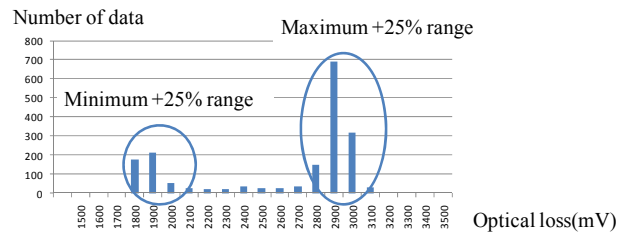


Figure 9. Polarization of Measured Values.

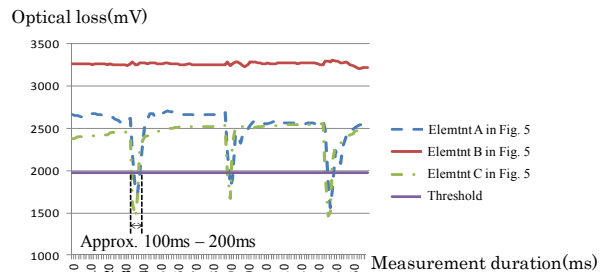


Figure 10. Measurement for a Tap Operation.

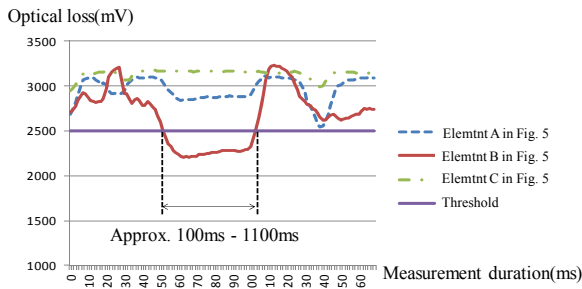


Figure 11. Measurement for a Push Operation.

B. Experiment Conducted using the Experimental System

We carried out an experiment to examine how the experimental system behaves. It was conducted in 4 steps:

- Step 1: Set the parameters
- Step 2: Establish a Bluetooth connection
- Step 3: Set calibration and threshold values
- Step 4: Select a function.

Figure 12 shows a test subject wearing the sensor shoe of the experimental system. Table II shows screenshots of the smartphone at each step, and the user's state that can be inferred from it.

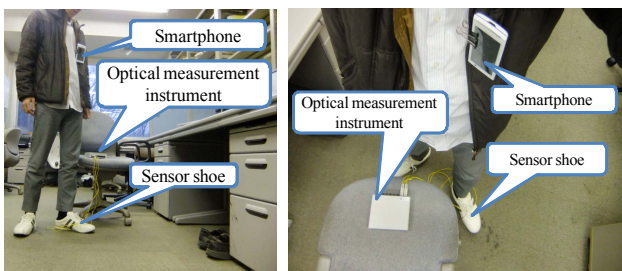


Figure 12. User wearing the Sensor Shoe.

TABLE II. SCREENSHOTS OF THE SMARTPHONE

Application State	Step1-1 : Parameters setting	Step1-2 : Display parameters	Step2 : Establish a Bluetooth Connection
Screenshot			
User State	Before putting on the shoe-embedded interface	Shoe-embedded interface worn	
Application State	Step3-1 : Calibrate and set thresholds	Step3-2 : Display the thresholds	Step4 : Selects a function
Screenshot			
User State	Several attempts of a push operation		Selects a function

C. Evaluation of the Successful Command Identification Rate

We had three test subjects. They learned how to operate the system for about 10 minutes before starting the experiment. They input the ten commands in sequence from command identifier 1 to 10. They tried these several times so that we could examine the probability at which the commands they intended to input were identified correctly. The parameter values used in this experiment were 200 ms for the tap operation detection duration, 400 ms for the push operation detection duration, and 0.7 for the weight ratio. The result of the experiment is shown in Table III. A screenshot of the experimental system taken during the experiment is shown in Fig. 13.

TABLE III. RESULT OF THE COMMAND IDENTIFICATION EXPERIMENT

Item \ Commands	1	2	3	4	5	6	7	8	9	10	Number of successful detection	Success rate
Subject 1	10	8	10	10	9	10	6	10	8	10	91	0.91
Subject 2	10	9	8	9	8	4	9	9	10	10	86	0.86
Subject 3	2	2	2	2	2	2	2	1	2	2	19	0.95
Average or Total	1.00	0.86	0.91	0.95	0.86	0.73	0.77	0.91	0.91	1.00	196	0.89

The three subjects conducted the experiment a total of 220 times, of which their input commands were identified correctly 196 times. The rate of successful identification for the three subjects ranged from 86% to 95%. The average rate was 89%.

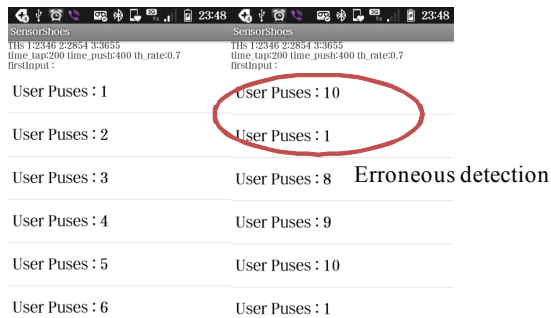


Figure 13. Screenshot taken in the Experiment.
(Each subject input commands in sequence from 1 to 10. An erroneous identification occurred in the seventh input attempt)

VI. CONCLUSION AND FUTURE WORK

We have focused on foot as a user interface that provides high mobility, a high command identification rate, and ability to complement information, hence the proposal of a shoe-embedded interface. This interface was implemented by attaching sensors at three points on the insole of a shoe. These points were selected based on the characteristics of the shape of a human foot. Commands were defined by a combination of two operations: push and tap. We have devised a method of indicating one of 10 alternative commands by a single foot operation. We have developed an experimental system that implemented the proposed method, and used it to evaluate the probability at which input commands are identified correctly. In our experiment with three subjects, the average rate of successful identification was 89%.

In the future, it will be necessary to examine the rate of correct identification and possible occurrences of system failures in cases where the user is running or walking. It is also necessary to study how providing recommended options to users can increase the amount of information the user can input without impairing usability.

REFERENCES

[1] Masafumi Nishimura and Gakuto Kurata, "Recent Advances and Possibilities of Innovation in Speech Interface Technology(<Special Feature>Toward Developing Practical Automatic Speech Recognition Technology)," Journal of Information Processing Society of Japan, vol. 51, no. 11, pp. 1434-1439, Nov. 2010.

[2] Kiyohiko Abe, Mikio Ohuchi, Shoichi Ohi, and Minoru Ohyama, "Eye-gaze Input System Based on the Limbus Tracking Method Using Image Analysis," vol. 57, no. 10, pp. 1354-1360, Oct. 2003.

[3] Yuki Ebina, Shuhei Nishida, and Masahiro Nakagawa, "On the Chaos and Fractal Properties in EEG and NIRS Signals and their Applications to Robotics," Technical Report on NLP, The Institute of Electronics, Information and Communication Engineers, vol. 107, no. 267, pp. 41-46, Oct. 2007.

[4] H.-K.J. Kuo and Lee Chin-Hui, "Discriminative training of natural language call routers," Speech and Audio Processing, IEEE Transactions on , vol.11, no.1, pp. 24- 35, Jan 2003.

[5] K. Tsukada and M. Yasumura, "Ubi-Finger: Gesture Input Device for Mobile Use," Proceedings of APCHI 2002, Vol. 1, pp.388-400, 2002.

[6] M. Bacchiani, F. Beaufays, J. Schalkwyk, M. Schuster, and B. Strope, "Deploying GOOG-411: Early lessons in data, measurement, and testing," Acoustics, Speech and Signal Processing, 2008. ICASSP 2008. IEEE International Conference on, vol., no., pp.5260-5263, March 31 2008-April 4 2008.

[7] Michiko Nishiyama, "Unconstrained measurement of respiration rhythm focusing on weight movement using hetero-core fiber optic sensors," IEICE Technical report Vol. 109, No. 429, pp. 49-52, Feb. 2010.

[8] Kazuhiro Watanabe, "Macrobending Characteristics of a Hetero-Core Splice Fiber Optic Sensor for Displacement and Liquid Detection," IEICE Trans. Electron., Special Issue on Optical Fiber Sensors, vol.E83-C, no.3, pp.309-314, 2000.

[9] Masako Sonobe, Michiko Nishiyama, and Kazuhiro Watanabe, "Unconstrained Pulse Monitoring for On-Site Usage Using a Hetero-core Fiber Optic Nerve," 2009 International Symposium on Smart Sensing and Actuator System, Proceedings of ISSS'09,pp.48-51, 2009.

[10] Mitsuo Miyamoto, Michiko Nishiyama, and Kazuhiro Watanabe, "Hetero-core Fiber Optic Nerve Weight Sensors for Unconstrained Respiration Monitoring during Sleep," 2009 International Symposium on Smart Sensing and Actuator System, Proceedings of ISSS'09, pp52-55, 2009.

[11] Kaname Takauchi, Mitsuaki Shimono, Michiko Nishiyama, Kazuhiro Watanabe, and Kazumasa Takami, "An information communication system operated by a sole placed on a hetero-core optical fiber sensor mat," IET Conf. Pub. 2010, 25 (2010), DOI:10.1049/cp.2010.

[12] Shinichi Nose, Michiko Nishiyama, Kazuhiro Watanabe, and Kazumasa Takami, "A Personal Web Service based on a User-Friendly Personal Identification Method in a Ubiquitous Environment," in proceedings of PDPTA'07-The 2007 International Conference on Parallel and Distributed Processing Techniques and Applications. 25-28 June 2007.

[13] Shinichi Nose, Mituaki Shimono, Michiko Nishiyama, Tetuya Kon, Kazuhiro Watanabe, and Kazumasa Takami, "Personal identification based on sole pressure distribution using a hetero-core optical fiber sensor network for personal web services," in proceedings of 2009 IEEE Congress on Services (SERVICES 2009) July 6-10, 2009.

[14] ISO 9241-11:1998 Ergonomic requirements for office work with visual display terminals (VDTs) -- Part 11: Guidance on usability.

[15] Timo Jokela, Netta Iivari, Juha Matero, and Minna Karukka, "The standard of user-centered design and the standard definition of usability: analyzing ISO 13407 against ISO 9241-11," CLIHC '03 Proceedings of the Latin American conference on Human-computer interaction, ACM New York, NY, USA, 2003.

[16] Alain Abran, Adel Khelifi, Witold Suryn, and Ahmed Seffah, "Usability Meanings and Interpretations in ISO Standards," SOFTWARE QUALITY JOURNAL, Volume 11, Number 4, 325-338, DOI: 10.1023/A:1025869312943, 2003.

[17] Yasushi Ishikawa, "UI Design and Usability : Subjects of Speech Interface," Technical Report on SLP, Information Processing Society of Japan, vol. 2007, no. 103, pp. 35-40, Oct. 2007

[18] Yuji Noda, "All about plantar arch," A Body on Viewpoint of Sole, pp. 70-77, Kohdansya Ltd., Tokyo, 1998.

[19] G. A. Miller, "The magical number seven, plus or minus two: Some limits on our capacity for processing information," Psychological Review, vol. 63, no. 2, pp. 81-97, March. 1956.

[20] G. A. Miller, "The cognitive revolution: a historical perspective," Trends in Cognitive Sciences 7 (3): 141-4. doi:10.1016/S1364-6613(03)00029-9. PMID 12639696, 2003.

[21] Ed Burnette, "Hello, Android: Introducing Google's Mobile Development Platform," 2009.

[22] Margaret Butler, "Android: Changing the Mobile Landscape," IEEE Pervasive Computing, vol. 10, no. 1, pp. 4-7, Jan.-Mar. 2011.

A Low-cost and Portable System for Real-time Impedimetric Measurements and Impedance Spectroscopy of Sensors

Michele Rossi, Marco Bennati, Federico Thei, and Marco Tartagni

ARCES – Advanced Research Center on Electronic Systems

Second School of Engineering, University of Bologna - Via Venezia 52, 47521 – Cesena (FC), Italy
 mrossi@arces.unibo.it, mbennati@arces.unibo.it, fthei@arces.unibo.it, mtartagni@arces.unibo.it

Abstract— This paper presents a low cost and portable system that is able to perform real time or spectra impedance characterization of impedimetric sensors interfaces. It is also able to perform simple amperometric measurements for real-time DC current-voltage characterization or studies of the behavior of the sensor with respect to different target stimuli. Due to its flexible design, the system can be easily adapted to different applications and experimental requirements. Synthetic devices under test (DUTs) were used for testing purposes and the performances have been compared to those obtained using a commercial dedicated impedance analyzer. The system allows displaying results in Nyquist and Bode plots using a friendly graphical user interface. Results show remarkable fair accuracy, considering the much lower price, smaller sizes and flexibility of use of the developed system.

Keywords – Biosensors; Sensor interfaces; Impedance spectroscopy; Real time; Amperometry measurements.

I. INTRODUCTION

In the last decade, the convergence of nanotechnology with biology and medicine and the ability to fabricate structures using standard wafer-scale semiconductor processing techniques has shown an emerging and evolving interest in the development of new classes of rapid, sensitive, and reliable biosensors devices, such as nanowires and carbon nanotubes [1][2][3][4][5].

These devices could have a great impact on many application fields related to our life: from health-care and environment, to food production and bio-warfare thanks to their properties of electrical, label-free and real time readout. Moreover, the possibility of integration of this class of sensors with the readout structure makes them even more interesting. However, the integration of sensors with interfaces demands a quick although accurate knowledge of electrical parameters (such as impedance, noise and bandwidth) [6] and their related behaviors to target stimulus, in order to understand the design constraints of the readout systems. Another important issue to point out is the lack of instrumentation able to perform both impedance spectroscopy and real-time impedance measurements in order to identify the electrical parameters model and real time behaviors of biosensors depending upon the specific structure and fabrication process [7][8].

For the above reasons, there is a demand for low cost, portable readout structures able to perform accurate preliminary tests on biosensors and/or to perform routine tests with respect to experimental conditions avoiding skilled personnel and bulky instruments.

The main characteristics needed for the readout system are:

- Compact and low cost;
- Flexible to cope with different kind of biosensors;
- Able to perform parallel acquisitions, allowing high throughput;
- Perform differential measurements in order to further increase sensitivity and selectivity;
- Perform a full characterization of impedance in the magnitude and in the phase, since the latter could offer a better understanding of the surface molecular interaction [9].

This paper presents a low cost, versatile and portable test board for sensors implementing a two electrode potentiostat, conjugated with a lock-in technique for complex impedance detection which allows obtaining comprehensive information on the impedance magnitude and phase (Figure 1). More specifically, the instrument has been designed to be interfaced to bionanosensors, such as nanowires or carbon nanotubes; however it is not the purpose of this paper to describe a single specific application related to this kind of biosensors, but rather investigate the potentiality of this system interface to be used for different kinds of sensors.

Section II will show the system architecture and functionalities. Section III will present the developed acquisition board features and working principles. Section IV will show the LabVIEW software interface and the implemented digital signal conditioning process. Finally, Section V will present the results of tests performed on synthetic DUTs simulating sensors behaviors and a comparison between the developed system and a commercial impedance analyzer.

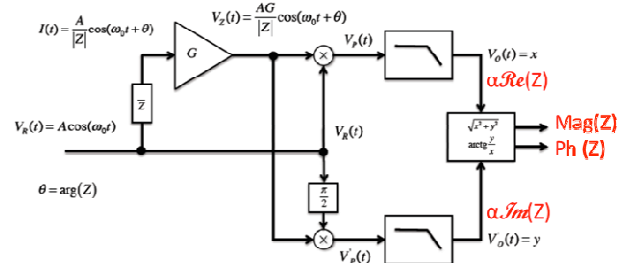


Figure 1. Schematic of the lock-in technique for complex impedance detection.

II. SYSTEM STRUCTURE AND SETUP

The system consists of a custom printed circuit mother board (PCB) hosting both the DUT and the readout interface. The latter performs the readout of the current signal coming out of the sensors in response to a sinusoidal or DC V_{ref} signal generated by a waveform generator (Tektronix AFG 3102 [10]) and digitized by a National Instruments 6009 DAQ card [11] whose output is sent to a laptop for storing and online (or post) processing using a LabView interface.

The above approach, based on performing the filtering and data manipulations in the digital domain, allows the system to be particularly flexible, maintaining a simple analog front-end for different applications with respect to the system required performances.

In particular, the developed system is designed to be as much versatile as possible allowing to perform the following measurements in lock-in readout configuration:

- 1) Real-time DC current measurements;
- 2) DC voltage sweeps, for device characterization;
- 3) Real-time AC measurements of sensor impedance/admittance magnitude and phase;
- 4) Impedance AC spectra.

The graphical user interface is able to reconstruct in real time both Nyquist and Bode plots.

III. ACQUISITION BOARD INTERFACE

The designed acquisition board (block diagram shown in Figure 2) is characterized by the following features:

- Two identical and independent readout branches to allow differential measurements on sensors (Z_{ref} and Z_{sens} in Figure 2). The board could be used for array of sensors as well;
- Addressable switching system to select, independently on the two branches, single sensors in a chip array (see Figure 1);
- Operating frequency in the range of 0.1Hz-2KHz (typical for nanowires or nanotube sensors lock-in readout measurements) [2][4][5][8][12][13];
- DC measurements bypassing the demodulation stage (this possibility is represented with switches on each branch of Figure 2);
- Four different current ranges selectable by mechanical switch, in particular $\pm 7.85\mu A$, $\pm 785nA$, $\pm 78.5nA$, $\pm 7.85 nA$.
- Auxiliary potential (V_{bulk}) control circuit to set the back-gate and/or liquid gate potential of nanowires or nanotubes chip [2][13][15].
- Real time parallel measurements of both real and imaginary part of sensors impedance using two independent demodulators for each branch of the system.
- Custom designed socket (4x4 cm) for hosting the DUT/sensor.

Special attention was paid to the four layer PCB layout in order to shield as much as possible the analog signals on the board from external noise sources.

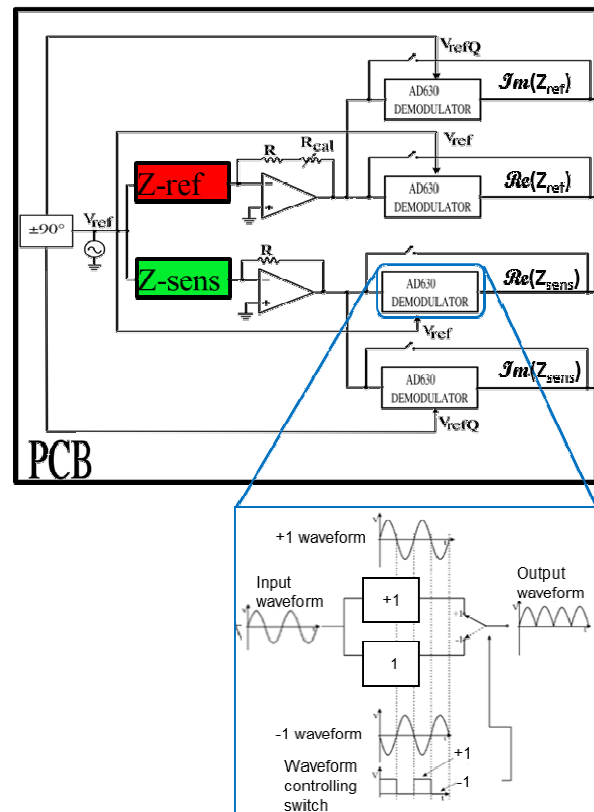


Figure 2. Block diagram of the designed acquisition board.

The zoom shows the working principle of the AD 630 demodulator. The switch is driven by a comparator that compares the reference signal (V_{ref} and V_{refQ}) with its DC offset level, resulting in a square wave in-phase with the reference signal.

Each branch of the circuit can be represented by two stages: a transimpedance input amplifier that converts the current signal coming from sensors to an amplified voltage signal prior to be sent to the integrated circuit (AD630) that performs the phase-sensitive detection. The signal is preamplified by an AD822 due to its low-power rail-to-rail and low noise operating performances (13 nV/ \sqrt{Hz} @ 10 kHz) and low input bias current [16].

The demodulation is implemented by using an AD630 since it is currently used in precision signal processing and instrumentation applications requiring wide dynamic range [16].

The AD630 demodulator is configured to have a gain of ± 1 and, since the positive or negative gain is controlled by a switch controlled by a comparator (zoom in Figure 2), thus the demodulator multiplies the input waveform for a unitary square wave whose Fourier series is [17]:

$$V_{square}(t) = \frac{4}{\pi} \cdot \sum_{k=1}^{\infty} \left(\frac{\sin((2k-1) \cdot \omega t)}{2k-1} \right) \quad (1)$$

and the reference waveform sent to both the DUT and the comparator input is:

$$V_{ref} = V_i \cdot \sin(\omega_i t) \quad (2)$$

the output of the in-phase branches of the circuit is:

$$V_o(t) = -V_i \cdot \left(\frac{R_f}{Z_{sens}}\right) \cdot \sin(\omega_c t + \varphi) \cdot \left(\frac{4}{\pi}\right) \cdot \sum_{k=1}^{\infty} \left(\frac{\sin((2k-1) \cdot \omega t)}{2k-1}\right) \quad (3)$$

where R_f and Z_{sens} are respectively the selected feedback resistance, which sets the range of measurements of the system, and the sensor impedance. As can be seen, the output signal presents a high harmonic content associated to the square wave components of the signal.

The output of the two “real part” branches of the PCB that are externally digitized and filtered could be derived from (3) as:

$$V_o(t) = -V_i \cdot \left(\frac{R_f}{Z_{sens}}\right) \cdot \left(\frac{2}{\pi}\right) \cdot \cos(\varphi) = \alpha \cdot \text{Re}(Y_{sens}) \quad (4)$$

Similarly, the output of the quadrature branches, in which the comparator input is shifted of 90° (V_{refQ} in Figure 2), of the circuit is:

$$V_o(t) = -V_i \cdot \left(\frac{R_f}{Z_{sens}}\right) \cdot \sin(\omega_c t + \varphi) \cdot \left(\frac{4}{\pi}\right) \cdot \sum_{k=1}^{\infty} \left(\frac{\cos((2k-1) \cdot \omega t)}{2k-1}\right) \quad (5)$$

by which it is possible to obtain the output of the two “imaginary part” branches of the PCB, then externally digitized and filtered yielding:

$$V_o(t) = -V_i \cdot \left(\frac{R_f}{Z_{sens}}\right) \cdot \left(\frac{2}{\pi}\right) \cdot \sin(\varphi) = \alpha \cdot \text{Im}(Y_{sens}) \quad (6)$$

Figure 3 shows a picture of the PCB where on one side are arranged:

- An input signal SMB connector for the V_{ref} ,
- A dual power supply connector,
- 4 output SMB connectors (Re_1 , Im_1 , Re_2 , Im_2).

The socket connectors provides the power supply, Ground, V_{ref} and V_{bulk} signals to the PCB plug interfaces for different (eventually based on active components) solutions and connects the selected sensor to the selected branch of the circuit (see Figure 1).

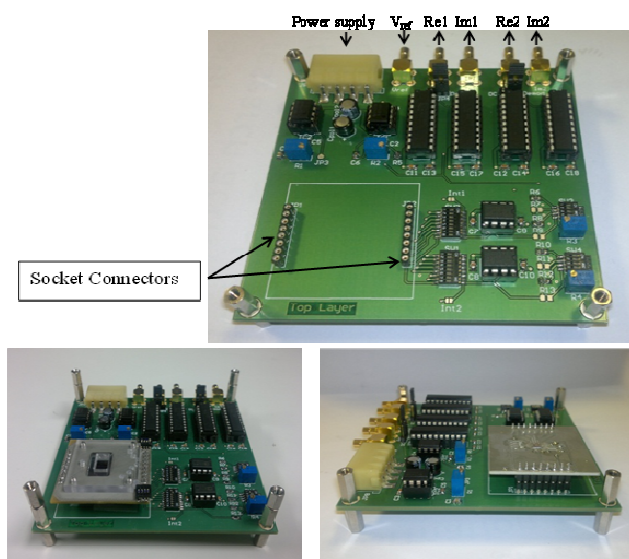


Figure 3. Picture of designed acquisition board PCB interface.

IV. LABVIEW INTERFACE AND FILTER DESIGN

The implemented software interface allows to:

- control the function generator and set V_{ref} waveform properties (frequency, amplitude, DC offset) using the USB interface;
- control the NI-DAQ, setting the proper (adapted to the V_{ref} frequency) sampling rate and DAQ acquisition voltage range;
- simultaneously control the real time signal value for the four outputs of the acquisition board to finally have the mean Re_1 , Im_1 , Re_2 , Im_2 values;
- perform real time calculation to finally display the real time Nyquist diagram of the admittance (or impedance), as well as Phase and Magnitude values and calculate the simple RC equivalent circuit.
- save data in users-specified text files.

The main signal conditioning process (represented in Figure 4) was segmented into 3 stages: two stages implementing finite impulse response digital low-pass filters (FIR Kaiser window) and one devoted to decimation. Weight taps have been calculated with MATLAB to have the best configuration for all the frequency in the functioning range. In order to optimize the computational resources, an adaptive filtering based on the input frequency (f_i) and the signal band (user selectable) cut off frequency (f_{cfinal}) was implemented in the software interface.

The interface also allows selecting the highest harmonic of the signal (see (3) and (5)) to be considered following the Nyquist criterion, consequently changing the sampling ratio of the NI DAQ.

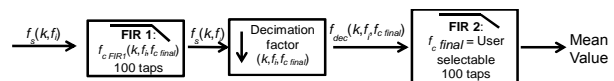


Figure 4. Representation of the adaptive two stages low pass FIR filter implemented in the LabView interface .

In order to perform real time, 4-channel measurements with a low final cutoff frequency (usually 1 or 0.1 Hz) and relatively limited computational resources (e.g., if using a laptop), a good trade-off between performances and computational complexity has been found to be the cascade of two 100-tap adaptive filters.

The two stages are dimensioned to satisfy the condition of same ratio between cutoff frequency and bandwidth:

$$\frac{f_{cFIR1}}{f_s} = \frac{f_{cfinal}}{f_{dec}} \quad (7)$$

whose expression, considering $f_{dec} = 2 \cdot f_{cFIR1}$, allows calculating the first filter cutoff frequency (f_{cFIR1}) and the decimation ratio as:

$$f_{cFIR1} = \sqrt{\frac{f_{cfinal} \cdot f_s}{2}} \quad (8)$$

$$dec\ ratio = \frac{f_s}{f_{dec}} = \sqrt{\frac{f_s}{2 \cdot f_{cfinal}}} \quad (9)$$

The obtained filtered voltage signals are then real time manipulated to evaluate magnitude and phase from each branch of the circuit:

$$|V_o(t)| = \sqrt{\text{Re}^2\{V_o(t)\} + \text{Im}^2\{V_o(t)\}} = V_i \cdot \left(\frac{R_f}{|Z_{sens}|}\right) \cdot \left(\frac{2}{\pi}\right) \quad (10)$$

$$\varphi = \tan^{-1} \frac{\text{Im}\{V_o(t)\}}{\text{Re}\{V_o(t)\}} \quad (11)$$

Other data manipulation implemented in the LabView software interface also allows to calculate in real-time the equivalent resistance and capacitance of the series and parallel RC models.

Figure 5 shows the implemented LabView interface.

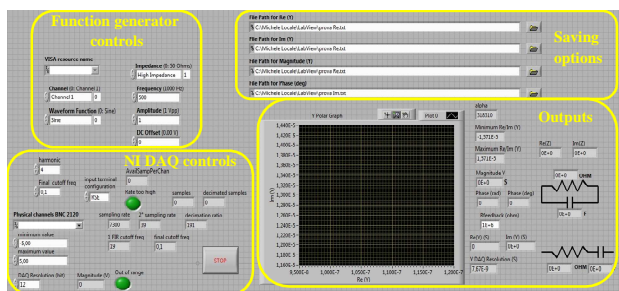


Figure 5. Implemented LabView interface.

V. RESULTS

Preliminary AC real time tests on synthetic DUTs (resistors, capacitors and RC combinations) in different measurement ranges and at different frequencies were performed connecting the DUT between V_{ref} and a selected socket connector. In particular, Vishay precision resistor of 1MΩ and 10MΩ, 0.005% tolerance and Dale RNX-3/8 100MΩ resistor, 1% tolerance and capacitor of 100pF and 1nF were used.

Figure 6 shows results of performed measurements using an R=1MΩ, C=1nF parallel circuit. The figure shows a full scale view of the admittance in the Nyquist plane, while the zoomed version shows the details of the measurement. As can be seen in the figure zoom, a small phase shift caused by parasitic effects is present; this could be compensated in post processing after the calibration.

Table I sums up the different configurations for the four different selectable ranges of measurements and shows the worst effective final resolution experimentally obtained for each configuration during the tests performed using different DUT circuits.

TABLE I. SYSTEM PERFORMANCES

Current Range [A]	±7.85μ	±785n	±78.5n	±7.85n
Full Scale (Y) [S]	±1.57x10 ⁻⁵	±1.57x10 ⁻⁶	±1.57x10 ⁻⁷	±1.57x10 ⁻⁸
Minimum detectable impedance [Ω]	6.37x10 ⁴	6.37x10 ⁵	6.37x10 ⁶	6.37x10 ⁷
Min experimental resolution (ENOB) (worst case)	11.3	9	11.4	8.5

In the above table, “Full Scale (Y)” should be considered in terms of admittance using a sinusoidal input amplitude of 1 V_{pp}; its reciprocal is the “Min readable impedance” and “Min experimental resolution (ENOB)” is the minimum effective final resolution experimentally obtained (considering all the experimental tests performed in testing conditions) in terms of effective numbers of bits (ENOB);

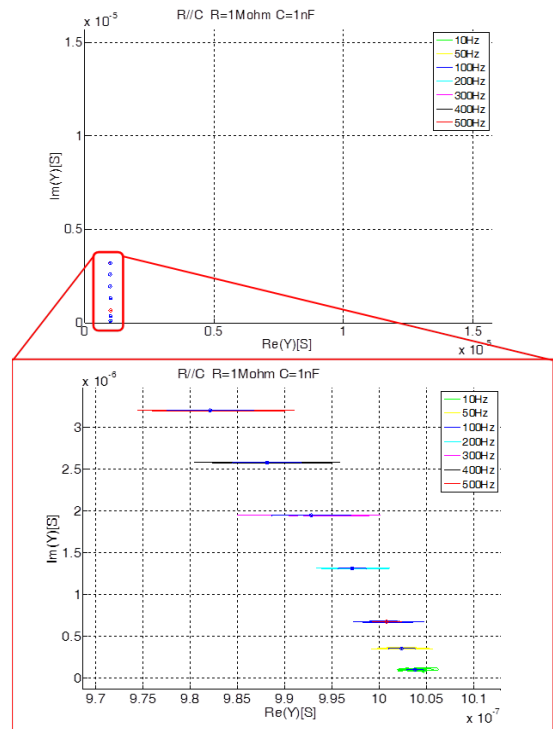


Figure 6. Example of AC real time admittance measurement of a RC parallel circuit in the Nyquist plane, for different input working frequencies.

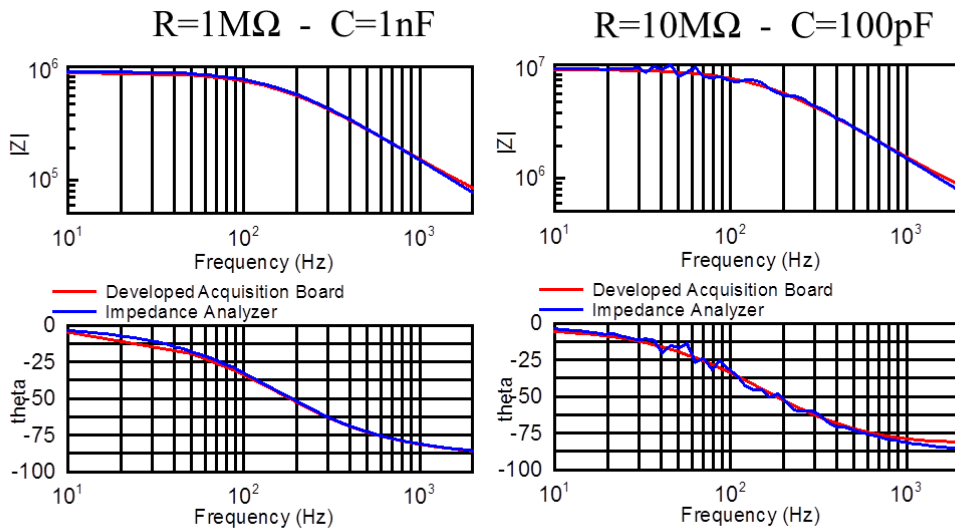


Figure 7. Bode plots obtained using the developed system interface and the commercial Novocontrol Alpha-A Impedance analyzer with two different parallel RC test circuits.

TABLE II. COMPARISON WITH IMPEDANCE ANALYZER

	R=1 MΩ - C=1 nF				R=10 MΩ - C=100 pF			
	Acquisition Board		Impedance Analyzer		Acquisition Board		Impedance Analyzer	
	R	C	R	C	R	C	R	C
Fitting error	0.5%	0.5%	0.06%	0.06%	0.6%	0.6%	0.8%	0.8%
Accuracy Error	0.6%	0.5%	0.04%	0.1%	1%	1.1%	0.04%	4.3%

Moreover a comparison between the developed system interface and specific commercial Novocontrol Alpha-A Impedance analyzer, performing 50 points frequency scans in the range 10 Hz-2 KHz on different test circuits were made in order to analyze measurements accuracy in impedance frequency analysis and to calibrate the system. Figure 7 shows the results obtained using two different parallel RC test circuits.

As can be seen the response of the commercial system seems noisier considering the higher impedance DUT; this can be explained considering that in the developed system each frequency point is obtained mediating (by the LabView software interface) the real time AC measurements of a selected number of acquired samples (usually 200 samples), thus reducing the final effective bandwidth of about ten times and thus reducing the external noise.

The obtained points are then saved in a text file in the ZView format and analyzed with ZView software. Table II shows the results in terms of fitting and accuracy errors, where the fitting error is directly calculated by ZView software taking into account the entire spectrum, where accuracy error is calculated using the expression:

$$Accuracy\ Error(\%) = \left| \frac{actual\ value - fitted\ value}{actual\ value} \right| \cdot 100 \quad (12)$$

The system shows a fair accuracy, which is sufficient for many purposes. The above statement should be taken into account considering the much lower price and smaller sizes of the developed system in comparison with commercial instruments currently used for impedance spectroscopy.

VI. CONCLUSIONS

A low cost, portable and versatile system, allowing both real time and frequency domain impedance characterization (as well as amperometric measurements) for sensor impedimetric interfaces has been successfully developed and tested. According to the tests, the proposed system has accuracy that is comparable with laboratory instruments on some ranges. Thus, it allows rapid and precise characterization of sensor interfaces at lower cost without highly equipped instrumentation. Moreover, the system could be further shrunk using surface mount device (SMD) implementation allowing to be directly coupled with sensors as readout system. The whole system can be improved and optimized implementing the digital filter stage and input signal generation by means of an FPGA, allowing to further increase the performance in terms of working ranges and time response.

ACKNOWLEDGMENTS

The research leading to these results has received funding from the European Community's Seventh Framework Programme (FP7/2007-2013) under grant agreement NANOFUNCTION (n°257375) and ENIAC END (n°120214) projects. The authors acknowledge M. Crescentini for helpful suggestions and comments.

REFERENCES

- [1] J. Li, H. T. Ng, and H. Chen, "Carbon nanotubes and nanowires for biological sensing", *Methods in molecular biology*, vol. 300, 2005, pp. 191-223.
- [2] N. S. Ramgir, Y. Yang, and M. Zacharias, "Nanowire-Based Sensors", *Small*, vol. 6, 2010, pp. 1705-1722.
- [3] E. Stern et al., "Label-free biomarker detection from whole blood", *Nature Nanotechnology*, vol. 5, no. 2, 2010, pp.138-142.
- [4] G. Zheng, F. Patolsky, Y. Cui, W. U. Wang, and C. Lieber, "Multiplexed electrical detection of cancer markers with nanowire sensor arrays", *Nature Biotechnology*, vol. 23, no. 10, 2005, pp. 1294-1301.
- [5] S. Sorgenfrei et al., "Label-free single-molecule detection of DNA-hybridization kinetics with a carbon nanotube field-effect transistor", *Nature Nanotechnology*, vol. 6, no. 2, 2011, pp. 126-132.
- [6] M. K. Joo, P. Kang, Y. Kim, G.T. Kim, and S. Kim, "A dual analyzer for real-time impedance and noise spectroscopy of nanoscale devices", *Rev. Sci Instrum.*, vol. 82, no. 3, 2011, 034702.
- [7] F. Patolsky, G. Zheng, and C. Lieber, "Fabrication of silicon nanowire devices for ultrasensitive, label-free, real-time detection of biological and chemical", *Nature Protocols*, vol. 1, no. 4, 2006, pp. 1711-1724.
- [8] S. Chen, J. G. Bomer, W.G. van der Wiel, E. T. Carlen, and A. van den Berg, "Top-Down Fabrication of Sub-30 nm Monocrystalline Silicon Nanowires Using Conventional Microfabrication", *ACS NANO*, vol. 3, no.11, 2009, pp. 3485-3492.
- [9] S. Ingebrandt et al., "Label-free detection of single nucleotide polymorphisms utilizing the differential transfer function of field-effect transistors", *Biosensors and Bioelectronics*, vol. 22, no. 12, 2007, pp. 2834-2840.
- [10] Tektronix, Inc., USA Data Sheet. Available at <http://www.tek.com/signal-generator/afg3000-function-generator> [retrieved: 07, 2012].
- [11] National Instruments Corporation, Data Sheet. Available at <http://sine.ni.com/nips/cds/view/p/lang/en/nid/201987> [retrieved: 07, 2012].
- [12] S. Deng, G. Jian, J. Lei, Z. Hu, and H. Ju, "A glucose biosensor based on direct electrochemistry of glucose oxidase immobilized on nitrogen-doped carbon nanotubes", *Biosensors and Bioelectronics*, vol. 25, no. 2, 2009, pp. 373-377.
- [13] S. Choi, I. Park, Z. Hao, H.Y.N. Holman, and A.P. Pisano, "Quantitative studies of long-term stable, top-down fabricated silicon nanowire pH sensors", *Applied Physics A*, 2012, doi: 10.1007/s00339-011-6754-9.
- [14] M.P. Lu et al., "Semiconducting single-walled carbon nanotubes exposed to distilled water and aqueous solution: Electrical measurement and theoretical calculation", *Applied Physics Letters*, vol. 88, no. 5, 2006, pp. 053114-053114-3.
- [15] O. Knopfmacher et al., "Nernst limit in dual-gated Si-nanowire FET sensors", *Nano Letters*, vol. 10, no. 6, 2010, pp.2268-2274.
- [16] Analog Devices, Inc., Norwood, MA, USA Data Sheet. Available at <http://www.analogdevices.com> [retrieved: 07, 2012].
- [17] Georgi P. Tolstov, *Fourier Series*, Courier-Dover, 1976.

Flexible Lightweight Films-based Physical Sensors with Wireless Data Transmission

Vladimir Laukhin

Dept. name: NANOMOL
 Institució Catalana de Recerca i Estudis Avançats,
 ICMA-B-CSIC, CIBER-BBN
 Bellaterra, Barcelona, Spain
 e-mail: vladimir@icmab.es

Elena Laukhina

Dept. name: NANOMOL
 CIBER de Bioingeniería, Biomateriales y Nanomedicina
 (CIBER-BBN) at ICMA-B-CSIC
 Bellaterra, Barcelona, Spain
 e-mail: laukhina@icmab.es

Bahareh Moradi, Victor Lebedev, Raphael Pfattner, Concepció Rovira, Jaume Veciana

Dept. name: NANOMOL
 Institut de Ciència de Materials de Barcelona (ICMA-B) -CSIC
 Bellaterra, Barcelona, Spain
 e-mails: bmoradi@icmab.es, vlebedev@icmab.es, rpfattner@icmab.es, cun@icmab.es, vecianaj@icmab.es

Abstract— This article is addressed to the development of flexible lightweight physical sensors suitable for body sensing technology. The polycarbonate films were covered with different organic molecular conductors to fabricate flexible strain and temperature sensing materials. The resulting surface-modified films were fully characterized by different microscopic and spectroscopic techniques and their electric transport and electromechanical properties were studied as well. The investigations demonstrated that the electrical responses of these films suffice to measure very small pressure or temperature changes. Prototypes of strain and temperature sensors with wireless data transmission are under development.

Keywords-flexible strain sensor; temperature sensing material; organic molecular conductors; electrical detection principle; wireless data transmission.

I. INTRODUCTION

The application of flexible lightweight sensors in electronics is a key point in the development of novel high-tech [1-4]. Engineering flexible all-organic sensing materials with electrical detection principle brings great opportunities in the field of physical sensors for their applications in intelligent textiles, robotic interfaces and body sensing devices [1-3]. A simple covering process of polymeric films with highly strain sensitive, piezoresistive, micro- or nano-crystals of BEDT-TTF-based molecular conductors has been developed previously; BEDT-TTF = bis(ethylenedithio)tetrathiafulvalene, Fig. 1 [4, 5].

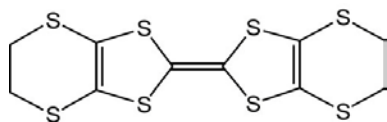


Figure 1. Skeletal formula of BEDT-TTF

We have shown that these bi layer (BL) films may have a great interest in sensor engineering due to important material properties, such as conductivity, high strain (pressure) and temperature sensitivity, excellent elasticity, weightless and biocompatibility [6]. Since the ultimate goal of our studies is to use the developed BL films in body sensing technology the biocompatibility of the BL film has been tested. Haematoxylin-Eosin staining of the tissues adjacent to the sensing BL film and to the silicon band showed the less inflammatory reaction to BL film samples as compared with the reaction to a silicone band [6]. So, the developed sensing BL films have a higher biocompatibility than standard silicone-based materials used in surgery.

The processing characteristics of polycarbonate films, covered with the layer of a BEDT-TTF-based organic molecular conductor, make them potentially useful for electronic applications where conductivity, lightweight, large or small area coverage and flexibility are required [4]. Recently, we have reported on the integration of polycarbonate films metalized with the highly strain sensitive β -(BEDT-TTF)₂I₃ metal in a polyester textile, that permits to demonstrate that the strain sensing properties of this unique organic molecular metal can be completely transferred on the fabric [7]. This result prompted us to develop a temperature sensing material that also uses the electrical detection principle. For this purpose we suggested to cover polycarbonate films with the highly temperature sensitive α' -(BEDT-TTF)₂I_xBr_{3-x} conductor [8]. Noteworthy also is that the BL film-based sensors have to be equipped for some particular applications especially in biomedicine with some electronic circuit to measure, amplify and transmit the deformation or temperature data.

Here, we present flexible, lightweight sensing BL films whose electrical resistance significantly responds to

deformation (piezoresistive) or temperature changes (pyzoresistive) depending on the type of molecular conductor used for covering the polycarbonate film. This article also demonstrated a system that can measure strain and temperature and a possibility to transmit the measured data to a data acquisition (DAQ) system. Prototypes of strain and temperature sensors with wireless data transmission being under development will be presented as well.

II. FABRICATING FLEXIBLE STRAIN AND TEMPERATURE SENSING FILMS WITH ELECTRICAL DETECTION PRINCIPLE

In line with the early reported method, [9] we first prepared a 25 μm thick polycarbonate (PC) films that contain a 2 wt. % of BEDT-TTF that is a precursor for various organic molecular metals. The films were cast on glass supports at 130 $^{\circ}\text{C}$ from a 1,2-dichlorobenzene solution of PC and BEDT-TTF. In order to cover the film with the layer of a BEDT-TTF-based conductor we exposed the film surface to the vapors of a solution of either iodine or IBr in dichloromethane. The surface of a polycarbonate film easily swells under its exposure to dichloromethane vapors; this swelling facilitates a migration of BEDT-TTF molecules from the film bulk to the swollen film surface where the part of donor molecules are oxidized to radical cations by halogen, which penetrates in the film surface together with dichloromethane vapors. This redox process induces the rapid nucleation of highly insoluble the $(\text{BEDT-TTF})^+(\text{halogen})_n^-$ conductor and the facing layer of an organic molecular conductor is formed. It should be stressed that the treatment of the film surface with iodine/dichloromethane vapors resulted in the formation of the covering layer of the α - phase of $(\text{BEDT-TTF})_2\text{I}_3$; gauge factor (GF) is equal to 10 [4]. On the other hand, we have shown that PC films covered with the layer of the beta-phase of $(\text{BEDT-TTF})_2\text{I}_3$ demonstrate GF being equal to 20 [4]. Taking into account that the highly piezoresistive layer of β - $(\text{BEDT-TTF})_2\text{I}_3$ may be formed via a thermo-activated $\alpha \rightarrow \beta$ phase transition that occurs at $T > 100$ $^{\circ}\text{C}$ [9], the BL film with the layer of α - $(\text{BEDT-TTF})_2\text{I}_3$ was annealed at 150 $^{\circ}\text{C}$ during 30 min. The formation of the both covering layers based on either the strain sensing β - $(\text{BEDT-TTF})_2\text{I}_3$ metal or the highly temperature sensing α' - $(\text{BEDT-TTF})_2\text{I}_x\text{Br}_{(3-x)}$ conductor was confirmed by the X-ray diffraction patterns. Referring to Figures 2(left) and 3 (left), both patterns demonstrate only (00 l) reflections that are characteristic of conducting layers formed by oriented crystals: the c^* axis of the crystals is perpendicular to the film surface and, consequently, their molecular ab conducting layers are parallel to it. The surface analysis on a micro scale, performed using "Quanta FEI 200 FEG-ESEM" scanning electron microscope (SEM), showed that the crystallites of the both types of sensitive covering layers are of submicro sizes (Fig. 2, right and 3, right).

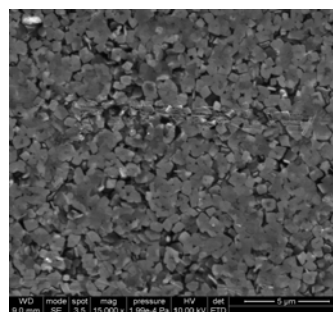
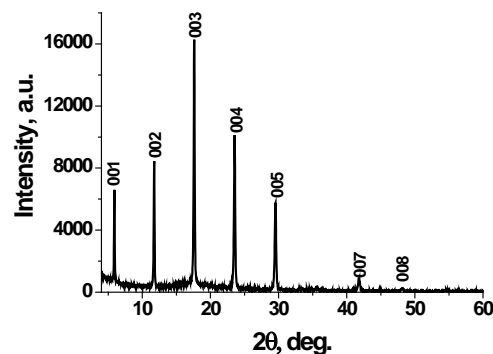


Figure 2. X-ray powder diffractogram (top) and SEM image (bottom) of the piezoresistive covering layer of β - $(\text{BEDT-TTF})_2\text{I}_3$.

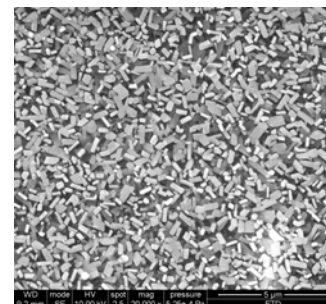
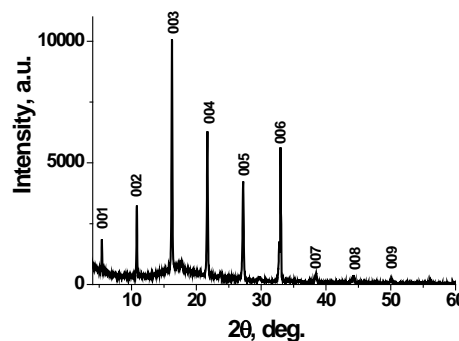


Figure 3. X-ray powder diffractogram (left) and SEM image (right) of the covering layer of α' - $(\text{BEDT-TTF})_2\text{I}_x\text{Br}_{(3-x)}$ whose electrical resistance highly sensitive to temperature changes.

As a final remark to this part, we would like to add that the temperature coefficients of resistance (TCR) were found as 0.3 %/°C and -1.3 %/°C, for the covering β -(BEDT-TTF)₂I₃ and α' -(BEDT-TTF)₂I_xBr_(3-x) layers, respectively (Fig. 4). The TCR were calculated as a relative resistance change per grade. The room temperature resistance of the films covered with the sensitive α' -(BEDT-TTF)₂I_xBr_(3-x) layer is equals to 25-30 k Ω . It is evident from the forgoing TCR that the film resistance changes as 320-390 Ω per grad. It is obviously that such sensitivity permits this BL film to control small temperature changes (0.01-0.005 grad) as a well definite electrical signal.

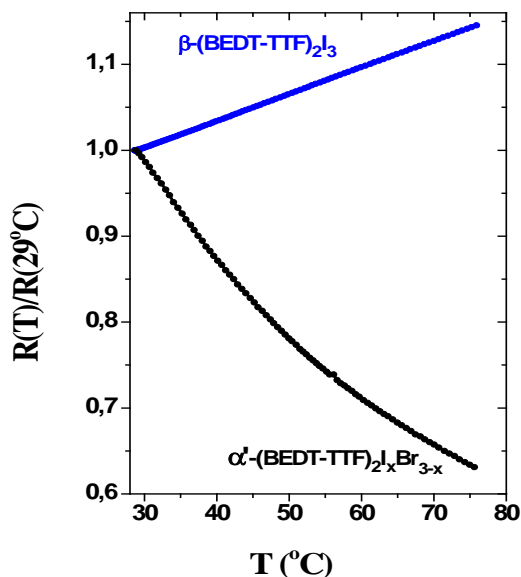


Figure 4. Temperature dependence of the resistance for sensing BL films.

III. ELECTRONIC AND ELECTROMECHANIC MEASUREMENTS – PROTOTYPES

With the aim to study the possibility to apply the highly sensitive BL films as physical sensors, different prototypes have been developed [4, 6, 7].

A. Portable Prototype capable of monitoring deformation induced resistance change displayed in a LED array

A new sensor prototype capable of measuring deformations of the BL-Film manifested in either compression or expansion of the crystalline network has been developed. For this purpose, a BL-Film covered with β -(BEDT-TTF)₂I₃, was mounted on top of a 30 μ m thick steel foil (see Figure 5 bottom right). An electronic circuit which includes a Wheatstone bridge, amplifiers and two transistor driven “staircase” light emitting diode (LED) schemes to monitor the deformation is also shown in Figure 5. Upon expansion of the BL-Film the and upon compression the corresponding LEDs turn on sequentially.

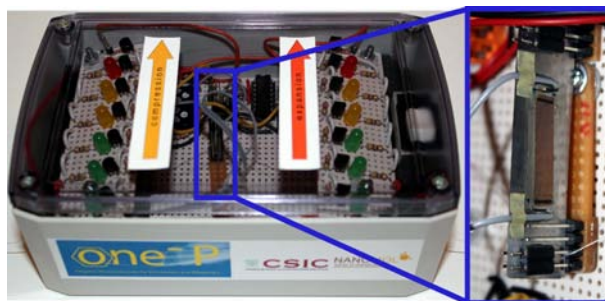
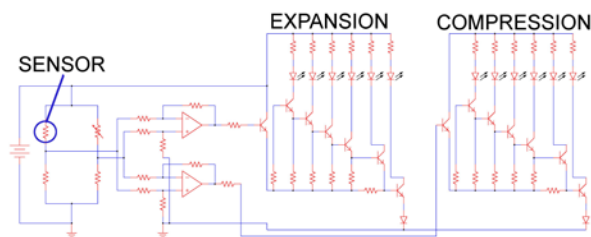


Figure 5. Demonstration proof of concept prototype to monitor the compression and expansion of BL-Film based sensor mounted on a thin steel foil. Electronic scheme (top) and finished prototype box developed at NANOMOL Department (ICMAB-CSIC) with a zoom of the sensor element (right).

B. Development of Prototypes based on piezoresistive and pyroresistive BL-Films with wireless data transmission

Our sensor prototypes developed up to now exhibited high sensitivity and reproducibility in the strain measurements; however the sensing unit was connected with an electrical cable to the measurement unit which was further connected to a measurement computer. In many real applications, especially in monitoring vital functions of the human body, sensors connected with the data acquisition (DAQ) system using wires limit the feasibility drastically. An important improvement in this regard is the development of a small measurement unit connected to the sensor element, either piezoresistive or pyroresistive, which than transmits the measured data set to a DAQ system or a computer.

A simple variant of such an electronic scheme includes a Wheatstone bridge for offset compensation and an operational amplifier [10]. Depending on the chemical nature of the BL-Film and the particular application one is interested in, the Wheatstone bridge also allows to include additional to the active strain sensing unit a passive (strain) sensors, which can be used for temperature compensation if needed. The analog electrical signal obtained after the amplifier has to be digitalized (A/D converter), encoded and transmitted. Figure 6 shows a simple block diagram of the complete sensor unit which works for both piezoresistive and pyroelectric sensors.

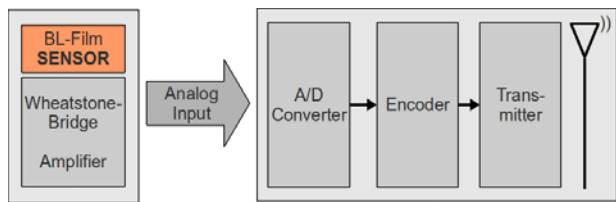


Figure 6. Simple block diagram of the BL-Film based sensor unit (either piezoresistive or pyroresistive), Wheatstone bridge with amplifier and transmitter scheme for wireless data transmission.

On the receiving side of the electrical circuit, the signal has to be decoded and transferred either directly to a DAQ-system (*i.e.*, computer) or back converted to an analog signal (Figure 7).

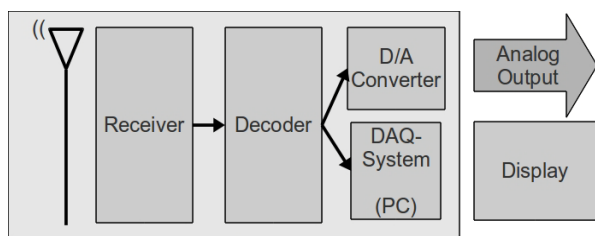


Figure 7. Simple electronic receiver scheme with decoder for either analog output or connected directly to a data acquisition (DAQ) system (*i.e.* Computer).

For the construction of a proof of concept device to measure, transmit and receive the variation of the electrical resistance induced in the BL-Film based sensor a commercial transmitter-receiver unit was purchased at ABACOM Technologies [11]. The transmitter unit (RF-AD-TX) consists of an 8 bit analog to digital converter able to convert a voltage range from 0 to 5 V of up to four independent channels and a corresponding step size of about 20 mV. The transmitter works at a frequency of 433 MHz. The receiver unit (RF-AD-RX) on the other hand consists of an 8 bit digital to analog converter and again for corresponding analog outputs. A schematic representation is

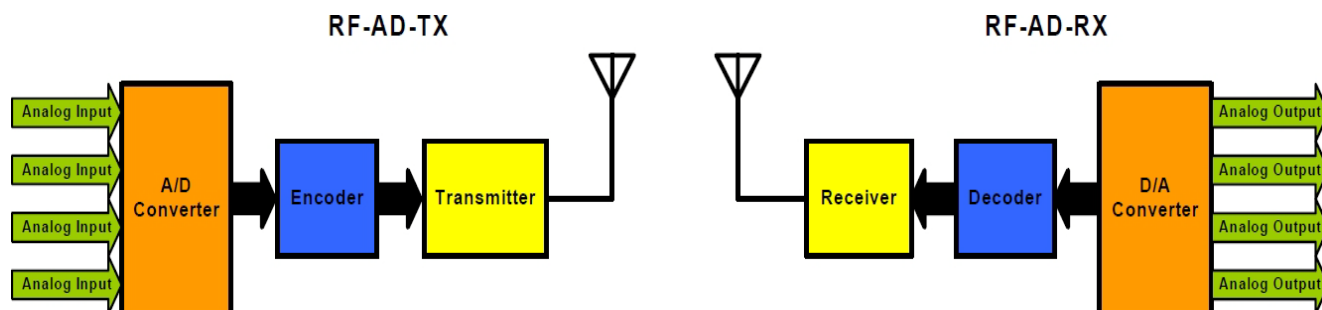


Figure 8. Commercially available analog to digital transmitter (RF-AD-TX) and digital to analog receiver (RF-AD-RX) used to transmit the measured and amplified signal of the BL-Film based sensor (scheme taken from data sheet, 11).

shown in Figure 8.

A complete system and a new generation of prototypes including similar schemes described above with wireless data transmission in smaller dimensions is currently under preparation. The development of similar prototype devices including wireless data transmission is desired especially for applications in biomedicine for human healthcare to monitor vital functions.

IV. SUMMARY

It was shown that covering polycarbonate films with the α' -(BEDT-TTF)₂I_xBr_(3-x) conductor makes a good promise of a flexible lightweight temperature sensor.

The small measurement unit connected to the BL film-based sensing elements which is able to transmit the measured data set to a DAQ system or a computer have been designed that permits to develop prototypes of the BL film-based strain and temperature sensors with wireless data transmission.

The preliminary data show that the polycarbonate films covered with molecular BEDT-TTF-based conductors show a considerable promise as flexible wireless physical sensors that are able to take the place of conventional metal-based strain and temperature sensors in biomedical high-tech. It is expected that developed sensing materials may have a large impact in biomedical applications.

ACKNOWLEDGMENT

The research was supported by Instituto Carlos III, through “Acciones CIBER” under CIBER-BBN, the MICINN, Spain (CTQ2006-06333/BQU and CTQ2010-19501/BQU), and Generalitat de Catalunya (2009SGR00516).

REFERENCES

- [1] S. Y. Yurish, N. V. Kirinaki, and I. L. Myshkin, "World Sensors and MEMS Markets: Analysis and Trends", *Sensors & Transducers Magazine (S&T e-Digest)*, vol. 62, Issue 12, pp. 456-461, 2005.
- [2] F. Axisa, P. M. Schmitt, C. Gehin, G. Delhomme, E. McAdams, and A. Dittmar, "Flexible technologies and smart clothing for citizen medicine, home healthcare and disease prevention", *IEEE Transactions on Information Technology in Biomedicine*, vol. 9, No. 3, pp. 325-336, 2005.
- [3] B. Adhikari, and S. Majumdar, "Polymers in sensor applications", *Progress in Polymer Science*, vol. 29, pp. 699-766, 2004.
- [4] E. Laukhina, R. Pfattner, L. R. Ferreras, S. Galli, M. Mas-Torrent, N. Masciocchi, V. Laukhin, C. Rovira, and J. Veciana, "Ultrasensitive Piezoresistive All-Organic Flexible Thin films", *Adv. Mater.*, vol. 22, pp. 977-991, 2010.
- [5] E. Laukhina, C. Rovira, and J. Ulanski, "Organic metals as active components in surface conducting semi-transparent films", *Synth. Met.*, vol. 21, pp. 1407-8, 2001
- [6] V. Laukhin, I. Sánchez, A. Moya, E. Laukhina, R. Martin, F. Ussa, C. Rovira, A. Guimera, R. Villa, J. Aguiló, J.-C. Pastor, and J. Veciana, "Prototype for Noninvasive IOP Monitoring with a Nanostructured Polymeric Sensor Embedded in a Contact Lens", *Transducers & Sensors*, vol. 170, pp. 36- 43, 2011. Patent: ES2330405-A1; WO2009147277-A1.
- [7] L. R. Ferreras, R. Pfattner, M. Mas-Torrent, E. Laukhina, L. López, V. Laukhin, C. Rovira, and J. Veciana J. "Highly piezoresistive textiles based on a soft conducting charge transfer salt", *Mater. Chem.*, vol. 21, pp. 637- 641, 2011.
- [8] E. Laukhina, V. Tkacheva, S. Khasanov, L. Zorina, J. Gomez-Segura, A. Perezdel Pino, J. Veciana, V. Laukhin, and C. Rovira, "Linked Crystallites in the Conducting Topmost Layer of Polymer Bilayer Films Controlled by Temperature: From Micro- to Nanocrystallites", *ChemPhysChem*, vol. 7 pp. 920 – 923, 2006
- [9] E. E. Laukhina, V. A. Merzhanov, S. I. Pesotskii, A. G. Khomenko, E. B. Yagubskii, J. Ulanski, M. Kryszewski, J. and K. Jeszke, "Superconductivity in reticulate doped polycarbonate films containing (BEDT-TTF)₂I₃", *Synth. Met.*, vol 70, pp. 797-800, 1995.
- [10] U. Tietze, and C. Schenk, "Halbleiter-Schaltungstechnik", Springer Verlag Berlin-Heidelberg, 1999, ISBN: 3-540-64192-0, pp. 1242-1260.
- [11] ABACOM Technologies: <http://www.abacom-tech.com> [retrieved : 07, 2012].

Performance Testing of a Low Power Consumption Wireless Sensor Communication System Integrated with an Energy Harvesting Power Source

Vlad Marsic, Alessandro Giuliano, Michele Pozzi, Meiling Zhu and Stewart Williams

School of Applied Sciences
Cranfield University

Cranfield, Bedfordshire, United Kingdom, MK43 0AL

E-mail: v.a.marsic@cranfield.ac.uk, a.giuliano@cranfield.ac.uk, m.pozzi@cranfield.ac.uk,
m.zhu@cranfield.ac.uk and s.williams@cranfield.ac.uk

Abstract— This paper presents the performance testing results of a wireless sensor communication system with low power consumption integrated with a vibration energy harvesting power source. The experiments focus on the system’s capability to perform continuous monitoring and to wirelessly transmit the data acquired from the sensors to a user base station, completely battery-free. Energy harvesting technologies together with system design optimisation for power consumption minimisation ensure the system’s energy autonomous capability demonstrated in this paper by presenting the promising testing results achieved following its integration with Structural Health Monitoring (SHM) and Body Area Network (BAN) applications.

Keywords - vibration scavenging; energy harvesting; low power consumption; wireless sensor communication system;

I. INTRODUCTION

Technological advances have led to increasing levels of automation, but have also contributed to creating new vulnerabilities to equipment failure, human error, weather conditions and other interfering factors. These vulnerabilities need to be addressed using evolutionary approaches. The continuity and viability of critical infrastructures can be ensured using adaptive approaches that monitor sensory data coming from various sensors situated in vulnerable locations. Such networks of sensors that monitor different physical or environmental conditions, and then communicate this data wirelessly to a base station, are known as wireless sensor networks (WSN).

A wireless sensor network consists of sensor nodes that possess computing power and the ability to transmit and receive messages wirelessly. Each sensor node is typically formed of a sensing unit (i.e., sensors), a processing unit (i.e., microcontroller), a transmitter/receiver unit (i.e. the part that connects the node to the network) and an energy source (i.e., a battery or an energy harvester). The energy source is one of the most important components of a sensor node, as this component determines its life span. The use of a battery as energy source would limit the lifetime of the sensor node, and of the entire sensor network. This shortcoming can be addressed by designing self-powered wireless sensor nodes that harvest energy from the surrounding environment and use this energy efficiently to ensure a potentially unlimited

functionality of the sensor node. Energy harvesting from external sources such as ambient vibrations, wind, heat or light could produce sufficient energy for the sensor nodes to be functional indefinitely, as long as the wireless sensor network uses this energy efficiently.

Energy efficiency is a major issue for wireless sensor networks. The most power-consuming activity of a WSN is communication. In our previous work ([1], [2]) this problem was addressed by proposing a novel design and implementation of an autonomous wireless sensor communication system with low energy consumption powered from a vibration piezoelectric harvester. The innovative design and implementation technique targeted power consumption minimisation at three different levels: hardware, software and data transmission, in order to reduce the power consumption of the off-the-shelf components included in the system with the aim of ensuring its energy autonomy through a smart energy flow management. The capability of the resulted system to perform continuous monitoring and to wirelessly transmit the data acquired from the sensors to a user base station was then evaluated in the context of SHM and BAN applications. The main motivation underlying this paper is to present the results of laboratory testing for the designed and implemented low power consumption communication sensing system in SHM and for BAN technology.

This article is structured as follows: Section II reviews previous related work in this field, Section III describes the general structure of our system, while Section IV focuses on its implementation. The testing results collected from the two different setups for SHM and BAN technology are presented in Section V. Conclusions are drawn in Section VI.

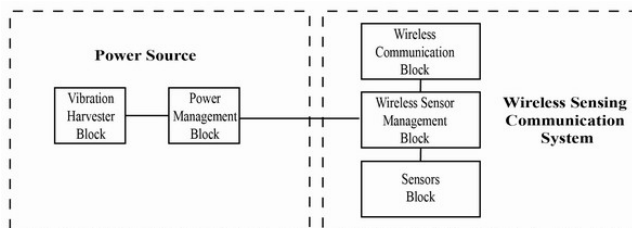


Figure 1. Block diagram of a wireless sensor node powered by a vibration energy harvester

II. STATE OF THE ART

In recent years, energy harvesting devices have attracted much interest due to an increasing need for battery free remote monitoring of different structural parameters. Vibration energy harvesters (EH) can scavenge and transform environmental vibration into electricity using electro-magnetic or piezoelectric structures and, according to their design purpose, one can distinguish two categories: vibration energy harvesters for SHM, and for BAN. The two groups are built differently because of environmental factors such as force, acceleration and displacement, which in the end determine the weight, internal structure, and the impedance of the designed harvester. The devices powered by the above presented groups of EH are used to collect, monitor and display different data directly related to the two domains of BAN and SHM. When powered from a weak power source such as an energy harvester, existing monitoring technology is not suitable to function and provide the full range of monitoring processes such as collecting data, processing and transmitting this information. This is why recent research has focused on the design and implementation of low power wireless communication systems that can be used as autonomous health monitoring systems while being powered only from an energy harvester.

In the case of BAN systems, the vibration harvesting technology was implemented in wrist watches [5], intelligent clothing [6], remote control radio press-buttons [7], [8] and implants [9]. In the case of SHM systems, EH technology was used for monitoring tyre pressure [10], vibrations from vehicles' rotating tyre engines [11], environmental characteristics [12], vibrations from buildings and bridges [13]. Some of these applications feature a low power wireless communication system whose autonomy is ensured through the use of a vibration energy harvester. For example, [11] presented a wireless system powered from a vibration harvester for an aircraft's SHM.

Our previous work [1], [2], focused on the design and implementation of a low power wireless communication system that uses off-the-shelf available technology and is powered from a vibration energy harvester. Laboratory measurements indicated a very good performance and confirmed the advantages of the three level energy consumption optimization approach: the main aim of the design and system implementation methodology was to reduce power consumption at the hardware, software and data transmission levels. The module resulted from our previous research is general enough to be employed in a variety of applications. Its wide generalization capability is demonstrated in the present article, whose novelty lies in the fact that it presents the same low power wireless communication module functioning with the energy produced by a vibrational piezoelectric harvester being successfully employed to provide continuous monitoring in the context of both SHM and BAN applications.

There are no previously published reports of any module relying on vibration energy harvesters capable of continuous self-powering and continuous monitoring both for SHM and BAN, and this is where the present work brings its original contribution.

III. SYSTEM DESCRIPTION

Fig. 1 illustrates a self-powered autonomous wireless sensor system composed of a power source and a wireless sensing communication system. These two main subsystems are further divided into five functional blocks: vibration energy harvester block, power management block, wireless communication block, wireless sensor management block and sensors block.

The vibration energy harvester block is the power supply. The energy it produces is directly dependent on the vibration provided by the wireless sensor deployment environment.

The power management block transforms and stores the energy generated by the vibration harvester.

The wireless sensor management block is the link between the sensors block and the wireless communication block. It takes data from the sensors block and processes it in order to be sent to the wireless communication block.

The sensors block interacts with the external environment and interprets specific stimuli (e.g., temperature, acceleration, light intensity, pressure, etc.) by transforming them in useful signals for the management block processing.

The wireless communication block transmits the data provided by the wireless sensor management block, to a base station which can be linked to the internet or directly to the user.

At the system design stage, the key-problems to be resolved are:

- Reduce the power consumption in the active mode (while executing the programmed instructions, reading sensors' data, and transmitting wirelessly the information), and in the passive mode (while the device is disconnected from the power source or enters an idle mode known as deep sleep, until the energy storage device regains enough energy for the system to function in active mode);
- Preserve the system's basic functionality and compatibility with standards after reducing the energy consumption (i.e., preserve the main function of transmitting data using a certified protocol like IEEE 802.15.4, and respect the restrictions involving power and license for certain geographic regions).

IV. SYSTEM IMPLEMENTATION

This section describes briefly the design and implementation of the system to overcome the challenges that appeared during the initial design stages presented in our previous articles ([1], [2]). The novelty of our approach lies in the analysis and implementation of the optimal strategy to reduce the power consumption for all the embedded off-the-

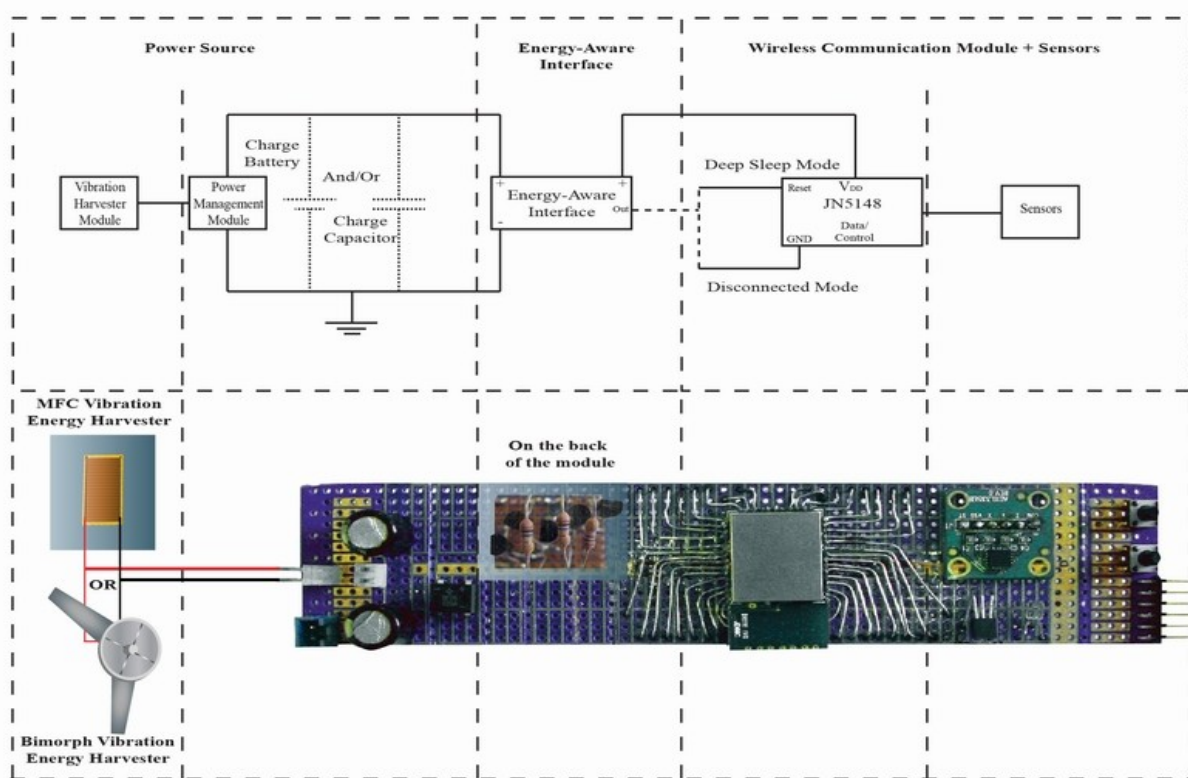


Figure 2. Implemented system architecture.

shelf subsystems at three different levels: hardware, software and data transmission.

At hardware level, the wireless microcontroller was isolated from the power management module during periods of inactivity by introducing an Energy Aware Interface (EAI) which monitored the amount of energy produced by the harvester stored in a charging element, and interrupted the power supply to the wireless communication module until the minimum level of energy required for the active state was reached. The current consumption of the whole system was reduced to 1.19µA for the disconnected mode – the passive mode of the functioning duty-cycle. This represents a 10-times reduction in current consumption before undertaking any modification of the system module.

At software level, the system was improved in terms of reducing power consumption by choosing the most suitable libraries for the application, the right sensors and by designing a suitable power-saving algorithm to read and transmit data.

The choices concerning data transmission were made with a view towards minimising data consumption, preserving the simplicity of the architecture, avoiding collisions and interferences, and ensuring data security. To this end, an IEEE 802.15.4 star configuration was selected for the data transmission level. The data was wirelessly transmitted using 3 different channels corresponding to the 2.4GHz world-wide free license frequency. This

multichannel mode favoured the implementation of a TDMA (Time Division Multiple Access) protocol, thus ensuring better transmission/reception and efficiency due to solving the problem involving the data packets collisions.

The energy harvester is different for each of the applications presented in the following, i.e. SHM and BAN, and it was chosen as the most suitable model for implementation in these two different technologies.

For SHM, the vibration energy harvester is based on the Macro-Fiber Composite (MFC) [14] and glued to an aluminium alloy substrate of the same type used in the airplane industry for producing the aircraft lower wing skin. The aluminium plate is mounted on a tensile testing machine which is used to simulate the airplane wing flying stress levels and vibration conditions.

For BAN, the vibration energy harvester is based on a design created at Cranfield University for a project involving body wearable energy harvesting sources, and described in [15] and [16]. It is composed of four fixed bimorph piezoelectric cantilevers which are fitted in the centre of a wearable rotating wheel. Small plectra are fixed on the interior side of the wheel's outer ring. The wheel is mounted on a stepper motor to simulate the joint-knee movements. When the wheel is rotating, the plectrum pluck the bimorph piezoelectric material, makes it vibrate, therefore converting the leg movement to bimorph vibration, and afterwards to electricity.

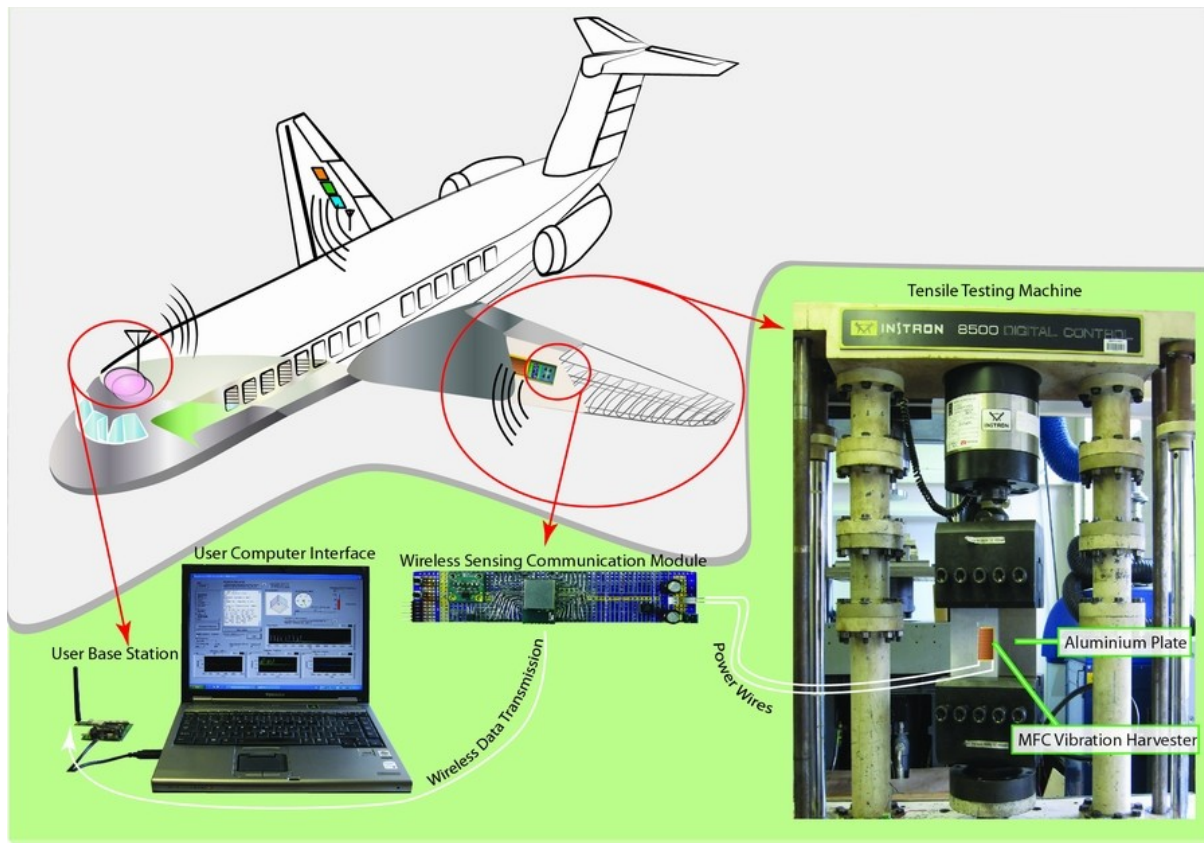


Figure 3. Structural Health Monitoring: application and laboratory testing set-up.

The implemented design of the wireless sensing module powered by a vibration piezoelectric energy harvester is presented in Fig.2. In the context of this architecture, the harvester which converts the vibration energy to electricity, correspondent to the block diagram illustrated in Fig.1 is different for each application: SHM and BAN. The power management module then rectifies the voltage and stores it in two 1mF reservoir capacitors. The energy is discharged when a pre-set threshold is reached. This is triggered by the energy aware interface present on the back of the module. The energy is distributed to each sensor by the wireless microcontroller. The microcontroller, represented by the JN5148 module manufactured by Jennic-NXP is one of the lowest power consumption products currently available on the market. It features a 32 bit CPU (Central Processing Unit), 4 to 32MHz clock frequency and 128Kb RAM (Random Access Memory) [17].

The three sensors were chosen to be included in the system because of their low power consumption, low initialisation time, and also due to the deployed environmental stimuli. The first-one is ADXL 335 3 axes accelerometer [18], the second one is the temperature sensor MCP9700 [19], and the last one is the light intensity sensor GA1A2S100 [20]. All sensors are interrogated by the JN5148 microcontroller, and afterwards the information is

sent to the wireless integrated transmitter/receiver (Tx/Rx). The Tx/Rx is compliant with the IEEE 802.15.4 protocol working at 2.4 GHz frequency and allowing the usage of 16 different channels. Out of those 16 channels, three channels were chosen for a multichannel transmission which allows the implementation of a simple TDMA (Time division multiple access) anti-collision algorithm, reduces the possibility of channel overlapping and interference with the existent wireless applications active in the same area, and also provides the user the possibility to calculate the location of the node using a TOF (Time-of-flight) algorithm. The data is sent wirelessly to the user base station equipped with the same JN5148 wireless microcontroller, powered by a stable power source (battery or DC power source) and linked via a USB cable to a computer. The information is displayed in LabView using a graphical interface especially designed and implemented for this purpose. The signal strength and data from the sensors are monitored and saved for further analysis in two output text files: one containing all the sensors and signal data, and another one counting the number of transmissions/receptions and measuring the time interval between two consecutive ones.

Due to the fact that the module is designed to continuously monitor the vibration, which is its energy source, the system duty cycle is directly related with the

TABLE 1. Experimental Data Transmission for SHM

Test Conditions		Time gap between two consecutive system duty cycle data transmissions [s]				
Frequency	Applied Force (Strain)	11kN (114 $\mu\epsilon$)	21kN (228 $\mu\epsilon$)	31kN (342 $\mu\epsilon$)	41kN (456 $\mu\epsilon$)	51kN (570 $\mu\epsilon$)
	1Hz		39.6	12.5	7	4.9
2.5Hz		13.5	4.9	2.7	2	1.5
5Hz		6.6	2.4	1.5	1	0.8
7.5Hz		6.2	1.7	1.1	0.7	0.6
10Hz		5.2	1.4	0.7	0.6	0.4

energy source: if there is vibration, there is energy to function, to monitor and transmit the data; if there is no vibration, there is no energy and nothing to be monitored.

In order to test the wireless sensing system’s ability to provide continuous monitoring, we powered it, in turn, from two different energy harvesting technologies related to SHM and BAN, the main criterion used to illustrate the performance of the system being the dimension of the time gap between two consecutive duty cycle transmissions.

The data is transmitted with the standard IEEE 802.15.4 speed of 250 kbps, using three different channels, and the total amount of data transmitted during one duty cycle (i.e., data payload, network addresses and correction Bytes) contains 100 Bytes. The system duty-cycle used for testing as presented above and in [2] consists of two stages:

- **Passive mode** – the system is waiting for the energy stored in the 2mF capacitor to reach the preset level in order to start the operations. At this stage, due to the smart management of the energy flow accomplished by the implemented energy aware interface (EAI), the current consumption is 1.19 μ A.
- **Active mode** – the system is reading data from the three sensors and transmits wireless the information to the user base station using a multichannel transmission. The whole process duration is 10ms and the average power consumption to read data and transmit 100 Bytes at +2.5dBm transmission power is 16.7mW.

V. TESTING RESULTS

A. SHM

As previously mentioned in Section III, the wireless sensing system integrated with SHM technology is powered by a vibration harvester based on NASA’s MFC glued on an aluminium plate which is then mounted into the Istron 8500 tensile testing machine. The tensile testing machine is used to apply a range of frequencies from 1 to 10 Hz and a force between 11 and 51kN to the aluminium plate, and the material stress generates a proportional strain, varying from 114 to 570 $\mu\epsilon$.

This investigation is motivated by the intention of implementing piezoelectric vibration harvesters in aircraft wings so that they power wireless sensing systems embedded or mounted in the same area.

The wirelessly transmitted data would be collected by a base station, powered from a regular power source, which can be located inside the airplane body.

The piezoelectric harvesters were chosen against electromagnetic ones due to their light weight, small volume and possibility to be embedded in layered structures or used as patches. The downside of the piezoelectric vibration harvester materials is the small amount of power output and, as a consequence, the power consumption of the wireless sensing system should be reduced at all three levels, hardware, software and data transmission, so that it is able to grant the continuous monitoring capability of the system. The targeted SHM application and the equivalent laboratory testing set-up are presented in Fig.3.

The continuous monitoring capability can be observed in Fig. 4 obtained by plotting the data stored by the LabView user interface. The data reveals a gap of only 0.4s between two consecutive data transmissions for 10Hz vibration frequency and 51kN (570 $\mu\epsilon$) of applied force.

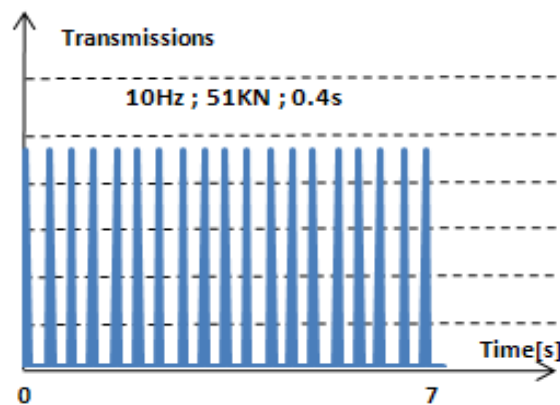


Figure 4. Time gap between transmissions for SHM.

The measured time gap between two consecutive system transmissions (duty cycle) is presented in Table 1, for all frequencies and strain outputs generated when the applied force is present. As results included in the table above demonstrate, the system’s continuous monitoring capability is achieved not only for higher vibration frequencies like 7.5-10Hz, when it can monitor and transmit new data every 0.4s, but even at a vibration level of 1Hz, when it can transmit the 100 Bytes of information every 3.5s.

B. BAN

In the case of the BAN technology, the power is supplied by the wearable “Pizzicato energy harvester”, [21], [22], developed at Cranfield University.

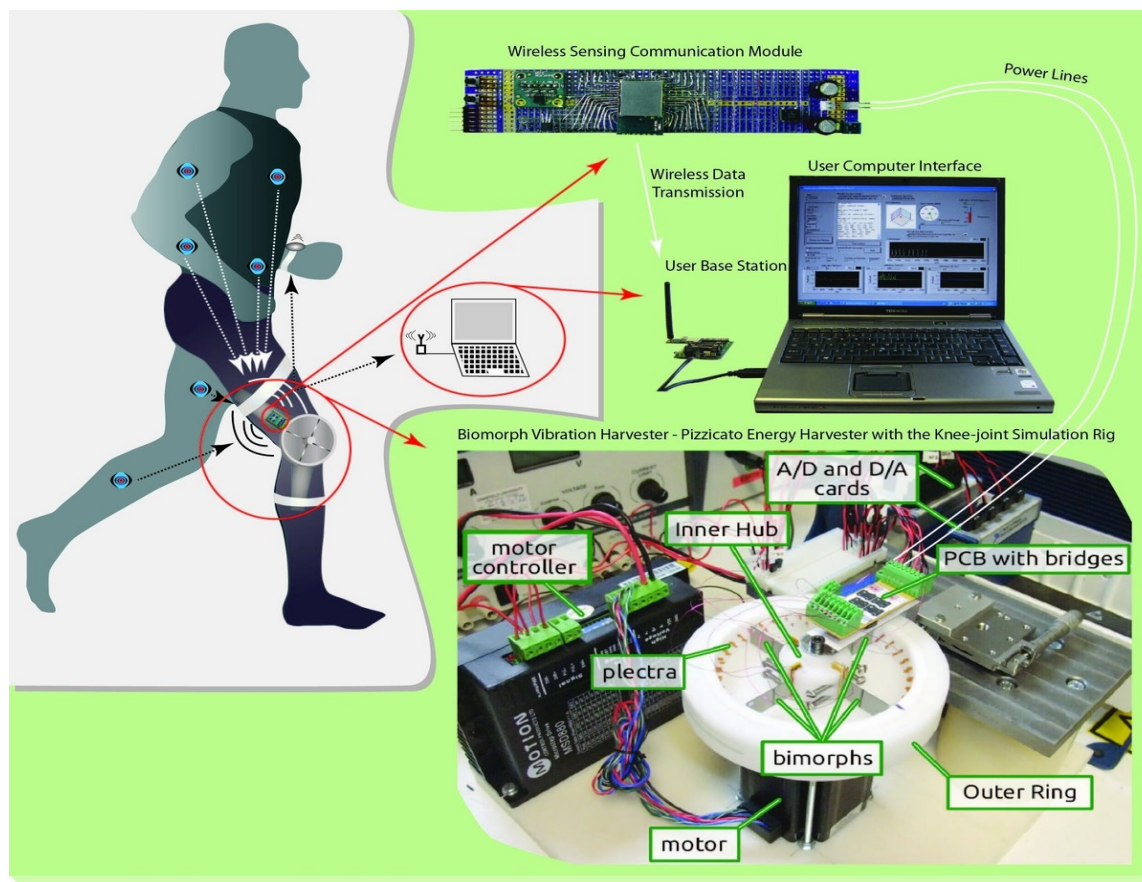


Figure 5. Body Area Network: application and laboratory testing set-up.

This system is designed to be fitted externally on the side of a human knee in order to produce energy by harvesting the body movement. For the tests presented in this paper, the harvester was fitted onto a stepper motor controlled via a controller driver interface and a National Instruments data acquisition card (DAQ).

The aim of the application is to monitor and to wirelessly transmit real time data about the bearer, using the three sensors already described, and/or to link future implantable sensors with shorter wireless range, interrogating them and retransmitting the data to the user base station which can be a regular computer or a wearable low power consumption display interface (i.e., wrist watch), as in Fig. 5.

Three simulated testing scenarios were used for the harvester movement based on real data gathered from human behaviour monitoring. The first scenario simulates the movements of a human carrying an empty backpack, the second one simulates a human carrying 12kg inside the backpack, and the third one a human that has 24kg inside the backpack. The power from the piezoelectric harvester, after rectification, is transferred via two wires to the wireless sensing module. The module stores the energy in the 2mF capacitors and transfers it to sensors and microcontroller when there is enough to perform the duty cycle. Afterwards,

it transmits the 100 Bytes to the user base station for further analysis.

A representative example of continuous monitoring capability can be observed in Fig. 6. The data shows a gap of only 1.1s between any two consecutive data transmissions for the simulated scenario when the backpack contains 0kg of weight.

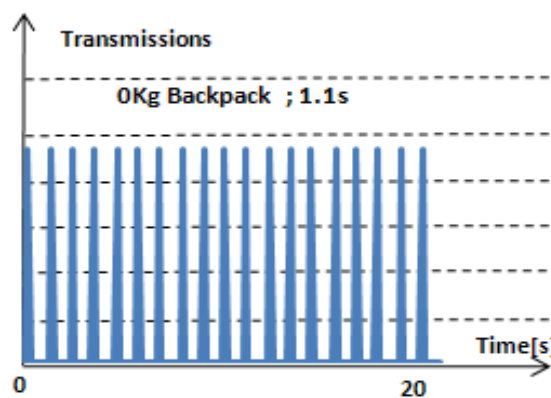


Figure 6. Time gap between transmissions for BAN.

The experimental test results obtained for the all three tests described above are presented in Table 2.

TABLE 2. Experimental Data Transmission BAN.

Simulated Situations	Time gap between two consecutive system duty cycle data transmissions [s]
0 kg Backpack	1.1
12 kg Backpack	1.1
24 kg Backpack	1.1

The results of these experiments demonstrate the system’s continuous monitoring capability for BAN energy harvesting technology, being able to transmit the 100 Bytes of data every 1.1s for all the three simulated scenarios.

VI. CONCLUSIONS

This work relies on a low power consumption wireless sensor communication system that was designed and implemented so that the power consumption was minimised at three levels: hardware, software and data transmission. This optimisation strategy that guided the system development was directed towards the aim of achieving energy autonomy, while at the same time ensuring the required functionality only with the power provided by a low power vibration energy harvester. The resulted battery-free wireless sensor communication system built using only off-the-shelf components, and powered by a low energy vibration harvester, was employed in two different applications: SHM and BAN monitoring. The successful testing scenarios presented in this paper illustrate the system’s ability to not only adapt for usage with two different energy harvesting technologies, but also to continue monitoring and to transmit wirelessly via multichannel the 100 Bytes of information, using a standard communication protocol and the transmitter power pre-set at the highest level of +2.5dBm at the same time achieving a speed between two transmission duty cycles of 0.4s for SHM and 1.1s for BAN.

Further directions of research will focus on each deployment environment scenario, and will investigate ways to decrease the power consumption either by replacing the set of general purpose sensors with one dedicated sensor, or by using a different transmission frequency or different transmission protocols, or by optimising other application-specific factors.

REFERENCES

[1] Marsic V., Zhu M., and Williams S., “Design and implementation of a wireless sensor communication system with low power consumption for energy harvesting technology”, Proceedings of the 19th Telecommunications Forum TELFOR 2011, pp. 607 – 610, 2011.
 [2] Marsic V., Zhu M., and Williams S., “Wireless sensor communication system with low power consumption for integration with energy harvesting technology”, TELFOR Journal, Volume 4, 2012.

[3] Lee T.H., “The design of CMOS radio-frequency integrated circuits a nonlinear history of radio”, A Nonlinear History of Radio, Cambridge University, pp. 1-34, 1998.
 [4] Theremin L. S., “Signaling apparatus”, U.S. 1658953, Feb 14, 1928.
 [5] Paradiso J. and Starner T., “Energy scavenging for mobile and wireless electronics”, IEEE Pervasive Computing, 4(1), pp. 18-27, 2005.
 [6] Hum A., “Fabric area network – a new wireless communications infrastructure to enable ubiquitous networking and sensing on intelligent clothing”, Computer Networks, 35(4), pp. 391-399, 2001.
 [7] Paradiso J. and Feldmeier M., “A Compact , Wireless , Self-Powered Pushbutton Controller Design”, pp. 299-304, 2001.
 [8] EnOcean, “PTM 100 User Manual”, http://docweb.khk.be/khk/remote/technologie/EnOcean/MAN_ENG1.pdf [Accessed 01 Feb. 2012].
 [9] Platt S., Farrant S., Garvin K., and Haider H., ”The use of piezoelectric ceramics for electric power generation within orthopedic implants”, Mechatronics, IEEE/ASME Transactions, 10(4), pp. 455-461, 2005.
 [10] Daniel S., “Piezoelectric reed power supply for use in abnormal tire condition warning systems”, U.S., 4510484, Apr 9, 1985.
 [11] Arms S., Galbreath J., Townsend C., Churchill D., Corneau B., Ketcham R., and Phan N., “Energy Harvesting Wireless Sensors and Networked Timing Synchronization for Aircraft Structural Health Monitoring”, Proceedings of the 1st International Conference on Wireless Communication, Vehicular Technology, Information Theory and Aerospace & Electronic Systems Technology, pp.16-20, 2009.
 [12] Del Balzo D., Chen H., Hughes B., Cranford C., and Stewart S., “Drag body design in support of wave energy harvesting”, OCEANS 2010, pp.1-6, 2010.
 [13] Galchev T., McCullagh, J., Peterson R.L., and Najafi, K., “Harvesting traffic-induced bridge vibrations”, Proceedings of the 16th International Solid-State Sensors, Actuators and Microsystems Conference (TRANSDUCERS), pp. 1661 – 1664, 2011.
 [14] High J. W. and Wilkie W. K., “Method of Fabricating NASA-Standard Macro-Fiber Composite Piezoelectric Actuators”, Technology, pp. 1-30, 2003.
 [15] Pozzi M. and Zhu M., “Characterization of a rotary piezoelectric energy harvester based on plucking excitation for knee-joint wearable applications”, Smart Materials and Structures, 21(5), 2012.
 [16] Pozzi M., “Analytical Modelling of a Plucked Piezoelectric Bimorph for Energy Harvesting”, arXiv.org Physics, arXiv:1204.0070, 2012.
 [17] Jennic-NXP, ”JN5148-001 Data Sheet”, http://www.jennic.com/files/product_briefs/JN-DS-JN5148-1v6.pdf [Accessed 01 Feb. 2012].
 [18] Analog Devices, “Small, Low Power, 3-Axis ±3 g Accelerometer ADXL335”, <http://www.sparkfun.com/datasheets/Components/SMD/adxl335.pdf> [Accessed 01 Feb. 2012].
 [19] Microchip, “MCP9700/9700A MCP9701/9701A, Low-Power Linear Active Thermistor™ ICs”, <http://www1.microchip.com/downloads/en/DeviceDoc/21942e.pdf> [Accessed 01 Feb. 2012].
 [20] Sharp, “GA1A2S100SS/GA1A2S100LY OPIC™ Linear Output Ambient Light Sensor”, http://sharp-world.com/products/device/lineup/data/pdf/datasheet/ga1a2s100ss_ly_e.pdf [Accessed 01 Feb. 2012].
 [21] Pozzi M. and Zhu M., “Plucked piezoelectric bimorphs for knee-joint energy harvesting: modelling and experimental validation”, Smart Materials and Structures, 20(5), 2011.
 [22] Pozzi M. and Zhu M., “Pizzicato excitation for wearable energy harvesters”, SPIE Newsroom, SPIE10.1117/2.1201104.003682, 2011.

On the Need for Low Phase Noise Oscillators for Wireless Passive Sensor Probing

Nicolas Chrétien, Bruno François,
Gilles Martin, Sylvain Ballandras
FEMTO-ST, Time & frequency
32 avenue de l'observatoire
25044 Besançon, France

Emails: {nicolas.chretien,bruno.francois,
gilles.martin,ballandr}@femto-st.fr

Jean-Michel Friedt
SENSeOR, Besançon, France
Email: jmfriedt@femto-st.fr

Pratyush Varshney
Centre for Applied Research in Electronics
Indian Institute of Technology Delhi
Hauz Khas, New Delhi-110 016, India
Email: varshney.pratyush@gmail.com

Abstract—Two oscillators are needed for passive wireless sensor readers: a radiofrequency local oscillator generating the carrier within the bandpass of the sensor, and a clock triggering analog to digital conversion of the signals returned by the sensor. We assess the influence on measurement resolution of these two oscillators, hinting at some design rules of the sensor based on the characteristics of the oscillators as driven by cost, size, or power consumption. We demonstrate that local oscillator phase noise is a significant parameter in assessing the resolution of passive acoustic sensor probed through a wireless link, although with different characteristic conditions whether the sensor is in a delay line configuration (short term – far from carrier – response) or a resonator (long term – close to carrier – response).

Keywords—surface acoustic wave; sensor; passive; wireless; phase noise; RADAR.

I. INTRODUCTION

Wireless passive sensors are either piezoelectric or dielectric transducers coupling with an incoming electromagnetic field following conditions dependent on the physical property under investigation. For instance, surface acoustic wave (SAW) delay lines convert an incoming electromagnetic pulse to a mechanical wave propagating on a piezoelectric substrate. Mirrors patterned on this substrate reflect a fraction of this wave back to the interdigitated transducer (IDT) connected to the antenna: the direct piezoelectric effect converts these acoustic pulses to electromagnetic signals detected by the receiver. Hence, a passive acoustic delay line reader operates following principles similar to RADAR, with a delayed echo not associated with reflections of the emitted signal over dielectric or conductive interfaces, but with delays associated with a measurement. Thus, all the well known RADAR techniques have been applied to passive wireless sensing, whether dielectric [1], [2], [3] or based on piezoelectric substrates [4], [5], [6], [7], [8], [9]: wideband pulsed RADAR [10], [11], FMCW RADAR [12], [13], FSCW RADAR [14], [8], [9], and chirped RADAR [15], [16].

Since it is well known that the local oscillator characteristics drives the detection capability of RADARs as will be discussed in the first introductory section of this presentation (Fig. 1), one might consider how local oscillator phase noise

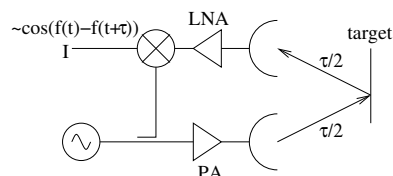


Figure 1. In case of a static target, a CW RADAR receiver noise detection limit is associated with the local oscillator frequency fluctuation between the emitted pulse at time t and the received pulse delayed by τ , the two-way transit duration.

affects passive wireless sensor resolution [17]. We extend in the third section the discussion from the classical passive target to the short-term – wideband – delay line acoustic sensor configuration in which the phase noise characteristics far from the carrier defines the measurement resolution. Since wideband acoustic delay lines are only compatible with the allocated 2.45 GHz band, we consider in the fourth section the same approach applied to narrowband resonators, compliant with the narrowband 434 MHz radiofrequency band, and the phase noise characteristics now shifted to the region close to the carrier. Such considerations will bring us in the fifth section to consider a second oscillator usually found on such circuits: the clock defining the analog to digital conversion rate. Thus, the reader is led throughout this paper to consider the various regions of the phase noise spectrum as a limiting factor for acoustic sensing resolution depending on the transducer characteristic time constants.

II. PHASE NOISE INFLUENCE ON CW RADAR

This introductory section reminds the reader of basic concepts related to phase noise of oscillators and their effect on RADAR detection capability. We will focus on the continuous wave (CW) RADAR where the explanation is straight forward.

CW RADARs are used whenever a velocity information is considered without ranging capability: a radiofrequency (RF) wave is generated by an oscillator. This signal is on the one hand fed to an antenna (after being amplified by a power amplifier, PA) and on the other hand a fraction of the output of the oscillator is sent to one input of a mixer. The second input of this mixer is fed with the signal detected by

either a second antenna in a bistatic configuration, or at the output of a circulator in a monostatic configuration, after amplification by a low noise amplifier (LNA). The output of the mixer m is the product of the frequency generated at time t by the oscillator but shifted by the Doppler frequency due to target motion δf , and the oscillator frequency delayed by a duration τ due to the electromagnetic wave propagation in air to and from the target:

$$m = \cos(2\pi(f(t) + \delta f)) \times \cos(2\pi(f(t + \tau))) \propto \cos(2\pi(f(t) + \delta f \pm f(t + \tau))) \quad (1)$$

with only the difference term remaining after filtering the output by a low pass filter aimed at removing the signal at frequencies above f . Let us consider the case of slowly moving targets, where δf will be considered negligible; then $m \simeq \cos(2\pi(f(t) - f(t + \tau)))$. Ideally this term should vanish when the target is not moving and assuming the oscillator ideally stable, *i.e.*, $f(t)$ constant; the only beat frequency would be associated to δf . However, oscillators do exhibit phase noise, and thus $f(t + \tau)$ and $f(t)$ differ: the phase noise spectrum of an oscillator is defined as the Fourier transform of the autocorrelation function of the oscillator output frequency [18].

The classical CW RADAR detection limit concludes that a moving target will only be detectable if its RADAR cross section is large enough so that the returned power (echo) is stronger than the power spectrum of the local oscillator: the phase variation is expressed in dBc/Hz, or a power with respect to the carrier power at an offset $1/\tau$ from the carrier frequency. As a concluding remark, long range RADAR is interested in the behavior of the oscillator close to the carrier (since $\tau = 2d/c$ with d the distance to the target and c the velocity of an electromagnetic wave: $d = 5 - 50$ km yields $\tau = 33 - 333 \mu\text{s}$ in vacuum and thus the behavior of the oscillator at 3 to 33 kHz from the carrier is of interest). On the other hand, RADAR aimed at detecting moving walking people with targets in the sub-100 m range will only be affected by the phase noise above 1.5 MHz from the carrier.

III. APPLICATION TO SAW REFLECTIVE DELAY LINE SENSING

One implementation of SAW delay line readers acts exactly as a CW reader: a carrier is chopped in pulses containing as many periods as there are electrodes in the sensor IDT (Fig. 2).

The reader on the one hand emits these pulses whose frequency is centered on the oscillator frequency output, and the returned signal from the sensor is centered on the same frequency, but shifted in time by a duration dependent on the physical property under investigation (which most significantly affects the acoustic wave velocity on the piezoelectric substrate). Thus, the mixer output exhibits a series of pulses whose rough delay is estimated through maximum returned power (threshold) or cross-correlation; but it is well

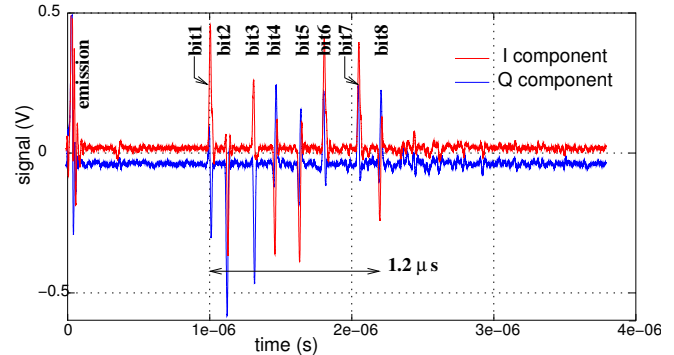


Figure 2. Typical response from a SAW delay line, here from a temperature sensor with 8-bit coding sold by CTR Carinthian Tech Research (Villach, Austria), here excited by a 40-ns long pulse centered on 2.40 GHz. The pulse at 0 s is the excitation pulse, and the returned echos are located between 1 and 2.2 μs .

known that only a phase measurement (with 2π uncertainty) provides the required high accuracy on the acoustic velocity and thus the measured physical quantity [19], [20].

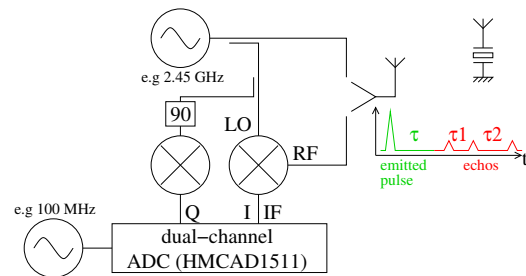


Figure 3. Demodulation circuit for probing wireless passive SAW sensors. The mixer might be replaced by an IQ demodulator in practical systems.

Let us now add to the time delay from the acoustic wave propagation another contribution to the detected phase: the local oscillator intrinsic noise as characterized by its phase noise. The phase noise of a signal $V(t) = (V_0 + \varepsilon(t)) \sin(2\pi f_0 t + \Delta\varphi(t))$ is defined as [21] the phase fluctuations in a 1 Hz-wide bandwidth

$$S_{\Delta\varphi} = \frac{\Delta\varphi_{RMS}^2}{\text{measurement bandwidth}} \text{ rad}^2/\text{Hz}$$

and the classical representation of the noise spectrum is given by $L(f) = \frac{1}{2} S_{\Delta\varphi}(f) = 10 \times \log_{10} \left(\frac{P_{SSB}}{P_S} \right)$ dBc/Hz.

Based on these informations, we will compute the phase noise fluctuations of the local oscillators during time intervals τ which are now given by the travel duration of the electromagnetic wave in the medium surrounding the sensor (negligible since readout ranges are in the tens of meters at most, or tens of nanoseconds) and the acoustic delay which is typically in the 1 to 5 μs range: the offset to the carrier of interest to acoustic sensing is in the 200 kHz to 1 MHz range.

This frequency range usually lies above the Leeson frequency $f_L = f_{LO}/(2Q_{LO})$ with f_{LO} and Q_{LO} the

local oscillator resonator frequency and quality factor. This characteristic frequency defines a frequency offset from the carrier at which the resonator no longer acts as an energy tank and becomes transparent to the feedback amplifier noise. Above this frequency, the phase noise of the oscillator is constant and solely defined by the power injected in the resonator, the noise factor of the feedback amplifier and the operating temperature. We shall come back to such considerations in the design section.

Two practical applications will focus on a poor oscillator assumed to exhibit -130 dBc/Hz, and an excellent oscillator assumed to exhibit -170 dBc/Hz as the frequency offset of interest. Another numerical application using -90 dBc/Hz is justified by the fact that the returned signal noise floor is the maximum of either the initial oscillator noise floor raised by the power amplifier (PA) and low noise amplifier (LNA), or the LNA noise floor set by its thermal noise $F_{LNA}k_B T/P_R$ with $F_{LNA} \simeq 1.5$ dB the noise factor of the reception amplifier, $10 \log_{10}(k_B T) = -174$ dBm the product of the Boltzmann constant with the temperature $T = 290$ K, and P_R the received power. From this consideration, the measurement resolution will first be constant as long as the LNA noise floor is lower than the LO noise floor, and drops once the returned power becomes so low that the LNA noise floor rises above the LO noise floor. The received power is related to the emitted power P_E – limited to $P_E = +10$ dBm by radiofrequency emission regulations in 434 and 2450 MHz ISM bands – through the free space propagation losses and the sensor insertion losses. Free space propagation losses $FSPL = \left(\frac{4\pi df}{c}\right)^2$ are associated with energy distribution on a sphere generated by the emitter, and in the case of a RADAR the link budget requires the use of $FSPL^4$ since the target itself acts as a point-like source generating a spherical wave. The SAW sensor insertion loss IL is a significant source of energy loss when probing SAW delay lines since a typical IL value is -35 dB. Thus, $P_R = P_E \times FSPL^4 \times IL$ and switching to a logarithmic description, the noise floor on the return branch reaching the mixer is either the floor of the oscillator raised by the noise floor of PA and LNA, or the noise floor of the LNA amplifier $F_{LNA,dB} + 10 \log_{10}(k_B T) - 10 \log_{10}(P_E \times FSPL^4) - IL$. The lower the oscillator phase noise floor, the smaller the range at which the LNA noise floor becomes dominant, as shown in the numerical application of Table I.

In such cases, the phase variations due to the local oscillator are $\Delta\varphi_{RMS} = \sqrt{2 \times 10^{-(130..170)/10}} \text{ rad}/\sqrt{\text{Hz}}$. Since we focus on measuring the phase within a 30 ns long pulse, the measurement bandwidth is 60 MHz and $\Delta\varphi_{RMS} = \sqrt{2 \times 10^{-(130..170)/10} \times 60 \times 10^6} \text{ rad}$ whose numerical application yields to phase fluctuations from 0.2° to 0.002° (for -130 and -170 dBc/Hz cases respectively).

We must now relate these phase fluctuations with the phase variations due to a physical quantity variation: we

Operating freq.	osc. noise floor	distance
100 MHz	-170 dBc/Hz	0.04 m
100 MHz	-130 dBc/Hz	0.4 m
100 MHz	-90 dBc/Hz	4.2 m
2450 MHz	-170 dBc/Hz	0.002 m
2450 MHz	-130 dBc/Hz	0.02 m
2450 MHz	-90 dBc/Hz	0.2 m

Table I
DISTANCE AT WHICH THE LNA NOISE FLOOR REACHES THE LOCAL OSCILLATOR NOISE FLOOR, THUS BECOMING DOMINANT AT THE MIXER OUTPUT.

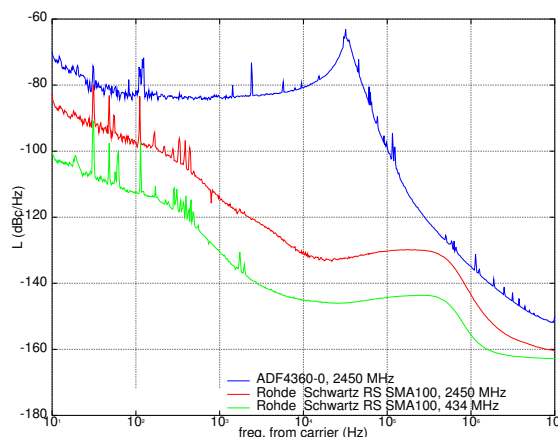


Figure 4. Phase noise of a 2.45 GHz source generated by an Analog Devices ADF4360-0 Phase Locked Loop (poorly controlled), and Rohde & Schwartz SMA 100A tabletop frequency synthesizer set to 2450 and 434 MHz.

focus on a temperature sensor. An acoustic sensor exhibits a phase rotation for every period, *i.e.*, for a propagation length of one wavelength λ . The elastic wave propagates on the piezoelectric substrate at velocity v and the time-difference due to the two-way trip d from IDT to the mirror yields a phase shift of

$$\Delta\varphi = 2\pi \times d/\lambda = 2\pi \times d \times f/v$$

The variation with temperature T of this phase difference is associated with the velocity variation, so that

$$\frac{\partial\Delta\varphi}{\Delta\varphi} \Big|_T = \frac{\partial v}{v} \Big|_T \Leftrightarrow \partial\Delta\varphi(T) = 2\pi \frac{d \times f}{v} \times \frac{\partial v}{v} \Big|_T$$

All quantities in this equation are known: for a LiNbO_3 substrate, we consider that $v \simeq 3000$ m/s, $\partial v/v \simeq 60$ ppm/K. Selecting $d = 10$ mm and $f = 100$ MHz (as used in [22]), we conclude that $2\pi \times 60 \times 10^{-6} \times 10^{-2} \times 10^8/3000 = 0.13 \text{ rad/K} = 7.2 \text{ }^\circ\text{/K}$.

By extending this analysis to various experimental parameters, we compare the local oscillator phase noise fluctuation implication on the measurement resolution in Table II.

We conclude that the local oscillator stability becomes a significant hindrance to high resolution temperature measurements, and reaching the mK resolution as was done

Phase noise	half distance between reflectors	resolution
-170 dBc/Hz	10 mm	2×10^{-4} K
-170 dBc/Hz	1 mm	2×10^{-3} K
-130 dBc/Hz	10 mm	0.02 K
-130 dBc/Hz	1 mm	0.2 K
-90 dBc/Hz	10 mm	2 K
-90 dBc/Hz	1 mm	20 K

Table II

TEMPERATURE MEASUREMENT RESOLUTION, ASSUMING A 60 PPM/K TEMPERATURE DRIFT OF THE DELAY-LINE SENSOR, AS A FUNCTION OF VARIOUS LOCAL OSCILLATOR PARAMETERS.

with the Hewlett Packard HP2830A resonator-based probes is challenging.

Beyond the compliance with radiofrequency emission regulations, the use of ultra-wideband (UWB) interrogation strategies, *e.g.*, Ground Penetrating RADAR based approaches [22], yields the question of optimum operating frequencies. Indeed, we have seen that the time delay is a function of the acoustic velocity and propagation path length (defined respectively by selecting appropriate single-crystal piezoelectric substrate orientations, and design considerations in positioning the mirrors on the sensor surface), but also of the operating frequency:

$$\Delta\varphi = 2\pi d/\lambda = 2\pi df/v = 2\pi f\tau$$

where τ is the propagation duration of the pulse, *i.e.*, $\partial\Delta\varphi = 2\pi f\partial\tau \Leftrightarrow \partial\tau = 1/(2\pi f)\partial\Delta\varphi$, providing the relationship between phase noise and delay noise through the inverse of the frequency.

The remaining design issue lies in the selection of the echo pair used for computing acoustic propagation time delay and thus identifying the physical quantity under investigation. The first and last echos of a tag (start and stop bits) are usually considered for such purposes. However, the further away mirrors are, the longer the delay and thus the larger the local oscillator fluctuations, associated with phase noise rise. One should thus take care that the inverse of the propagation delay does not reach the Leeson frequency f_L where the noise floor meets the rising phase noise slope: $f_L = f_0/(2Q)$. Considering a (very favorable) $Q = 20000$ resonator used for generating a 2.45 GHz oscillator, $f_L = 60$ kHz and the associated propagation delay is $16 \mu\text{s}$, far above any practical limitation (such a delay would be associated with a 24 mm-long propagation path). However, for a more reasonable $Q = 2000$ [23], the Leeson frequency reaches 600 kHz or a propagation delay of $1.6 \mu\text{s}$. In this case, using echos returned by mirror at extreme positions of the delay line should be avoided (*i.e.*, exhibiting propagation delays larger than $1.6 \mu\text{s}$) and adjacent echos should yield results with higher resolutions.

IV. SENSOR DESIGN WITH RESPECT TO LOCAL OSCILLATOR CHARACTERISTICS

Consider two applications: a 434 MHz delay line (which would not comply with RF regulations) and a 2450 MHz

delay line. Resonators in the former frequency range exhibit typical quality factors of 10000, and $f_L = 22$ kHz, well below the 200-1000 kHz range we have been considering: a classical delay line design will be probed at best by the reader. However at 2450 MHz, since the product $Q \times f$ is constant for a given technology, the local oscillator Q drops to 1800, and the Leeson frequency rises to 680 kHz. The designer of a 2450 MHz delay line would be wise to avoid the phase noise rise below f_L and limit the maximum time delay on the acoustic path to $1.5 \mu\text{s}$. Since electromagnetic clutter fades within the first 700 ns (assuming 100 m range) and the typical pulse length is 40 ns spaced by at least 100 ns to account for manufacturing variability, limiting the delay to $1.5 \mu\text{s}$ still leaves enough space for 5 reflections, more than enough for multi-parameter-sensing (one reference pulse and 4 pulses for probing 4 different physical quantities, *e.g.*, temperature [24], pressure [25] and two chemical compounds [26]).

V. APPLICATION TO SAW RESONATOR SENSING

SAW resonator probing aims at identifying a characteristic frequency: in one embodiment of this approach, a frequency sweep network analyzer sequentially probes multiple frequencies in order to identify the frequency at which the sensor returns a maximum power. SAW resonators store energy during the electromagnetic signal emission phase, and release this energy (as an electromagnetic wave at the sensor resonance frequency f_0) during the listening stage: the time constant of each step is $Q/(\pi f_0)$ with Q the sensor quality factor. The fastest approach to the best of our knowledge [27] for probing a resonance frequency of a resonator requires two signals at different frequencies, one above and one below f_0 (Fig. 5).

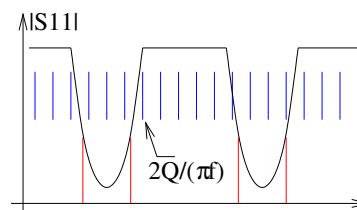


Figure 5. For a dual-mode resonator, required for a differential measurement, a minimum of 4 measurements each lasting $2Q/(\pi f)$ seconds, with f the resonance frequency of one mode and Q its quality factor, is needed (red). A more classical approach of a frequency sweep network analyzer requires up to 128 measurements in the 434-MHz European ISM band (blue).

Hence, the minimum measurement duration is $2Q/(\pi f_0)$ for each probed frequency. For $f_0 = 434$ MHz and $Q = 10000$ in a dual resonator configuration, eight time constants (two resonators, and for each two-measurement points, and for each one time constant for loading and unloading the resonator) yield $59 \mu\text{s}$ measurement duration, so that the oscillator stability at 17 kHz from the carrier is of interest.

Phase noise	frequency	Q	$\Delta f_{RMS}(Hz)$	resolution
-170 dBc/Hz	434 MHz	10000	0.01	4.10^{-7} K
-130 dBc/Hz	434 MHz	10000	1	4.10^{-5} K
-90 dBc/Hz	434 MHz	10000	140	5 mK
-170 dBc/Hz	2.450 GHz	1500	2	10^{-5} K
-130 dBc/Hz	2.450 GHz	1500	230	1 mK
-90 dBc/Hz	2.450 GHz	1500	23000	0.1 K

Table III
 FREQUENCY STANDARD DEVIATION AS A FUNCTION OF THE
 CHARACTERISTICS OF THE RESONATOR USED AS SENSOR (DEFINING
 THE TIME CONSTANT OF THE INTERROGATION).

The phase noise $S_{\Delta\varphi}$ and frequency noise (or stability) $S_{\Delta f}$ at f from the carrier are related through

$$S_{\Delta f} = f^2 \times S_{\Delta\varphi} = \frac{\Delta f_{RMS}^2}{BW}$$

So, with a measurement bandwidth BW of $2f$, frequency fluctuations are given by

$$\Delta f_{RMS} = \sqrt{BW \times f^2 \times 2L(f)}$$

The result of this calculation is summarized in table III, assuming that the $Q \times f$ product is constant, as is usually considered for a given technology, with values representative of SAW resonators patterned on a quartz substrate. The temperature resolution – last column of Table III – is computed assuming a 60 ppm/K sensitivity. This last result scales as the temperature sensitivity of the substrate: a sensor allowing for a 170 K measurement range within the 1.7 MHz wide 434 MHz European ISM band – as sold by SENSEOR (Mougins, France) – only exhibits a 5.7 ppm/K sensitivity and hence the values in the last column are multiplied by 10.

Here again, for resonators acting as temperature sensors with 2.5 kHz/K temperature sensitivity (in order to fit a 170 K measurement range within the 1.7 MHz wide 434 MHz Industrial, Scientific and Medical (ISM) band, accounting for manufacturing variations), the 25 Hz frequency resolution (10 mK resolution) is only met if a reasonably stable local oscillator is used as reference, with a phase noise below -105 dBc/Hz. This result is consistent with the phase noise spectra provided in [28], with a phase noise around -105 dBc/Hz in the 500-5000 Hz carrier offset range at the 434 MHz DDS output. The former range boundary is met when probing 128-samples in a frequency-sweep network analyzer approach: 128 points each requiring $2Q/(\pi f_0)$ requires a duration of 1.8 ms or an update rate of 530 Hz.

VI. ANALOG TO DIGITAL CONVERSION JITTER

We now change oscillator type to consider the analog to digital conversion (ADC) stage. The phase measurement requires two simultaneous measurements of the I and Q components of the returned signal after mixing with the local RF oscillator. The typical pulse duration is 30 ns so that the ADC bandwidth must be at least in the $f_s = 60$ MHz range, or practically (3 points/period at least) 100 MHz.

Measuring a phase with 0.13 rad resolution over the full 2π range requires $bits = 6$ bit resolution. Since the jitter on the clock controlling the ADC yields a resolution loss (linear scale) of $SNR = (2\pi f_s \sigma_t)$, the jitter σ_t must not exceed

$$\sigma_t \leq 2^{-bits}/(2\pi \times f_s)$$

which is here equal to 42 ps [29]. However, increasing 10-fold this resolution yields a 9 bit ADC resolution and a maximum jitter of 5 ps.

On the other hand, let us estimate the jitter induced by an oscillator exhibiting a -130 dBc/Hz phase noise level in the 200 kHz-200 MHz range, representative of the influence of the clock controlling the ADC sampling at 100 MS/s for a maximum duration of 5 μ s. The RMS jitter (in seconds) is given [30] by

$$\sigma_t = \frac{\sqrt{2 \times 10^{-130/10} \times 10^8}}{(2\pi \times 10^8)}$$

which is equal to 7 ps, dropping the lower integration limit (200 kHz) by assuming that the constant phase noise level extends to the carrier. Thus, although even a very poor reference oscillator controlling the ADC meets the requirements of 9-bit resolution needed for high resolution temperature measurements, care should nevertheless be taken to reach sub-10 ps jitter. As an example, the Digital PLL generating the clock output of an iMX27 CPU as used on the APF27-board from Armadeus Systems (Mulhouse, France) for prototyping our experiments is specified at a maximum of 200 ps, hardly usable for the application described here [31].

VII. CONCLUSION

While the debate on the advantages between delay line and resonator approaches is still ongoing, local oscillator characteristics brings some hint on which strategy might bring the most accurate result. From a local oscillator perspective, moving the frequency offset as far as possible from the carrier, *i.e.*, allowing for as short a duration between various measurements of the sensor characteristics as possible, clearly hints at an advantage towards delay lines. However, this partial picture does not include the receiver noise level, especially the high bandwidth on the ADC sampling required to recover and digitize the fast delay line response: only an extremely stable (low jitter) clocking circuit for the receiver ADC will provide measurements with resolutions comparable to those of resonators. Furthermore, as opposed to FMCW or frequency sweep approaches which require tunable frequency sources (VCO, frac-PLL, DDS), a pulsed (UWB-like) delay line approach only requires a *fixed frequency* source generating a stable signal within the bandpass of the sensor, hence allowing for improved stability. Such results are most significantly the target of high quality factor piezoelectric resonator based oscillators aimed at reaching the targetted radiofrequency band.

Design rules concerning the oscillator characteristics are provided for delay lines: the maximum two-way trip duration should be lower than the inverse of the Leeson frequency, while only low noise floor enables high resolution measurements as explicitly stated with relationships between local oscillator phase noise densities and measured returned signal phase resolution. For resonator probed through a frequency sweep network analyzer approach, the tunable local oscillator source is clearly a limiting factor in the measured resonance frequency resolution.

REFERENCES

- [1] C. Allen, K. Shi, and R. Plumb, "The use of ground-penetrating radar with a cooperative target," *IEEE Transactions on Geoscience and Remote Sensing*, vol. 5, no. 2, pp. 1821–1825, 36 1998.
- [2] V. Sridhar and K. Takahata, "A hydrogel-based passive wireless sensor using a flex-circuit inductive transducer," *Sensors and Actuators A: Physical*, vol. 155, no. 1, pp. 58–65, 2009.
- [3] M. Jatlaoui, F. Chebila, S. Bouaziz, P. Pons, and H. Aubert, "Original identification technique of passive em sensors using loaded transmission delay lines," in *European Microwave Conference (EuMC)*, Sept. 2010, pp. 1106–1109.
- [4] A. Pohl, F. Seifert, L. Reindl, G. Scholl, T. Ostertag, and W. Pietsch, "Radio signals for SAW ID tags and sensors in strong electromagnetic interference," in *IEEE Ultrasonics Symposium*, Cannes, France, 1994, pp. 195–198.
- [5] L. Reindl, G. Scholl, T. Ostertag, C. Ruppel, W.-E. Bulst, and F. Seifert, "SAW devices as wireless passive sensors," in *IEEE Ultrasonics Symposium*, 1996, pp. 363–367.
- [6] W. Bulst, G. Fischerauer, and L. Reindl, "State of the art in wireless sensing with surface acoustic waves," *IEEE Transactions on Industrial Electronics*, vol. 48, no. 2, pp. 265–271, April 2001.
- [7] A. Stelzer, R. Hauser, L. Reindl, and R. Teichmann, "A low-cost interrogation unit and signal processing for a SAW identification-tag for a pressure sensor," in *XVII IMEKO World Congress*, June 2003, pp. 672–675.
- [8] G. Bruckner, A. Stelzer, L. Maurer, J. Biniasch, L. Reindl, R. Teichmann, and R. Hauser, "A high-temperature stable SAW identification tag for a pressure sensor and a low-cost interrogation unit," in *11th International Sensor Congress (SENSOR)*, Nuremberg, Germany, 2003, pp. 467–472. [Online]. Available: http://www.rfid.co.uk/knowledge_centre/pdfs/hightemp.rfid.pdf
- [9] S. Schuster, S. Scheiblhofer, L. Reindl, and A. Stelzer, "Performance evaluation of algorithms for SAW-based temperature measurement," *IEEE Transactions on Ultrasonics, Ferroelectrics, and Frequency Control*, vol. 53, no. 6, pp. 1177–1185, June 2006.
- [10] Y. Wen, P. Li, J. Yang, and M. Zheng, "Detecting and evaluating the signals of wirelessly interrogational passive SAW resonator sensors," *IEEE Sensors journal*, vol. 4, no. 6, December 2004.
- [11] M. Hamsch, R. Hoffmann, W. Buff, M. Binhack, and S. Klett, "An interrogation unit for passive wireless SAW sensors based on Fourier transform," *IEEE Transactions on Ultrasonics, Ferroelectrics, and Frequency Control*, vol. 51, no. 11, pp. 1449–1456, November 2004.
- [12] A. Stelzer, G. Schimetta, L. Reindl, A. Springer, and R. Weigel, "Wireless SAW sensors for surface and subsurface sensing applications," in *SPIE Proceedings – Subsurface and Surface Sensing Technologies and Applications III*, vol. 4491, 2001, pp. 358–366.
- [13] J. Beckley, V. Kalinin, M. Lee, and K. Voliansky, "Non-contact torque sensor based on SAW resonators," in *IEEE Int. Freq. Control Symposium and PDA Exhibition*, New Orleans, LA, USA, 2002, pp. 202–213.
- [14] G. Scholl, F. Schmidt, T. Ostertag, L. Reindl, H. Scherr, and U. Wolff, "Wireless passive SAW sensor systems for industrial and domestic applications," in *IEEE International Frequency Control Symposium*, 1998, pp. 595–601.
- [15] A. Springer, M. Huemer, L. Reindl, C. W. Ruppel, A. Pohl, F. Seifert, W. Gugler, and R. Weigel, "A robust ultra-broadband wireless communication system using SAW chirped delay lines," *IEEE Transactions on Microwave Theory and Techniques*, vol. 46, no. 12, pp. 745–756, December 1998.
- [16] D. Puccio, D. Malocha, D. Gallagher, and J. Hines, "SAW sensors using orthogonal frequency coding," in *IEEE Frequency Control Symposium*, 2004, pp. 307–310.
- [17] V. Kalinin, "Influence of receiver noise properties on resolution of passive wireless resonant SAW sensors," in *IEEE Ultrasonics Symposium*, vol. 3, 2005, pp. 1452–1455.
- [18] E. Rubiola, *Phase Noise and Frequency Stability in Oscillators*. Cambridge University Press, 2010.
- [19] J. H. Kuypers, M. Esashi, D. A. Eisele, and L. M. Reindl, "2.45 GHz passive wireless temperature monitoring system featuring parallel sensor interrogation and resolution evaluation," in *IEEE Ultrasonics Symposium*, 2006, pp. 1453–1458.
- [20] L. Reindl, "Wireless passive SAW identification marks and sensors," *2nd Int. Symp. Acoustic Wave Devices for Future Mobile Communication Systems*, pp. 1–15, March 2004.
- [21] "Phase noise characterization of microwave oscillators – phase detector method," *Agilent Product Note*, vol. 11729B-1.
- [22] J.-M. Friedt, T. Réturnaz, S. Alzuaga, T. Baron, G. Martin, T. Laroche, S. Ballandras, M. Griselin, and J.-P. Simonnet, "Surface acoustic wave devices as passive buried sensors," *Journal of Applied Physics*, vol. 109, no. 3, p. 034905, 2011.
- [23] U. Knauer, J. Machui, and C. Ruppel, "Design, fabrication, and application of GHz SAW devices," in *Microwave Symposium Digest – IEEE MTT-S International*, vol. 3, 1997, pp. 1821–1824.
- [24] R. Fachberger, G. Bruckner, R. Hauser, and L. Reindl, "Wireless SAW based high-temperature measurement systems," in *IEEE International Frequency Control Symposium and Exposition*, 2006, pp. 358–367.

- [25] W. Buff, M. Rusko, M. Goroll, J. Ehrenpfordt, and T. Vandahl, "Universal pressure and temperature SAW sensor for wireless applications," in *IEEE Ultrasonics Symposium*, 1997, pp. 359–362.
- [26] Y. Dong, W. Cheng, S. Wang, Y. Li, and G. Feng, "A multi-resolution passive SAW chemical sensor," *Sensors and Actuators B*, vol. 76, pp. 130–133, 2001.
- [27] J.-M. Friedt, C. Droit, S. Ballandras, S. Alzuaga, G. Martin, and P. Sandoz, "Remote vibration measurement: a wireless passive surface acoustic wave resonator fast probing strategy," *Rev. Sci. Instrum.*, vol. 83, p. 055001, 2012.
- [28] J.-M. Friedt, C. Droit, G. Martin, and S. Ballandras, "A wireless interrogation system exploiting narrowband acoustic resonator for remote physical quantity measurement," *Rev. Sci. Instrum.*, vol. 81, p. 014701, 2010.
- [29] D. Redmayne, E. Trelewicz, and A. Smith, "Understanding the effect of clock jitter on high speed ADCs," available at cds.linear.com/docs/Design%20Note/dn1013f.pdf, last accessed 08/08/2012, 2006.
- [30] W. Kester, "Converting oscillator phase noise to time jitter," available at <http://www.analog.com/static/imported-files/tutorials/MT-008.pdf>, last accessed 08/08/2012, 2008.
- [31] "i.MX27 and i.MX27L data sheet," available at www.freescale.com/files/dsp/doc/data_sheet/MCIMX27EC.pdf, last accessed 08/08/2012, 2011.

Efficient Suboptimal Detectors for Maritime Surface Surveillance High-Resolution Radar

Blas Pablo Dorta-Naranjo^{#1}, Jaime Calvo-Gallego⁺², Cristina Carmona-Duarte^{#3}, Félix Pérez-Martínez^{*4}

⁺ *Instituto para el Desarrollo Tecnológico y la Innovación en Comunicaciones (IDeTIC), University of Las Palmas de G. C. Campus de Tafira s/n, E-35017, Las Palmas, Spain*

¹ pdorta@dsc.ulpgc.es

³ ccarmona@idetec.eu

#Department of Computing and Automatics, University of Salamanca E.P.S. de Zamora, Campus Viriato, Av. Requejo, 33, E-49022, Zamora, Spain

² jaime.calvo@usal.es

**Department of Signals, Systems and Radio Communication, Polytechnic University of Madrid E.T.S.I. de Telecomunicación, Av. Complutense s/n, E-28040, Madrid, Spain*

⁴ felix@gmr.ssr.upm.es

Abstract— This paper presents some efficient suboptimal detectors, based on statistical descriptors, which take advantage of the high-resolution characteristics of the high-resolution radars (HRR). Which are one of the first stages of the sensor-based localization and tracking technologies. The detection performance has been studied under noise and sea clutter conditions, with non-coherent data from both real and synthetic extended targets. We have also made an adaptation of the classical moving window detection technique for the high-resolution radars, making use of it as a reference technique to evaluate the results obtained with the detection techniques that we present. The experimental results were obtained with the ARIES radar, a maritime surface surveillance LFM-CW HRR operating in X-band.

Keywords-HRR radar; detectors; statistical descriptors.

I. INTRODUCTION

The specific characteristics of high-resolution radars (HRR) [1] suggest the interest to analyze the possibilities of new detection algorithm for global detection purposes of the extended targets (composed of a number of scatterers, where the target extent in any dimension is greater than the radar resolution in that dimension) [2]. This means, the development of detection algorithms oriented to the radar images, and not just to perform the detection process in each one of the resolution cells, as conventional radar detection techniques do. This paper presents detectors based on statistical descriptors, widely used in the field of digital image processing [3].

Nowadays, the operating HRR typically have the sliding window technique built in [4], [5], (also called moving window, depending on the references) originally developed for conventional radar, without any adaptation to the characteristics of the high resolution. The sliding window detector [4], [5] has been chosen as reference in this paper to compare with the results provided by the proposed algorithms.

In order to explore the possibilities for some of these detectors, a comparative study has been obtained in terms of

probability of detection (P_d) for a given probability of false alarm (P_{fa}) using the of Neyman-Pearson criterion [6], widely accepted and widely used in radar. This work has been carried out through a theoretical and experimental analysis with real and synthetic targets. Since from the operational point of view, the significant parameter is the time between false alarms (the inverse of the product of the P_{fa} by the number of decisions per second the sensor should take), image sensors work with probabilities of false alarm several orders of magnitude higher than the pixel-oriented sensors, as a direct result due to the fact that the radar requires a smaller number of decisions made per second.

Some synthetic targets have been generated to verify the quality of the presented algorithms in this article for the detection of extended targets in two dimensions. The HRR targets have multiple scattering (individual targets) not fluctuating. Each resolution cell (or pixel, in the radar image) is well defined by its Cartesian coordinates (x , y), and its amplitude level. Thus non-fluctuating targets have been modelled (according to bibliography: Marcum model, or Swerling 5 or 0) [7], which correspond with the HRR real targets. In addition, in order to corroborate the reliability of the algorithmic developed operating in real-world scenarios, real targets have been processed, which have been captured with the ARIES HRR [8], a maritime surface surveillance linear frequency modulated continuous wave (LFM-CW) HRR, operating in X-band, in scanning mode, and non-coherent detection, which data are range-azimuth matrices.

In this paper, first the problem statement is presented, then the suboptimal efficient detectors based on statistical descriptors for HRR are introduced, after that the results vs. noise and results vs. clutter are described and finally the conclusions are exposed.

II. PROBLEM STATEMENT

Based on the classical statement of the problem, the problem is dealt starting with the analysis of a point target (where the size of the target is smaller than the resolution cell of the radar system). The second step of the analysis deals the generalization for extended targets.

In order to provide a comparison of the results provided by the techniques presented in this article, we make use of the sliding window detector as a reference technique [7], which has been adapted to the HRR characteristics. This paper presents the results obtained with three significant targets:

- Point target: the Fig. 1 shows the range–azimuth matrix obtained at the envelope detector output in conventional surveillance radars, in which the size of the target is smaller than the range resolution cell. The level of the clutter considered is far below the thermal noise of the system. This assumption is a quite common situation and it is according to the real operation of the HRR, due to the small surface inside the considered resolution cell. In most of the resolution cells the radar signal is a Rayleigh random variable [7]. The target amplitude shape is affected by the antenna radiation pattern, which can be considered as a Gaussian distribution.

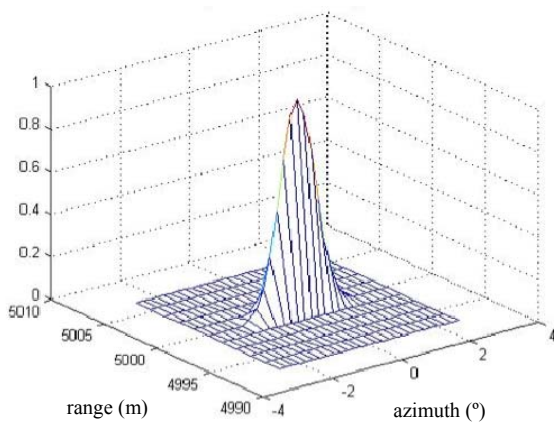


Figure 1. Range–azimuth data matrix of a synthetic point target, synthesized according to the operating parameters of the ARIES radar

- Extended targets: Fig. 2 presents the range–azimuth data matrix from a HRR for a simple model of extended target, a linear target. Fig. 3 shows a real extended target (with a high enough signal-to-noise ration, SNR, and also large enough) captured with the ARIES HRR, which demonstrates the extended targets can be considered as a collection of single point targets, provided that the range resolution cell is small enough (e.g. close to 1 m), compared to the size of the target.

In all considered cases, the data matrices, containing each of the targets, are of the same size, and have a large enough number of bins in order to have a sufficient statistic [9], in order to provide an accurate results.

The main ARIES radar operating parameters for both real and synthetic targets are shown in Table I. The specific parameters to synthesize the point target and the linear extended target, Fig. 1 and Fig. 2, are shown in Table II.

The simulation results were obtained making use of the Monte Carlo method, widely accepted in the radar simulation field [10]. The adopted relative accuracy was 10% to reach probabilities indicated in each case.

The thermal noise model is an additive white Gaussian noise (AWG) with zero mean. Therefore, it can be calculate the receiver operating characteristics curves (ROCs).

TABLE I
MAIN ARIES RADAR OPERATION PARAMETERS

Parameter:	Value:
Center frequency:	9 GHz
Period of the sawtooth wave (also can be considered as 1/PRF for pulsed radars):	2,0384ms
Angular velocity of the antenna:	15 rpm
-3 dB antenna beamwidth:	1,2°
Azimuth resolution:	0,2°
Antenna beam shape:	Gaussian distrib.

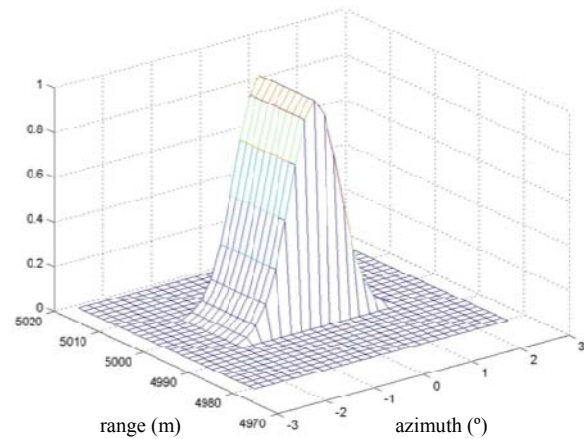


Figure 2. Range–azimuth data matrix of a synthetic linear extended target, synthesized according to the operating parameters of the ARIES radar

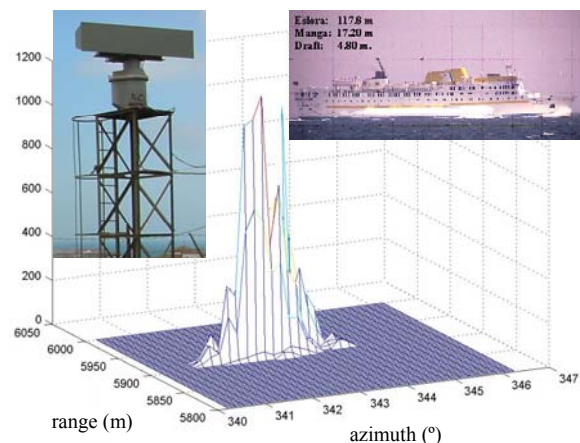


Figure 3. A real extended target, the Boughaz ship: raw range-azimuth data matrix, and the photo (inset right). Inset left: radar ARIES

Many models of sea clutter statistical distributions have been considered over the years, including Weibull, K distribution, etc. [11]–[15]. Experimentally, for the operation parameters used in the capture of targets with the ARIES radar, and for moderate sea conditions, the best suited statistical model of this sea clutter has been a log-normal distribution with a shape factor $\sigma = 0.8$ (standard deviation), which corresponds to the 3 Beaufort number, on the Beaufort scale, according to [16]. This result is consistent with [13]. In this way, the ROC, P_d against signal to clutter ratio (SCR) have been computed.

TABLE II
SPECIFIC RADAR PARAMETERS FOR THE SYNTHESIZED TARGETS

Parameter:	Value:
The operation range of the ARIES radar:	11112m (6nmi)
The target's position in range:	5000m
The target's position in azimuth:	0°
Aspect angle:	0°
Maximum target relative amplitude:	1

III. SUBOPTIMAL EFFICIENT DETECTORS BASED ON STATISTICAL DESCRIPTORS FOR HRR

The vast amount of information obtained by the HRR, leads to develop simple detectors which are able to work with 2-dimensional image (2D), instead of analyse pixel by pixel, and they must also computationally very efficient, producing results in the extended target detection at least comparable with conventional techniques working with point targets. Based on this goal, we have developed the detectors shown in the Fig. 4. This group of techniques process 2D radar raw images, instead of processing each range profile individually (in contrast to classical techniques). Basically the input data to the proposed detectors directly are the range–azimuth matrices of raw video from the output of the FFT stage of the FM–CW radar sensor. The proposed techniques can be applied to any other type of HRR, and even to other kind of sensors.

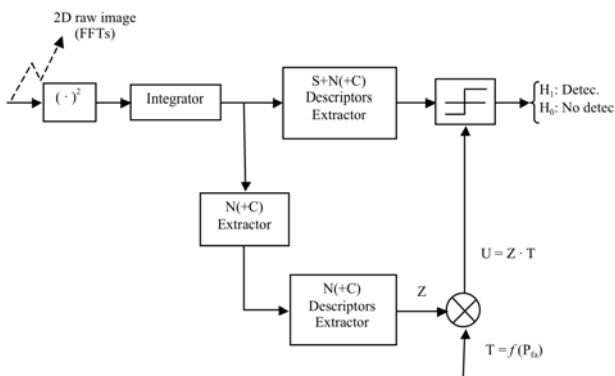


Figure 4. Block diagram of the detectors based on integration and descriptors extraction

For each range row the *Integrator* performs a sum of all resolution cells in azimuth weighted by the considered

number of elements, resulting in an improved signal to noise ratio (in other words, it is possible to detect a target with a lower level of SNR, with the same P_{fa} and the same level of the P_d), and causing the clutter becomes Gaussian.

From the resulting vector, the *Descriptors Extractor* gets the statistical descriptor, which compares with a threshold descriptor (U) in the *Comparator* block, which carries out the detection of the target. According to [7], the threshold descriptor is calculated to ensure a detection process with a constant probability of false alarm.

The integrator used is not the optimal one and there is a loss (i.e. it is needed a higher value of SNR to detect a target) due to the shape of the antenna radiation pattern. A real system, in which is known the shape of the beam, makes use of an integrator well matched to it to minimize such loss. Thus, the optimal integrator has not been introduced into the simulation model because it does not provide additional information for the intended purpose: to compare the characteristics of different detectors. In any case it should be noted that the antenna radiation pattern is a given parameter in many applications and it should be considered.

Among the evaluated descriptors have been found to have a performance suitable for use as detectors: the mean (*Med*), the contrast (*Con*), the fourth-order central moment (*M4O*), and the entropy (*Ent*). The analytical expression of the mean and the fourth-order central moment descriptors can be found in [3], and the equations for the contrast and the entropy descriptors are presented in [17].

IV. RESULTS VS. NOISE

Fig. 5 shows the comparative results of the behaviour of the proposed detectors vs. the Sliding Window detector, in terms of the P_d and under conditions of zero-mean AWG noise for each one of the targets presented above. The results are presented separately for each of the two considered P_{fa} (10^{-3} and 10^{-4}).

Under noise conditions, the behaviour of the detectors, based on integration and extraction of descriptors, is nearly identical to the behaviour of the sliding window technique. This statement is well suited in the cases of the detectors based on the contrast descriptor and based on the fourth-order moment descriptor, and this is not true in the case of the mean descriptor. This latter is sensitive in both cases the point target and the extended targets. Thus, for point targets, the mean descriptor works worse than the sliding window detector. This is a reasonable fact since the mean detector integrates all of the noise of an image in which there are very few cells containing the target. On the other side, this is not consistent with the fact of working with HRR systems.

Assuming the situation of working with extended targets, the detector based on the integration and the extraction of the mean descriptor, is better because of its extreme simplicity and computational efficiency (about one order of magnitude). Although the results provides by this detector are worst than the results obtained with the sliding window detector (between -2dB and -5dB, depending on relative size of the target with regard to the image size), the proposed detector is well suited for some applications where the aforementioned limitations are not significant.

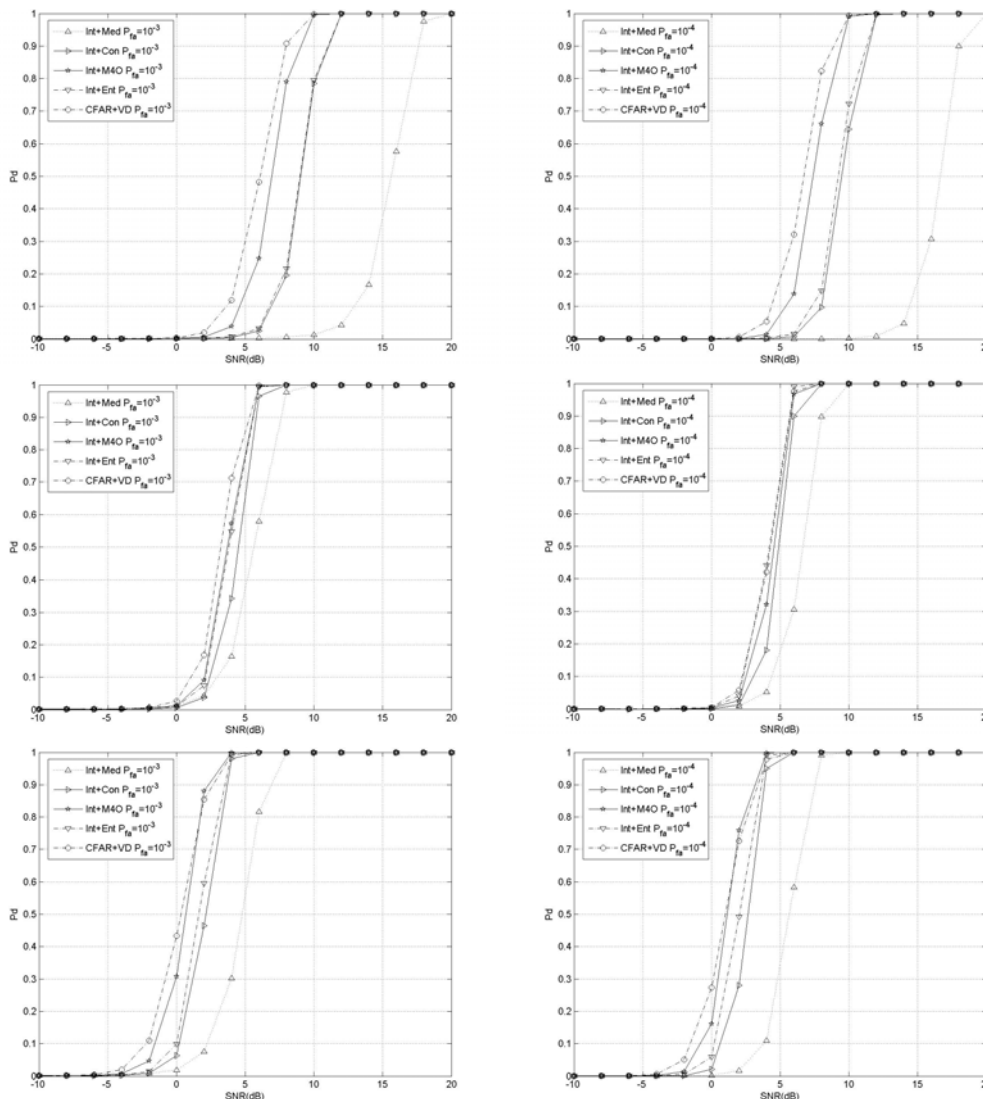


Figure 5. Sliding window (CFAR+VD) vs. presented detectors (Int+: Med, Con, M4O, Ent), under noisy conditions. On the top: for the point target; on the middle: for the linear extended target; on the bottom: for the real extended target, the Boughaz ship. Left side: for a $P_{fa} = 10^{-3}$; and right side: for $P_{fa} = 10^{-4}$.

V. RESULTS VS. SEA CLUTTER

The performance of the presented descriptors under high-resolution sea clutter conditions has been evaluated in the same way as the sliding window with a lognormal distribution with shape parameter $\sigma=0.8$, previously indicated.

Fig. 6 shows the comparative results of the behaviour of the proposed detectors vs. the Sliding Window detector behaviour, in terms of the P_d , under sea clutter conditions, for each of the three targets. The results are presented separately for each of the two considered P_{fa} (10^{-3} and 10^{-4}).

Under sea clutter environments, the effect of the Integrator block is a significant performance improvement of all descriptors, and corrects the malfunction of some descriptors in these settings, as the case of the contrast descriptor. This is a direct result of increasing its near-Gaussian shape of its statistical distribution obtained from the

statistical distributions of the sea clutter at the output of the Integrator stage. Moreover, for all the descriptors, the integrator makes comparable the number of false alarms to that number obtained with the sliding window detector, being slightly worst to the case of the entropy descriptor.

In all cases, the number of false alarms increases rapidly, in sea clutter environments. Obviously, in the presence of impulsive clutter, such as modelling, you cannot keep the detection thresholds (in order to maintain a constant values of P_{fa} and P_d), but they should be amended to set the detector into reasonable rates of false alarms. If this is done, it is straightforward to check that the mean descriptor is the best one (with a loss of 3 dB with respect to sliding window detector, while maintaining an approximately equal P_{fa}).

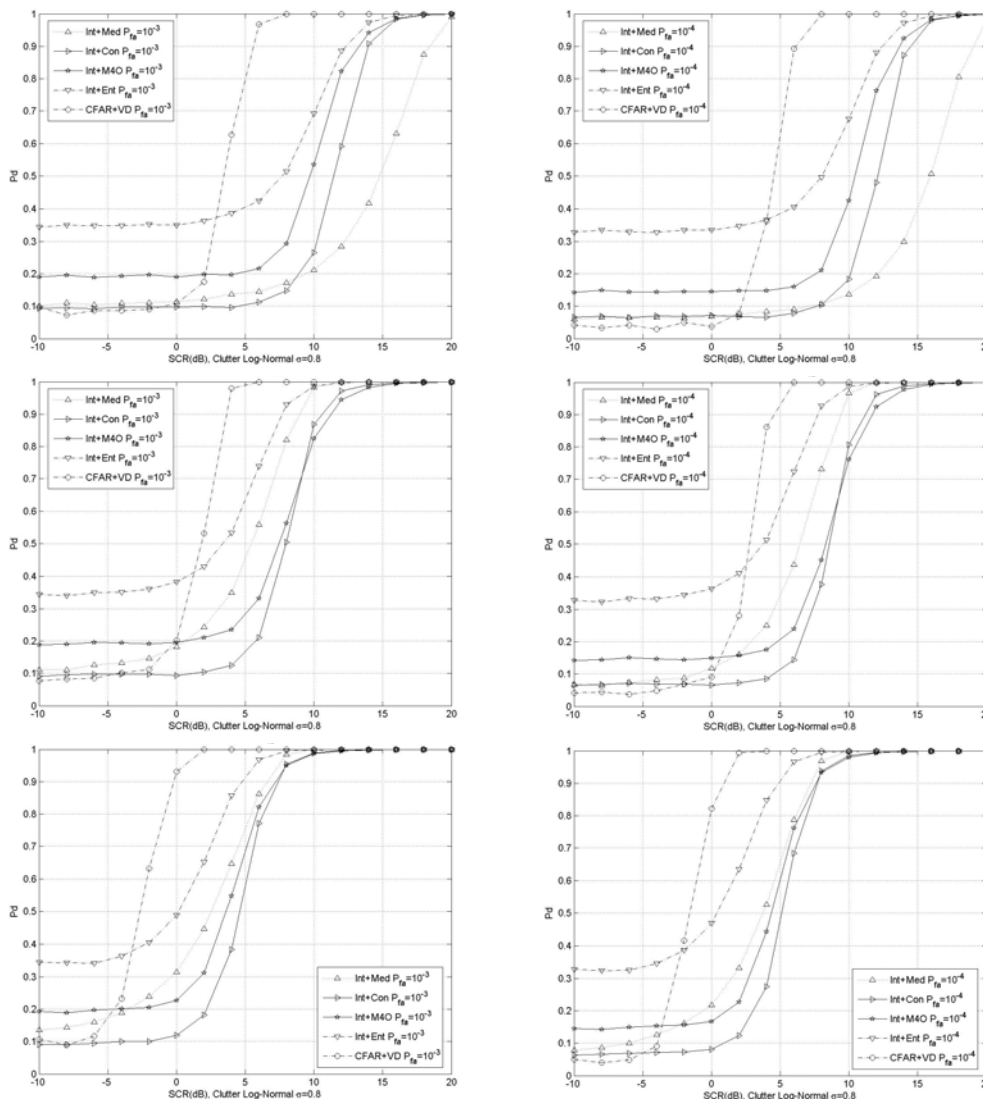


Figure 6. Sliding window (CFAR+VD) vs. presented detectors (Int+: Med, Con, M4O, Ent), under sea clutter conditions. On the top: for the point target; on the middle: for the linear extended target; on the bottom: for the real extended target, the Boughaz ship. Left side: for a $P_{fa} = 10^{-3}$; and right side: for $P_{fa} = 10^{-4}$.

VI. CONCLUSION

It has been demonstrated that the efficiency of presented detectors in terms of P_d , for a given P_{fa} , depends on the relative area occupied by the target within the image, confirming they are particularly suitable for large extended targets. These algorithms have a lower computational burden than the conventional sliding window, allowing to maintain existing radar coverage even when is increased by several orders of magnitude the number of resolution cells, as is the case of HRR systems, in which the technological developments (with the ability to transmit and process the higher bandwidth RF signals) involves reducing the size of the resolution cells in range, and therefore increasing the size of processed matrices.

The used clutter model is especially difficult for the parametric detectors, which are matched to the thermal noise, due to the strong impulse (spiky, typically) character of the clutter, characteristic of HRR's real operation scenarios. Furthermore, one of the main characteristics of the HRR systems that the cell resolution is much lower than in a conventional radar, which means that the received clutter levels are much lower, in many situations below the level of the noise of the system itself. In summary, the curves shown above have been obtained as a function of the SCR, and our experience is that the HRR systems easily handle high SCRs for most of the targets.

Finally we must remark that the techniques discussed in this paper can also be applied, with minor adjustments, to range-Doppler radar images, which are not affected by the shape of the antenna radiation pattern, and the most

significant difference, due to its operating principle, is that they are able to separate the targets from the clutter, so that the presented detectors may offer, in any real situation, similar results to the sliding window detector, providing computational advantages.

ACKNOWLEDGMENT

This work was supported by the National Board of Scientific and Technology Research under Projects TEC2010-21217-C02-01, TEC2008-02148/TEC and TEC2005-07010-C02.

REFERENCES

[1] D. R. Wehner, High Resolution Radar. 2nd ed., Artech House Publishers, 1995.

[2] R. V. Ostrovityanov, and F. A. Basalov, "Statisticheskaya teoriya radiolokatsii protyazhennykh tseley (Statistical Theory of Extended Radar Targets)," in Russian, Radio i Svyaz, 1982; (trans.) Artech House, 1985.

[3] R. C. González and R. E. Woods, Digital Image Processing. 3rd ed., Addison Wesley Publishing Company, 2008.

[4] G. M. Dillard, "A Moving Window Detector for Binary Integration," IEEE Transactions on Information Theory, vol. IT-13, no. 1, pp. 2–6, January 1967.

[5] N. Levanon, "Analytic comparison of four robust algorithms for post detection integration," IEE Proceedings-F, vol. 139, no. 1, pp. 67–72, February 1992.

[6] J. Neyman and E.S. Pearson, "On the problem of the most efficient tests of statistical hypotheses," Philosophical Transactions of the Royal Society of London, Series A, 231, pp. 289–337, 1933.

[7] M. I. Skolnik, Introduction to Radar Systems. 3rd ed., McGraw Hill, 2001.

[8] F. Pérez, A. Asensio, J. Gismero, J. I. Alonso, J. M. Monje, F. Casanova, R. Cortijo, and J. Pérez Ojeda, "ARIES: A High Resolution Shipboard Radar," in Proc. IEEE Radar Conference, April 2002, pp. 148–153.

[9] A. S. Kholevo, A.S., "Sufficient statistic," Encyclopedia of Mathematics, Springer, 2001.

[10] M. N. Almarshada, M. Barkatb, S. A. Alshebeili, "A Monte Carlo simulation for two novel automatic censoring techniques of radar interfering targets in log-normal clutter," Springer, Elsevier, Signal Processing, vol. 88, issue 3, March 2008, pp. 719–732

[11] D. C. Schleher, "Radar Detection in Weibull Clutter," IEEE Transactions on Aerospace and Electronic Systems, vol. AES-12, no. 6, pp. 736–743, Nov. 1976.

[12] L. P. Roy, and R.V.R. Kumar, "Accurate K-distributed clutter model for scanning radar application," IET Radar, Sonar & Navigation, vol. 4, issue 2, pp. 158–167, 2010.

[13] J. Carretero-Moya, J. Gismero-Menoyo, A. Blanco-del-Campo, and A. Asensio-Lopez, "Statistical Analysis of a High-Resolution Sea-Clutter Database," IEEE Transactions on Geoscience and Remote Sensing, vol. 48, no. 4, pp. 2024–2037, April 2010

[14] F. L. Posner, "Spiky sea clutter at high range resolutions and very low grazing angles," IEEE Transactions on Aerospace and Electronic Systems, vol. 38, no. 1, pp. 58–73, Jan. 2002.

[15] M. Greco, F. Bordonni, and F. Gini, "X-band sea-clutter nonstationarity: influence of long waves," IEEE Journal of Oceanic Engineering, vol. 29, no. 23, pp. 269–28, April 2004.

[16] A. Farina, F. Gini, M.V. Greco, L. Verrazzani, "High resolution sea clutter data: statistical analysis of recorded live data," IEE Proceedings Radar, Sonar and Navigation, vol. 144, issue 3, pp. 121–130, June 1997.

[17] J. M. Munoz-Ferreras, J. Calvo-Gallego, F. Perez-Martinez, et al, "Motion Compensation for ISAR Based on the Shift and Convolution Algorithm," in Proc. IEEE Radar Conference, April 2006, pp. 366–370.

Acoustic Emission Sensor Module

Irinela Chilibon

National Institute of Research and Development
for Optoelectronics, INOE-2000,
Bucharest-Magurele, Romania
e-mail: qilib@yahoo.com

Marian Mogildea, George Mogildea

Institute of Space Sciences, ISS
Bucharest-Magurele, Romania
e-mails: marian_mogildea@yahoo.com;
georgemogildea@yahoo.com

Abstract—This paper presents a wireless acoustic emission sensor module with microcontroller for monitoring systems of structures under stress, prevailed by a piezoelectric AE sensor on the investigated material surface. The module performs the analogue/digital conversion of signals, the microcontroller commands the wireless interface, may send and receive information from other emitting - receiver wireless modules. The microcontroller could vary the amplifier gain and make the appropriate analogue / digital conversion. Many wireless modules with acoustic emission sensors could be successfully applicable to the AE monitoring systems of complex construction structures in the civil engineering, using a dedicated software.

Keywords-AE; acoustic emission; non-destructive testing; NDT; μ C; microcontroller

I. INTRODUCTION

Acoustic emission (AE) techniques [1] draw a great attention to the diagnostic applications, material testing and study of deformation, fracture and corrosion, because they give an immediate indication of the response and behavior of materials under stresses, intimately connected with strength, damage, fracture and failure. Also, AE technology involves the use of ultrasonic sensors (20 kHz - 1 MHz) to listen to the sounds of failure occurring in materials and structures.

The roughest localization method is guessing the source origin using the “first hit” technique. The advantage of first hit techniques is that no sensor arrays and no data analysis are necessary. The sensor which detects an AE first defines a radius or a half sphere, respectively, in which the signal originated. The utilizer’s experience denotes whether that technique is accurate enough. This can be done for some cases in combination with other techniques or knowledge from bridge inspectors to “localize” the source of failures.

More sophisticated methods use planar techniques by recording AE signals at more than two sensors at the same time [2].

Also, 3D-Localization of acoustic emission [1] events is a powerful tool in quantitative AE techniques. Signal-based procedures, such as accurate 3D localization of damage sources, solutions for fault plane orientation, and moment

tensor inversion, are applied in civil engineering. Other promising options are methods based on array techniques [3].

3D-Localization [4] of acoustic emission events is the basis of advanced signal interpretation and the discrimination between signal and noise. The more quantitative analysis of the signals is based on a 3D localization of AE sources (hypocenters) and the recordings obtained from a sensor network. Using moment tensor inversion methods, the radiation pattern of acoustic emission sources and the seismic moment (as an equivalent to the emitted energy) as well as the type (Mode I, Mode II, and mixed modes) and orientation of the cracks, can be determined [4].

During the long-term experiments of materials fatigue tests a great amount of signals, including the noises from the load-chain, can be detected by the sensitive AE sensors. According to the time sequence for the guard and main sensors to receive the signals, the signals originating from outside the test section can be detected and discarded.

Crack initiation is determined by the first appearance of the AE signal at low stress levels. This stage has a steady-state dislocation motion that will eventually result in microvoids and initiate microcracks. In the next AE-active stage cracks start to grow and propagate. Many AE signals can come from the crack-tip plastic deformation, fracture of hard inclusions, microcrack coalescence, transgranular cleavage, and fracture along grain boundaries, each producing an acoustic emission [5]. Ultrasound wave propagation in construction materials is presented in [6].

The structure of this paper is based on: 4 chapters, Conclusion and future work and References.

II. ACOUSTIC EMISSION TECHNIQUE APPLICATIONS

AE techniques have been widely used in the domain of non-destructive testing of material structures, such as: metal and composite pressure vessels for the local plastic deformation of ductile pressure vessels [7], [8], piping for locating the position and estimating the severity of leaks in pipeline networks [9], the detection of failures in various types of equipment in the petroleum industry (pressure vessels, tanks and pipelines) [10].

Also, AE generated during fatigue mechanism of steel was widely use as gas pipeline materials testing [11].

A new method to detect leakage in a water-filled plastic pipe through the application of tuned wavelet transforms to Acoustic Emission signals was proposed [12].

Acoustic Emission generated during fatigue mechanism of steel showed that AE Count gives a significant value during cyclic softening effect. Crack initiation was indicated by a rapid increase of AE count values at positive peak stress, followed by high AE count values around zero stress which indicated the crack closure phenomena [11].

Acoustic emission techniques (AET) are an alternative monitoring method to investigate the status of bridges or some of their components, because it has the potential to detect defects in terms of cracks occurring during the routine use of bridges [5].

Monitoring techniques based on wireless AE sensors for large structures in civil engineering [5] were developed, basing on a new kind of sensors using MEMS (Micro-Electro-Mechanical-Systems) techniques. These sensors should be intelligent, self-networking, asynchronous, wireless, adaptive, dynamically reprogrammable, cheap and small. The implemented wireless communication techniques will reduce the application and maintenance costs significantly [5].

Some techniques work as a maintenance monitoring system sending data (alarm data) via intranet to a data centre or alarm messages per SMS automatically to the monitoring engineer. Therefore, the public safety is assured as unseen structural damage is identified without costly and dangerous deconstruction.

Modern acoustic emission (MAE) techniques have applications in aviation industry, fully digital AE apparatus with low noise, high speed of data transmission and accurate AE source locating capability [13].

Acoustic emission techniques are an additional monitoring method to investigate the status of a bridge or some of its components. It has the potential to detect defects in terms of cracks propagating during the routine use of structures. However, acoustic emissions recording and analysis techniques need powerful algorithms to handle and reduce the immense amount of data generated. These algorithms are developed on the basis of neural network techniques and by array techniques [14].

III. NON-DESTRUCTIVE TECHNIQUE EXAMPLES

Some of AE application types are: **Crack detection**, **Fatigue testing** – collect data and give notification to a cyclic fatigue event occurrence in order to determine the plastic deformation, **Chip detection** - Detect the presence of a chip in a tool, also detect chipping as it occurs, **Tool Breakage Detection** - Instantly shut down a process when the tooling breaks, **Deep Drawing** – determine defects when they occur during drawing, stop draw press during

“necking”, **Stamping** - Determine **Good** vs. **Bad** stamping operation, **Piercing** - Indicate the presence of a missing or malfunctioning punch, **Scoring** - detect scratches and gouges as they occur in metal.

Nondestructive techniques were not accepted long time for the testing of bridges, and other components of the infrastructure because of two primary reasons: the difficulty in separating valid signals from extraneous noise and the inability of the AE technique to determine the size of the crack [15]. The acoustic emission (AE) signal can be divided into successive type signal and sporadic type signal, in order to be analyzed through the signal processor in the form of variables such as the existence of a signal generation or the shape of signal [1].

Locating of monitored fatigue cracks, destructive NDE technique has indicated that the first crack has run into a flange and the second crack is in both the weld and web and is growing at both ends. These cracks are referred to here as the "flange crack" and the "weld crack," respectively (Fig. 1).

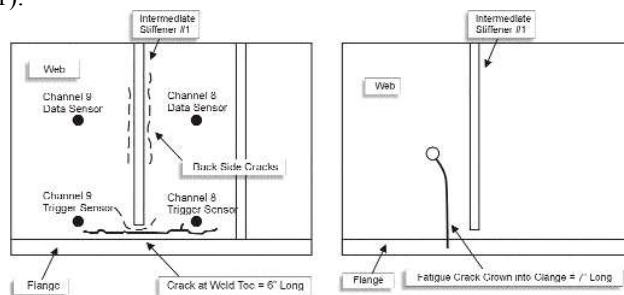


Figure 1. Example of location of fatigue cracks monitored [15].

In the location of fatigue cracks monitored experiment, it is confined only to the case that the direction of force is vertical applied to the surface of the test piece.

Other method of Acoustic Emission based on expert system for evaluating the structural integrity of the *metallic pressure vessels, spheres, columns and tanks* utilizes the Multichannel Acoustic Emission Systems and Sensors, which detect the high-frequency signals resulting from deterioration in the structure when the sample is stressed. The systems have sufficient speed and resolution to ensure real-time, on-screen indications of the development of any defects.

Structural health monitoring (SHM) deals with the more or less continuous recording of data obtained from several parts of the structure. Based on the experience of the constructor, owner, or inspector the damaged regions where data are obtained can be restricted and in many cases it is necessary to just detect a deviation of the “usual” behavior of the structure [14].

IV. EXPERIMENTAL MODULE

The AE sensor converts the mechanical vibration propagated through the material into electrical signal. The

amplifier magnifies the electrical signal, making useful for the dedicated software. The microcontroller (μC), as the central unit of the module, commands the amplifier gain and makes the appropriate analogue – digital conversion

The sensor was designed to be used with an amplifier, of 40 dB maximum gain, which can be controlled by the μC .

The wireless acoustic emission sensor module with microcontroller for monitoring systems of structures under stress, processes signals received from a piezoelectric AE sensor on the investigated material surface. The module performs the analogue / digital conversion of signals, the microcontroller commands the wireless interface, may send and receive information from others emitting - receiver wireless modules. The microcontroller could vary the amplifier gain and makes the appropriate analogue/digital conversion. As remark, this module could be applied to complex AE monitoring systems of structures.

The experimental wireless module of acoustic emission sensor is composed by a piezoelectric AE sensor, a signal amplifier, a PIC 18F452 microcontroller (μC), a pair of emitting - receiver wireless modules (ES and RS wireless, i. e. TX2-433-5V and RX2-433-5V), and a whip antenna of 433 MHz. The block diagram of the experimental wireless module of acoustic emission sensor is presented in Fig. 2.

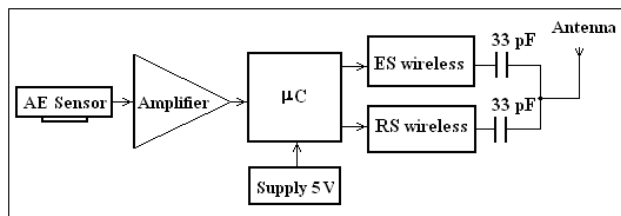


Figure 2. Block diagram of the experimental wireless module for acoustic emission sensor.

The output signal from μC is converted by the ES wireless module and transmitted in air by Antenna (433 MHz) to another antenna of 433 MHz (under the control of the monitoring system with μC) at distance. Also, the Antenna may receive signals from another antenna in order to command the μC and the amplifier gain of this wireless module (Fig. 2).

Three types of antennae for the wireless transmission module which could be used for RF propagation, namely: helical antenna, loop antenna and whip antenna (Fig. 3). For this experimental module, we have chosen the RF whip antenna of 15.5 cm length and 433 MHz work frequency.

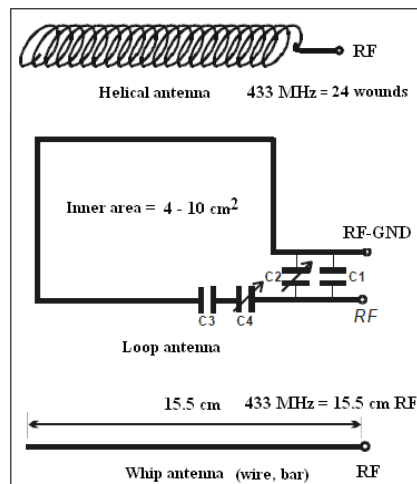


Figure 3. Three types of antennae for wireless module.

The piezoelectric sensor realizes the mechanical to electrical energy conversion, revealing the AE signals from the material samples, under mechanical stretches (Fig. 4). Mounting to the test specimen is typically achieved using silicon rubber or epoxy adhesives in order to realize the optimum electroacoustical transmission between the studied material and the sensor active surface.



Figure 4. AE piezoelectric sensor.

The main characteristics of some broadband AE piezoelectric sensors are presented in the Table 1.

TABLE I. PROPERTIES OF SOME AE PIEZOELECTRIC SENSORS

Properties	AE sensor
Outer dimension	Diameter: 20.5 mm x 14 mm
Effective sensing area	Around 230 mm ²
Total mass (g)	12
Piezoelectric mass (g)	5 – 6
Capacitance (pF)	350
Piezoelectric charge coefficient d 31 (10 ⁻¹² m/V)	-150
Frequency range (kHz)	100 - 450



Figure 5. Experimental wireless module for acoustic emission sensor.

The experimental wireless acoustic emission sensor module with microcontroller for monitoring system has small size and is protected by a metallic case (Fig. 5).

Fig. 6 presents the AE signals prevailed by the sensor in the breaking moment of a concrete sample at the maximum stretch. A large data base, which contains information about different kind of construction materials (metals, concrete, rocks, minerals, etc.), referring to the AE signal parameters (amplitude, duration, number of pulses, etc.) could be then used in order to predict the material failure or the moment of the cracks initiation into material.

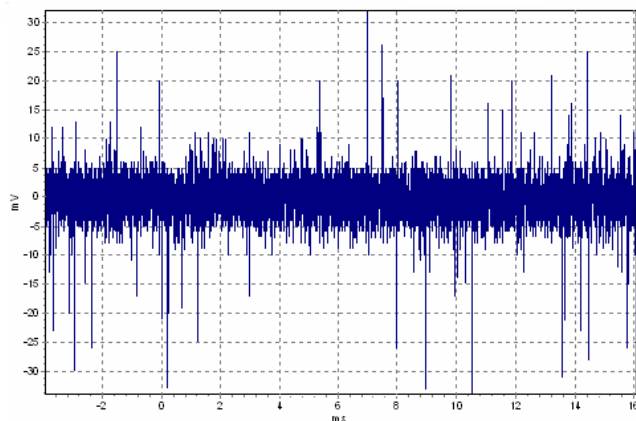


Figure 6. AE signals from a concrete sample at breaking point at mechanical stretch.

Also, the pulses calibration is necessary to be introduced to the test specimen under the control of the monitoring system. The generated acoustic signal is collected during the press or stretched work. A preset filter ensures the optimum response from individual channel by matching the amplifier and transducer responses.

The ratio filtering techniques are used for eliminating outer noise signals, as well as observing the ratios of valid signals to estimate crack depth of the growing crack.

A digital memory oscilloscope type Tektronix TDS 2022 was used to the experimental researches. Fig. 7 shows AE signal converted by AE piezoelectric sensor, prevailed from an outstretched metallic bar and Fig. 8 present the processed signal from AE piezoelectric sensor by the microcontroller software, displayed on TDS Tektronix oscilloscope, which is limited at 2.0 V level.

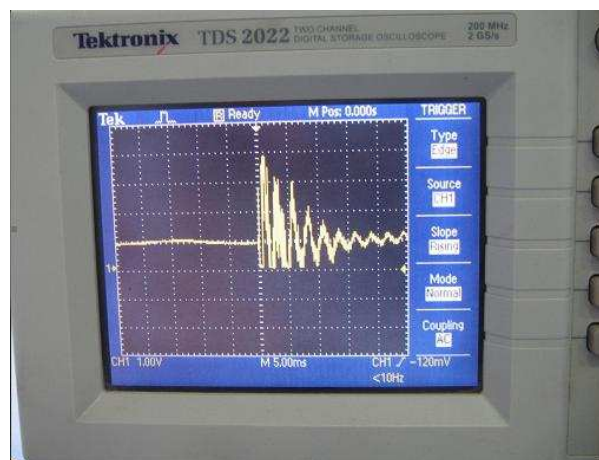


Figure 7. AE signal converted by AE sensor, prevailed from an outstretched metallic bar.

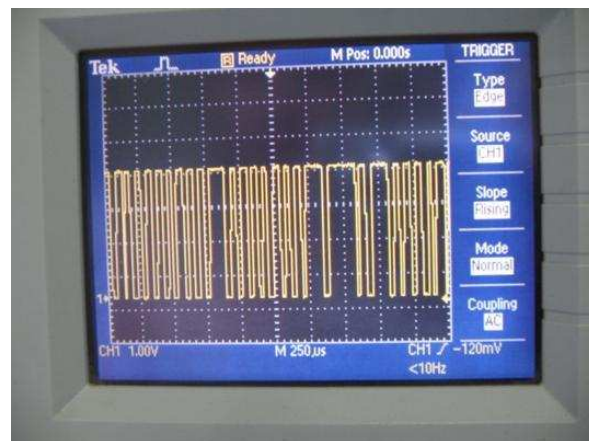


Figure 8. Processed signal from AE sensor by microcontroller software, displayed on TDS Tektronix oscilloscope.

The microcontroller software is able to realize the processing of signal received from the AE sensor, such as: the magnification in the case of a small AE level signal or to realize the sensor calibration, function of material characteristics (type, metal or nonmetal, acoustic velocity, density, structure, porosity, etc.).

For instance, we chosen to set the tension threshold at 1.0 V (above the reference line), in order to form the pulses, which exceed 1.0 V and correspond to the AE events, arisen in material under mechanical efforts (Fig. 8). The master

system is positioned at 100 m distance from the wireless AE module. It collects all these pulses received from the wireless AE module, counts the number of these events and/or determines their duration. Further, this information can indicate the starting crash or braking into material or a possible irreversible material deterioration. This algorithm is preordained by the special software of PIC 18F452 microcontroller.

TABLE II. MECHANICAL PROPERTIES OF SOME METALLIC MATERIALS

Material	Longitudinal elasticity module, E, daN/cm ²	Transversal elasticity module G, daN/cm ²	Poisson Coefficient μ
Soft steel	(2.0-2.15) · 10 ⁶	(7.8-8.5) · 10 ⁵	0.24-0.28
Hard steel	(2.0-2.2) · 10 ⁶	8.5 · 10 ⁵	0.25-0.29
White wrought iron	(1.0-0.6) · 10 ⁶	4.5 · 10 ⁵	0.23-0.27
Tin	0.2 · 10 ⁶	0.7 · 10 ⁵	0.42

Table II presents some mechanical properties of metallic materials, which could be used in the specialized software data processing, as material constants.

CONCLUSION AND FUTURE WORK

Crack initiation of structures could be determined by the appearance of the AE signal at low stretch stress levels. After the crack initiated, the AE signals around the zero stress were thought to be caused by crack-face grinding when the cracks were closed. More experimental wireless modules with acoustic emission sensors could be well used into complex AE monitoring systems of important structures, such as bridges, buildings, metallic rails or underground. Inspection methods can be applied more efficiently by monitoring systems with many wireless AE sensor modules for large structures in the civil engineering. Next researches will be dedicated to obtain complex software around PIC 18F452 microcontroller, for controlling several AE modules of an AE monitoring system.

ACKNOWLEDGMENT

This work was supported in part by the National Authority for Scientific Research (ANCS) and the Executive Agency for Higher Education and RDI Funding (UEFISCDI).

REFERENCES

- [1] D. H. Kim, W. K. Lee, and S. W. Kim, "Analysis of Acoustic Emission Signal for the Detection of Defective Manufactures in Press Process", World Academy of Science, Engineering and Technology, Vol. 53, pp. 1301-1305, 2009.
- [2] ADVANCED ULTRASONIC FLAW SIZING HANDBOOK, 1998 Edition J. Mark Davis, DAVIS NDE, INC., <http://www.ndt.net/article/1198/davis/davis.htm>
- [3] C. U. Grosse, Acoustic emission localization methods for large structures based on beamforming and array techniques, NDTCE'09, 2009
- [4] C. U. Grosse, H. W. Reinhardt, and F. Finck, "Signal-Based Acoustic Emission Techniques in Civil Engineering", Mat. in Civ. Engrg., Vol. 15, pp. 274, 2003.
- [5] C. Grosse, F. Finck, J. H. Kurz and H. W. Reinhardt, "Monitoring techniques based on wireless AE sensors for large structures in civil engineering", Proc. EWGAE 2004, BB 90-CD, Sept. 2004, pp. 843-856.
- [6] I. Chilibon and S. Velizar, "Ultrasound propagation in asphalt", B.H.V. Topping and M. Papadrakakis, (Editors), Civil-Comp Press, Stirlingshire, Scotland, paper 91, Reference CST91, 10 pages, 2008.
- [7] F. Rauscher, "Defect Detection by Acoustic Emission Examination of Metallic Pressure Vessels", Proc. EWGAE 2004, BB 90-CD, Sept. 2004, pp. 83-90.
- [8] P. Tscheliesnig, "Corrosion testing of ship building materials with acoustic emission (AE)", Proc. EWGAE 2004, BB 90-CD, Sept. 2004, pp. 51-59.
- [9] M. Taghvaei, S.B.M. Beck, and W.J. Staszewski, "Leak detection in pipeline networks using low-profile piezoceramic transducers", Structural Control and Health Monitoring, Vol. 14 (8), pp. 1063-1082, 2007.
- [10] Z. H. Hanafi, N. Jamaludin, S. Abdullah, M. F. M. Yusof, and M. S. M. Zain, Acoustic emission study of corrosion fatigue and fatigue for API 5L X70 gas pipeline steel, Applied Mechanics and Materials, Vol. 138-189, pp. 635-639, 2012.
- [11] M. F. M Yusof, C. K. E Nizwan, N. Jamaludin, and S. Abdullah, "Acoustic emission behavior during fatigue crack of API5LX70 gas pipeline steel", Applied Mechanics and Materials, Vol. 80-81, pp. 148-152, 2011.
- [12] M. Ahadi and M. S. Bakhtiar, "Leak detection in water-filled plastic pipes through the application of tuned wavelet transforms to Acoustic Emission signals", Applied Acoustics, Vol. 71, 634-639, 2010.
- [13] R. Geng, "Modern acoustic emission technique and its application in aviation industry", Ultrasonics, Vol. 44 Suppl 1, e1025-9, Dec. 2006.
- [14] C. U. Grosse, M. Krüger, and S. D. Glaser, "Wireless Acoustic Emission Sensor Networks for Structural Health Monitoring in Civil Engineering", ECNDT 2006 - Tu.1.7.3, 2006, pp. 1-8.
- [15] S. Uppal, D. Yoshino, and H. L. Dunegan, "Using Acoustic Emission to Monitor Fatigue Cracks on the Bridge at FAST", Technology Digest, February 2002.

Investigation on Electrode Size of High Frequency Ultrasonic Transducers

Yangjie Wei^{1,2}

¹ Graduate School of Chinese Academy of Science, &
State Key Laboratory of Robotics
Shenyang Institute of Automation, CAS
Shenyang, China
weiyangjie@sia.cn, &
Yangjie.Wei@izfp-d.fraunhofer.de

Thomas Herzog² and Henning Heuer²

² Department of Sensor and Sensor System
Fraunhofer Institute for Non-Destructive Testing, IZFP
Dresden Branch
Dresden, Germany
Thomas.Herzog@izfp-d.fraunhofer.de, &
Henning.Heuer@izfp-d.fraunhofer.de

Abstract—This paper presents a concept to increase the performance of high frequency ultrasonic transducers. For a sandwich high frequency ultrasonic transducer, the top electrode should be smaller than the piezoelectric plate to avoid shortcuts and edge effects. However, its size can influence properties of the transducer, and until now there is no research about it published. A theoretical investigation about influence of the top electrode size on properties of a transducer is conducted in this paper. First, two factors related with the top electrode size based on transmission coefficient and stored energy are proposed; Then, analysis on an Al-AlN-Al on silicon wafers with different electrode sizes are performed and the results prove the effectiveness and the validity of the proposed factors. Finally, electrical impedance matching experiments are conducted to improve the properties of transducers with different electrode sizes, and the experiment results show that the improved resolution and sensitivity after matching.

Keywords-Electrode size; electric impedance matching; ultrasonic transducer

I. INTRODUCTION

In high-power ultrasonics and underwater acoustics, a sandwich piezoelectric structure is the most popular one. It is composed of piezoelectric elements, sandwiched between two metal films[1-2], and the analysis of sandwich piezoelectric ultrasonic transducers has been studied for many years[3-5].

Generally, sizes of the top electrode, the bottom electrode and the piezoelectric plate in a sandwich piezoelectric structure are same. However, for high frequency transducers, it is very easy for the two electrodes to get shortcuts or edge effects, as the thickness of the piezoelectric plate is very thin. Therefore, some researchers proposed the pyramid structure: the bottom electrode size is the biggest, then the smaller piezoelectric plate, and the top electrode is the smallest[1, 6-7]. Although, this structure can effectively avoid shortcuts and edge effects, the smaller top electrode can decrease the effective size of the active element, and it must have influence on the properties of the transducer. Therefore, it is important to research how the size of the top electrode can influence the properties of high frequency ultrasonic transducers. In this paper, through analysis on the echoes of transducers with different top electrode sizes and the Fourier transformation of them, we proposed two factors to explain the pattern that the top

electrode size influences the transducers' properties and conducted electrical impedance matching experiments to improve the properties of them.

The content of the paper is listed as follows: in Section II, two factors are proposed to explain the relationship between the transducers' properties and the top electrode size; then in Section III, analysis on an Al-AlN-Al structure on silicon wafers with different electrode sizes are performed and the results present the effectiveness of the proposed factors; Electrical impedance matching experiments are conducted to improve the properties of transducers with different electrode sizes in Section IV, and Section V is the conclusion.

II. TWO IMPORTANT FACTORS

In a sandwich ultrasonic transducer with pyramid structure, the top electrode is smaller than the piezoelectric plate, and the active area of the piezoelectric plate is equal to the size of the top electrode, that means $A=A'$ in Fig. 1. So the size of the top electrode can influence the properties of the piezoelectric plate. In this section, we would explain its influence from the following two aspects.

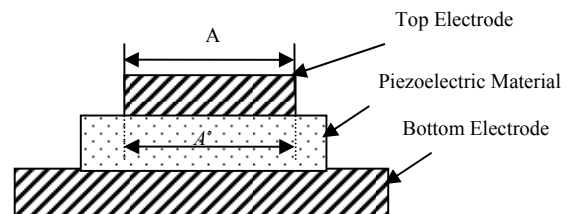


Fig. 1 Sketch of a pyramid structure transducer

A. Energy transmission coefficient

In electronics, when the electrical impedance of a load and a source is known, the fraction from the load can be calculated with Eq. (1), and the value produced is known as the reflection coefficient.

$$R = \left(\frac{Z_l - Z_s}{Z_l + Z_s} \right)^2 \quad (1)$$

where Z_l and Z_s are the impedances of the load and the source, respectively.

The transmission coefficient, which represents the transmission fraction from the load to the source, is calculated by simple substrate the reflection coefficient from one,

$$T = 1 - R = 1 - \left(\frac{Z_1 - Z_s}{Z_1 + Z_s} \right)^2 \quad (2)$$

Therefore, in order to transmit more energy into a transducer, the first important factor in practice is to match the electrical impedance of the transducer and the source, and increase the transmission coefficient.

$$\max(T) = \max(P_T) = \min(Z_s - Z_{in}) \quad (3)$$

where T is the transmission coefficient; P_T is the energy transmitted into the transducer; Z_{in} is the electrical impedance of the transducer. If the electrical impedance, which is in proportion with the top electrode size, is far away from the ideal value, the signal-to-noise ratio (SNR) will be influenced and more noise will be received by the receiver [8].

B. Stored Energy

For a sandwich ultrasonic transducer, energy stored in it can be calculated with voltage, electrode area and capacitance,

$$P_s = \frac{1}{2} C'_0 A V^2 \quad (4)$$

where P_s is the energy stored on the capacitor; A is the top electrode size of the transducer; C'_0 is the capacitance per unit area given as,

$$C'_0 = \frac{\epsilon}{L} \quad (5)$$

where L is the maximal displacement along the thickness direction; ϵ is the permittivity of the piezoelectric under no applied voltage.

The voltage between two electrodes is,

$$V = \frac{q(t)}{C_0} - h\psi_T(t) \quad (6)$$

where $q(t)$ is the electric charge per surface area on each electrode; $h\psi_T(t)$ is the mechanical displacement of a plate from its equilibrium position,

$$h\psi_T(t) = h(\psi(L,t) - \psi(0,t)) \quad (7)$$

where h is the piezoelectric constant; $\psi(L,t)$ is the mechanical displacement of a plate from its equilibrium position.

Suppose $P_{s0} = C'_0 V^2$, if the thickness of the piezoelectric plate is fixed, the bigger the electrode is, the higher the stored energy. Therefore, the sensitivity, which is the ability of an ultrasonic system to detect defects, of a transducer with a constant thickness is proportional to the top electrode size.

In order to design a transducer with high sensitivity, we should consider,

$$\max(P_s) = \max\left(\frac{1}{2} P_{s0} A\right) = \max(A) \quad (8)$$

Since both the transmission coefficient and the stored energy are related with the top electrode size, we should choose an optimal electrode size to improve the sensitivity and resolution of a transducer in real applications.

III. ANALYSIS ON DIFFERENT ELECTRODE SIZE

In order to validate these factors, we analyzed Al-AlN-Al transducers on silicon wafers with different top electrode sizes. In the experiment, a 500µm thick silicon substrate is used, on which a square shaped Al electrode with a large area is deposited. On the top of it, a squared shaped AlN layer with thickness of 10µm and area of 25mm² is deposited, followed by a squared Al top electrode with an area of 25mm², 1mm², 0.25mm² and 0.09mm², respectively as shown in Fig. 2.

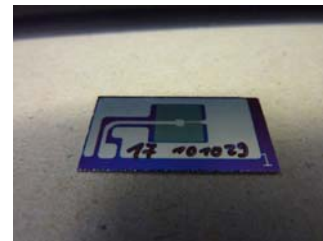


Fig. 2 Our AlN transducer

First, we calculated the transmission coefficient from the source to the transducers with different electrode sizes and the energy stored on the capacitors with our theory, and the result can be seen in Table 1.

TABLE 1 TRANSMISSION PARAMETERS AND ELECTRODE SIZE

Electrode Size (mm ²)	25	1	0.25	0.09
Transmission Coefficient(%)	19.8	97.3	51.9	22.9
Stored Energy* P _{s0} (Joules)	12.5	0.5	0.125	0.045

From it, we can see that when the electrode size is 1mm², both the transmission coefficient and the stored energy are high. While when the electrode is 25 mm², even its transmission coefficient is as low as 19.8%, the energy stored on the capacitor is 12.5P_{s0} in Joule, which is very high. So the amplitude of it should be higher than that of the echoes whose transmission coefficient is 51.9%, but the stored energy is only 0.125P_{s0} in Joule. When the electrode size is 0.09mm², the stored energy and the transmission coefficient are both low, so the amplitude should be too low to be separated with noise.

Then, we measured the practical echoes of the transducers above and did Fourier transformation for them. The pulser and receiver DPR 500 (JSR Ultrasonics) was used

to excite the transducers with a needle pulse at high amplitude (-143V) and very short pulse time (~1.4ns), and the input impedance of DRP 500 is 50 ohms. The receiver was set to a gain of 10 dB and a high frequency pass filter between 5MHz and 500MHz was used. The illustration in Fig. 3 shows the schematic setup of the measurement and the detailed measurement can be seen in Literature [9, 10]. Fig. 4-5, Fig. 6-7, Fig. 8-9 and Fig. 10-11 are the results when the top electrode size is 25mm², 1mm², 0.25mm² and 0.09mm², respectively.

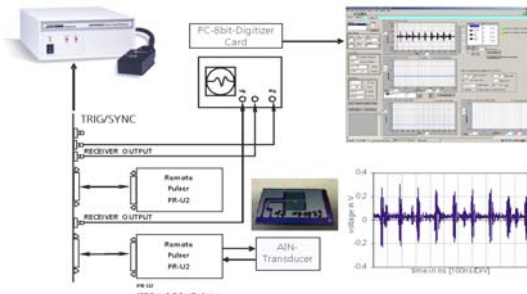


Fig. 3 Measurement setup and connection

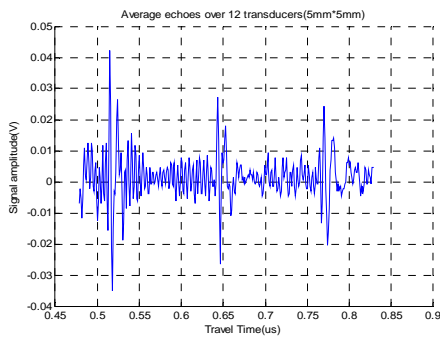


Fig. 4 First three echoes from substrate back wall

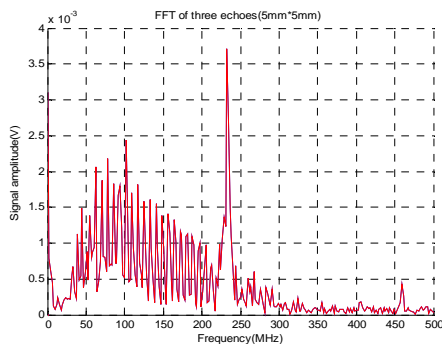


Fig. 5 FFT of first three echoes

From Fig. 4-5, we can see that when the electrode is 25mm², the maximal amplitude of the echoes is about 0.041 V, which is related with the sensitivity of the transducer.

That means the higher the amplitude of an echo is, the higher the sensitivity of the transducer is. However, the noise is also serious compared to the signal due to the lower transmission coefficient. From the Fourier transformation result, we can see that there is an obvious narrow peak at 232.5MHz. However, most frequency concentrates on the range from 50MHz to 200MHz, and there is a smaller peak around 100MHz because of noises.

Therefore, although the amplitude, or the sensitivity, of this kind of transducers is high, the transmission coefficient is lower and the bandwidth of the maximal frequency is only about 7.8 MHz.

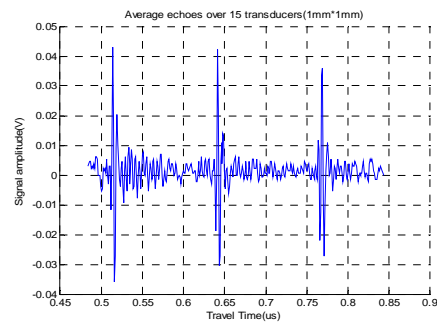


Fig. 6 First three echoes from substrate back wall

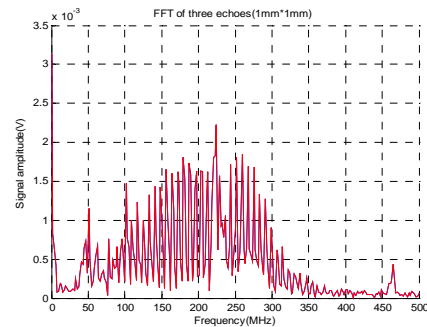


Fig. 7 FFT of first three echoes

When the electrode is 1mm², the maximal amplitude of the echoes is about 0.042 V and the noise is very small. That means the sensitivity of it is higher and at the same time the transmission coefficient is higher. From Fig. 7, we can see that there is only a peak at about 222MHz which is a little smaller than the peak frequency when the electrode is 25mm². However, on the both sides of the peak, the voltage decreases slowly, and there is no other peak. While in Fig. 8, when the electrode is 0.25mm², the maximal amplitude of the echoes is about 0.013 V and the noise is also obvious. There two obvious peaks at 235MHz and 100MHz in Fig. 9, and both of them are very sharp.

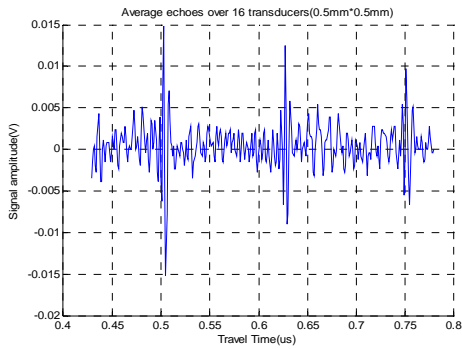


Fig. 8 First three echoes from substrate back wall

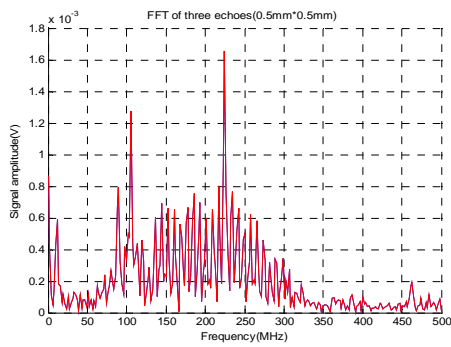


Fig. 9 FFT of first three echoes

When the electrode is 0.09mm^2 , the maximal amplitude of the echoes in Fig. 10 is about 0.001 V and the noise is too obvious that it is hard to distinguish the signal. From the Fourier transformation result in Fig. 11, we can see that there are two obvious peaks at 222MHz and 100MHz. At the both sides of the peaks, the voltage decreases sharply. Therefore, the sensitivity and resolution of the transducer are both lower.

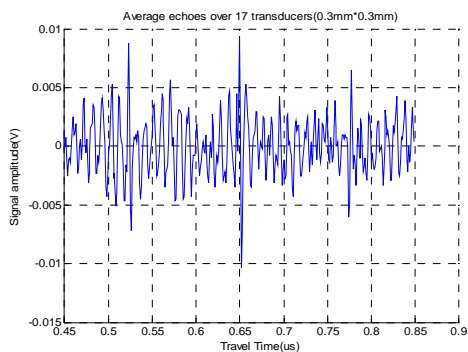


Fig. 10 First three echoes from substrate back wall

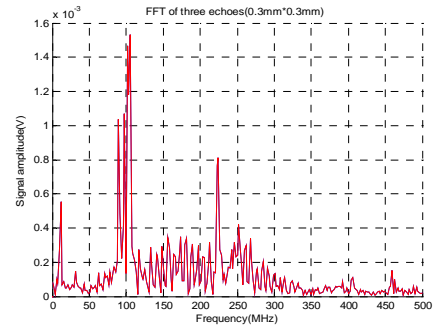


Fig. 11 FFT of first three echoes

From these results, we can see the top electrode size of a transducer not only can influence the amplitude of echoes, but also can influence the maximal frequency and the bandwidth. For our transducers, when the area is 1mm^2 , the echoes from the substrate back wall are very clean, the resonant frequency of the transducer is high and the bandwidth is large. That means the sensitivity and resolution are both higher compared with other situations. In Table 1, from theoretical calculation the transmission coefficient of 1 is the highest, and the stored energy is $0.5P_{s0}$ in Joule which is also high. Therefore, the measurement results match our calculations in Table 1 very well.

During designing a transducer, both of the stored energy and the transmission coefficient need to be considered appropriately, and the top electrode size is a really important parameter. In real applications, we could choose an appropriate top electrode size of a transducer first and then improve the resolution and the sensitivity through electrical impedance matching.

IV. ELECTRICAL IMPEDANCE MATCHING

During electrical impedance matching, normally the first step is to suppress the influence of the clamped capacitor C_0 with a parallel inductor, and use a transformer or a parallel resistor to regulate the input impedance, as shown in Fig. 12. For our transducer, when the electrode size is 1mm^2 , the inductor is 10nH , and the electrical impedance after inductor matching is 414ohms , so we can use a parallel 55ohms resistor to match the electrical impedance to 50ohms . When the electrode size is 0.25mm^2 , the matching inductor is 40nH and the parallel resistor is 50ohms .

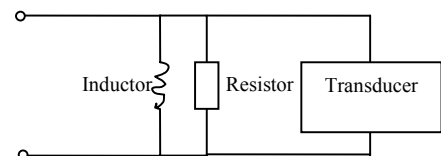


Fig. 12 Electrical impedance matching circuit

First, we matched the electrical impedance with electrode size of 1mm^2 , and the echoes and the FFT of the first echo are shown in Fig. 13-14, where the blue line represents the result after matching and the red line with “x” represents the situation before matching.

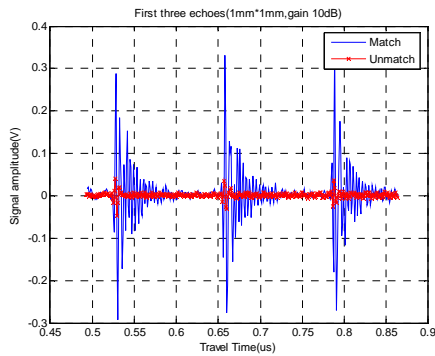


Fig. 13 Echoes from the substrate

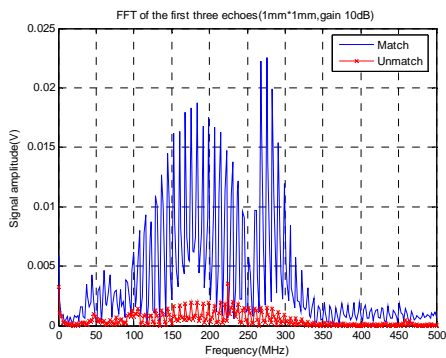


Fig. 14 FFT of the first echo

From them, we can see that the maximal amplitude of the first three echoes before matching is 0.0391V , while after matching it is 0.3438V , so it increases 8.8 times; The peak frequency of the first echo before matching is 225MHz , while after matching it is 275MHz . Therefore, after matching, the resolution and the sensitivity are both improved.

Second, we matched the electrical impedance with electrode size of 0.25mm^2 , and the result is shown in Fig. 15-16. In this case, the maximal amplitude of the first three echoes before match is 0.0164V , while the maximal amplitude of the first echo after match is 0.0651V ; the peak frequency of the first echo before match is 225MHz , while the peak frequency of the first echo after match is 275MHz .

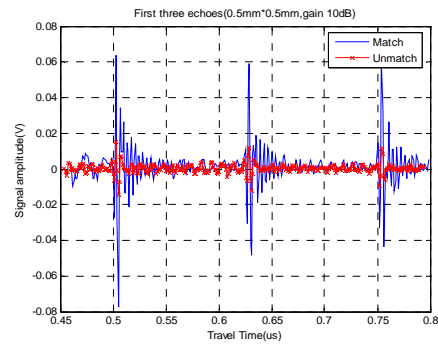


Fig. 15 Echoes from the substrate

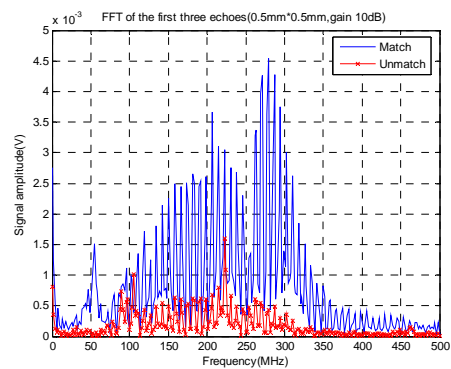


Fig. 16 FFT of the first echo

From these experiment results, we can see that through electrical impedance matching, the energy transmission coefficient can be improved and more energy can be transmitted into the transducers. So the amplitude of echoes improves so much and the working frequency of the transducers is close to the ideal frequency.

V. CONCLUSION

In this paper, we analyzed the influence of the top electrode size on the properties of a high frequency ultrasonic transducer based on transmission coefficient and stored energy in it. It turns out from our investigation that the top electrode size should be larger to improve the sensitivity of it, and the transmission coefficient, as well as SNR, can be improved by electrical impedance matching. Our contributions are as following aspects: 1) Two factors related with the top electrode size are proposed to explain the relationship between the top electrode size and the properties of the transducer; 2) Analysis on an Al-AlN-Al structure on Si wafers with different electrode sizes are performed and the results present the effectiveness and the validity of the proposed factors; 3) Electrical impedance matching experiments are conducted to improve the properties of transducers with different electrode sizes, and

it turns out that the resolution and sensitivity have been improved by electrical impedance matching.

ACKNOWLEDGMENT

Authors thanks Fraunhofer Institute for Electron Beam and Plasma Technology FEP in Dresden for the deposition Processes.

REFERENCES

- [1] P. M. Martin, M. S. Good, H. W. Johnston, G. J. Posakony, L. J. Bond, and S. L. Crawford. "Piezoelectric films for 100 MHz ultrasonic transducers," *Thin Solid Films*, vol. 379, 2000, pp. 253-258.
- [2] K. J. Kirk, C. K. Lee and S. Cochran. "Ultrasonic thin film transducers for high-temperature NDT," *High Temperature NDT*, vol. 47, no. 2, 2005, pp. 85-87.
- [3] S. Y. Lin, "Optimization of the performance of the sandwich piezoelectric ultrasonic transducer". *Journal of the Acoustical Society of America*, vol. 115, no. 1, 2004, pp. 182-186.
- [4] M. P. Johnson, "Velocity control and the mechanical impedance of single degree of freedom electromechanical vibrations," *Journal of the Acoustical Society of America*, vol. 115, no. 1, 1988, pp. 1994-2001.
- [5] R. S. Naik, J. J. Lutsky and R. Reif. "Measurement of the bulk, C-Axis electromechanical coupling constant as a function of AlN films quality," *IEEE Transactions on Ultrasonic, Frequencies and Frequency Control*. vol. 47, no. 1, 2000, pp. 292-296.
- [6] B. Dubus and J. C. Debus, "Analysis of mechanical limitations of high power piezoelectric transducers using finite element modeling," *Ultrasonics*, vol.29, 1991, pp. 201-207.
- [7] D. F. Liu and K. C. Kao, "Piezoelectric, dielectric, and interfacial properties of aluminum nitride films," *Journal of Vacuum Science & Technology A* , vol. 16, no. 4, 1998, pp. 2360-2366.
- [8] B. A. J. Angelsen, H. G. Torp and S. Holm, "Waves, signals and signal processing", 2000.
- [9] S. Walter, T. Herzog, and H. Heuer. "Investigations on aluminum nitride thin film properties and design considerations for smart high frequency ultrasound sensors," *The Second International Conference on Sensor Device Technologies and Applications*, Prague, Czech Republic, April 18-20, 2011, pp. 129-134.
- [10] D. Gloess, H. Bartzsch, M. Gittner, T. Herzog, S. Walter, and H. Heuer. "Reactive pulse magnetron sputter deposition of piezoelectric AlN layers," *Proceedings of the 4th International MPA meeting 2010*, Braga, Portugal, July 28-30, 2010, pp. 135-138.

Surface Acoustic Wave Devices Exploiting Palladium Layer Properties for Selective Detection of Hydrogen

Meddy Vanotti, Virginie Blondeau-Patissier, David Rabus, Loic Richard, Sylvain Ballandras
Time and Frequency Department
FEMTO-ST Institute
Besançon, France

Email: meddy.vanotti@femto-st.fr, virginie.blondeau@femto-st.fr, david.rabus@femto-st.fr,
loic.richard@femto-st.fr, sylvain.ballandras@femto-st.fr

Abstract—For an increasing number of application (energy production, car industry, space, etc.), hydrogen represents a solution of the future as it is the most common body in the Universe (and therefore on Earth). However, due to its unstable properties, a particular care must be dedicated to control possible gaseous leaks close to tanks and facilities using this resource. In this paper, surface acoustic wave sensors are proposed for detecting gaseous hydrogen in standard environmental conditions (atmospheric pressure and room temperature). The proposed SAW sensors consists in two Rayleigh-wave delay lines built on Quartz, one equipped with a Palladium overlay and the other exhibiting a free path between the two interdigitated transducers. A specific gas test cell has been developed to test various sensor configurations submitted to hydrogen-composed atmospheres. A particular care was paid to avoid hydrogen leakage in the working environment and to perform the regeneration of the gas absorbing layer. The developed device allows for identifying different concentrations of hydrogen (in the 1-4% range) diluted in N_2 and is also able to detect H_2 in current atmosphere. SAW devices exploiting hydrogen absorption capabilities of palladium thin films have been here used to make the detection and the identification of hydrogen concentrations in the 1-4% range and the influence of outer parameters such as temperature and relative humidity variations on the sensor operation is also reported.

Index Terms—gas sensors; hydrogen; Palladium; SAW device; Rayleigh waves.

I. INTRODUCTION

The raising shortage of fossil energy resources added to the increasing concern towards environmental issues have led to consider hydrogen as one of the most promising energy resource. This odorless and colorless gas being highly explosive over 4% concentration in air, the availability of a fast and accurate detection system close to storing facilities and equipping hydrogen-operated machines is mandatory for obvious security reasons. Such a system must exhibit a significant selectivity as it must detect the presence of gaseous hydrogen in air with concentrations smaller than the above-mentioned critical limit at standard conditions (room temperature and atmospheric pressure) as well as in harsher environment (very low or significantly high temperature). Although some solutions have been proposed [1] [2] [3]

[4] [5] [6] [7]. The current availability of such a detection system meeting modern specifications of hydrogen use and storage is still questionable. The mains improvements for such sensors are their sensitivity, their selectivity and their reliability together with sensor size, cost reduction, energetic needs and response time [8]. Many methods of detection of hydrogen and a comprehensive review can be found in the literature [9], providing a substantial material base to try and address the above challenges. Among the possibilities, SAW (Surface Acoustic Wave) sensors have been widely studied in the last decades because of their attractive capabilities. Indeed, SAW devices exhibit high sensitivity to surface perturbation since the quasi totality of the energy propagates in a region that thickness is a few times the wavelength of the propagating acoustic wave. It is also a mature technology, SAW device do exhibit limited size (less than 1 cm^2) and they allow for wireless use [10]. Initial works were made by D'Amico et al. [11] using the properties of palladium layer to trap the targeted gas. Since this pioneer work, innovations concerning the selectivity and stability of sensitive layers versus external parameter have been proposed to improve hydrogen detection using SAW devices [12] [13] [14] [15] [16] [17] [18] [19]. In this paper, a SAW sensor is proposed for detecting gaseous hydrogen in standard environmental conditions (atmospheric pressure and room temperature). The proposed SAW sensor consists in two Rayleigh-wave delay lines built on Quartz, one equipped with a Palladium (Pd) overlay and the other exhibiting a free path between the two interdigitated transducers (IDTs) used to excite and detect the acoustic wave. These IDTs are built using aluminum electrodes, as this metal is known to be inert versus gaseous hydrogen. An innovative aspect of the proposed sensing system consist in the open-loop strategy for phase changes monitoring [20]. Moreover, delay lines are monitored in parallel using a synchronous detection approach that provides high frequency measurement resolution and that permits a systematic characterization of the device before operated. Along this approach, the impact of changes of intrinsic properties of the devices such as working frequency drift with aging can be minimized. These sensors

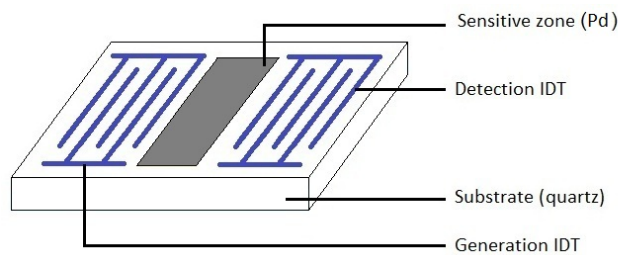


Fig. 1. Scheme of a SAW delay line using Rayleigh surface acoustic wave at 78MHz.

have been tested in a specific gas cell developed to experiment with various sensor configurations submitted to hydrogen-composed atmospheres. A particular care has been dedicated to avoid hydrogen leakage in the working environment and to promote the gas absorbing layer regeneration. The developed device allows for identifying different concentrations of hydrogen diluted in N₂ and is also able to detect H₂ in current atmosphere. The first section of the paper presents the SAW sensor as well as the exploited monitoring system. Experimental validation of H₂ detection then is reported, with a description of the chemical test bench and detection results for various H₂ concentrations. An analysis of the influence of H₂ adsorption on SAW propagation is proposed to provide routes for the proposed device optimization. In the same purpose, the last section of the article is devoted to characterizing the influence of external parameters such as temperature and relative humidity variations on the sensor operation, yielding conclusive discussions.

II. SAW SENSOR AND ASSOCIATED MONITORING SYSTEM

Selective detection of hydrogen at room temperature and pressure have been achieved using SAW delay lines exploiting Rayleigh waves on AT-cut Quartz, as the corresponding first order temperature coefficient of frequency (TCF) is close to zero, yielding frequency-temperature compensation for the above-mentioned operating conditions. The sensor structure correspond to a differential set-up in, which a sensitive track is achieved by depositing a Pd layer in between two IDTs whereas the reference track surface is left free to detect non-specific gas/surface interaction. Along this approach, one can significantly increase the sensitivity of the device and its robustness to correlated perturbations (temperature, vibration, non-specific adsorption). The configuration of both generation and detection IDTs used for the sensor consist in 50 fingers pairs with a grating period of 10 μm and a center-to-center spacing of 5mm (the reactive surface). The wavelength is 40μm, yielding a frequency operation in the vicinity of 78MHz as the wave velocity approaches 3100m.s⁻¹. The Pd film was deposited by thermal evaporation on a single run and shaped by a lift-off technique. Its length along the propagation path was 3mm and its thickness equal to 300nm. The device configuration is shown on Fig. 1.

Using a network analyzer, the transfer function of the device can be easily determine and hence the phase shift induced by

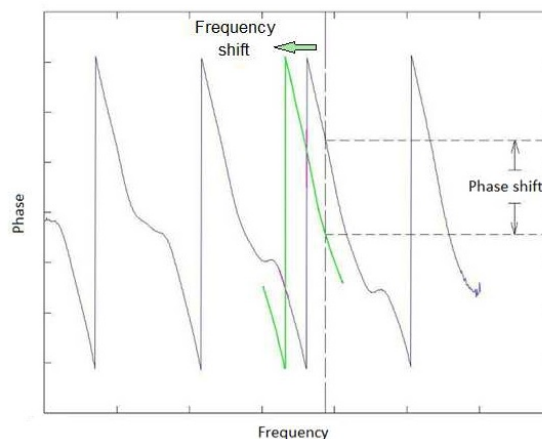


Fig. 2. Phase shift measurement principle using a dedicated instrumentation.

gas absorption has been first monitored that way. However, the use of a dedicated electronics has been experienced and delivers similar information [20]. This system actually operates as a network analyzer to detect the optimal operation condition (zero phase at maximum bandpass amplitude) and then tracks the phase shift in a phase-locked-loop protocol to keep the excitation frequency meeting the above condition. The sensitivity of the set-up allows for some tens mill-degrees resolution and is easily transportable. The response of the bare device and the functionalized one are respectively measured. This configuration has been used so as to make a systematic characterization of each new device used for H₂ detection. Fig. 2 illustrates the way the phase shift measurement is achieved.

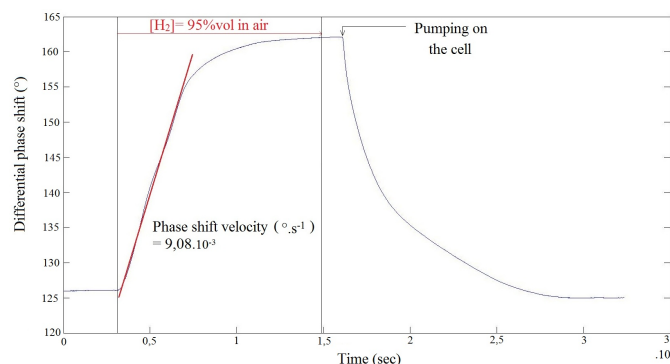


Fig. 3. Detection of hydrogen at high concentration in air.

A. Detection of hydrogen at room temperature and atmospheric pressure.

Hydrogen detection in the percent order have been achieved at room conditions. Figs. 3 and 4 present experimental results when using either nitrogen or air as carrier gas. As it can be observed in Fig. 4, the detection of about 95%vol of hydrogen in air at 35% RH and 20°C can be achieved with a response delay of about 20 seconds considering that the determination

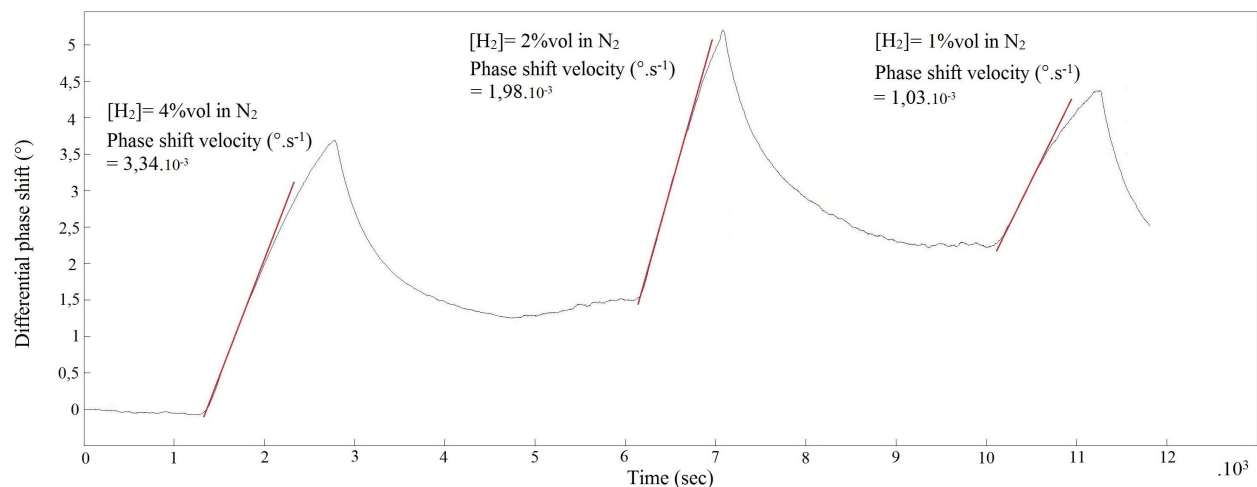


Fig. 4. Detection of hydrogen in the range 4% to 1%vol in N₂.

of the H₂ concentration in the melting gas is derived from the phase shift velocity during the exposure and not from the steady state. It is notable that this value depends on a large part on the performance of the hydrogen generation setup. Therefore, the intrinsic response delay of the device is expected to be shorter. Fig. 3 shows that the device allows for identifying different concentrations of hydrogen diluted in a nitrogen flow of 100scm.

III. ANALYSIS OF HYDROGEN ABSORPTION ON Pd FILMS AND ITS INFLUENCE ON SAW PROPAGATION.

Absorption of hydrogen into Pd layer induce modifications on the SAW propagation conditions. The effective physical characteristics of the wave then varies with the amount of absorbed H₂ (especially its phase velocity). It has been shown [21] that the two main parameters that influence the phase velocity change of elastic waves are mass- and elastic-loading as it can be seen on the equation bellow [21]. Since only devices using quartz substrates have been used here, changes in electrodes conductivity is not consider as possible origin of the observed phase velocity drift and therefore will not be taken in account. Electromechanical coupling of Rayleigh waves on Quartz substrates is actually smaller enough to consider conductivity changes negligible.

$$\frac{\Delta\nu}{\nu} = \left(\frac{\pi h}{2\lambda}\right) \left[-\frac{\Delta\hat{\rho}}{\hat{\rho}} \{(A_x^2 + A_y^2 + A_z^2)\hat{\rho}\nu_0^2\} \text{ mass-loading term} \right. \\ \left. + \frac{\Delta\hat{C}_{44}}{\hat{C}_{44}} \{(4A_z^2 + A_x^2)\hat{C}_{44}\} \text{ elastic-loading term} \right. \\ \left. + \left\{ \frac{\left(1 - \frac{\Delta\hat{C}_{44}}{\hat{C}_{44}}\right)^2}{\left(1 - \frac{\Delta\hat{C}_{11}}{\hat{C}_{11}}\right)} - 1 \right\} \left(4A_z^2 \frac{\hat{C}_{44}^2}{\hat{C}_{11}}\right) \right] \text{ elastic-loading term}$$

In case of H₂ adsorption on Pd layer that thickness is h traversed by a SAW that wavelength is λ , the mass density $\hat{\rho}$

and the elastic constants \hat{C}_{11} are both decrease, whereas the \hat{C}_{44} constant increases. The values of normalized mechanical displacement A_i for palladium are reported in [22] and [23]. Numerical calculations of hydrogen absorption in Pd layers [21] predict an increase of \hat{C}_{44} elastic constant, yielding an increase of the phase velocity of the Rayleigh wave propagating under such an overlay. These calculations are in agreement with the experimental observations presented here.

IV. THE INFLUENCE OF HUMIDITY AND TEMPERATURE ON HYDROGEN DETECTION.

As SAW devices are known to suffer from interference due to humidity and temperature, the influence of these parameters on the sensor operation have been investigated and are exposed here. The observations reported in this section are expected to provide information allowing for the improvement of the differential acquisition setup. One can see in Fig. 5 that an increase of the relative humidity (RH) of the injected gas causes a mass-loading effect that results in a decrease of the measured phase of the delay line. Indeed, the adsorption of condensed water onto the surface of the device leads to a raise of the mass at the surface of the device (mass loading) leading to the decrease of the phase velocity experimentally observed. Fig. 6 evidences the impact of temperature variations on the capability of the SAW sensor to detect hydrogen at atmospheric pressure. Temperature changes lead to a shift down of the delay line synchronicity frequency characterized by a sensitivity of $-219.10^{-3} \text{ } ^\circ\text{C}^{-1}$. That phase decrease totally compensates the phase shift toward the high frequency observed when detecting hydrogen in absence of any temperature changes. It appears that the delay line used as a reference do not undergoes any phase shift when exposed to heated gas since the device is temperature compensated. However, the TCF of the Pd detection channel notably changes as the Pd overlay tends to lower the 1st order TCF. This behavior currently represents an obstacle

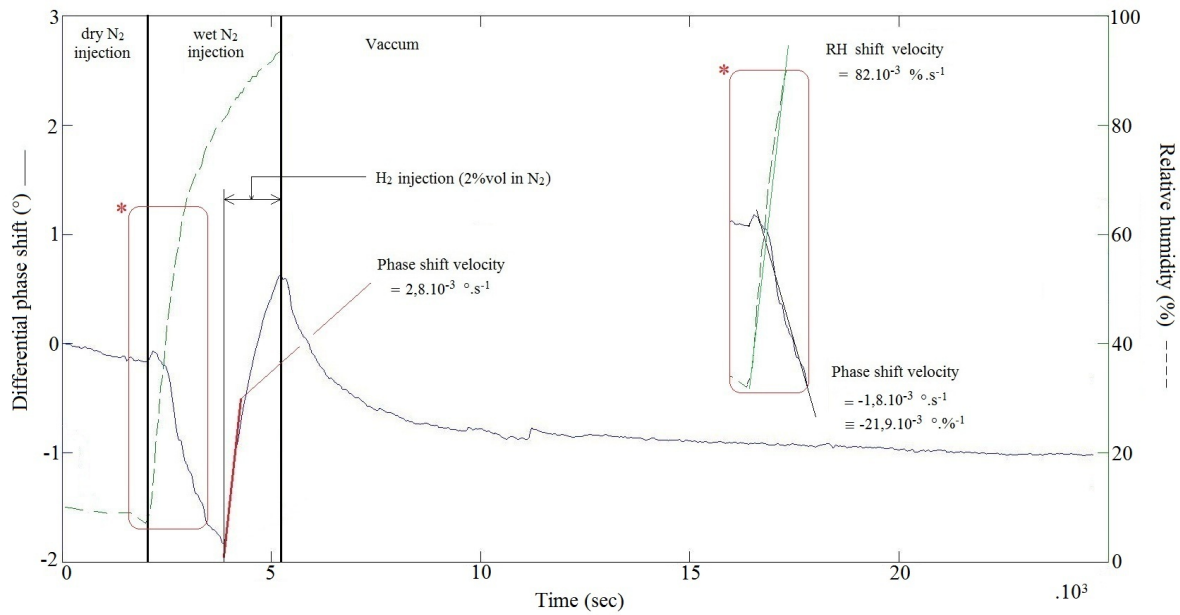


Fig. 5. Influence of humidity on the detection of hydrogen at constant room temperature ($19.3 \pm 0.1^\circ\text{C}$).

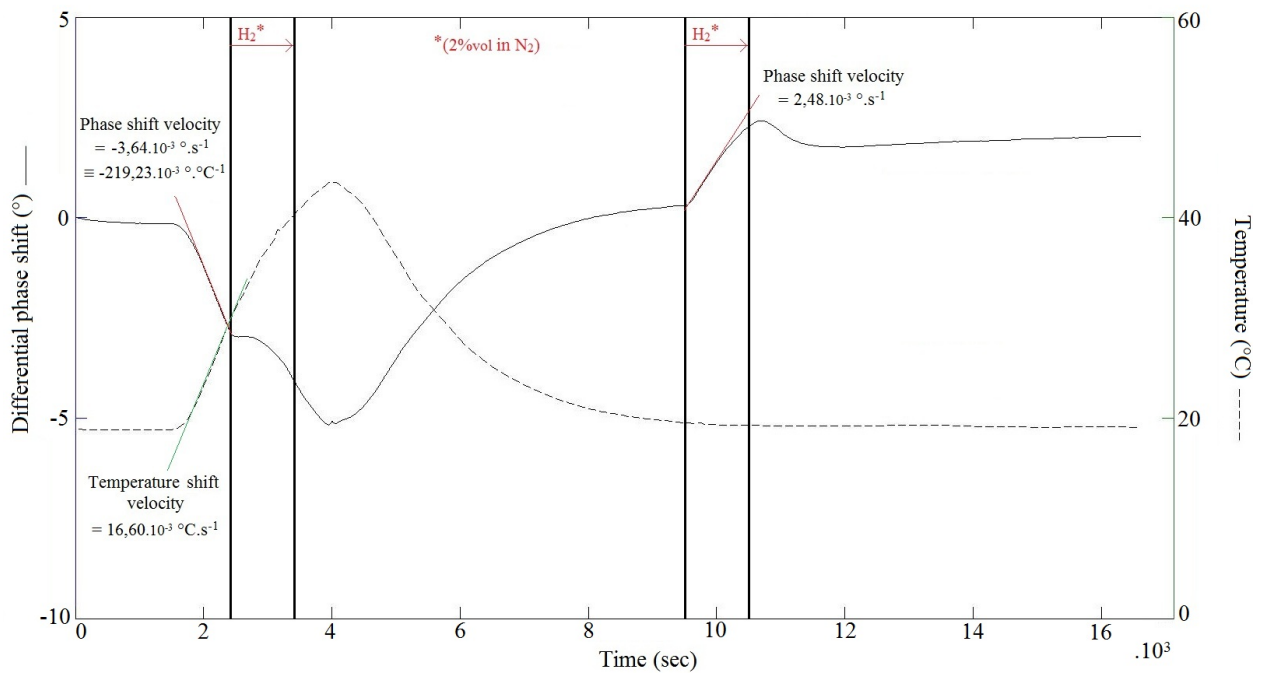


Fig. 6. Influence of temperature on the detection of hydrogen (RH in the 3-8% range).

to accurate hydrogen detection but can be avoided by the use of an appropriate reference (covered by a layer inert to hydrogen which induces the same TCF change as experienced here for the detection channel). Simulations are engaged to provide the information needed for the development of such a device. As one can see on the second part of the graph, the detection of H_2 at 2%vol in N_2 is still clearly possible considering a stable operation temperature at room conditions.

V. CONCLUSION AND FUTURE WORK

In this paper, a differential SAW sensor based on Rayleigh wave on quartz has been developed and successfully tested. The sensor consist of two adjacent delay lines, one being used as a reference and the second one being functionalized with a Pd overlay, a metal known to be affected by gaseous hydrogen. The observation of specific phase shifts on the sensitive track compared to reference in presence of gaseous hydrogen using different gas carrier did assess the operation of the sensor. The use of the Pd overlay actually allows to segregate the nature of the gas inserted in the reaction cell and provides quantitative information about its composition. The impact of temperature and humidity on the sensor operation also were analyzed. Although the differential nature of the sensor is expected to reject such interferences, it appears necessary to control this parameters at very minimum. Concerning the analysis of the sensor operation itself, some work still has to be carried out even if strong convictions arise from the experiment that the main change is related to the elastic properties of the Pd film due to hydrogen absorption. The crystalline structure of the film having an effective influence on the way hydrogen interact with the metallic film, it still has to be determined in order to improve simulation accuracy of the leverage of hydrogen absorption on the SAW device response. In this optic, further work will consist in the elaboration and characterization of palladium layers with different crystalline structures. Simulation of SAW device exhibiting different sensing layers will also be carried out in order to validate the experimental observations and to predict the structure of the delay-line to use in order to improve the differential acquisition setup. These investigations are expected to enhance the performance of our sensor in terms of sensitivity and selectivity toward outer parameters such as temperature and humidity.

REFERENCES

- [1] V. Katti, A. Debnath, S. Gadkari, S. Gupta, and V. Sahni, "Passivated thick lm catalytic type h2 sensor operating at low temperature," *Sens. Actuators B: Chem.*, vol. 84, pp. 219 – 225, 2002.
- [2] C. Ramesh, N. Murugesan, M. Krishnaiah, V. Ganesan, and G. Periaswami, "Improved naon-based amperometric sensor for hydrogen in argon," *J. Solid State Electrochem.*, vol. 12, pp. 1109 – 1116, 2008.
- [3] I. Simon and M. Arndt, "Thermal and gas-sensing properties of a micro-machined thermal conductivity sensor for the detection of hydrogen in automotive applications," *Sens. Actuators B: Chem.*, no. 9798, pp. 104 – 108, 2002.
- [4] T. Anderson, H. Wang, B. Kang, F. Ren, S. Pearton, A. Osinsky, A. Dabiran, and P. Chow, "Effect of bias voltage polarity on hydrogen sensing with algan/gan schottky diodes," *Appl. Surf. Sci.*, vol. 255, pp. 2524 – 2526, 2008.

- [5] F. D. et al., "Mems-based hydrogen gas sensors," *Sens. Actuators B: Chem.*, vol. 117, pp. 10 – 16, 2006.
- [6] T. Kiefer, A. Salette, L. Villanueva, and J. Brugger, "Large arrays of chemo-mechanical nanoswitches for ultralow-power hydrogen sensing," *J. Micromechn. Microeng.*, vol. 20, 2010.
- [7] Z. Zhao, M. Carpenter, H. Xia, and D. Welch, "All-optical hydrogen sensor based on a high alloy content palladium thin lm," *Sens. Actuators B: Chem.*, vol. 113, pp. 532 – 538, 2006.
- [8] L. Boon-Brett, J. Bousek, G. Black, P. Moretto, P. Castello, T. Hubert, and U. Banach, "Identifying performance gaps in hydrogen safety sensor technology for automotive and stationary applications," *International Journal of Hydrogen Energy*, vol. 35, no. 1, pp. 373 – 384, 2010.
- [9] T. Hubert, L. Boon-Brett, G. Black, and U. Banach, "Hydrogen sensors a review," *Sensors and Actuators B: Chemical*, vol. 157, no. 2, pp. 329 – 352, 2011.
- [10] T. Rétornaz, N. Chrétien, J.-M. Friedt, G. Martin, and S. Ballandras, "Time reversal: a flexible approach for identifying and measuring surface acoustic wave delay lines acting as wireless, passive sensors," *IFCS Proceeding*, 2012.
- [11] A. D'Amico, A. Palma, and E. Verona, "Palladium surface acoustic wave interaction for hydrogen detection," *Appl. Phys. Lett.*, vol. 41, p. 300, 1982.
- [12] W. P. Jakubik, M. W. Urbaczyk, S. Kochowski, and J. Bodzenta, "Bilayer structure for hydrogen detection in a surface acoustic wave sensor system," *Sensors and Actuators B: Chemical*, vol. 82, no. 23, pp. 265 – 271, 2002.
- [13] W. P. Jakubik, "Hydrogen gas-sensing with bilayer structures of wo3 and pd in saw and electric systems," *Thin Solid Films*, vol. 517, no. 22, pp. 6188 – 6191, 2009.
- [14] D. Phan and G. Chung, "Identifying performance gaps in hydrogen safety sensor technology for automotive and stationary applications," *Sensors and Actuators B: Chemical*, vol. 161, no. 1, pp. 341 – 348, 2012.
- [15] S. Ippolito, S. Kandasamy, K. Kalantar-Zadeh, and W. Wlodarski, "Layered saw hydrogen sensor with modified tungsten trioxide selective layer," *Sensors and Actuators B: Chemical*, vol. 108, no. 12, pp. 553 – 557, 2005.
- [16] A. Sadek, W. Wlodarski, K. Shin, R. Kaner, and K. Kalantar-zadeh, "A polyaniline/wo3 nanofiber composite-based zno/64 yx linbo3 saw hydrogen gas sensor," *Synthetic Metals*, vol. 158, no. 12, pp. 29 – 32, 2008.
- [17] D.-T. Phan and G.-S. Chung, "Surface acoustic wave hydrogen sensors based on zno nanoparticles incorporated with a pt catalyst," *Sensors and Actuators B: Chemical*, vol. 161, no. 1, pp. 341 – 348, 2012.
- [18] N. Dewan, S. Singh, K. Sreenivas, and V. Gupta, "Influence of temperature stability on the sensing properties of saw nox sensor," *Sensors and Actuators B: Chemical*, vol. 124, no. 2, pp. 329 – 335, 2007.
- [19] S. Fardindoost, A. Zad, F. Rahimi, and R. Ghasempour, "Pd doped wo3 films prepared by solgel process for hydrogen sensing," *International Journal of Hydrogen Energy*, vol. 35, no. 2, pp. 854 – 860, 2010.
- [20] D. Rabus, J. Friedt, S. Ballandras, G. Martin, E. Carry, and V. Blondeau-Patissier, "A high sensitivity open loop electronics for gravimetric acousticwave-based sensors," *EFTF Proceeding*, 2010.
- [21] V. Anisimkin, I. Kotelyanskii, P. Verardi, and E. Verona, "Elastic properties of thin-film palladium for surface acoustic wave (saw) sensors," *Sensors and Actuators B: Chemical*, vol. 23, no. 23, pp. 203 – 208, 1995.
- [22] B. Auld, "Acoustic fields and waves in solids," *Wiley*, pp. 271 – 332, 1973.
- [23] A. Slobodnik, E. Conway, and R. Delmonico, "Microwave acoustic handbook," *Air Force Cambridge Research Laboratories (distr. NTIS)*, vol. 1A, no. Report AFCRL-TR-73-0597, 1973.

Protocol Awareness: A Step Towards Smarter Sensors

Hoel Iris, François Pacull
CEA-LETI MINATEC Campus
17 rue des Martyrs, 38000 Grenoble, France
Email: hoel.iris@cea.fr ; francois.pacull@cea.fr

Abstract—Low power consumption and reliability are two important properties in the wireless sensor network area. The approach presented here to improve these aspects is to use a rule-based middleware enforcing a coordination protocol on top of the communication protocols imposed by the different wireless sensor networks. In addition, we move the callee side of this protocol from the gateway to the sensors/actuators in order to make them able to directly respond to this protocol.

The high-level coordination protocol brings on the one hand the control from the application side the activities (sleep/awake) of the sensors and on the other hand the transactional processing of operations involving a group of sensors / actuators. This has a positive impact on the consumption and on the reliability.

Keywords—Coordination Middleware; Smart Sensor; Transaction; Power Consumption.

I. INTRODUCTION

A Wireless sensor network (WSN) is a set of sensors or actuators connected together through a wireless connection. WSNs are nowadays commonly used in various domains because the absence of wire helps the deployment and decreases the installation cost.

The main components of a sensor/actuator are some sensing or acting units, a micro-controller, a transceiver and a power unit.

Basic objectives of sensor networks were accuracy, flexibility, cost effectiveness and ease of deployment. As these properties are now taken for granted, low power consumption and reliability are the next steps to consider.

The paper presents our approach to improve these aspects through a rule-based middleware [1] enforcing a coordination protocol on top of the communication protocols imposed by the different WSN. The high-level coordination protocol brings on the one hand the control from the application side the activities (sleep/awake) of the sensors and on the other hand the transactional processing of operations involving a group of sensors / actuators.

The paper is organised as follows. Section II introduces the problem to solve. We describe in Section III our approach based on the high level coordination protocol enforced by our middleware and the design of smart sensors able to react smartly to this protocol. Section IV presents the hardware we considered. In Section V we exemplify our approach both for power consumption and reliability. We conclude in Section VI.

II. PROBLEM TO SOLVE

The usual way actuator/sensor wireless networks are designed does not help to solve the two problems of *reliability* and *power consumption* as described here after.

A. Reliability

Most of the time the wireless communication policy in WSNs is only best effort. In addition, sensors are battery powered for autonomy reasons and they may stop their activities or decrease the wireless signal strength just because the battery is partially or totally discharged. Thus, there is no guaranty that a sent message is eventually received.

A traditional way to enforce reliability in an asynchronous system in presence of failures is to embed the operations involving the sensors/actuators within transactions [2]. For instance, we consider to open a windows (actuator) and to store this information in a database responsible for keeping the state of the system. If this is not embedded in a transaction, it may happen that the change in the database is done while the actuator is not reachable or on the contrary that the window is opened but the database is locked for some external reasons. As a transaction unrolls a two-phase commit (2PC) protocol if an actuator is not reachable in the first phase (i.e. reservation) then the transaction is aborted preventing the database update.

Obviously, this makes sense only if the transaction protocol really involves the actuator and not only the gateway otherwise a failure may happen in between the gateway and the actuator after the commit of the transaction.

We propose to implement smart sensors/actuators that directly provide the required transactional capabilities.

B. Power consumption

Power consumption is the sum of the powers consumed for sensing and computing activities plus the power used for the delivery of information through the radio. In general, both of these parts can be slept when they are not used. However, the main issue is precisely to define when they are not used. Indeed, we can distinguish two categories of sensors. The first one, based on an alarm (e.g. presence detector) can be easily slept until something external happens. On the contrary, the second type (e.g. temperature sensor) regularly emits the information without any idea if it is useful or not for the application. Among the improvements proposed, we may find systems that offer configuration facilities allowing the user to

define the delay between two emissions. It is also possible to avoid to emit the information if it did not change or if the change is inside a given interval that can be configured [3]. However, even if these efforts are noticeable it is far to be optimal because in general the user has little information to efficiently configure the sensors in advance since most of the knowledge appears during the execution of the application

Part of the solution is to let the initiative of the application to interrogate the sensors (pull mode) rather than trying to optimise its emission rate (push mode).

C. Our approach

Our approach is based on the combination of a rule-based middleware which coordinates the actions of a group of software components through a high level protocol. This protocol, thanks to a limited yet effective set of primitives allows on the one hand to control the interrogation of the sensors from the application side and on the other hand to embed a set of operations on sensors, actuators and software components within transactions.

In addition, we have designed sensors/actuators aware of this protocol and then able to behave like first class components of our middleware. In other words, we replaced the classical approach where the sensors are accessed via a gateway with no control on what is actually done beyond the gateway to an architecture unrolling our protocol until the physical devices. The transport layer of the sensor network is in this case a vehicle for our coordination protocol.

The usage of this protocol together with sensors aware of this protocol propose a response to the both mentioned issues: power consumption and reliability.

We describe in the next sections the middleware and its protocol and the global design of our sensors/actuators both at the software and hardware levels.

III. ARCHITECTURE APPROACH: SOFTWARE

A. Coordination Middleware

The middleware provides a uniform abstraction layer that eases the integration and coordination of the different components (software and hardware) involved in WSNs. It relies on the *Associated memory* paradigm implemented in our case as a distributed set of bags containing resources (tuples). Following Linda [4] approach the bags are accessed through the three following operations:

- `rd()` which takes as parameter a partially instantiated tuple and returns a fully instantiated tuple from the bag whose fields match to the input pattern;
- `put()` which takes as parameter a fully instantiated tuple and insert it in the bag;
- `get()` which takes as parameter a fully instantiated tuple, verifies its presence in the bag and consumes it in an atomic way.

The bag abstraction can encapsulate real tuple spaces but also databases, services, event systems, sensors and actuators. From the sensor point-of-view, a couple of bags map a set of sensors and contains the resources corresponding to basic

information: e.g. tuples (sensorid, value, timestamp) or (sensorid, type) allows to model all the data and metadata required to manipulate sensors through the `rd()` or the `get()` operations. For the actuators, the `put()` operation is used to introduce tuples under the form (actuatorid, function, parameter1, parameter2). Once inserted, the bag can actually trigger the correct action on the physical actuator with the appropriate parameters.

The tree operations `rd()`, `get()` and `put()` are used by the *Production rules* [5] to express the way these resources are manipulated in the classical *pre-condition* and *performance* phases. The rules are enacted by dedicated components called *coordinators*.

Precondition phase: It relies on a sequence of `rd()` operations to find and detect the presence of resources in several bags. This can be sensed values, result of service calls or states stored in tuplespaces or databases.

The particularity of the precondition phase is that:

- the result of a `rd()` operation can be used to define some fields of the subsequent `rd()` operation
- a `rd()` is blocked until a resource corresponding to the pattern is available
- a `rd()` operation at the right hand side of a blocked `rd()` is not active and will invoke its bags only when the previous `rd()` receives a response.

This mechanism will be used to access the sensors only when it is required by the application.

1) Performance phase: It combines the three operations `rd()`, `get()` and `put()` to respectively verify that some resources found in the precondition phase are still present, consume some resources and insert new resources. In this phase, the operations are embedded in *distributed transactions*. This particularity ensures several properties that go beyond traditional production rules. In particular it ensures that

- we can verify that the important conditions responsible for firing the rule (precondition) are still valid in the performance phase.
- the different involved bags are effectively all accessible.

These properties can improve reliability provided that the sensors are aware of the coordination protocol.

B. Protocol aware sensor

In order to make the sensors/actuators capable to understand the coordination protocol we need to implement at the sensor level the different operations that will be invoked during the enactment of the rules. In addition, we need to implement stubs that encapsulate the communication layer in order to provide to the coordinator the way to invoke transparently the remote bags.

Stub: We briefly describe how the stub mechanism is used in our middleware in figure 1. When the coordinator needs to access a given bag, it asks the nameserver in order to obtain the stub that will be used to invoke the `rd()`, `get()` and `put()` operations.

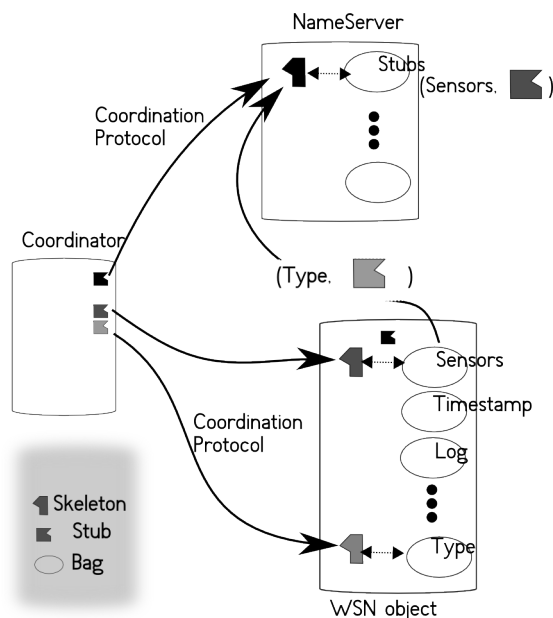


Fig. 1. stub

The name server stores the information related to the stubs as resources of one of its bag called Stubs. A stub is inserted by each bag in the name server at starting time. Once obtained by the coordinator the latter just calls the appropriate primitives via the stub and has no idea about the way they are implemented. This means that the transport layer is completely hidden at this level. A corresponding skeleton able to receive and decode the requests coming through the stub is present at each bag.

A stub allows to invoke two distinct `rd()` operations: one for the precondition phase that may block when no corresponding resource is currently available and one for the performance phase which is decomposed into a `pre_rd()` and `commit_rd()` or `abort_rd()` according to the 2PC used to enforce the transaction. The `get()` and `put()` operations are also decomposed for the same reasons.

Another point concerns the management of the wake up of the sensor since we consider that the sensor is in sleep mode by default, and wakes up before calling a primitives of the protocol. Then a signal, whose role is to wake up the sensor, is sent to it before any request. Moreover, we consider that the sensor returns in sleep more right after the termination of the `rd()` and the `commit_*`() or `abort_*`() . Different type of signals are discussed further.

Skeleton: at the sensor side: We consider now, the treatment to be done at the micro-controller side for operation of the precondition and performance phases.

The only operation required in the precondition phase is the `rd()` operation. It has the following behaviours.

If a resource is available (i.e. a value may be read and returned immediately) then the read is non-blocking. This corresponds to sensors like temperature or humidity measuring most of the time a physical value. The resource based on the

sensed value is directly returned to the stub call and nothing else has to be done.

If a resource is not available then the read needs to be blocked until a resource becomes available. This corresponds to sensors like presence sensor or threshold detector that are bind to an alarm. As it would not be efficient on a power consumption point of view to let the sensor alive just to block the `rd()` operation, we implement it in a different way. The value returned to the `rd()` warns the calling stub that nothing is currently available and that the sensor will take the initiative to send the resource when it becomes available. At the stub level, we just block. When the sensor receives the alarm (e.g. detection of a presence), which wakes it up, the resource is returned to the stub along with an identifier which allows the stub to retrieve to which `rd()` it corresponds. The resource remains stored locally in RAM at the sensor level for the performance phase. The sensor can return in sleep mode and the stub can end the process corresponding to this `rd()` .

For the performance phase, during the `pre_*`() operations, the sensor has to store intermediate informations that will be used during the `commit_*`() or `abort_*`() operations: i.e. the considered resource passed as parameter.

For the `pre_rd()` and `pre_get()` the concerned resource, if available, is locked to prevent any other `pre_*`() operation coming from other transactions to be accepted. If the resource may be locked, `ok` is returned and the lock status is locally stored. Otherwise `notok` is returned.

For the `pre_put()` we need to verify that the operation is possible. We can verify for instance that the actuator can be manipulated. Accordingly, `ok` or `notok` is returned.

If a `commit_*`() is invoked then the considered operation is effectively done: nothing for a `commit_rd()`, the destruction of the resource for a `commit_get()` and the action associated to the actuator parametrised according to the resource for a `commit_put()` . If an `abort_*`() is received then nothing is done. In all cases, the intermediate informations (locks, ...) are cleaned.

C. Model of a sensor/actuator network object

To define a prototype object that encapsulates a sensor/actuator network we can consider the following set of bags required for its management.

For the sensors part we have the following bags.

- `Sensors`: stores the sensor id and the value read
- `TimeStamps`: stores the id and last reading time
- `Log`: stores the id and reading time
- `Type`: stores the id and its type (i.e.: temperature, ...)

For the actuators part we have specific bags for the different types of actuators. These bags implement for the `put()` method the actual action to be realized to act on the physical actuator.

With a classical approach, this object is located at the gateway level as shown on Figure 2 with the first object.

With a smart sensor approach, we have decomposed the set of bags in order to let some of the bags at the gateway level and to move the others at the micro-controller side.

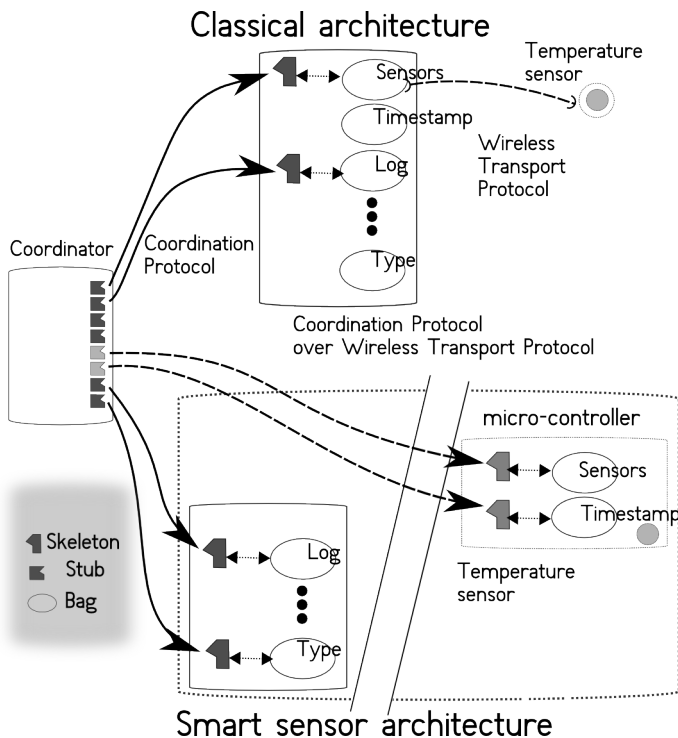


Fig. 2. Sensor network object: the smart sensor approach

Sensors and TimeStamp bags which contain respectively the value associated to a sensor and the timestamp corresponding to the last sensed value are implemented on the micro-controller side. All the other bags are implemented at the gateway side. The main reason is these bags contain information that either records the sensed value or store some status updated very sparsely. Thus, in order to save memory space and power-on time on smart sensor we keep these bags on the gateway level and we implement the bags which makes sense at the micro-controller side. For instance, if we need to access the log of the successive values read by a temperature sensor, it is not required to ask the micro-controller itself, this can be done at the gateway level. On the contrary, the current temperature needs to be asked to the micro-controller.

For an actuator, we implement the bag which is responsible for the real action on the environment on the micro-controller side since we want to ensure the transactional property. Some verifications are done during the `pre_put()` operation. For instance we can verify that the rotation we would like to do on a motor is possible without damage. We could also verify that the command is sensible: to ask to close a window that is already close is typically something that is not normal. We can also verify that the actuator is physically able to do the requested command or that the remaining energy is enough to perform the action. In case of trouble, a `notok` is returned.

IV. ARCHITECTURE APPROACH: HARDWARE

We present in this section the hardware details corresponding to the different smart sensors we implemented.

A. The platforms

We have considered three embedded platforms to experiment different levels of performance at the microcontroller level and different communication standards: *OpenPicus Flyport (Wifi-802.11)* [6], *Atmel SAM3N-EK (802.15.4)* [7] and *Arduino Pro 3.3V (802.15.4)* [8]. These three architectures are widely used for their low power and low cost characteristics. They all three offer easy-to-use development environments avoiding most of cross-compilation problems and micro-controller driver development part.

OpenPicus Flyport (Wi-Fi): This platform is based on a Microchip MRF24WB0MA/RM Wi-Fi chip and a Microchip PIC 24F 16bits processor.

The board embeds a small web-server, running on top of FreeRTOS operating system. This web server allows to encapsulate remote function call through simple URLs over HTTP protocol with a mechanism closed to cgi-scripts.

This is very similar to what is done in our middleware for the default transport layer within the stub. This allowed us a straight forward implementation of the smart sensor. This is the main reason for the choice of this board.

For the integration of physical sensors/actuators, the board offers eighteen digital I/Os and four analog inputs. Digital pins can be mapped between one I2C, one SPI, four UARTs and nine PWMs. Three different external interrupts can wake up the Flyport from standby mode.

The associated communication link is a classical Wi-Fi which allow a very easy integration in existing installation with a range that may cover the entire floor of a building.

Atmel SAM3 (802.15.4): We have used a SAM3N-EK board that was available in our laboratory with a Cortex-M3 32bits based micro-controller. This board offered a convenient experimentation framework and as the Atmel environment allows, with a same API, to target every ARM and AVR micro-controller belonging the Atmel family the solution is quite generic. This is the reason why we used this platform. The ARM Cortex-M3 core is used by many constructors, including ST Microelectronic, Atmel and Texas Instrument, to build low power but still powerful chips.

The board offers 64 I/Os including PWMs, I2Cs, SPIs, UARTs and ADCs. Some I/Os are connected at on-board LCD, buzzer, SD card host, user switch, RS232 connector or touch sensors. Sixteen different external interrupts can wake up SAM3N-EK from standby mode.

We use for the communication Digi-XBee series one modules [9], which provides IEEE 802.15.4 wireless networking protocol. A module is connected to the board via one UART and an other is plugged on the gateway via an FTDI breakout board. We use them in peer-to-peer mode. The data rate is 250Kbit/s on the 2.4GHz RF band. The maximum frame length is one hundred bytes. This is less than the Wi-Fi solution but with an adhoc encoding it is efficient enough to allow serialized procedure calls to hold into a single frame.

Arduino (802.15.4): The Arduino board we used is based on Atmel AVR 8bits architectures. It is open source and supported

by a large community. This is the reason that conducted us to use this board.

We chose the Pro 3.3V version due to the reduced on-board electronics and a working voltage that corresponds directly to XBee modules we use for the communication. The XBee module is connected to the micro-controller via the UART interface like for the Atmel board.

The board offers fourteen digital I/Os and six analog inputs. Digital pins support one UART, six PWMs and one SPI. Analogue pin could also be used for adding one I2C interface. Two different external interrupts can wake up Arduino from standby mode.

B. Power consideration

Boards: Power consumption of considered micro-controllers are under $10\mu A$ at 3.3V in standby-mode, while it is at least $5mA$ in run mode. However, in the case of the SAM3-EK Atmel board, the complete board is a development board for which at least one electronic device was not designed for low power usage. Thus, we did not considered this board for the power consumption experiment. On the contrary, openPicus Flyport and Arduino Pro 3.3V boards are designed for low power, in particular in standby-mode. The respective consumption measured with a full charge lithium-ion battery (4.1V) with wireless unit in the same state than the micro-controller are summarized in Table 1.

Micro-controller+wireless	standby	run mode
Arduino + Xbee	206 μA	57.1mA
OpenPicus Flyport + Wifi	97 μA	127.5mA

Table 1: consumption of the full board.

Wireless communication unit: XBee (802.15.4) and Wifi (802.11) have been considered: They both offer power down mode to control their power state from the micro-controller. Respective consumptions are in Table 2

Wireless module	standby	communication
Xbee	10 μA	50mA
Wifi	0.1 μA	120mA

Table 2: consumption of the wireless communication unit

The first is more expensive in standby mode but can be integrated to a larger number of micro-controllers. The second is more expensive in communication mode but it handles a bigger amount of data with a higher communication range.

Radio control: Primitives radio wake up and radio go sleep are called during the board power down and power up procedures. In this way, when micro-controllers are in run mode, the wireless communication link is available. We could have used smarter radio power control but since we are considering that the board should be sleeping most of the time we did not go further in this direction.

Sleep mode and wake up events: As in sleeping mode, the consumption is divided by at least one hundred, our approach is to force the sensor to be in sleeping mode almost all the time. It is wake up on demand either because the coordinator

send a signal before invoking the appropriate primitive or because an alarm is triggered by a physical sensor linked to the board. Both events raise a different interrupt received by the micro-controller and thus they are treated accordingly in order to execute the appropriate code (See Section III-B).

Wake up signal: For the wake up signal sent by the coordinator (gateway side) we envisaged different solutions that could be used. The first is based on a simple modulated IR signal that can be used if the gateway is in the same location than the sensor. The second is based on a less expensive wireless signal [10] (e.g. 433Mhz) that can be used to this purpose. Finally, the third may consider the new passive RFID technology working in a range of 15 meters. This problem is open and still under investigation and in our first experiment we only used the IR solution.

V. EXAMPLES

First example: consumption aspect

We consider a simple application where we collect external temperature in order to control the heating system according to the variation of the temperature and the speed of this variation. Then, we have an algorithm that defines according to a window of sensed temperatures the most appropriate time to make the next set of measures. Basically, if the temperature does not change a lot we increase the delay between two measures and we decrease it if the variation increase. It is impossible to compute in advance the time when the measurement need to be done.

The classical way is to ask the sensors to send the information each $\delta(t)$ and to sleep the rest of the time. With $\delta(t) = 5mn$, we have $24 * 12$ measures sent by each sensor to the gateway per day. Most of them will not be used at all and for some of them we have inaccuracy due to the acquisition rate that does not match exactly the algorithm.

If we use a rule triggering the interrogation of the sensors upon the insertion of a resource by the algorithm, we first remove the inaccuracy and second we can decrease the activity of the sensors to the exact required number of measures. We consider that the number of really useful measures is only 50 per day. The ratio is 0.17 (5 times less).

The average power consumption PC is given by

$$PC = R * C_{RunMode} + (1 - R) * C_{StandbyMode} \quad (1)$$

with R the run time ratio $R = \frac{RunTime}{TotalTime}$. We have measured that a run period (wake-up, send, sleep) takes 0.04 seconds for the Arduino and 1 second for the Flyport. It gives the following ratio for classical (C) and smart sensor (S) implementations.

$$R_C = \frac{24 * 12 * 1}{24 * 60 * 60} = 0,333\%$$

$$R_S = \frac{50 * 1}{24 * 60 * 60} = 0,058\%$$

Reported to equation (1) we obtain with the figures of Table 1 for the Flyport board the both implementations.

$$C_C = 33310^{-5} * 127.5 + (1 - 333.10^{-5}) * 0.091 = 0.516mA$$

$$C_S = 57.810^{-5} * 127 + (1 - 57.8.10^{-5}) * 0.091 = 0.165mA$$

and for the Arduino

$$R_C = \frac{24 * 12 * 0.04}{24 * 60 * 60} = 0,0133\%$$

$$R_S = \frac{50 * 0.04}{24 * 60 * 60} = 0,00231\%$$

$$C_C = 13310^{-6} * 57.1 + (1 - 13310^{-6}) * 0.206 = 0.2135mA$$

$$C_S = 23.110^{-6} * 57.1 + (1 - 23.110^{-6}) * 0.206 = 0.2073mA$$

If we consider a battery capacity Cap , the following formulae gives the saved time in hour.

$$H = \frac{Cap}{C_S} - \frac{Cap}{C_C} \tag{2}$$

With a capacity $Cap = 1300mAh$ for the battery we save $H = 7892 - 2521 = 5371 hours$ i.e. 244 days for the Flyport and $H = 6270 - 6087 = 183 hours$ i.e. 8 days for the Arduino. The battery allowing respectively 328 days for the Flyport and 261 days for the Arduino.

Micro-controller+wireless	Classical	Smart	Gain
Arduino + Xbee	253 days	261 days	3%
OpenPicus Flyport + Wifi	105 days	328 days	68%

Table 3: Battery autonomy for both approach.

The interesting result is that solving the power consumption issue only acting on the consumption of the wireless communication unit is probably not the unique research direction. Indeed, with the classical approach the Arduino is far better thanks to its very low consumption when running while with the smart sensor approach the Flyport is far better the Arduino thanks to its very low consumption in standby. This means that using a simpler to deploy communication protocol (i.e. Wifi) is affordable if used in a smarter way.

Second example: transactional aspect

We consider a mobile robot equipped with a pan-tilt camera that follows a moving object. We have an external software component that computes from captured images the next positions of the robot and the camera in order to have the object centred. New positions are inserted in the respective bags as parameters of the motors controlling the pan, the tilt and the robot.

We have different competing rules moving the robot and the camera. They use a common ticket resource which ensures that only one of them will be performed. This means that we can have the object centred by moving the robot or by moving the camera. If the rule moving the camera is aborted because for instance the requested move for the pan cannot be physically done. Then, the rule moving the robot can be triggered to compensate the default of the camera. On the contrary, if the robot is blocked and thus cannot move, the rule controlling the camera may be considered. The possibility to propose alternative treatments to solve a problem that can take into account physical limitation of an actuator is provided almost for free at the middleware level.

VI. CONCLUSION

We have presented an approach to improve power consumption and reliability in the wireless sensor network area. This approach is based on a high level rule-based middleware that coordinates the operations involving the sensors and actuators. This offers the possibility to activate the sensors with a signal (external to the communication) when they are really needed and thus let them most of the time in standby mode to reduce power consumption. In addition the coordination protocol allows to embed actions on sensors and actuators within transactions to improve reliability. We have implemented three different smart sensor boards able to understand the coordination protocol of our rule based middleware.

Finally our contribution has been illustrated from a power consumption and reliability improvement point of view with two basic examples that show the possibilities offered by our approach.

ACKNOWLEDGMENT

This work has been partially funded by the FP7 SCUBA project under grant nb 288079.

REFERENCES

- [1] L.-F. Ducreux, C. Guyon-Gardeux, S. Lesecq, F. Pacull, and S. R. Thior, "Resource-based middleware in the context of heterogeneous building automation systems," in *38th Annual Conference of the IEEE Industrial Electronics Society (IECON 2012)*, 2012.
- [2] P. A. Bernstein, V. Hadzilacos, and N. Goodman, *Concurrency control and recovery in database systems*. Boston, MA, USA: Addison-Wesley Longman Publishing, 1987.
- [3] S. Feizi, G. Angelopoulos, V. Goyal, and M. Medard, "Energy-efficient time-stampless adaptive nonuniform sampling," in *Sensors, 2011 IEEE*, oct. 2011, pp. 912 -915.
- [4] N. Carriero and D. Gelernter, "Linda in context," *Commun. ACM*, vol. 32, pp. 444-458, April 1989.
- [5] T. A. Cooper and N. Wogrin, *Rule Based Programming with OPS5*. Morgan Kaufmann, July 1988.
- [6] "OpenPicus Flyport Documentation Repository ," <http://http://www.openpicus.com/site/downloads/downloads>, 2012.
- [7] "SAM3N-EK Documentation Repository ," <http://www.atmel.com/tools/SAM3N-EK.aspx?tab=overview>, 2012.
- [8] "Arduino board Documentation Repository," <http://arduino.cc/en/Main/ArduinoBoardPro>, 2012.
- [9] "XBee-PRO 802.15.4 OEM RF Modules," <http://http://www.digi.com/xbee>, 2012.
- [10] S. J. Marinkovic and E. M. Popovici, "Nano-power wireless wake-up receiver with serial peripheral interface." *IEEE Journal on Selected Areas in Communications*, vol. 29, no. 8, pp. 1641-1647, 2011.